The Dissertation Committee for Vaidyanathan Mathamangalath Sethuraman certifies that this is the approved version of the following dissertation:

Inverse Coarse–Graining Methodologies to Understand Ion Transport in Block Copolymer Electrolytes

Committee:

Venkat Ganesan, Supervisor

Isaac Sanchez C.

Thomas M. Truskett

Christopher J. Ellison

Pengyu Ren

Inverse Coarse–Graining Methodologies to Understand Ion Transport in Block Copolymer Electrolytes

by

Vaidyanathan Mathamangalath Sethuraman,

DISSERTATION

Presented to the Faculty of the Graduate School of

The University of Texas at Austin

in Partial Fulfillment

of the Requirements

for the Degree of

DOCTOR OF PHILOSOPHY

THE UNIVERSITY OF TEXAS AT AUSTIN

December 2017

Dedicated to my parents, Jyothi Akka and Lallu Akka.

Acknowledgments

I express my sincere gratitude to Prof. Venkat Ganesan for his constant support throughout the project. Without his profound help, I would not have reached so far. He was extremely patient with me and was there to guide me when I lost track of my work. He was very supportive when I made errors during the course of my thesis work. I take this opportunity to thank Prof. Venkat Ganesan for patiently guiding me through my studies.

I also want to thank Dr. Victor Pryamitsyn for helpful discussions and guidance. He was very enthusiastic in clearing the conceptual doubts I had and it was a pleasure to discuss with him on both subject matters and otherwise. I also thank Dr. Santosh Mogurampelly for his patient efforts to teach me fundamentals of different molecular dynamics techniques and packages. He was extremely uncomplaining while clearing both technical doubts and conceptual doubts. I also thank Dr. Grant Willson for giving me an opportunity to collaborate with his experimental work.

At this juncture, I would like to thank all the teachers and gurus in my life who made me what I am. Their constant inspiration, guidance and support have helped me to reach this level successfully.

My life in lab would not have been enjoyable without the amazing company of my labmates. I take this opportunity to thank Dylan and Gunja

who helped me to get accustomed to the new place and in helping me to get through the difficult phases in my first few years. I am grateful to Dylan for the countless hours that have been spent discussing everything from work to life.

My latter part of my life in lab was made colorful, thanks to the company of Rituparna, Jordan and Bill. I take this opportunity to sincerely thank them for all the support they gave me while I was writing the thesis and looking for job opportunities. I also thank the undergraduates and summer interns who worked in the lab and gave me an opportunity to guide them.

Life in Austin was made happy and cheerful, thanks to the company of my beautiful friends and family - Bharathwaj, Mahesh, Arjun, Kiran, Hiranmayi, Padmini, Sangeetha, Jaison Chetan and family, GAMA association, Srijith, Ashwin, Kurian, Ritu, Tushti and Ajinkya. I thank each and everyone of them from the deepest of my heart.

I also thank my parents and sisters for their unwavering support throughout my studies. Without their love, compassion and support I would not have completed my studies successfully. Lastly, I also thank God Almighty for His blessings.

Inverse Coarse–Graining Methodologies to Understand Ion Transport in Block Copolymer Electrolytes

Publication No. _____

Vaidyanathan Mathamangalath Sethuraman, Ph.D.
The University of Texas at Austin, 2017

Supervisor: Venkat Ganesan

This research is focused on two fronts (i) developing multiscale simulation strategies for multicomponent polymers to generate equilibrated self–assembled morphologies at both mesoscopic and atomistic length scales (ii) understanding the conformational attributes and dynamics of polymers in structured morphologies to understand the ion–transport mechanisms in block copolymer electrolytes.

First part of the work is devoted in developing strategies to create equilibrated block copolymer morphologies below ODT with hard repulsive potentials. To this end, ordered morphologies with the help soft repulsive potentials are generated which possess equilibrated long range order within very short computational time. A rigorous mapping between the interaction

parameters of the hard and soft potentials is then utilized to obtain the intermolecular interaction parameter of the soft potential corresponding to the target hard potential repulsion parameter.

Subsequent to establishing the long range structure, short repulsive potential (within a coarse-grained framework) is reintroduced and equilibrated to generate ordered morphologies using hard repulsive potentials. Further to this, both topological and dynamic properties in ordered lamellar phases were characterized. The topological constraints are seen to increase with increasing degree of segregation. On characterizing the local dynamics of polymeric segments, we found that inhomogeneities exist in the spatially local dynamics and the length scale of perturbation of such inhomogeneities is controlled by the interfacial width of the block copolymer.

The last part of the work involved the generation of ion–doped block copolymer melts at the atomistic level and to compare the results obtained therein with those for pure homopolymeric melts. To this end, we employed a multiscale simulation method to generate PS–PEO block copolymer doped with $LiPF_6$ ions. Our results demonstrate that the cation-anion radial distribution functions (RDF) display stronger coordination in the block copolymer melts compared to pure PEO homopolymer melts. Radial distribution functions isolated in the PEO and PS domains demonstrate that the stronger coordination seen in BCPs arise from the influence of both the higher fraction of ions segregated in the PS phase and the influence of interactions in the PS domain. Further, the cation-anion RDFs display spatial heterogeneity, with a

stronger cation-anion binding in the interfacial region compared to bulk of the PEO domain.

Investigations into the ion transport mechanisms in PS-PEO block copolymer melt reveal that ions exhibit slower dynamics in both the block copolymer (overall) and in the PEO phase of the BCP melt. Such results are shown to arise from the effects of slower polymer segmental dynamics in the BCP melt and the coordination characteristics of the ions. Polymer backbone-ion residence times analyzed as a function of distance from the interface indicate that ions have a larger residence time near the interface compared to that near the bulk of lamella, and demonstrates the influence of the glassy PS blocks and microphase segregation on the ion transport properties. Ion transport mechanisms in BCP melts reveal that there exist five distinct mechanisms for ion transport along the backbone of the chain and exhibit qualitative differences from the behavior in homopolymer melts.

Table of Contents

List of Tables

List of Figures

Chapter 1

Introduction

1.1 Introduction

Recent developments in different industries like microelectronics [4–7], water filtration [8, 9], fuel cells [10–14], food and drug processing [15] etc. have demanded materials possessing multiple physical properties. Such developments have resulted in a paradigm shift in the research of polymeric materials wherein the focus changed from processing single component polymeric materials to multicomponent materials like block copolymers [16, 17], rod–coil polymers, polymer blends [18, 19], and polymer solutions. A unique property common to many such polymeric systems is the occurrence of micro and nanoscale equilibrium morphologies below a particular temperature [20]. The ability to form such patterns along with the intrinsic physical properties of the individual components has attracted such materials as suitable candidates for the applications mentioned above.

The nanoscale patterns and material properties exhibited by the multicomponent polymers have been shown to be intrinsically coupled to the composition of its constituent components and temperature. As a consequence, recent experimental studies have focused on tuning composition and temper-

ature to obtain the desired morphologies having required material properties [9, 21–23]. One of the major areas wherein such developments are at large is the area of batteries [12]. We discuss some of the latest developments in the area of lithium ion batteries which utilized multicomponent polymer systems to render the desired material properties for different applications and discuss the pertinent unresolved issues in such studies which motivate the present research work.

The latter half of the last century witnessed a significant development on researches related to renewable and sustainable energy sources. Such studies have paved the way to the development of electrochemical devices such as Lithium ion batteries and fuel cells as an alternative to the conventional energy sources [7, 9, 21, 24]. One of the key components that affects the performance of such batteries and fuel cells is the electrolyte that facilitate ion transport between electrodes. Solid polymer electrolytes (SPE) have emerged as attractive candidates for such a function owing to its nonflammability characteristics [21]. Until early 2000s, homopolymeric electrolytes were the focus of research and have been proven to be extremely successful in the battery industry.

Pioneering experiments by Shi *et.al.,* [25] demonstrated that the ionic conductivity reduced at high molecular weights (MW) of the polymer. Since the mechanical strength increased with MW, such results showed a trade–off between mechanical strength and ionic conductivity, especially at high MWs. Hence the development of polymer membranes with both high conductivity

and mechanical strength has become one of the primary goals in researches conducted in this field.

The inherent limitation of homopolymer membranes is the lack in ability to control multiple physical properties independently. Recent experiments on block copolymer systems with blocks made up of conducting and non-conducting blocks have showed that both the conductivity and the mechanical strength increases for block copolymers with increasing molecular weight (MW) [21, 24, 26–28]. This result contrasts with its homopolymer counterparts wherein the conductivity decreases with increasing MW, thereby leading to a trade off between the mechanical and transport properties in homopolymer systems. Nevertheless, beyond some speculative arguments [28, 29], the microscopic origins of such observations remain unresolved. Moreover, the role of morphology in influencing the ion transport properties is not clarified.

To develop a fundamental understanding on the interplay between the morphological characteristics and physical properties of multicomponent systems, an extremely large parametric space needs to be studied. Such analyses are prohibitively expensive from an experimental point of view. In contrast, computer simulations can be used as an alternative to both obtain deeper insights into the experimental observations and to propose guidelines for experiments for developing materials with desired qualities at a low cost. However, the major impedance for such simulations is that achieving equilibrated self assembled phases of block copolymers within models incorporating harsh excluded volume interactions proves to be a computationally involved task

because such systems evolve extremely slow towards their equilibrium morphologies [30]. To circumvent this issue, researchers have focused on using soft intermolecular interaction potentials that can equilibrate block copolymer morphologies within reasonable computational time [31–33]. However such approaches coarse grain over many degrees of freedom and hence eliminate potentially many of the interesting dynamical properties of the polymer chains. As an alternative to the use of such approaches, some works have used a prebuilt configurations of models of more realistic potentials [30, 34–36]. However, it is not clear if such morphologies necessarily correspond to the true equilibrium configurations at the specified conditions.

To address the above mentioned issues, this research work focuses on developing multiscale simulation strategies which can be applied to a wide variety of multicomponent polymeric systems. In particular, we target self–assembled morphologies of such systems and propose to explore inverse coarse graining strategies. In such approaches, we start with soft coarse-grained potentials to equilibrate the long range structure of the system which is then followed by a reintroduction of the more realistic interactions. The final equilibrated morphologies can be utilized either to understand the transport and mechanical properties of block copolymers in such phases or to understand the transport properties of ions through such systems at different length scales.

In pursuit of answering the ion transport mechanisms in such self–assembled morphologies, we achieved the following through this work:

1. Developed a multiscale modeling which can be utilized to generate equilibrium configurations using realistic potentials.

2. Studied the static and dynamic properties of the polymers in ordered phases from a coarse–grained perspective.

3. Studied the influence of microphase segregation on both entanglements and normal modes of the diblock copolymer melts.

4. Dynamic properties of the melts were studied at both the chain level and at the spatially local level.

5. Generated equilibrium atomistic structure of ion doped block copolymer system in the ordered lamellar phase and such atomistic structures were used to understand the backbone–ion coordination features and the ion transport mechanisms in microphase segregated block copolymer melts.

A small summary of the results obtained for each of the above studies are discussed in the next section along with the organization of the rest of the thesis.

1.2 Organization of Thesis

This section discusses a brief outline of the rest of the thesis. The theoretical methods and the application of such theoretical methods to generate ordered polymer phases are described initially. Subsequently, the results

obtained for various conformational and dynamic properties of such ordered polymeric phases at both mesoscopic and atomistic length scales are discussed.

1.2.1 Chapter 2: Coarse-Graining in Simulations of Multicomponent Polymeric Systems.

In this Chapter, we investigated the mapping required between the interaction parameters of two different coarse-grained simulation models to ensure a match of the long-range structural characteristics of multicomponent polymeric system. The basis for our studies is the recent work of Morse and workers, which demonstrated the existence of a mapping between the interaction parameters of different coarse-grained simulation models which allows for a matching of the peak of the disordered state structure factor in symmetric diblock copolymers. We investigate the extensibility of their results to other polymeric systems by studying a variety of systems, including, asymmetric diblock copolymers, symmetric triblock copolymers and diblock copolymer-solvent mixtures. By using the mapping deduced in the context of symmetric diblock copolymers, we observe excellent agreement for peak in the inverse structure between both two popular coarse grained models for all sets of polymeric melt systems investigated, thus showing that the mapping function proposed for diblock copolymer melts is transferable to other polymer melts irrespective of the blockiness or overall composition. Interestingly, for the limited parameter range of polymer-solvent systems investigated in this article, the mapping functions developed for polymer melts are shown to be equally effective in mapping the structure factor of the coarse-grained simula-

tion models. We use our findings to propose a methodology to create ordered morphologies in simulations involving hard repulsive potentials in a computationally efficient manner. We demonstrate the outcomes of methodology by creating lamellar and cylindrical phases of diblock copolymers of long chains in the popularly used Kremer-Grest simulation model.

1.2.2 Chapter 3: Entanglements in Lamellar Phases of Diblock Copolymers

Subequent to generating ordered lamellar phases using coarse–grained potential in the previous Chapter. We employed (MD) simulations in conjunction with topological analysis algorithms to investigate the changes, if any, in entanglement lengths of flexible polymers in ordered lamellar phases of diblock copolymers. Our analysis reveals a reduction in the average entanglement spacing of the polymers with increasing degree of segregation between the blocks. Furthermore, the results of the topological analysis algorithms indicates an inhomogeneous distribution of entanglement junctions arising from the segregated morphology of the block copolymer. To understand such trends, we invoke the packing arguments proposed by Kavassalis and Noolandi in combination with the framework of polymer self-consistent field theory (SCFT) and Monte Carlo simulations. Such an analysis reveals qualitatively similar characteristics as our MD results for both the average entanglement spacing and the inhomogeneities in entanglements. Together, our results provide evidence for the changes in entanglement features arising from compositional inhomogeneities and suggests that the ideas embodied in packing arguments

may provide a simple means to semi-quantitatively characterize such modifications.

1.2.3 Chapter 4: Influence of Molecular Weight and Degree of Segregation on Local Segmental Dynamics of Ordered Block Copolymers

In this Chapter, we discuss results of molecular dynamics simulations studying the spatial inhomogeneities in segmental dynamics of lamellar diblock copolymer systems where the blocks possess different mobilities. We probed the local average relaxation times and the dynamical heterogeneities as a function of distance from the interface. Our results suggest that the relaxation times of rubbery segments are strongly influenced by both the spatial proximity and the relative mobility of the glassy segments. Scaling of our results indicate that the interfacial width of the ordered phases serves as the length scale underlying the spatial inhomogeneities in segmental dynamics of the fast monomers. We also present results on the relationship between the local segmental dynamics and the tagged monomer dynamics in lamellar phases of diblock copolymers. Our results demonstrate that monomer relaxation times do not provide directly a quantitatively accurate measure of the spatial variations in segmental dynamics. However, a convolution of the monomer density distributions with their corresponding relaxation times is shown to provide an approximate, but accurate quantitative characterization of the average local segmental dynamics.

1.2.4 Chapter 5: Segmental Dynamics in Lamellar Phases of Tapered Copolymers

Recent experiments have reported that the lamellar phase of salt-doped tapered copolymers exhibit higher ionic conductivity compared to those seen in similar morphologies of diblock copolymers. Such observations were in turn rationalized by invoking the corresponding glass transition temperature of the segregated copolymers. In this Chapter we report the results of coarse–grained molecular dynamics simulations to identify the mechanisms underlying such characteristics. Explicitly, we present results for the combined influences of the degree of segregation and the disparity in mobilities of the segments of the two blocks, upon the local relaxation dynamics of tapered copolymers segregated in lamellar phases. Our results show that the local dynamics of tapered copolymers depend on two independent factors, *viz.,* the degree of segregation of such copolymers relative to their order-disorder transition temperature, and the relative mobilities (glass transition temperatures) of the two blocks. In qualitative correspondence with experiments, we find that for appropriate combinations of mobility ratios and degree of segregation, the lamellar phases of tapered copolymers can exhibit faster local segmental dynamics compared to diblock copolymers.

1.2.5 Chapter 6: Normal Modes and Dielectric Spectra of Diblock Copolymers in Lamellar Phases

In this Chapter, we present results for the normal mode dynamics and frequency dependent dielectric relaxation spectra of diblock copolymers in

lamellar phases using molecular dynamics simulations. In contrast to previous works which have relied on the applicability of Rouse modes, we effect an explicit normal mode analysis of the chain dynamics in the ordered phases in the directions parallel and perpendicular to the lamellar plane. We consider two models to isolate the specific effects arising from the morphological ordering and mobility disparities between the blocks. For systems with no mobility disparity between the blocks, our analysis demonstrates that both the normal modes and their relaxation dynamics in the planes parallel and perpendicular to the lamella exhibit deviations from the Rouse modes. For systems in which the mobility of one of the blocks was frozen in the lamellar phase, the normal modes closely resembled the Rouse modes for tethered polymers. However, the relaxation dynamics of such modes exhibited deviations from expectations for tethered chains. The changes in the normal mode dynamics manifest as shifts and broadening of the normal dielectric spectra. Together, our results serve to clarify the dielectric spectra effects resulting from the ordering of diblock copolymers into self-assembled morphologies.

1.2.6 Chapter 7: Multiscale Simulations of Lamellar PS-PEO Block Copolymers doped with $LiPF_6$ Ions

In this Chapter we present results after extending our simulation methods to identify the conformational properties of block copolymer melts at the atomistic level. We present atomistic simulations of the structural equilibrium properties of PS-PEO block copolymer (BCP) melt in the ordered lamellar phase doped with $LiPF_6$ salt. A hybrid simulation strategy, consisting of steps

of coarse-graining and inverse coarse-graining, was employed to equilibrate the melt at an atomistic resolution in the ordered phase. We characterize the structural distributions between different atoms/ions and compare the features arising in BCPs against the corresponding behavior in PEO homopolymers for different salt concentrations. In addition, the local structural distributions are characterized in the lamellar phase as a function of distance from the interface. The cation-anion radial distribution functions (RDF) display stronger coordination in the block copolymer melts compared to pure PEO homopolymer melts. Further, the cation-anion RDFs display spatial heterogeneity, with a stronger cation-anion binding in the interfacial region compared to bulk of the PEO domain. Radial distribution functions isolated in the PEO and PS domains demonstrate that the stronger coordination seen in BCPs arise from the influence of both the higher fraction of ions segregated in the PS phase and the influence of interactions in the PS domain. Such a behavior also manifests in the cation-anion clusters, which show a larger fraction of free ions in the BCP. Whilst the average number of free anions (cations) decrease with increasing salt concentration, higher order aggregates of $LiPF_6$ increase with increasing salt concentration. Further, the cation-anion RDFs display spatial heterogeneity, with a stronger cation-anion binding in the interfacial region compared to bulk of the PEO domain.

1.2.7 Chapter 8: Ion Transport Mechanisms in Lamellar Phases of Salt–Doped PS-PEO Block Copolymer Electrolytes

We present results which investigateg the mechanisms underlying ion transport in the lamellar phase of polystyrene-polyethylene oxide (PS-PEO) block copolymer (BCP) electrolytes doped with $LiPF_6$ salts in this Chapter. Explicitly, we compare the results obtained for ion transport in the microphase separated block copolymer melts to those for salt–doped PEO homopolymer melts. In addition, we also present results for dynamics of the ions individually in the PEO and PS domains of the BCP melt, and locally as a function of the distance from the lamellar interfaces. When compared to the PEO homopolymer melt, ions were found to exhibit slower dynamics in both the block copolymer (overall) and in the PEO phase of the BCP melt. Such results are shown to arise from the effects of slower polymer segmental dynamics in the BCP melt and the coordination characteristics of the ions. Polymer backbone-ion residence times analyzed as a function of distance from the interface indicate that ions have a larger residence time near the interface compared to that near the bulk of lamella, and demonstrates the influence of the glassy PS blocks and microphase segregation on the ion transport properties. Ion transport mechanisms in BCP melts reveal that there exist five distinct mechanisms for ion transport along the backbone of the chain and exhibit qualitative differences from the behavior in homopolymer melts. We also present results as a function of salt concentration which show that the ion diffusivity decreases with increasing salt concentration, and correspondingly the ion residence times

near the polymer backbone increase with increasing salt concentration.

1.2.8 Chapter 9: Summary and Future Work

In this final Chapter, we summarize the salient results of our work. We also present the scope for future work in this Chapter.

Chapter 2

Coarse-Graining in Simulations of Multicomponent Polymer Systems

2.1 Introduction

Ordered morphologies of block copolymers are used in a wide range of applications, such as serving as templates for semiconductor materials [6], battery materials which integrate mechanical strength and functionality [7], photonic bandgap materials [37] etc. A precise understanding of the morphologies of self-assembly [38], their kinetics of formation [39], and their properties is essential for fruition of many of these applications. In this context, theoretical models and computer simulation tools have emerged as an efficient option to study such phenomena over a wide range of parametric conditions [32, 40–44]. Indeed, over the past few decades, efficient approaches have been developed to characterize the equilibrium morphologies in di- and multiblock copolymers [32, 45–47], study the influence of confining surfaces [48, 49], identify the kinetic pathways of self assembly [50, 51] etc. [1]

Despite the seminal advances discussed above, computer simulation

[1] Citation: Vaidyanathan Sethuraman, Bryan H. Nguyen, Venkat Ganesan, "Coarse Graining in Multicomponent Polymers", *J. Chem. Phys*, **141**, 244904 (2014). Bryan H. Nguyen ran simulations for some parts and Venkat Ganesan guided the project.

methodologies which can characterize the *properties* of ordered phases of block copolymers are still considerably lagging relative to the developments focusing on their morphological characteristics. One of the issues is that much of the structural methodologies and tools have been based on coarse-grained descriptions of the polymeric molecules and their architecture [52, 53]. Such coarse-grained descriptions have typically used simple micromechanical models to characterize the conformations of the macromolecules and supplement such descriptions with soft intermolecular interaction potentials which capture the essential physics underlying self-assembly in such systems [54, 55]. Simulations of such models have either been facilitated by the analytical descriptions [41–44] accommodated by such coarse-grained models or the fast equilibration times accompanying their simulations [55–58]. In contrast, characterizing the properties of such ordered phases requires, in many instances, an atomistic level of detail or at least models which retain the hard repulsive interactions between the polymer segments [59, 60]. Unfortunately, there is a lack of methodologies or toolsets to create self-assembled morphologies while accommodating such level of detail in the interaction potentials.

A possible approach to overcoming the above issue is to use soft coarse-grained interaction potentials to create the equilibrium configurations of self-assembled morphologies, and then reintroduce (progressively, if needed) finer scale details. Such an idea is loosely based on the fact that in the context of multicomponent polymers, the dynamics of phase separation and self-assembly are determined by the evolution of the composition fields [32, 41, 61]. The in-

stantaneous chain conformations at the segmental level are closely tied to the prevailing inhomogeneous concentration fields, and they relax almost "instantaneously" on the time scales of evolution of the composition fields. At an even finer level, the atomistic scale chain details may be assumed to be tied to the prevailing segmental level conformations, and relax almost "instantaneously" to the prevailing segmental level conformations. Hence, one may envision a strategy which captures the compositional ordering and its equilibration through the use of coarse-grained models and interactions, and then introduce the missing fine scale details within the pervading morphology to equilibrate such degrees of freedom [62]. Finally, the equilibrated ordered morphologies may be used as the starting point for probing properties such as glass transition, mechanical strength etc.

A key to the success of the above methodologies is the requirement that the coarse-grained interactions faithfully capture the physics embodied in the finer scale descriptions which promotes the ordering and structure of the underlying material. There are atleast two approaches to achieve this: (i) One approach would be to use many of the recently developed coarse-graining formalisms to rigorously relate the coarse-grained interactions to the fine scale potentials [63–70]. While such methodologies provide an in-principle exact means to obtain the coarse-grained interactions, a disadvantage is the need to effect such coarse-graining procedure for every system parameter and condition of interest. Moreover, the coarse-graining formalisms themselves are computationally intensive and involves different approximations. Finally, ex-

cepting a few isolated reports of inverse coarse-graining studies [62], we are not aware of anyone using such methodologies as a means to achieve self-assembled phases in multicomponent polymers; (ii) An alternative approach, is to choose the parameters in the coarse-grained simulations such that they correspond to some appropriate coarse-grained macroscopic interactions characterizing the polymer monomers or segments of the finer scale model. For instance, in the context of multicomponent polymer systems, the Flory Huggins interaction parameter, typically denoted as χ, has served as a useful macroscopic and experimentally characterizable measure of the interactions between different polymer monomers [20]. Hence, by performing coarse-grained simulations with the interactions chosen to correspond to χ parameters between the monomers or segments, one may expect to achieve realistic morphological characteristics corresponding to the system of interest. Subsequently, one may reintroduce the finer scale details into the coarse-grained system and allow the system to relax within the ordered morphologies.

This work is specifically concerned with our efforts to pursue approach (ii) discussed above as a means to achieve ordered morphologies in multicomponent polymeric systems at a level wherein the atomistic details or the hard-core intermolecular interactions are retained. As test case, we chose two popular models which embody different levels of coarse-graining:
(i) A soft-core potential based model which has formed the basis for many dissipative particle dynamics [58] (DPD) simulations of polymer systems. Despite the fact that the interaction potential can be used within the context of

any classical simulation approach, for ease of notation in this work we term such an approach as the DPD approach. In such a model, the potentials used are often of the form

$$U_{ij}(r) = \begin{cases} \frac{a_{ij}(r-r_c)^2}{2r_c^2}, & r \leq r_c \\ 0, & r > r_c \end{cases} \tag{2.1}$$

where r_c is the cut off radius and a_{ij} is the DPD interaction parameter between components i and j. For such a model, Groot and Warren [58] published a simple parametrization, based on interfacial density profiles of polymer blends, to relate the a_{ij} in Eq. (2.1) to the Flory-Huggins interaction parameter χ_{ij} between the components i and j,

$$\chi_{ij} = (0.286 \pm 0.002)\Delta a \tag{2.2}$$

where $\Delta a = a_{ij} - (a_{ii} + a_{jj})/2$. The above equation has served as the basis for most of the works which have followed it and used it for simulating complex mixtures of multicomponent polymers [31, 58, 71–75] (see Wijmans *et al.,* [76] for an alternate parametrization);
(ii) A hard-core potential model, commonly referred to as the Kremer-Grest [40] model which has formed the basis of many MD simulations of homopolymer and some block copolymer systems and has an intermolecular potential of the form:

$$U_{ij}(r) = \begin{cases} 4\epsilon\left[(\sigma/r)^{12} - (\sigma/r)^{6}\right] + \epsilon, & r \leq 2^{1/6}\sigma \\ 0, & r > r_c \end{cases} \tag{2.3}$$

where ϵ is the interaction parameter between monomers and σ diameter of the monomer. Such a potential retains the strongly repulsive interactions between

the polymer segments and is closer in representation to the united atom force fields developed for describing the interactions between molecules [77]. In this work, we refer to the above interaction model (Eq. (2.3)) as the KG model. In such a case, most works have used the mapping derived from the Flory's theory for polymer blends [78] which posits that

$$\chi_{ij} = \frac{z\Delta\epsilon}{k_B T} \tag{2.4}$$

where z denotes inter-molecular coordination number and $\Delta\epsilon = \epsilon_{ij} - (\epsilon_{ii} + \epsilon_{jj})/2$.

The work presented in this Chapter has two main objectives:

(i) A number of past works [31, 71, 72, 79] have used equations Eq. (2.2) and/or Eq. (2.4) implicitly to justify the choice of the coarse-grained parameters accompanying their simulations. However, as far as we know, there has not been any critical test (except the work of Morse and coworkers, which is discussed further below) of the above parameterizations in the context of other multicomponent polymeric systems. Explicitly, it is not evident if such parameterizations, which were deduced based on selected properties such as interfacial tensions are equally applicable to more complex multicomponent systems, especially in the context of being able to reproduce the long-range structural characteristics in such systems.

Recently, Morse and coworkers [80, 81] examined the influence of thermal fluctuations on the structure of disordered diblock copolymer melts. They developed an elegant analytical theory for the static structure factor of dis-

ordered diblock copolymer melts [80, 82] as a function of an effective Flory Huggins interaction parameter χ (Morse and coworkers denoted this effective interaction parameter as χ_e. However, in this work, we use the notation χ to denote this parameter) and the molecular weight (MW) of the block copolymers. As an offshoot of their work, they considered simulations [81, 83, 84] of *symmetric* diblock copolymer melts and showed that there exists a MW weight independent mapping between pairs of parameters a_{ij} and χ, and ϵ_{ij} and χ. However, unlike the previous articles, their mapping satisfied the requirement that the long-range structure (explicitly, they considered the peak in the structure factors of the disordered melts of diblock copolymers) of the DPD and KG models match each other. These results of Morse and coworkers are especially significant since it serves to provide a mapping of the interaction parameters of KG and DPD models to each other and to a Flory-Huggins interaction parameter, in such a manner that the long range structural characteristics are preserved. However, their simulation results were restricted to the case of symmetric diblock copolymer and it is not evident if the mapping deduced for such a case would equally be applicable for more complex polymeric systems.

Motivated by the above considerations, in this work we examined a wider class of systems which include, asymmetric block copolymers, symmetric triblock copolymers and some selected block copolymer-solvent systems and probed whether the mapping between ϵ_{ij} of the KG model and a_{ij} of the DPD model deduced for symmetric diblock copolymers serve to ensure a mapping of

the long-range structure (we use the intensity of the peak in the structure factor as a measure for comparison) of different simulation models, for other class of block copolymer systems. Through our results, we demonstrate that such a mapping indeed serves to successfully match the long-range characteristics of the different simulation models. Thereby we establish a rigorous mapping between the interaction parameters of the KG and DPD models, and in turn, to the Flory Huggins interaction parameter χ, which serves to match the long-range structural details in the different models.

(ii) A second related objective is to use the above idea as a means to obtain equilibrated ordered morphologies of systems which are difficult to equilibrate by other means. Within the contexts of the above models, we note that the DPD model is computationally efficient and simulations have been effected for a wide variety of systems like vesicles [85–87], colloidal suspensions [88], polymeric fluids [73, 89] etc., to study interfacial [58], mechanical [85, 87, 90], and rheological [71, 72, 88] properties. in contrast the KG model is much more expensive and except for some isolated instances [30, 79] simulations of ordering and self-assembly have been restricted to small chain lengths. An outcome of the above identification of the mapping between DPD and KG parameters is that we can potentially use coarse-grained DPD simulations to facilitate the ordering and self-assembly in multicomponent, long-chain polymer systems and then equilibrate the resulting structures by turning on the KG interactions. While this procedure is similar in spirit to other methodologies pursued in the literature [62, 91], the difference in our approach is that

by choosing the a_{ij} and ϵ_{ij} based on the rigorous mapping, we ensure that the coarse-grained structure is indeed tuned to achieve the same long-range structure as the finer-scale system. We demonstrate that we can use such a methodology to produce ordered phases over chain lengths up to $N = 200$ within a shorter computational time.

The paper is organized as follows. A background discussion on the work of Morse and co-workers is presented in Section 2.2. Simulation results pertinent to diblock copolymers of different compositions are presented in Section 2.3. Other systems such as triblock copolymers and multicomponent systems are explored in Section 2.4, where we demonstrate that the mapping obtained for block copolymers are equally well applicable to other multicomponent systems. Such a mapping was used to create ordered phases of diblock copolymers in such systems. In Section 2.5, we describe the procedure we implemented and present illustrative results for two test cases, corresponding to the lamellar and cylindrical phases. We conclude with a brief summary and outlook.

2.2 Theoretical Background and Methodology

2.2.1 Universal Behavior of Compositional Structure Factor

The work reported in the present Chapter draws upon the recent publications of Morse and coworkers pertaining to the behavior of the structure factor $S(q)$ in simulations of symmetric diblock copolymer melts [84]. $S(q)$ is a correlation function for composition fluctuations, defined in explicit particle

coordinates as,

$$S(\boldsymbol{q}) = \frac{1}{4n_p} \left\langle |\sum_{i=1}^{n_p} \left[(\gamma_A(i) - \gamma_B(i)) - \left(\bar{\phi}_A - \bar{\phi}_B\right) \right] e^{-i\boldsymbol{q}\cdot\boldsymbol{r_i}}|^2 \right\rangle \tag{2.5}$$

where $\boldsymbol{q}$ represents the wave vector, $\boldsymbol{r_i}$ represents the position vector of the i^{th} monomer and n_p represents the total number of A and B monomers in the system. $\gamma_j(i)$ is 1 if the i^{th} segment is of type A or B and 0 otherwise. $\bar{\phi}_A$ and $\bar{\phi}_B$ represents the average composition fraction of A and B monomers respectively. For symmetric diblock copolymers, Morse and coworkers suggested [80] (and provided an approximate analytical expression [82]) that expresses the structure of symmetric diblock copolymers in a universal form,

$$\rho N S^{-1}(\boldsymbol{q}) = P(qR_{g0}, \chi N, \bar{N}) \tag{2.6}$$

R_{g0} denotes the radius of gyration, ρ denotes the density, N represents the chain length, and $\bar{N}$ represents the invariant degree of polymerization [92] ($\bar{N} = N(\rho b^3)^2$) which in turn quantifies the number of chains a single chain interacts within its own volume and b represents the segment length. The scaling hypothesis of Eq. (2.6) suggests that the scattering intensity $S(q)$ should exhibit a universal dependence upon all of the invariant dimensionless parameters that appear in Eq. (2.6). Such a hypothesis was tested by Morse and coworkers for symmetric diblock copolymers by considering a number of different lattice and off-lattice simulation models. Explicitly, by considering the models at the same $\bar{N}$, they demonstrated that they could collapse the inverse of the magnitude of the peak in the structure factor ($S^{-1}(q^* R_{g0})$), where q^* denote the peak location of the structure factor) by mapping the respective

interaction parameters to a universal parameter χN. More importantly, they demonstrated that mapping function was independent of $\bar{N}$ and thereby served as an identification of the Flory-Huggins like interaction parameter for a specified simulation model. For instance, for the KG model, they demonstrated that the relationship [84] between ϵ and χ was given as:

$$\chi = \frac{z_K^{\infty}\alpha_K + a\alpha_K^2}{1 + b\alpha_K + c\alpha_K^2} \tag{2.7}$$

where α_K represents the difference in interaction parameters between AB and AA/BB monomers given by $\alpha_K = \epsilon_{AB} - (\epsilon_{AA} + \epsilon_{BB})/2$, with parameters a, b and c obtained by simultaneous fitting of the simulation results [84]. For the DPD model, they deduced the mapping as,

$$\chi = \frac{z_D^{\infty}\alpha_D + a'\alpha_D^2}{1 + b'\alpha_D} \tag{2.8}$$

where $\alpha_D = a_{AB} - (a_{AA} + a_{BB})/2$ and the corresponding fitting parameters are a' and b'. The intermolecular coordination number values used for KG model and DPD models [83] (which is dependent on intramolecular interactions) were $z_K^{\infty} = 0.237$ and $z_D^{\infty} = 0.2965$ unless otherwise specified.

2.2.2 Coarse-Grained Simulations and Fine-Graining

The work of Morse and coworkers discussed in Section. 2.2.1 identified the existence of a mapping between the parameters of different simulation models which preserves the long-range structural characteristics between the simulations. Morse and coworkers were primarily interested in such characteristics to test the universality of the different models and their comparisons

to the analytical theory developed by their group [80–82, 93]. In this work however, we propose to explore the possibility of using such relationships as a means to perform long-time simulations of models which are otherwise time-consuming to equilibrate. Explicitly, our idea is that due to the existence of a mapping between the interaction parameters, one could in principle use coarse-grained simulations performed at the same χ corresponding to the fine-scale model. Upon equilibration of the coarse-grained simulations, one could reintroduce the finer scale interactions and perform a (likely) shorter time simulation serving to equilibrate the short length-scale features.

Implementation of the above idea presupposes that the mapping deduced specifically for symmetric diblock copolymers by Morse and coworkers (Eq. (2.7) and (2.8)) is applicable for multicomponent polymer systems. Indeed, if the mapping between ϵ_{ij}, a_{ij} and χ were to be influenced by the architecture of the polymer and/or the composition of the mixture, then the above-described fine-graining approach is expected to be of little to no utility. Motivated by such an objective, in this work, we examine three classes of systems: diblock copolymers, triblock copolymers and multicomponent systems. For diblock copolymers, we consider the case of both symmetric and *asymmetric* compositions of the block, whereas for triblock copolymers we restrict our investigations to the symmetric case. In multicomponent systems, we consider cases of both selective and non-selective solvents.

We note that the mappings (Eqs. (2.7) and (2.8)) differ from the functions commonly used in the literature to relate the interaction parameters

of the KG and DPD models to the Flory-Huggins interaction parameter, χ. Specifically as discussed earlier (Eqs. (2.2) and (2.4)) and for the convenience of referencing, the KG and DPD models can be related to the χ parameters through a linear function of the form,

$$\chi = \frac{z^{\infty}\alpha}{k_B T} \tag{2.9}$$

where z^{∞} represents the intermolecular coordination number which represents the number of interchain neighbors in the limit of an infinitely long homopolymer chain [82] and α represents the difference between interaction parameters of unlike and like monomers of DPD and KG models. We note that Eq. (2.9) is just a convenient way to represent Eqs. (2.2) and (2.4) in a single equation. In our studies, we also explicitly examined the transferability of the above mapping across different polymeric systems. In our results presented in Sections. 2.3 and 2.4, the above mapping (Eq. (2.9)) is referred to as the "linear mapping" function. Moreover, to distinguish the χ defined by different expressions, we denote the χ obtained from Eqs. (2.7) and (2.8) as χ_{NL} and the χ from Eq. (2.9) as χ_L.

We note that while the mapping between the parameters α_{ij} and ϵ_{ij} does not explicitly depend on $\bar{N}$, however, the parameters accompanying the mapping Eqs. 2.7 and 2.8 do depend on the intramolecular interactions (such as the value chosen for the spring constants). Moreover, matching of the long-range structure is ensured only as long as $\bar{N}$ is maintained identical between the different simulations [83]. In examining transferability, we have used the

parameters deduced for symmetric diblock copolymers possessing the same intramolecular interactions. The approach we have followed with regard to maintaining identical $\bar{N}$ will be explained in more detail in the relevant sections.

2.2.3 Simulation Details

KG model uses a shifted Lennard-Jones potential for intermolecular interactions as presented in the introduction. The bonded interactions are governed by a harmonic potential (U_b) of the form,

$$U_b = \kappa_K (r - \sigma)^2 \tag{2.10}$$

where κ_K is the spring constant and is set at $200 k_B T/\sigma^2$, where k_B is the Boltzmann constant. The interaction parameter between like monomers (AA,BB) is set as $\epsilon_{AA} = \epsilon_{BB} = 1.0\ k_B T$. The system is evolved in a NVT ensemble with a Nosé-Hoover thermostat [94] with a damping constant of 0.5 and a time-step of 0.005 in reduced units. The monomer density ρ_K was chosen as $0.7\ \sigma^{-3}$. For $\epsilon_{AB} = 1.0$, we prepare melt from a random initial configuration, using a slow push-off method [91] followed by equilibrating the system for about 1.5 to 2.2×10^7 steps. For $\epsilon_{AB} > 1.0$, the system is quenched from the equilibrated melt obtained at $\epsilon_{AB} = 1.0$.

The bonded interactions for the DPD model is modeled using,

$$U_b = \kappa_D r^2 \tag{2.11}$$

The time-step (Δt) was set at 0.01 unless other wise specified. The interaction between like monomers for DPD monomers is set as $a_{AA} = a_{BB} = 25.0\ k_BT$. The monomer density ρ_D was chosen as 3.0 in r_c^{-3} units. The equations were integrated using a Velocity-Verlet algorithm [95]. The system is evolved in a NVT ensemble using a DPD thermostat. The parameters chosen for DPD thermostat was identical to those used in earlier researches [58]. Without loss of generality, we set $\sigma = m = k_B = T = 1.0$ in both the models. All simulations were performed using LAMMPS software [96]. For brevity, henceforth the KG model will be denoted as "K" and whereas that governed by the DPD potential will be denoted as "D". The intramolecular bond constants, densities and the chain lengths used for validating the transferability of scaling hypothesis remain identical to those used previously for symmetric diblock copolymers [84].

The propensity for segregation between the A and B monomers can be controlled by varying the α parameter of the corresponding model while keeping the temperature fixed. For our studies which tested the mapping between the parameters of the two CG models, we kept the degree of polymerization (N) to be 64 for model "K" and to be 16 for model "D". The radius of gyration of the system, $R_{g0} = \sqrt{Nb^2/6}$, where b is the statistical segment length was obtained by the methodology prescribed in the works by Wittmer *et al.,* [97, 98] and others [84]. Explicitly, simulations were conducted on a homopolymer chain ($\alpha = 0$) with $N = 16$, 32, 64 and 128 in both the models to determine the chain length dependent segment length from which the sta-

tistical segment length (b) was obtained from extrapolating the chain length dependent segment length $b(N) = \sqrt{6/N} R_g(N)$ to $b = \lim_{N\to\infty} b(N)$. We obtain $b = 1.408\sigma$ for model "K" with $\kappa_K = 200 k_B T/\sigma^2$. For ensuring identical $\bar{N}$, where $\bar{N} = N(\rho b^3)^2$, we tuned the spring constant κ_D to $1.703 k_B T/r_c^2$ which corresponds to a desired $b = 1.088 r_c$.

2.3 Diblock Copolymers

2.3.1 Symmetric Diblock Copolymers

Morse and coworkers have extensively studied the case of *symmetric* diblock copolymers using a variety of simulation methods [40, 43, 58, 84]. In this Chapter, we include the results for such a case mainly for the sake of completeness. To obtain the mapping between the coarse grained parameters for symmetric diblock copolymer, simulations were performed in the disordered phase. The $S(q)$ results were obtained for both the models with α varying between 0.0 – 4.0 for model "D" and 0.0 – 1.0 for model "K." Representative results for $S(q)$ as a function of qR_{g0} are displayed in Fig. 2.1. The discrete points obtained after spherical averaging is then fit to a cubic spline curve to extract the peak intensity $S(q^*)$ and the corresponding wave number q^*. Peak inverse intensities were then plotted as a function of $\chi_{NL}N$ using the non-linear mapping function (Eqs. (2.7) and (2.8)) for the model parameters chosen (see Fig. 2.2(a)).

As shown previously [83], the results for the two simulation models are seen to collapse when displayed (Fig. 2.2(a)) as a function of $\chi_{NL}N$ (Eqs. (2.7)

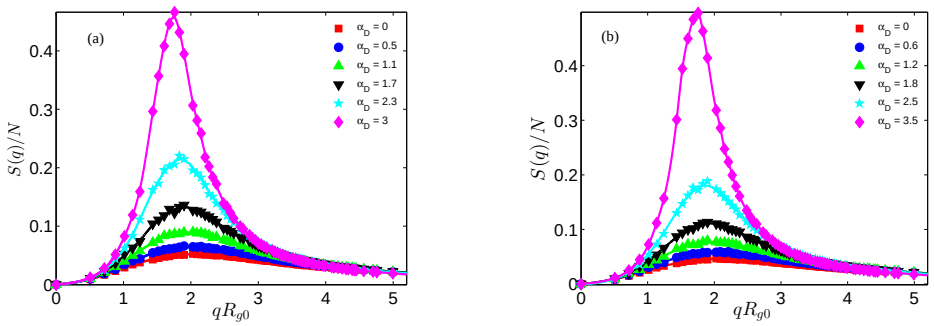

Figure 2.1: Typical plots of $S(q)$ as a function of qR_{g0} for (a) $f = 0.5$ and (b) $f = 0.375$ for model "D" at different values of $\alpha_D = a_{AB} - a_{AA}$. All the simulations were performed with $N = 16$.

and (2.8)). Fig. 2.2(b) displays the same results if when plotted against $\chi_L N$ (Eq. (2.9)). The fit is seen to be relatively poor compared to that obtained from the nonlinear function. The collapse of the data displayed in Fig. 2.2(a) allows us to draw two conclusions: (i) There exists a unique, albeit nonlinear, mapping between the interaction parameters α_K and α_D and the Flory-Huggins parameter χ. (ii) More pertinent to our strategy for coarse-graining and fine-graining, we identify that there exists a unique mapping function of the form $\alpha_D = f(\alpha_K)$ between the K and D models.

2.3.2 Asymmetric Diblock Copolymers

In this section, we examine whether the mapping function given in Eqs. (2.7) and (2.8) (and tested for symmetric diblock copolymers) works equally well for *asymmetric* diblock copolymers to map the long range struc-

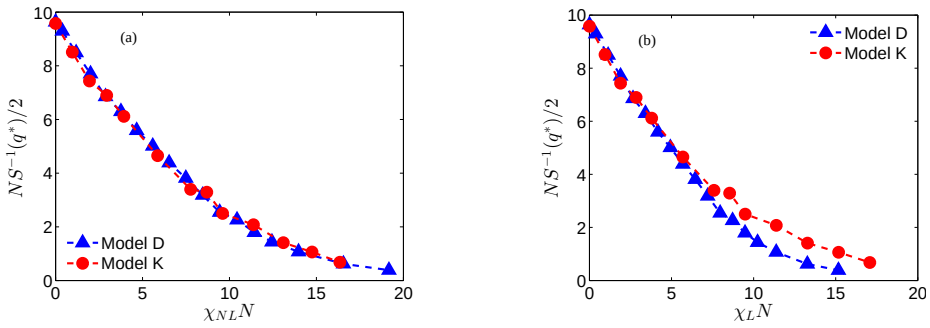

Figure 2.2: The peaks of the inverse of structure factor is shown for the symmetric block copolymer. $NS^{-1}(q^*)$ is plotted against (a) $\chi_{NL}N$ (Eq. (2.7) for model "K" and Eq. (2.8) for model "D") (b) $\chi_L N$ (Eq. (2.9)). All simulations were performed with $N = 16$ for model "D" and with $N = 64$ for model "K".

ture (as qualified by $S(q^*)$). The composition fraction (f) of A type monomer chosen in this study were 0.25 and 0.375. Since the effective co-ordination number (z^∞) and the bond length b_∞ for the "K" and "D" models were obtained by considering the reference homopolymer system ($\alpha = 0$) they remain unchanged while considering other systems.

The results obtained for $f = 0.375$ and $f = 0.25$ are shown in Fig. 2.3 and Fig. 2.4 respectively. Figure 2.3(a) and the main panel of Fig. 2.4 uses the mapping corresponding to χ_{NL} (Eqs. (2.7) and (2.8)), whereas Fig. 2.3(b) and the inset of Fig. 2.4 considers the mapping corresponding to χ_L (Eq. (2.9)). On plotting the inverse peak intensities as a function of $\chi_{NL}N$, we observe that the match between the result of the different simulation models is nearly perfect and similar to the correspondence observed for the case of a symmetric diblock copolymer. However, in the present case, we observe that the peak inverse

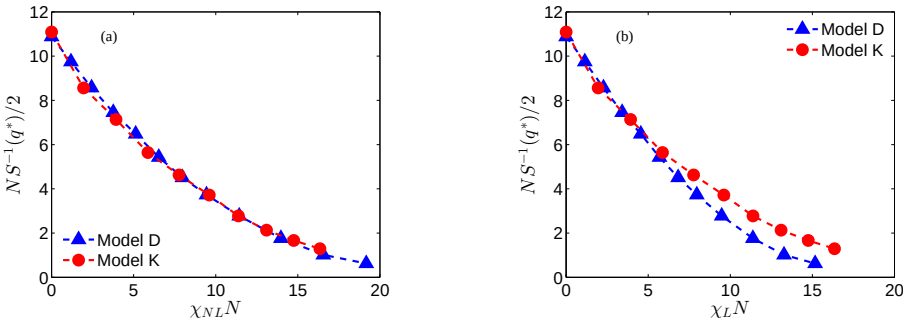

Figure 2.3: The peaks of the inverse of structure factor is shown for the asymmetric block copolymer with $f = 0.375$. (a) $NS^{-1}(q^*)$ is plotted for $\chi_{NL}N$ (Eqs. (2.7) and (2.8)). (b) $NS^{-1}(q^*)$ is plotted against $\chi_L N$ (Eq. (2.9)). All simulations were performed with $N = 16$ for model "D" and with $N = 64$ for model "K"

intensities do exhibit a reasonable match even when using "linear mapping" function (Eq. (2.9)).

The above results shows that the mapping function between α_K and α_D deduced based on the results of symmetric diblock copolymer is equally applicable to the case of asymmetric copolymers. The compositions chosen for our study were chosen in an arbitrary manner. We have also confirmed that the mapping is applicable for $f = 0.125$ (results are not shown here). Based on these correspondences, we conclude that the mapping function between the "D" and "K" models are independent of the overall composition of the diblock copolymer. Nevertheless, it needs to be noted that the test cases performed here have structurally identical monomers and no generalizations may be expected for structurally asymmetric models [82].

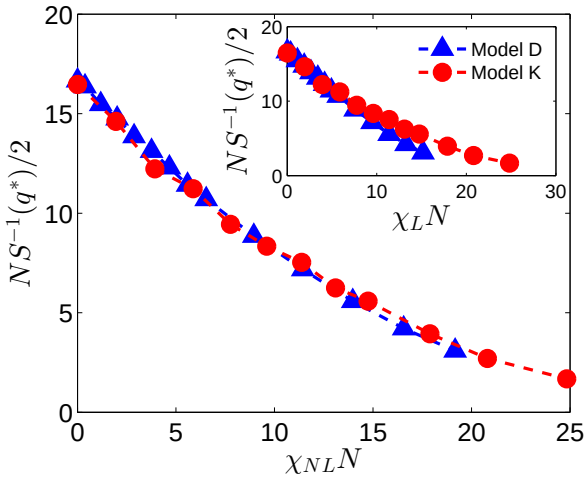

Figure 2.4: The main plot shows peak inverse intensities as a function of $\chi_{NL}N$ for the asymmetric block copolymer with $f = 0.25$ (Eqs. (2.7) and (2.8)). All other parameters remain the same as that for $f = 0.375$. The inset displays peak inverse intensities against $\chi_L N$ obtained using Eq. (2.9).

2.4 Other Polymeric Systems

2.4.1 Triblock Copolymer

In Secs. 2.3.1 and 2.3.2, we demonstrated that a unique mapping function exists between the interaction parameters of different CG models which serves to map the long range structure of diblock copolymers. In this section, we consider a broader class of systems to probe if the mapping deduced in Sec. 2.3 is equally applicable for other kinds of block copolymers. In this section we consider a symmetric triblock copolymer of the form ABA. Similar to diblock copolymer, N is fixed at 16 for model "D" whereas the value of N is 64 for model "K".

In Fig. 2.5, we display the peak inverse intensities based on the map-

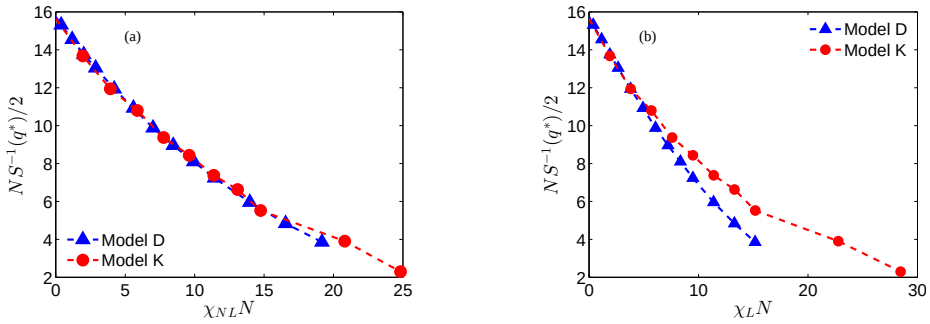

Figure 2.5: $NS^{-1}(q^*)$ is plotted against χN for symmetric triblock copolymers for both model "K" and "D" using (a) nonlinear mapping and (b) linear mapping. All corresponding mapping functions (Eqs. (2.7), (2.8) and (2.9)) remain identical to that of symmetric diblock copolymer.

ping deduced for diblock copolymers. We observe that the nonlinear mapping (Eqs. (2.7) and (2.8)) between χ and interaction parameters of both the models provides an excellent agreement between the structure factors of the models under consideration. Similar to the results obtained for diblock copolymers, the quality of collapse observed for triblock copolymers using the linear mapping is not as accurate as the nonlinear mapping. Based on the results it can be concluded that the nonlinear functions (Eqs. (2.7) and (2.8)) provide a mapping function between two coarse grained models for block copolymers irrespective of the number of blocks in the polymer.

2.4.2 Multicomponent Systems

An intriguing test that can be performed in favor of the scaling hypothesis is if an identical mapping could work equally well for a broader class

of multicomponent polymers which includes mixtures. We note that the direct extension of the mapping functions deduced for diblock copolymers to the case of polymer-solvent mixtures can only be based on a number of assumptions. Indeed, the environment of a polymer-solvent mixture is different from that of a polymer melt system. Thus, a thorough analysis on the transferability of mapping function would in principle require a re-calibration the intermolecular coordination number and the statistical segment length for the polymer-solvent mixture. Another hurdle for an exact implementation is the lack of a fundamental theory (like renormalized one-loop theory [80] for block copolymers) for polymer-solvent mixtures which allows the refitting of the parameters in Eqs. (2.7) and (2.8). Despite these caveats, from a practical perspective, a mapping such as the ones proposed in Eqs. (2.7) and (2.8) is expected to be most useful if it can be extended *empirically* to a wider class of systems than originally intended. Indeed, such an assumption is implicit in many articles [74, 75, 99–104] which have used the Groot and Warren mapping (cf. Eq. (2.2)) for polymer solvent systems. Motivated by such considerations, in this section, we present some preliminary results which examine the applicability of the mapping functions Eqs. (2.7) and (2.8) to symmetric diblock copoloymer system in the presence of solvents.

Similar to the case of block copolymer melt studies, we chose to examine the correspondence of the long range composition fluctuations of A-B system to study the mapping between the interaction parameters. However, it needs to be mentioned that in the presence of a selective solvent the mode governing

the dominant composition correlation need not necessarily correspond to the difference in the AB compositions [105]. Nevertheless, since we are interested in the functional form of the peak inverse intensity curve, and not in determining the exact ODT, we have chosen to probe $S(q^*)$ as defined in Eq. (2.5) as the measure of the long range order even in block copolymer-solvent mixtures.

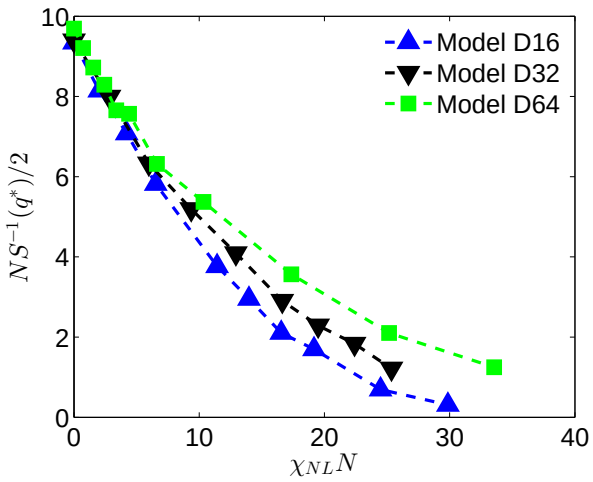

Figure 2.6: $NS^{-1}(q^*)$ for solvent systems with DPD model is plotted against $\chi_{NL}N$ (see main text for definition). This shows the effect of explicit chain length dependence in solvent systems.

We note that the universality relation of Eq. (2.6) is expected to explicitly embody a dependence on the molecular weight of the polymer for the case of solvent-polymer mixtures. As a consequence, to compare the results of DPD to KG simulations, we need to effect the simulations for the same molecular weight of the polymer. To identify the N dependence of $S(q^*)$ considered in this section, we performed DPD simulations for different chain lengths, while keeping the $\bar{N}$ identical (by tuning the parameter κ_D). The

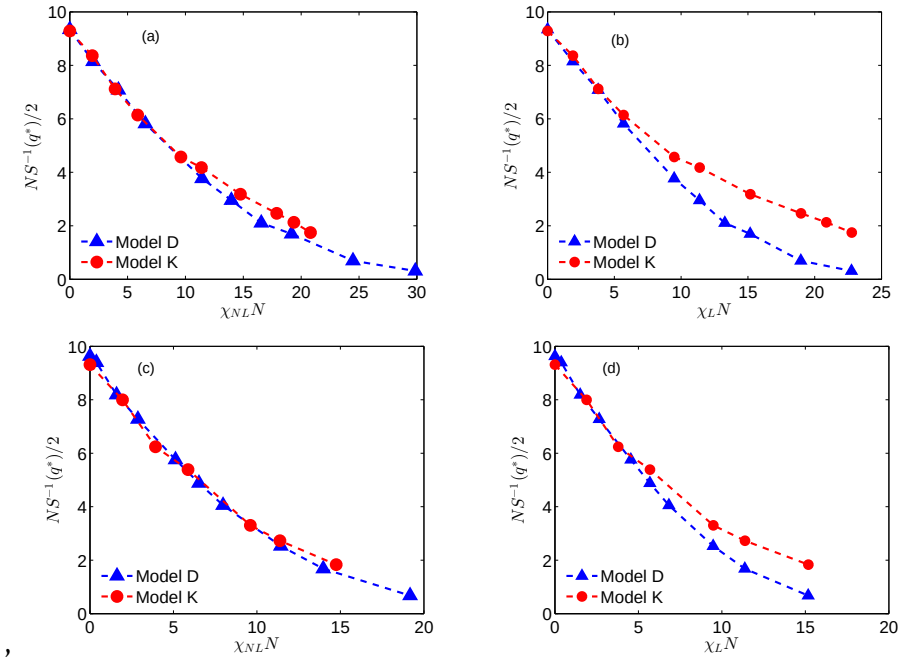

Figure 2.7: $NS^{-1}(q^*)$ is plotted for both model "K" and "D" for both selective ((a) and (b)) and non-selective solvents ((c) and (d)) using a non-linear mapping (χ_{NL}) in (a)/(c) and using a linear mapping (χ_L) in (b)/(d). Volume fractions of solvent used for selective and non-selective solvents are 0.3 and 0.1 respectively.

results (Figure 2.6) indicated that the $S(q^*)$ exhibits only a weak chain length dependence, provided that consistent mapping parameters are used for the intramolecular interaction parameters. Hence, to maintain consistency with the results of Secs. 2.3 and 2.4.1, below we display the results for $N = 16$ for the model "D."

In the present study, selected parameters for the models of both selec-

tive and non-selective solvents were probed for testing the validity of scaling hypothesis. The volume fractions (ϕ) considered for non-selective solvents are $\phi = 0.1$, whereas for selective solvent ϕ is chosen as 0.3. For non-selective solvents, we kept $a_{AB} = a_{AS} = a_{BS}$. Chain lengths and the range of interaction parameters probed remain identical to the ones considered for *symmetric* diblock copolymer case. We keep the net monomer density fixed by adjusting the number of chains in the system. In the selective solvent systems, to create selectivity for the solvents to A and B blocks of the copolymer, a_{AB} is chosen equal to a_{AS} ($\epsilon_{AB} = \epsilon_{AS}$), where S represents the solvent particle. and the interaction parameter for model "K" between B and S monomers (ϵ_{BS}) was set at 1.33. The corresponding interaction parameter a_{BS} is obtained as 26.5 by solving Eqs. (2.7) and (2.8) for the same $\chi_{NL}N$. We note that in this approach to parametrization, the selectivity of the solvent is modified when a_{AB} (and ϵ_{AB}) is changed. Such a framework was adopted so as minimize the number of parameters which are varied while still enabling a study of the quality of the mapping of the long-range structure when the selectivity was varied.

Fig. 2.7(a) displays $S^{-1}(q^*)$ curves for the selective solvent case. We observe an excellent agreement between the peak intensity curves of the two CG models confirms when plotted as a function of $\chi_{NL}N$. Similar agreement on the collapse of $S^{-1}(q^*)$ curves can be observed in Fig. 2.7(c) for the case of nonselective solvents. Such a result demonstrates that the mapping (Eqs. (2.7) and (2.8)) remains equally applicable even for block copolymer-solvent mixtures.

In both Fig. 2.7(b) and (d) we display the corresponding results arising from the linear mapping (Eq. (2.9)). We note that, however Eqs. (2.7) and (2.8) were used to obtain the DPD interaction parameter for solvent-block copolymer interactions (a_{BS}) corresponding to the chosen KG interaction parameter (ϵ_{BS}), but the linear mapping (Eq. (2.9)) was used to obtain χ_{AB} in the case of selective solvents. Compared to the correspondences noted for the nonlinear mapping function, the results for the linear mapping function are seen to indicate poorer fits. These results suggest the nonlinear mappings embodied in Eqs. (2.7) and (2.8) provide a superior way to map the parameters of the DPD and KG models to the Flory-Huggins like interaction parameter χ and in turn to each other.

The transferability of mapping function as shown in the specific cases presented here is an intriguing result which has significant implications for effecting coarse-grained simulations in a wide class of polymer-solvent mixtures [99, 101, 103]. However, considering the limited parameters we have investigated, our results are to be strictly viewed as preliminary and not as conclusive evidence for the applicability of the parameter mappings to solvent based systems. To make a stronger argument for the case of solvent-polymer mixture, a wider class of systems including different solvent concentrations and composition fractions needs to be tested. Moreover, a more appropriate parametrization would maintain the ϵ_{AS} and ϵ_{BS} fixed (at different selectivities) and vary ϵ_{AB}.

2.5 Inverse Coarse Graining Methodology to Create Ordered Morphologies

We recall that the results presented in Secs. 2.3 and 2.4 were meant as a step towards creating ordered morphologies in the "K" model by using the configurations generated by model "D" as a precursor. In this section, we present a proof of concept of the preparation of ordered phases with relatively short computation effort using CG potential using by taking advantage of the mappings between CG parameters.

As a test case, we considered a $N = 200$ beads polymer (shorter chain simulations were also performed, but the results are not displayed) melt system. Our procedure hinges on the assumption that the mapping function deduced for disordered phases (Eqs (2.7) and (2.8)) works equally well for the ordered phases. With this hypothesis, we initially identified the DPD interaction parameter (a_{ij}) corresponding to target KG interaction parameter (ϵ_{ij}) by solving Eqs (2.7) and (2.8).

Recall that the mapping works under the assumption of identical $\bar{N} = N(\rho b^3)^2$. Unlike previous studies [62] (and our results presented in Secs. 2.3 and 2.4), we chose to retain the same number of beads for the models D and K. Moreover, the radius of gyration (R_g) and densities (in dimensional units) has to be identical in both the models, to ensure a matching of the structural characteristics. To effect these considerations, we fixed the target densities for the models "K" and "D" and the spring constant for the model "K". Explicitly, the corresponding values were 0.7 σ^{-3}, 3.0 r_c^3 and 200 k_BT/σ^2

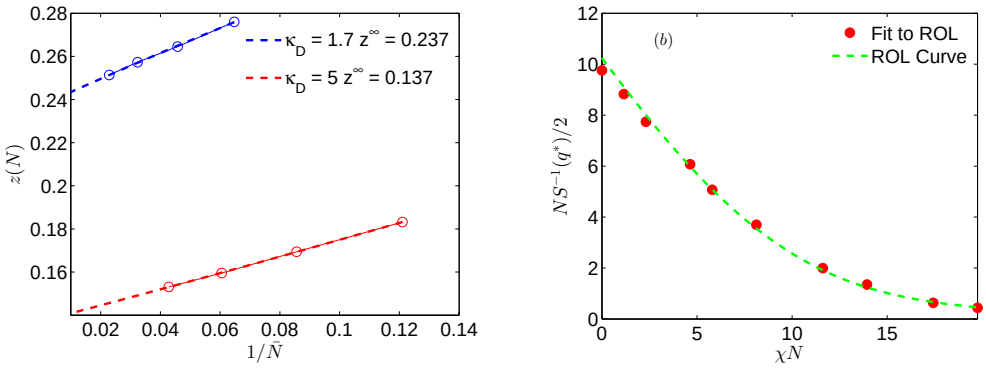

Figure 2.8: (a) Fit to perturbation calculations to obtain z^{∞} (b) Fit of $S^{-1}(q*)$ as a function of χN to the corresponding curve generated by ROL.

respectively. The identical density constraint fixes the ratio, r_c/σ, which in our cases is 1.624. The spring constant for model "D" is then chosen as 5.0 k_BT/r_c^2 to satisfy identical radius of gyration constraint.

We note that, with the specified constraints, the intramolecular bond constants used for Model "D" used in this section differs from that of the one used for testing the validity of scaling hypothesis. Changing the bond constant implies a change in change in z_D^{∞} and can be calculated by counting the inter-chain neighbors for a corresponding homopolymer system. In the present case, the value of z_D^{∞} was found to be 0.136 for $\kappa_D = 5k_BT/r_c^2$. Such modifications also require a corresponding refitting of the parameters in Eq. (2.7) [84]. To accomodate such features, we performed the fit for one value of $\bar{N}$ and values obtained were then used to calculate the corresponding α_D for a given α_K. For the present case we chose $\alpha_K = 0.31$ which corresponds to $\alpha_D = 25.7$. The procedure used for refitting is described in brief below.

For the results presented in this section, for the DPD simulations we chose the $\kappa_D = 5k_BT/\sigma^2$, which yields an R_g which is within 2% of the R_g of the KG model. To calculate the z^∞ corresponding to the new κ_D we used the methodology suggested in Morse *et.al.* [82]. Explicitly, we used the results of a series of homopolymer simulations with $N = 16, 32, 64$ and 128 and obtained the chain dependent intermolecular coordination number, $z(N)$ as,

$$z(N) = \int_0^\infty u_{ij}(r) g_{inter}(\mathbf{r}) \mathbf{dr}. \tag{2.12}$$

Subsequently, by using

$$z(N) = z^\infty \left[1 + \frac{(6/\pi)^{1.5}}{\bar{N}^{0.5}} + \frac{\delta}{N} \right] \tag{2.13}$$

we obtained z^∞ (see Figure. 2.8(a)). Following the calculation of z^∞, we performed a fit to the renormalized one-loop theory (see Figure. 2.8 (b)). The parameters obtained from such a fit were $a = 45.373$ and $b = 250.6493$ and were used for the results reported in the corresponding section of the manuscript.

We note that instead of performing the ROL fit by using the results for four different $\bar{N}$ as was implemented in Glaser *et. al.* [84], we performed the fit only based on the results for a single $\bar{N}$. Moreover, to obtain the ROL curve for the corresponding $\bar{N}$, we utilized the approximate functional form given in Qin et.al [93] for symmetric diblock copolymers. We admit that there could be some errors from both the preceding approximations. However, we felt that starting from a close enough χ (instead of an arbitrarily set initial lamellar configuration as is commonly adopted) would suffice to ensure correct

equilibrium characteristics for the KG model. Whence we did not expend the computational resources needed for a more accurate, multi $\bar{N}$ fit of the models to the ROL theory.

The technique used here is in similar spirit to the techniques used previously to create ordered lamellar phases [30] or multiple stacks of lamellae [106]. Specifically, a DPD system with random initial configurations is initially subjected to a NPT simulation in a rectangular box with $P = 19.3\ r_c^{-3}$ (corresponding to the pressure obtained by running a homopolymer system for $kT = 1.0$). The box sizes were coupled in two directions and the third direction was allowed to vary independently, but the pressure was kept the same in all the three directions. In a short simulation run, we obtain the lamellar spacing commensurate with the box size. Total length of the DPD simulations ranged between 10 to 13 $\times 10^6$ time-steps. The equilibrium configuration obtained from DPD simulations is then fed as input to the simulations which used KG potential. We then employ the slow push off scheme [91] for 500 to 1500 timesteps to remove the strong overlaps of monomers, after which hard repulsive interactions were turned on. Further equilibration and production runs were performed in a NVT ensemble. The equilibrated configurations obtained for the test system under consideration is shown in Fig. 2.9, wherein we observe the formation of well-aligned lamellar morphologies.

The methodology used to create cylindrical phases is very similar to those used for creating lamellar phases. The test case presented corresponds to $f = 0.3$ with $N = 100$. The interaction parameter chosen was $\alpha_D = 3$. All

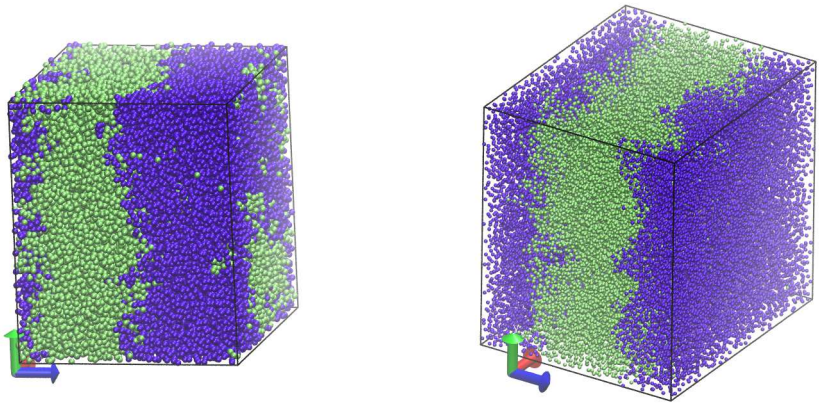

Figure 2.9: The ordered lamellar phases are shown using DPD potential (left panel) and KG potential (right panel). The equilibrated structure in DPD is fed as input to the KG system for faster equilibration. The configurations are generated from the data file using VMD software [1].

other parameters remains identical to the case of the corresponding lamellar phase system. DPD simulations took slightly longer time ($\mathcal{O}(10^7)$ timesteps) to form equilibrated cylindrical phases. The equilibrated DPD configurations were used as an input to KG simulations and were equilibrated as discussed earlier. The equilibrated systems using both the models are shown in Fig. 2.10.

2.5.1 Evidence for the Successful Implementation of Inverse Coarse Graining

In this subsection, we compare the structural characteristics of ordered lamellar phases obtained after the reintroduction of the hard potentials with

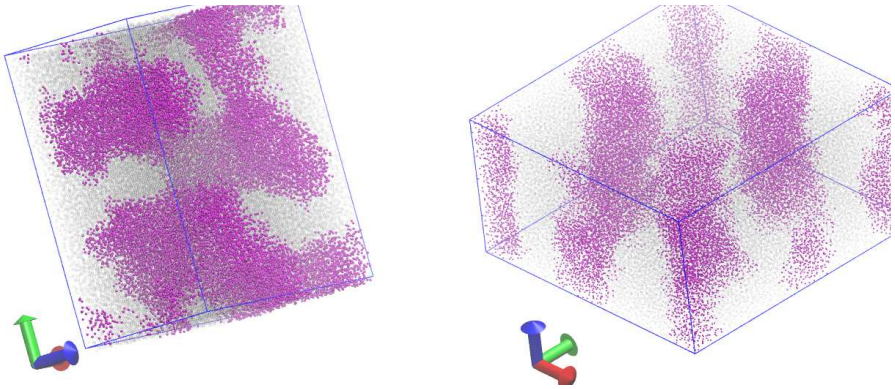

Figure 2.10: The ordered cylindrical phases are shown using DPD potential (left panel) and using KG potential (right panel). The equilibrated structure in DPD is fed as input to the KG system for faster equilibration. One of the blocks of the chain are made transparent to visualize the cylindrical patterns formed using both KG and DPD potentials.

that of the soft potentials as an evidence for the successful implementation of the inverse coarse graining procedure. Towards this objective, we investigated the density profiles obtained in the lamellar phases perpendicular to the interface ($g(z)$) for both the models where z represents the direction perpendicular to the interface in units of σ. We equilibrate the system for about 30 - 40 million steps after the reintroduction of hard potentials, before the statistics are collected. For the present study, we chose to examine the density profiles for a chain length of $N = 100$ at $a_{AB} = 29.0$ and $a_{AB} = 30.0$. The corresponding ϵ_{AB} values are 4.8 and 7.0 respectively.

In Figs. 2.11(a) and (b), we display a comparison of the density profiles resulting in the DPD and KG models which demonstrate very good agreement between the final configurations. Additionally, we also verified that the domain

widths and the the structure factors of ordered phases (not shown here) also displayed a quantitative match between the two simulations. We note that in the absence of rigorously mapped interaction parameters, introduction of an arbitrary set of coarse-grained KG parameters to an initial configuration derived from DPD simulations is expected to render the configuration unstable and would lead to substantial modifications to the morphology. The stability of the configurations as reflected in the near-identical density profiles of the KG and DPD simulations serves as evidence of successful implementation of the inverse coarse-graining procedure.

Overall, the absence of entanglements in DPD even for longer chain lengths [107] enhances equilibration of ordered morphologies. Recent work by Steinmüller*et al.* [62] suggested that the computer time required to obtain equilibrated morphologies with hard core potential for random block copolymers was reduced by two orders of magnitude when pre- equilibrated configurations obtained from other soft potentials were used. In our study, we obtain equilibrated ordered morphologies within a few million steps using KG potentials when DPD potentials were used to generate starting configurations for the same, and hence expect that our procedure yields a comparable reduction in computer time in contrast to directly equilibrating the original KG model.

2.6 Conclusions and Outlook

Simulations of a variety of different block copolymer and multicomponent systems were performed to confirm the "transferability" of the mapping

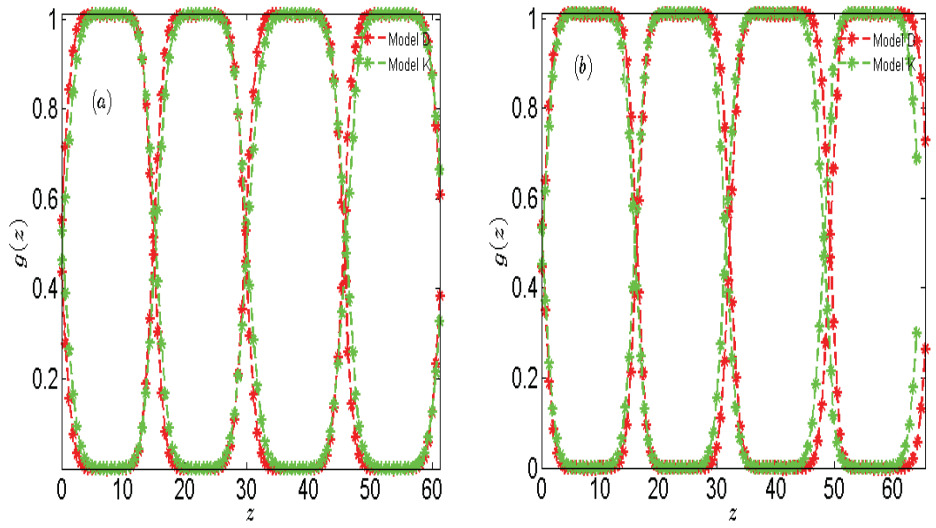

Figure 2.11: Density profiles for (a) $a_{AB} = 29.0$, (b) $a_{AB} = 30.0$ for both Model "D" and Model "K". Interaction parameters of Model "K" are calculated using Eqs. (2.8) after accounting for change in z^{∞} and other parameters in the equation.

between the interaction parameters of the different models and the Flory-Huggins like interaction parameter. The simulations reveal that there exists a *unique*, albeit, nonlinear mapping between the parameters of the chosen CG models, which is independent of the composition of the diblock copolymer and the architecture of the copolymer. Moreover, the commonly used linear mapping between χ and CG parameters was shown to not yield a comparably satisfactory agreement between the peak of the structure factors. Similarly, in the case of polymer-solvent mixtures our preliminary results for a few selected parameters indicate that the same nonlinear mapping deduced for diblock copolymers is effective in mapping the long range structure of different mod-

els. However, we defer a more comprehensive parametric study of the latter class of systems to a future work.

The above feature of universality in the mapping function was shown to open up a possible strategy for obtaining ordered phases for asymmetric diblock copolymer. As test cases, we demonstrated the creation of ordered phases in symmetric diblock copolymer and showed that the structural characteristics of lamellar phases obtained before and after the introduction of hard potentials displayed a very good match.

In principle, the method proposed in this Chapter can be extended to any soft CG potential and to any realistic hard CG potential. The parameters of the nonlinear mapping does depend on the intramolecular interactions of the underlying polymer and hence needs to be reparametrized when different intramolecular interactions are utilized. Despite this additional step, the equilibration time is expected to be reduced significantly when compared to a simulation procedure which directly implements the fine-grained simulations. In the subsequent Chapters, we will present results for the properties of the self-assembled phases generated through such an inverse-coarse graining procedure which were hitherto inaccessible due to the difficulties creating equilibrated configurations involving long chains.

Chapter 3

Entanglements in Lamellar Phases of Diblock Copolymers

3.1 Introduction

There has been a significant revival of interest in the theoretical descriptions of the topological interactions that accompany high molecular weight polymer melts and concentrated solutions [81, 93, 108–110, 110–131, 131–134] . Since the original pioneering works of deGennes [135–137], and Doi and Edwards (DE) [138], it has been a common approach to replace such interactions by fictitious constraining junctions termed as "entanglements" acting on different segments of a chain. In the original theoretical descriptions, the number of segments characterizing the spacing between such junctions, termed the entanglement molecular weight N_e, was viewed as a phenomenological, experimentally determined physical property specific to the entangled polymer, and independent of the chain length [138]. Recently however, there have been two developments which have significantly impacted the theoretical modeling of entangled polymer dynamics. On the one hand, a number of approaches have been proposed which invoke molecular dynamics or Monte Carlo simulations in combination with geometric [93, 118, 127, 139–144] or energy minimization [145, 146] algorithms to enable a direct calculation of the entangle-

ment molecular weight for models of coarse-grained models of polymer chains. Such approaches have been used to study the influence of confinement [132], rings [147], crazing [148, 149], nucleation events, crystallization [150], nanoparticles [151] etc. upon polymer entanglements. A second important development has been the formulation of coarse-grained *single-chain/multi-chain* simulation approaches which can probe the linear and nonlinear dynamics of entangled polymer chains. Such simulations [108, 109, 112, 120, 131, 152–155, 155–158], broadly referred to as "slip-link models,' incorporate the presence of entanglements acting at different points along the chains and invoke rules regarding the motion of such entanglement junctions [108, 109, 112, 120, 131, 152–155, 155–158]. Such simulations have been shown to be capable of rendering quantitative predictions for the rheology and mechanical properties of polymeric melt systems [131, 155–157, 159–163]. [1]

Recently, there has been a shift in the focus to multicomponent polymers like block copolymers, rod-coil polymers, and mixtures of polymers like polymer blends and polymer solutions to achieve applications with physical property requirements that cannot be met by commodity polymers alone[164–175] . With the widespread utilization of such materials, there has also arisen a number of fundamental questions pertaining to the dynamics [20, 40] and rheology of such materials [176–178], and their response to external flow fields [119, 179, 180]. Addressing such issues (especially for the case of long

[1]Citation: Vaidyanathan Sethuraman, Dylan Kipp, Venkat Ganesan, Entanglements in Lamellar Phases, *Macromolecules* **48** (17), 6321-6328 (2015). Dylan Kipp wrote and ran SCFT codes and Venkat Ganesan guided the project.

molecular weight chains) requires, in turn an examination of the concept of entanglements in such materials and their influence upon the dynamics of polymer chains. Specifically, multicomponent polymeric materials often undergo phase separation, leading to macroscopic domains such as in polymer blends or to microphase separated morphologies as in diblock and rod-coil block copolymers [61, 181–183]. Pertinently, the chain conformations accompanying such morphologies are expected to be influenced by the resulting compositional inhomogeneitiesc̃iteMatsen2002. Some outstanding questions include: "Are the entanglement molecular weight N_e of the chains in such compositionally inhomogeneous regions any different from those in the bulk, homogeneous phases?" "Do the compositional inhomogeneities lead to a corresponding inhomogeneous distribution of entanglement junctions?" Since the slip-link models discussed above typically incorporate a spatially prespecified distribution of entanglement junctions, the resolution of such questions is especially important for the extension and implementation of such models to multicomponent polymeric systems [119, 180].

Motivated by the above considerations, in this article we present the results of a two-pronged simulation study of the topological constraints and entanglements of polymer chains in ordered lamellar phases of diblock copolymers. On the one hand, we use molecular dynamics simulations and topological analysis algorithms to calculate both the local and the global average entanglement spacing in the ordered lamellar phases of block copolymers. In the present work, we focus on the influence of the interactions between the

dissimilar blocks of the diblock copolymers as quantified by the Flory Huggins parameter (χ) and identify the variations of entanglement spacing as a function of χ. A second part of our study concerns with the use of packing considerations to understand the results observed in our MD simulations. Explicitly, we adapt one of the popular version of such approaches [184–187] proposed by Kavassalis and Noolandi (KN) which postulates that the ratio of the volume of space pervaded by a chain of length N_e to its hard core volume to be a universal constant (of the order 10) [185]. In later studies, Fetters and coworkers [188–190] have demonstrated that such a model can correlate the entanglement molecular weights of a wide variety of (homogeneous) polymeric materials. Inspired by such successes, we use the KN model in conjunction with polymer self-consistent field theory and Monte Carlo simulations to probe whether the changes in chain conformations resulting due to the self-assembly of the block copolymer can rationalize the trends seen in our MD simulations/topological analysis.

We note that in an earlier work [191], we had used similar packing ideas to identify the influence of interfaces upon the entanglement lengths in polymer blend systems. However, such analysis was effected without the corresponding MD simulations and topological analysis results, and relied on the *unproven* hypothesis that the KN ideas apply equally well to inhomogeneous systems. Hence our results in such a context were to be construed as speculative rather than a conclusive proof of the changes in entanglement spacing. In the present work, by employing two distinct kinds of analyses, which includes the rigorous

topological analysis approaches developed in the time frame since our original publication [141, 144, 145], we hope to unequivocally establish the influence of compositional inhomogeneities upon the entanglement molecular weights in multicomponent polymeric systems. Moreover, by probing the quantitative validity of the KN approach through our results, we seek to open up the possibility of using the simpler and more rapidly implementable packing arguments as a viable framework to deduce the local changes in entanglement molecular weights for complex multicomponent polymeric systems.

The rest of the article is organized as follows. We briefly discuss the methodology used to calculate the constraints in both MD and KN analysis in Section 3.2. Further methodological details are presented in the supplementary information (SI). The results obtained using MD, SCFT and the comparisons between them are presented in Section 3.3. Conclusions and a brief outlook of the article is presented in Section 3.4.

3.2 Simulation Methodologies

3.2.1 Molecular Dynamics Simulations and Z1 Analysis

A number of recent approaches have been proposed for the calculation of entanglement lengths based on the configurations arising in molecular dynamics and Monte Carlo simulations [93, 118, 127, 139–144] . However, a key requirement for all these methodologies is the availability of well-equilibrated morphologies [139, 143]. Due to the long relaxation times involved for collective density fields, such a requirement becomes a challenge in the context of

self-assembled phases of multicomponent copolymers [62, 192]. To overcome this hurdle, in this work we take advantage of a strategy recently proposed by us to achieve equilibrated morphologies in *ordered* phases of long chain multicomponent polymer systems [193]. Briefly, our strategy exploited a rigorous mapping approach proposed by Morse and coworkers,[83, 84] between the parameters of different simulation approaches to ensure the preservation of the long-range structural characteristics of ordered phases in multicomponent polymer systems. Our methodology took advantage of such a mapping to use soft interaction potentials to equilibrate the long-range order in multicomponent polymer systems, and subsequently reintroduce the potentials of interest to equilibrate (in a more rapid manner) the short range structural characteristics of the system [193].

In the present context, we use the above idea to create initial configurations for the lamellar phase of the diblock copolymer by using a soft coarse-grained potential such as that used in dissipative particle dynamics (DPD) [58] simulations. Explicitly, the soft coarse-grained intermolecular potential, (U_{ij}^s) used in this work was:

$$U_{ij}^s = \begin{cases} \frac{1}{2} a_{ij} \left(r - r_c\right)^2 & , r \leq r_c \\ 0 & , r > r_c \end{cases} \tag{3.1}$$

where a_{ij} represents the interaction parameters between monomers i and j, r_{ij} represents the distance between monomers and r_c represents the cut-off radius. The corresponding intramolecular potential, U_b^s was:

$$U_b^s = \kappa_s r^2 \tag{3.2}$$

where $\kappa_s = 5k_BT/r_c^2$ represents the soft intramolecular bond constant between the bonded monomers and k_B and T represents the Boltzmann constant and temperature respectively. Subsequent to equilibration of the above system, we introduce the hard core interactions representative of the system of interest[40] and re-equilibrate the configurations rapidly within the lamellar configurations. For the latter, we chose the Kremer-Grest model [40], where the intermolecular potentials (U_{ij}^h) between the particles are governed by a shifted Lennard-Jones potential of the form,

$$U_{ij}^h = \begin{cases} 4\epsilon_{ij}\left[\left(\frac{\sigma}{r_{ij}}\right)^{12} - \left(\frac{\sigma}{r_{ij}}\right)^{6} + \frac{1}{4}\right] & , r \leq 2^{1/6}\sigma \\ 0 & , r > 2^{1/6}\sigma \end{cases} \tag{3.3}$$

where ϵ_{ij} represents the interaction parameter between monomers i and j, σ represents the diameter of a monomer and r_{ij} represents the distance between the monomers. The intramolecular interactions are of the form

$$U_b^h = \kappa_h(r - \sigma)^2 \tag{3.4}$$

where $\kappa_h = 200\ k_BT/\sigma^2$ represents the hard intramolecular bond constant. By choosing the parameters of the DPD simulation and the hard-core potential in a manner consistent with the mapping discussed in the previous work [193], we ensure that the second stage of equilibration process involves only short-range structural details and can be effected in a rapid manner. All simulations were performed using LAMMPS software [96]. Without loss of generality, we set $\epsilon_{AA} = \epsilon_{BB} = k_BT = 1.0$. To maintain brevity, details regarding the equilibration procedure (thermostats, time constants etc.) are discussed in the supplementary information (SI).

Subsequent to equilibration of the lamellar configurations, we used the methodology termed "Z1-analysis"[139–142] to study the variation of average entanglement lengths. We considered a situation of a fixed chain length of $N = 100$ and varied the compositional interactions between the dissimilar segments of the diblock copolymer. The Z1-analysis proposed by Kröger and coworkers,[139–142] calculates the number of "kinks," which are representative of the entanglement junctions experienced by the chains. These topological constraints are identified for different equilibrium snapshots of the system by minimizing the chain length of all the chains while imposing the noncrossablity constraint. The output of such analysis is the instantaneous number of kinks per chain (averaged over the chains) Z, which can then be averaged over different configurations to obtain the average number of kinks, $\langle Z \rangle$ in the system. In addition to the $\langle Z \rangle$ for all the chains, we also characterize the local variation of $\langle Z \rangle$ by using the locations of the kinks for the instantaneous configurations of the chains. The value of $\langle Z \rangle$ was obtained after averaging over a long MD trajectory of $1.5 - 2 \times 10^5$ τ, with snapshots analyzed every 90 τ, where τ represents time in reduced units. The entanglement length N_e is usually directly obtained from $\langle Z \rangle$ through a variety of correlations (termed as estimators)[140]. In this work however we chose to focus on $\langle Z \rangle$ itself as an unambiguous measure of the entanglement junctions, and only use the qualitative interpretation that an increase (decrease) in $\langle Z \rangle$ is equivalent to a decrease (increase) in N_e. We also note that $\langle Z \rangle / N$ by itself exhibits a dependence on N [140]. However, earlier results in the context of homopolymers[140] have

shown that $\langle Z \rangle / N$ approaches its asymptotic value for $N \simeq 100$, and hence we expect such effects to be minimal for the chain length investigated in our work.

3.2.2 Implementation of KN Analysis

In this section, we present a brief review of the ideas behind the KN analysis used in our work. Further details of the methodology are presented in the SI and in earlier references[184–187, 191]. The fundamental quantity in Kavassalis and Noolandi (KN) analysis is the coordination number, $\bar{N}$, experienced by N_e chain segments of a test chain:

$$\bar{N}(N_e) = \frac{1}{N_e} \sum_{m=1}^{N} m S_{nontails}(m) \tag{3.5}$$

where $S_{nontails}(m)$ represents the number of nontail segments of other polymers with a contour length of exactly m units in the elemental volume (V_e) that encloses the test chain. $\bar{N}$ serves as a measure to quantify the number of constraints experienced by the chain segment. The key postulate of KN was that the coordination number, $\bar{N}$, is a universal quantity which is independent of the underlying chemical structure of the polymer. Such a hypothesis allows one to deduce the entanglement molecular weight by inverting Eq. (3.5).

For implementation of the KN postulate in block copolymer systems, we follow the methodology which was presented in Ganesan *et. al.* [191] for inhomogeneous polymer blends. Due to the presence of compositional inhomogeneities and its influence on the chain conformations V_e and $\bar{N}$ are now

expected to be explicit functions of position, $\boldsymbol{r}$, and hence will be denoted as $V_e(\boldsymbol{r})$ and $\bar{N}(\boldsymbol{r})$ respectively. A lattice based model was used to count the statistics of conformations of the polymer chain in the external fields arising as a consequence of the microphase separation between the unlike segments of the diblock copolymer. To obtain the latter, we used polymer self consistent field theory (SCFT)[61] on the classical model in which the polymers were modeled as Gaussian chains and the overall melt was assumed to be incompressible (details of SCFT are presented in SI). Polymer SCFT provides the self-consistent potential fields acting on the individual segments of the polymer, which in turn serves to enumerate the conformational characteristics of the polymer in the compositionally inhomogeneous phases. In addition SCFT also furnishes chain propagator, $q(\boldsymbol{r}, s)$, which denotes the probability of finding the sth segment at the location $\boldsymbol{r}$. For the case of diblock copolymers, a complementary chain propagator, $q^{\dagger}(\boldsymbol{r}, s)$ can also be defined analogously with respect to the other end of the chain. Together, these propagators serve as a measure of probability of finding a given segment of a chain at different locations in the lamellar phase[61].

Given the chain propagators and the potential fields, we calculate the elemental volume ($V_e(\boldsymbol{r})$) spanned by a chain segment of size N_e centered at the location $\boldsymbol{r}$ by executing random walks in the presence of the self-consistent potential fields. Further, to enumerate $S_{nontails}(m)$ at different locations, a monomer is chosen at random within the chain and is placed at a random position inside $V_e(\boldsymbol{r})$. Random walks in the external potential fields are then

performed to reach the ends of the chain. In the event the chain escapes the elemental volume V_e before the chain is terminated (i. e. corresponding to a non-tail section), the number of segments (m) within V_e were counted and was added to $S_{nontails}(m)$. The above procedure was repeated for different monomers in the chain, and for different positions inside the simulation box (statistics were collected over 5×10^6 such walks). Such statistics was used to calculate $S_{nontails}(m)$ and $\bar{N}(\mathbf{r})$ (Eq. 3.5).

The output of the above lattice simulations is the "local" coordination number of the polymer chains for the ordered morphologies. The latter serves as a measure of the number of constraints experienced by the polymer segments at a specified location and can be directly compared with the $\langle Z \rangle$ obtained from topological analysis. Similar to the methodology prescribed in Ganesan *et. al* [191], the results obtained in this article are based on a fixed value of N_e. By comparing only the changes in the number of constraints relative to the homopolymer case we expect to minimize the effects, if any, arising from the specific choice of N_e. The values of N and N_e chosen in our simulations are 3000 and 27 respectively. The value of $\bar{N}$ obtained for a homopolymer configuration ($\bar{N}^h$) using these values was 7.92.

We note that in principle, the KN analysis described above can be directly applied to the equilibrated configurations obtained using MD simulations. However, such calculations require one needs to analyze the chain configurations to identify the chain segments located within the volume V_e of a specified segment and then effect the calculation of the coordination number.

Such a procedure needs to be repeated for different test segments present at different locations in the lamella to obtain a statistically meaningful result. Since this procedure is somewhat cumbersome, and moreover since the Z1 analysis furnishes a result which is directly consistent with the physical meaning of entanglements, we did not embark on such a task. Nevertheless, results for preliminary investigations which involved the computation of the volume occupied by a chain segment of size approximately equal to the entanglement length of the homopolymer as a function of the positions along the simulation box is given in the Supplementary Information (see Figure S1).

3.3 Results and Discussion

3.3.1 Molecular Dynamics and Z1 Analysis

Figure 3.1(a) displays one of the main results of our MD simulations and Z1 analysis, viz., the average number of kinks present in the system as a function of the Flory-Huggins interaction parameter χ between the A and B segments (in SI, we describe the approach used to relate the strength of interaction parameter in MD simulations to the χ parameter). A clear monotonic increase in the number of kinks is seen for increasing values of χN (the corresponding value of $\langle Z \rangle$ in a homopolymer system for $N = 100$ is 1.82). Since prior studies have indicated that the instantaneous number of kinks Z may exhibit significant fluctuations between different configurations [144], in Figure 3.1(b) we also present the instantaneous Z as a function of the time in molecular dynamics simulations. Even with the evident fluctuations, it can be

seen that there is a clear upward movement of Z with increase in the interaction parameter. These results clearly demonstrate that the number of kinks increase, or equivalently, the entanglement molecular weight decreases, with an increase in the degree of compositional segregation between the blocks of the copolymer. In view of the fluctuations, Steenbakkers *et. al* [121] suggested that considering only the average value of entanglements may not be a representative measure of the distributions. However, since we wish to compare the local values of the entanglement spacings for which such distributions are difficult to characterize in a statistically accurate manner, we nevertheless decided to use $\langle Z \rangle$ (normalized by their respective homopolymer values) to compare our MD results with packing arguments.

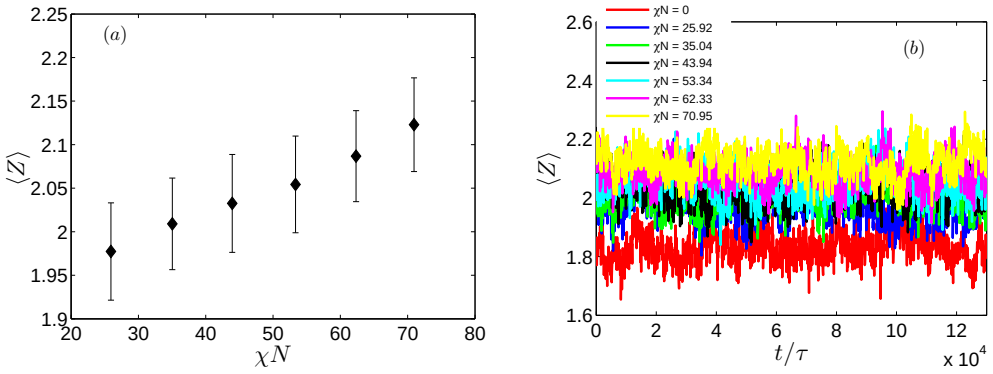

Figure 3.1: (a) Average number of kinks as a function of χN obtained using MD simulations. (b) Fluctuations in the ensemble average of number of kinks as a function of time for different values of χN.

As mentioned earlier, the "Z1-analysis" furnishes both the system average as well as the coordinates of the kinks. Figure 3.2(a) shows the distribution

of kinks as a function of the coordinate in the direction perpendicular to the plane of the lamellae. Yet again, we observe that there is an increase in the local number of kinks (note that the values reported in Figure 3.2(a) are on a per chain basis) when compared to the corresponding values seen for a homopolymer system ($\chi = 0$). More interestingly, we observe that the modifications in the number of kinks occur mainly at the interfacial locations (compare with the overlaid composition profiles presented in Figures 3.2(b) – 3.2(d)), with the magnitude of the peaks in the number of kinks increasing with increasing χN.

3.3.2 Packing Arguments of Kavassalis and Noolandi

To rationalize the results presented in the preceding section, we invoke the influence of microphase segregation upon the chain conformations. Indeed, it is well known that the chains in the lamellar phase are stretched relative to their conformations in homopolymer and/or bulk phases. This suggests that on average, each chain can interpenetrate more and experience a larger of number of constraints (arising from the other chains) within such ordered morphologies. Moreover, we expect that such stretching effects to be (i) more pronounced near the interfaces; and (ii) increase with increasing χN. Together, these considerations suggest that the results presented in Figures 3.2(b) – 3.2(d) to be a likely result of the modifications in chain conformations in ordered phases.

We note that the above reasoning forms the basis of packing arguments

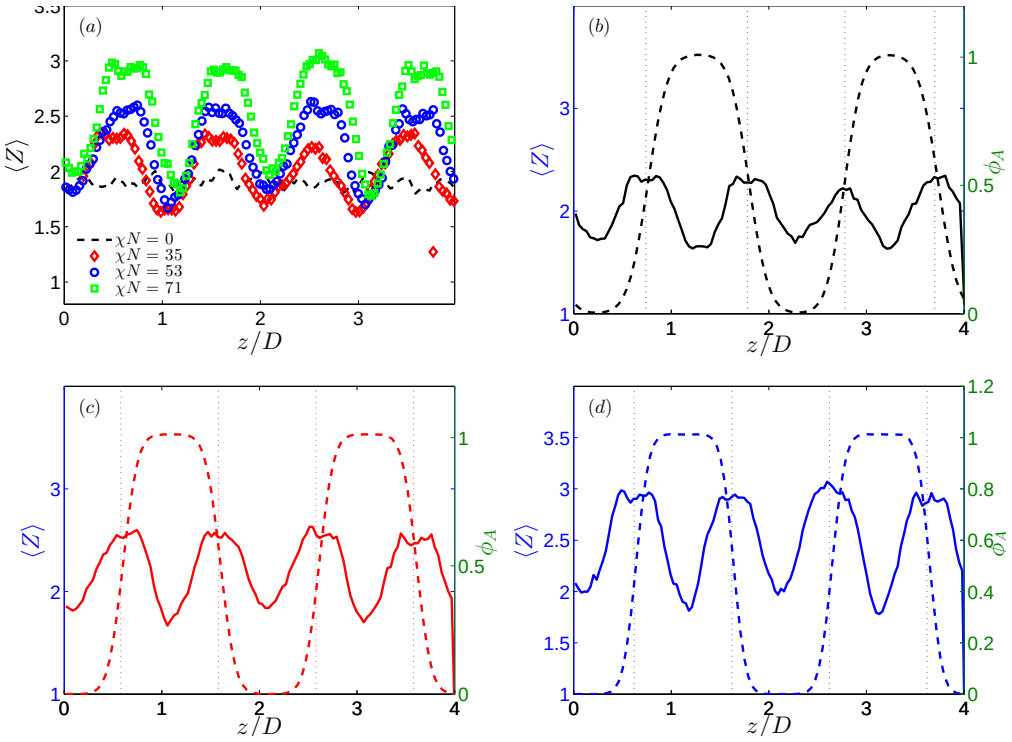

Figure 3.2: (a) Distribution of the number of kinks as a function of distance perpendicular to the interface for different values of χN. The X-axis is scaled by the respective domain widths D for different values of χN; Local values of the average number of kinks for (b) $\chi N = 35$ (c) $\chi N = 53$ and (d) $\chi N = 71$ along with the corresponding composition profile for A monomers (dotted lines). The dotted vertical lines show the interfacial positions for the respective compositional interactions.

which have been proposed to quantitatively identify the entanglement molecular weights of polymeric systems[185–187]. Specifically, we consider the theory of Kavassalis and Noolandi (KN) which postulates entanglement molecular weight can be determined by using the hypothesis that the ratio of the volume of space pervaded by a chain of length N_e to its hard core volume to

be a universal constant (of the order 10) [185]. Or, stated more succinctly by Milner[187] "when enough different chains (a constant number) get into the same room together, an entanglement happens." Since changes in the chain conformations modify the volume pervaded by the chain, the room required to bring a specified number of chains together also changes and leads to concomitant changes in the entanglement molecular weights.

To probe whether the above packing arguments can actually rationalize our MD results at a quantitative level, we implemented the theory proposed by Kavassalis-Noolandi [185] (KN) to analyze the changes in the entanglement lengths arising from the conformational characteristics of the diblock copolymer chains in the ordered lamellar phases (details of the methodology are furnished in supplementary information). Specifically, we use such a methodology to analyze the normalized ratio $\hat{N}(\boldsymbol{r}) = \bar{N}(\boldsymbol{r})/\bar{N}^h$, where $\bar{N}(\boldsymbol{r})$ denotes the average number of constraints experienced by a test polymer chain at equilibrium at the location $\boldsymbol{r}$ in the ordered phase. The quantity $\bar{N}^h$ denotes the corresponding number of constraints in homopolymer phases. The number of constraints $\bar{N}(\boldsymbol{r})$ can be viewed as directly proportional to the *local* $\langle Z \rangle$ deduced in our MD simulations, and by normalizing with the value of the corresponding homopolymers we characterize only the changes arising as a consequence of the compositional ordering.

Figure 3.3(a) displays the normalized local number of constraints ($\hat{N}(\boldsymbol{r})$) for different χN. The distance r is normalized with the domain width D for each χN, and the location $r = 0$ corresponds to the interface between the

A and B phases. As expected, the number of constraints in the bulk A and B phases is seen to be independent of χ and remains equal to that of the homopolymer $\bar{N}^h$. More interestingly, an increase in the local number of constraints is seen near the interface of the lamellar phases. At weak degrees of segregation between the unlike segments, the magnitude of maxima of $\hat{N}(\boldsymbol{r})$ is seen to be small. However, with increasing compositional interactions between A and B monomers, the magnitudes of the inhomogeneity as well as the maxima is seen to increase monotonically. These results are to be compared with those displayed in Fig. 3.2 which displayed similar characteristics. Moreover, in Figure 3.3(b) we display the KN results for the average of the normalized number of constraints $\hat{N}_a$ for different χN . We observe that the average number of constraints increase with χN — again consistent with the trend which was observed in our MD results.

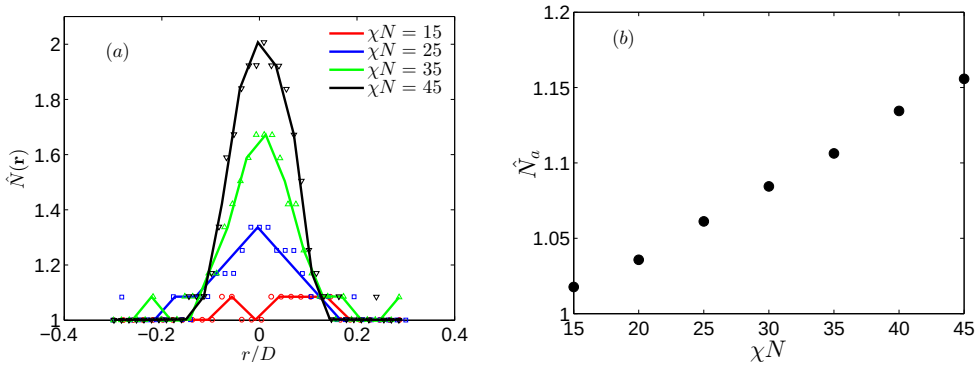

Figure 3.3: (a) Normalized number of constraints ($\hat{N}(\boldsymbol{r})$) is shown as a function of distance from the interface. Distance from the interface is normalized to the domain width, D. Lines are guidelines to eye; (b) Average of the normalized number of constraints ($\hat{N}_a$) is plotted as a function of χN.

Together, the results presented in Figs. 3.1 - 3.3 explore two different methodologies to enumerate the number of constraints experienced by the flexible chains in lamellar phases. We observed that both methodologies yield qualitatively similar trends which indicate that both the local and the average number of constraints (and kinks) in the block copolymer lamella to be higher than the corresponding homopolymer values. Such a qualitative correspondence, when considered in conjunction with the fact that the packing arguments explicitly concerns with the changes in chain statistics, confirms that our MD results can indeed be rationalized as a consequence of the influence of microphase segregation upon the chain conformations.

3.3.3 Quantitative Comparison between MD and KN Analysis

While the preceding section demonstrated a qualitative agreement between MD and KN results, an outstanding question is whether there is a quantitative correspondence between the two approaches. There is a strong motivation to consider such a comparison. Indeed, while there have been some demonstrations of the quantitative accuracy of the KN approach for homopolymer systems,[188–190] to our knowledge, there has been no proof of the quantitative validity of the packing arguments for inhomogeneous systems. If on the other hand such a basis can be established for such packing arguments, then it would substantially expedite the characterization of local variations of entanglements in situations where achieving equilibrated configurations of long chains using MD simulations is a computationally arduous task. Further,

in our previous article[191] we demonstrated that the such packing arguments can be adapted to also probe other quantities such as entanglements between A and B chains which are expected to be different near the interfaces when compared to the bulk situation. In contrast, such information is a lot more cumbersome to extract from MD simulations and topological analysis.

In Figures 3.4(a) and (b), we present a comparison of the local variations and the average number of the number of kinks and constraints (normalized by the corresponding values for the homopolymer system). In comparing the local variations, we observe that the peak values of the normalized KN results displays a reasonable quantitative equivalence to the MD results. However, it is evident that the local variations exhibit a much broader spatial perturbation in MD simulations when compared to the KN results. To justify such differences we point out that the MD simulations incorporate the effect of thermal fluctuations and interfacial undulations upon the resulting morphologies. By virtue of the mean-field nature of the SCFT simulations (which is used an input to the KN analysis), such fluctuation effects are absent in our packing arguments. Indeed, a comparison of the composition profiles of the MD and SCFT approaches for the same χN (Figure 3.4(c)) demonstrates the much broader profiles in MD arising as a consequence of such fluctuation effects. Moreover, the MD simulations correspond to a system with finite compressibility (there is a dip in the total density at the interface, which sometimes manifests as a dip in the $\langle Z \rangle$ in Figure 3.4(a)). In contrast, the SCFT results correspond to a perfectly incompressible system. In addition, we point out

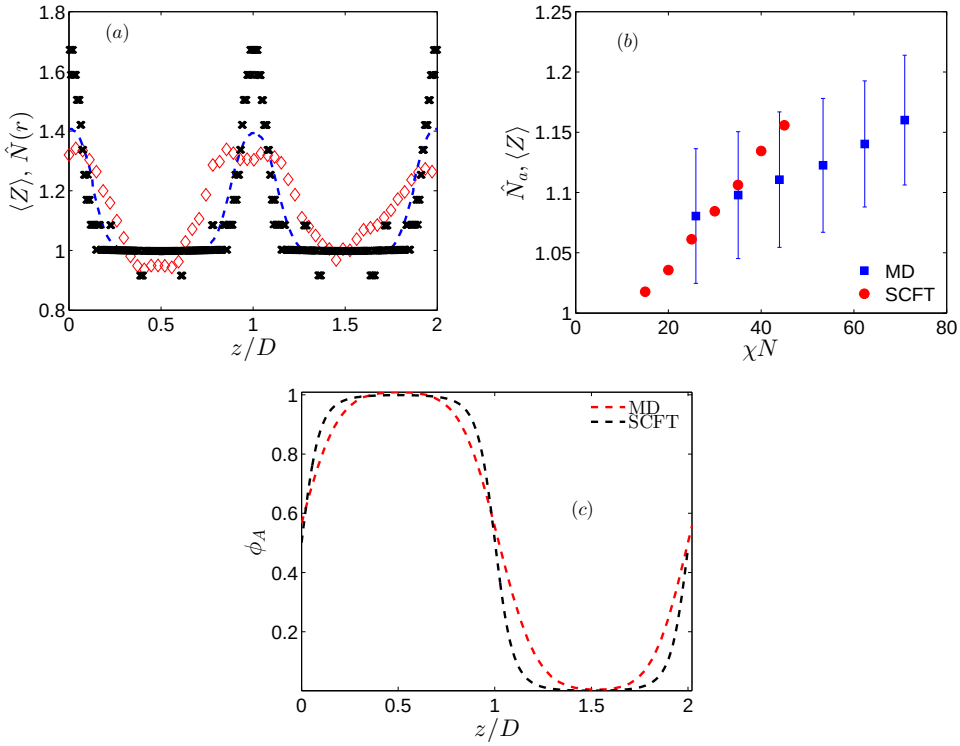

Figure 3.4: (a) Normalized number of constraints as a function of distance perpendicular to the interface for both MD and KN analysis. Legends: red diamonds - MD; black cross - KN analysis without averaging; dotted blue - KN analysis after moving average. (b) Comparison of average number of constraints (kinks) normalized with the corresponding homopolymer values between MD and KN analysis as a function of χN. (c) Composition profile for both MD and SCFT. The results shown in the figure are for $\chi N = 35$

that that the topological analysis underlying our results invokes a geometrical minimization of the chain lengths during which the ends of the chain are fixed whereas the position of other monomers are allowed to relax to achieve the

minimum total chain length of the system. Hence, the kink locations are not necessarily expected to correspond to the monomer coordinates themselves and there is expected to be a broadening of the results of the order of the spatial scale corresponding to an entanglement length. A crude moving average of the KN results by using a length scale corresponding to the tube diameter of the MD results generates a curve (shown in blue dotted lines) which exhibits a closer agreement with MD for the same χN. We suggest that the quantitative deviations between the results of the topological analysis and the KN framework arise as a consequence of such aspects. Not surprisingly, in comparing the average values arising out of MD and KN results (cf. Fig. 3.4(b)), we observe that there is a reasonable, but not perfect, quantitative agreement between the MD and KN results.

3.4 Conclusion

In summary, in this article, we presented the results of a two-pronged simulation study of the topological constraints and entanglements of polymer chains in ordered lamellar phases of diblock copolymers. Results from topological analysis of MD simulations indicated an increase in the average number of entanglements in the lamellar phase of diblock copolymers. To our knowledge, such a trend has not been reported for diblock copolymers using the methods discussed in this article. A second part of this study used packing considerations to understand the results observed in our MD simulations. We demonstrated that the trends in average and the local number of constraints

obtained using KN model as a function of the compositional interaction parameter agrees qualitatively with the variations of number of kinks observed in MD simulations. However, due to the fluctuation effects and other differences, discrepancies were noted between the quantitative values of the topological analysis and KN results. Considering the reasonable quantitative agreement between MD and KN results, and the relative ease with which the packing arguments can be implemented, our results do promote the use of the latter approach for characterizing the local variations of entanglements in inhomogeneous polymeric systems. In conjunction with slip-link models which use such information,[108, 109, 112, 120, 131, 152–155, 155–158] the influence of compositional inhomogeneity upon the rheology of self-assembled phases can then be more faithfully modeled.

Chapter 4

Influence of Molecular Weight and Degree of Segregation on Local Segmental Dynamics of Ordered Block Copolymers

4.1 Introduction

Recently, polymer electrolyte membrane materials have emerged as attractive candidates for devices such as batteries, fuel cells and for applications such as water purification membranes.[194] Unfortunately, electrolyte membrane materials possessing high ionic conductivities often tend to lack the requisite mechanical strength for applications. In this context, significant interest has arisen in the use of ordered phases of multicomponent block copolymers, in which one or more of the blocks (glassy) serves to furnish mechanical strength to the membrane while the other "functional" (rubbery) block facilitates transport of ions and permeants [9, 22, 24, 26, 195–198] . Inspired by the successes in the context of polymer electrolytes, other studies have extended this general idea to design alcohol separation membranes, fuel cells etc.[198, 199] [1]

[1]Citations: (i) Vaidyanathan Sethuraman, Victor Pryamitsyn, Venkat Ganesan, "Influence of Molecular Weight and Degree of Segregation on Local Segmental Dynamics of Ordered Block Copolymers", *J Polym. Sci Part B: Polym. Phys*, **54**, 859-864 (2016). (ii) Vaidyanathan Sethuraman, Venkat Ganesan, "On the Relationship between the Local Segmental Dynamics and the Tagged Monomer Dynamics in Lamellar Phases of Diblock

In the use of block copolymer membranes, the expectation is that the conductivity (or permeability) of the self-assembled systems would be identical to that of the corresponding conducting polymer when normalized appropriately for the volume fraction of the blocks and the large scale orientational disorder of the self-assembled morphologies.[24, 26, 198] While such expectations have borne out in some results,[24, 200] a number of intriguing, nontrivial observations have also been noted. In this work, we are concerned with the molecular weight dependence of the conductivity noted in experiments for the lamellar phase of block copolymer electrolytes. Specifically, a number of experiments have observed that increasing the molecular weight (MW) of the conducting block (at a fixed composition of the block copolymer) leads to an increase in the conductivity of the electrolyte.[24, 26, 201] Similar results were also recently reported for permeability characteristics of ethanol separation membranes [202]. Such results contrast with the trends for a homopolymer in which conductivities have been observed to decrease with increasing molecular weight.[25] These results have sparked an interest in developing a fundamental understanding of the conductivity behavior of self-assembled block copolymers and the mechanisms underlying differences from that of homopolymers.

Motivated by the above results, in an earlier article we presented coarse-grained simulations of the sorption and transport of penetrant cations in block copolymer systems. Our results for ion conductivities exhibited MW behavior

Copolymers", *J Chem Phys* (Accepted). Victor Pryamitsyn was helpful in discussions pertaining to the project and Venkat Ganesan guided the project.

similar to those seen in experimental results [29]. Our analysis suggested that with increasing molecular weight of the block copolymer there was a reduction in the overlap of the ions with the interfacial zone of the block copolymer. We hypothesized that the interfacial zones in such rubbery-glassy block copolymers are likely to possess reduced mobilities, and hence, a reduction in the number of ions in such regions would lead to the observed increase in the conductivities.

In this Chapter, we revisit the above issue and focus specifically on the hypothesis regarding the length scale of dynamical inhomogeneities in ordered block copolymer systems. A number of experiments have demonstrated that ion and penetrant transport in polymer electrolyte materials to be strongly slaved to the segmental dynamics of the matrix [10, 25, 201, 203, 204]. Within such a framework, the success and viability of block copolymer electrolytes is expected to critically hinge on the influence of the glassy segments on the dynamics of the rubbery (conducting) segments. Indeed, if the dynamical influence of the glassy phase on the rubbery phase behavior is independent or only weakly dependent on the molecular weight, long molecular weight block copolymers can potentially be used to achieve larger conducting regions and overcome the unfavorable regions characterized by slow dynamics. In contrast, if the length scale of dynamical influence of the glassy block depends on the molecular weight of the block copolymer, then, success of such electrolytes would depend on the relative volumes of the mobile and slow regions and their variations with the molecular weight of the copolymer.

A number of experiments have demonstrated that dynamics of polymers in confined spaces can be dramatically different in comparison to bulk, and that the perturbations induced by surfaces can, in some instances, extend to distances many times the polymer size [205–209] . However, there have been only very few experimental studies which have studied the above issue in multicomponent polymer systems. Nealey and coworkers studied the glass transition temperatures in tethered polymer films (which are superficially similar to ordered block copolymer morphologies) and found long-range perturbations in the dynamics similar to those observed in polymer films [210–212]. In a recent article, Baglay and Roth studied the local glass transition temperature (T_g) across an immiscible glassy-rubbery interface and found that T_g exhibited variations over a length scale which was many orders of magnitude larger than the interfacial width [213]. An earlier study by Roth and Torkelson suggested that the *dynamics* in the interfacial region of block copolymers should resemble the characteristics of immiscible polymer blends [214].

Further, in the above contexts, Torkelson and coworkers has pioneered the use of fluorescence dyes for characterizing the *local* glass transition temperature (T_g) of polymeric materials in a variety of confinement situations.[213, 215–217] Such experiments measure the steady-state fluorescence intensity of the dyes, a characteristic sensitive to the polarity, rigidity and density of local environment, and thereby serves to provide a measure of the temperature at which the local polymer surroundings transition from a melt to glass state. Using such studies, Torkselson and others have suggested that "interfacial"

effects manifesting in dynamics can persist to extremely long length scales relative to the physical dimensions of the polymer.[213, 215–217].

Recent works by Priestley, Register and coworkers [218], which sought to adapt the experimental approach of fluorescent dye tagged polymers as a means to characterize the spatial variations in T_g in the ordered phase of block copolymers.[218] Explicitly, through appropriate synthesis techniques, Priestley and coworkers were able to covalently tag specific monomers along the backbone of block copolymers such that the fluorescent dyes were all located at the same monomer location along the chain. Subsequently, by measuring the steady-state fluorescence intensity of the dyes, they characterized the local glass transition characteristics in lamellar phases of block copolymers. Their results were interpreted by assuming that the T_gs reported by the tagged dyes at a specific location along the polymer backbone corresponds to the average T_g at a given distance from the interface (scaled to domain width) [218]

In microphase separated systems such as in the lamellar phases of block copolymers, even monomers which are located at the same position along the polymer backbone are expected to have a spatial distribution within the morphology. Viewed in such a context, it becomes questionable whether indeed the T_gs reported by the dyes tagged to a specific location along the polymer backbone corresponds to the average T_g at a given distance from the interface [218].

Motivated by the lack of clarity on the above issues for ordered block copolymer systems, in this work we used computer simulations to study the

following questions:

1. What is the influence of microphase separation on the segmental dynamics of block copolymers?

2. On what length scale does the segmental dynamics transition, if at all, from interfacial to the bulk properties?

3. Is the length scale of transition from interface to bulk dynamics dependent on the molecular weight of the blocks?

4. Is the length scale of transition from interface to bulk dynamics dependent on the mobility disparity between the two blocks?

5. Is there any relationship between the spatial variations of segmental dynamics of block copolymers in lamellar phases and their correspondence to the relaxation times reported by tagged monomers identified by their position along the polymer chain.

A recent work by Slimani *et al.,* [34–36] used computer simulations to study some of the issues identified in the previous paragraph. They used a model of a AB diblock copolymer in which the strength of the AA and BB repulsive interactions were tuned to achieve the density, and thereby mobility, differences between the A and B monomers, and also to drive the segregation between A and B components. Using such a model, they studied the spatial variations of segmental dynamics in ordered block copolymer morphologies

and found that the length scale of dynamical heterogeneities to be limited to a fraction of the lamellar width. However, as a consequence of the framework they employed, modifying the degree of segregation results simultaneously in mobility and density changes of the respective phases, thereby rendering it difficult to isolate the interfacial effects from the influence of mobility disparities. Moreover, their study was concerned with a single molecular weight for the block copolymer, and as a consequence, did not shed light on the explicit dependence of the length scale of dynamical inhomogeneities individually upon the degree of segregation, molecular weight and mobility disparity between the blocks.

The rest of the Chapter is organized as follows. Simulation details and the measures used to analyze the local heterogeneties are discussed in Section 4.2. Results and discussion pertaining to the local relaxation times are discussed in Section 4.3.1. Results and discussion regarding the probability distribution of monomers and non-Gaussianity parameter are discussed in Sections 4.3.2 and 4.3.3 respectively. In Section 4.4 we report the results of coarse-grained simulations which probed the relationship between the spatial variations of segmental dynamics of block copolymers in lamellar phases and their correspondence to the relaxation times reported by tagged monomers identified by their position along the polymer chain. A summary of the Chapter is given in Section 4.5

4.2 Simulation Methods

In this work, we used molecular dynamics simulations to study the spatially resolved segmental dynamics in ordered lamellar phases of block copolymers. Towards this objective, we employed methodologies that were developed recently in our group [193], to achieve equilibrated morphologies in multicomponent polymeric systems possessing realistic hard-core interactions. For our dynamical studies, we chose the popular Kremer-Grest model [40]. The force–fields and method of parameterization have already been discussed in previous Chapter (Section 2.2.3). Additional simulation details, pertaining specifically to this Chapter are discussed below.

4.2.0.1 Implementing Mobility Asymmetry

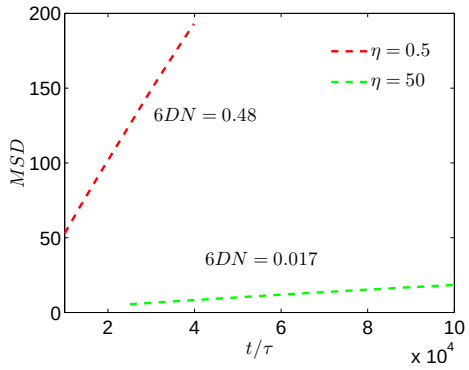

Figure 4.1: Center of mass mean squared displacements for the parameters chosen for Model L.

To study the influence of mobility differences between the different blocks upon the local dynamics of segments, the dynamics of the equilibrated systems were studied using three approaches: (i) *Model N*: The system was

evolved in a constant temperature ensemble using a Nosé-Hoover thermostat. With the friction coefficient denoted as ζ_i, where i represents the type of monomer, the present case corresponds to $\zeta_A/\zeta_B = 1.0$; (ii) *Model L*: We used a Langevin thermostat with different friction coefficients acting on the A and B monomers. Explicitly, we set the friction coefficient acting on A monomers (ζ_A) to be 50 $\bar{\tau}^{-1}$ and that on B monomers to be 0.5 $\bar{\tau}^{-1}$ (where $\bar{\tau}$ denotes monomer time unit). We display the mean squared displacements and the center of mass diffusivities calculated for homopolymer melts with such friction coefficients (Figure 4.1). For the specific values we adopted ($\zeta_A = 0.5$, $\zeta_B = 50$), the diffusivities differ by a factor of ≈ 30, suggesting that the mobilities of the different blocks differ by more than an order of magnitude; (iii) *Model* L_∞: To mimic experimental systems wherein one of the blocks has an extremely low mobility, a block copolymer system with one of the components possessing infinite friction coefficient was also simulated (subsequent to equilibraton of the morphologies). To this end, a harmonic restraining potential with a very high spring constant was added to the slow monomers to constrain the motion of slow monomers. Since this model also results in asymmetric mobilities along the lines of Model L, this model will be designated as Model L_∞ in the subsequent discussion.

4.2.1 Local Dynamics

To quantify the spatially resolved dynamics of monomers constituting the copolymer, the position of the lamella interface (z_{int}) was identified for each

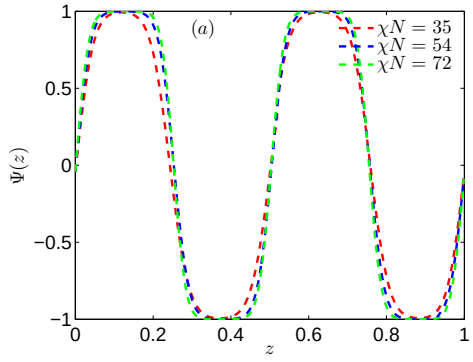

Figure 4.2: (a) Normalized density profile, $\Psi(z) = \frac{\phi_A - \phi_B}{\phi_A + \phi_B}$ as a function of distance scaled with respect to the box length L for different χN values investigated.

degree of segregation (χN) as the location corresponding to the intersection of the averaged number density profiles of A and B monomers (Figure 4.2). The monomers that constitute the block copolymer were then divided into layers based on their distance (z) from the nearest interface. Positive values of z were assigned to the set of monomers which were present at a distance of z in their corresponding lamellar domain (for *e.g.*, A monomers in A domain), and negative coordinates were ascribed if the monomers were present in the lamellar domain corresponding to the other block (for *e.g.*, A monomers in B domain). Subsequent to cataloging the initial location of the monomers, we calculated the following dynamic properties:

4.2.1.1 Incoherent Self-Intermediate Scattering Functions

Incoherent self-intermediate scattering functions ($S(q,t,z)$) based on the location z of the monomers at time $t = 0$ can be described using:

$$S(q,t,z) = \langle \cos(\mathbf{q} \cdot \Delta\mathbf{r}) \rangle \tag{4.1}$$

where $\Delta\mathbf{r} = \mathbf{r}(t) - \mathbf{r}(0)$ represents the displacement of monomers the lamellar plane at a given distance z and $\mathbf{q}$ represents the wave vector.

In this Chapter, we analyzed the local inhomogeneities by considering the displacements ($\Delta\mathbf{r}_{xy}$) parallel to the lamellar plane for segments initially located at the position z at $t = 0$. For all the analysis, $q = |\mathbf{q}|$ was chosen to be 0.71 σ^{-1} (we chose a variety of different q values and found the qualitative features of the results to be insensitive to the magnitude). Typical $S(q,t)$ plots for both Model L and Model N are displayed in Figure 4.3. $S(q,t,z)$ was fit to a Kohlrausch-Williams-Watts (KWW) [219] function of the form: $e^{(-t/\tau^s)^\beta}$ to extract the relaxation time $\tau^s_{xy}(z)$ and the stretching parameter $\beta^s(z)$. Further, the average relaxation time, $\hat{\tau}^s_{xy}$ was obtained using $\hat{\tau}^s_{xy} = \tau_{xy}\Gamma(1 + 1/\beta^s)$, where $\Gamma(n)$ denotes the Gamma function. In all the cases presented below, the relaxation times are scaled with respect to that of the corresponding homopolymer, $\tau_{norm,xy} = \hat{\tau}^s_{xy}/\hat{\tau}_h$.

4.2.1.2 Probability Distribution of Monomers

We also computed the distribution of displacements as a function of the distance from the interface by using self part of the van Hove functions

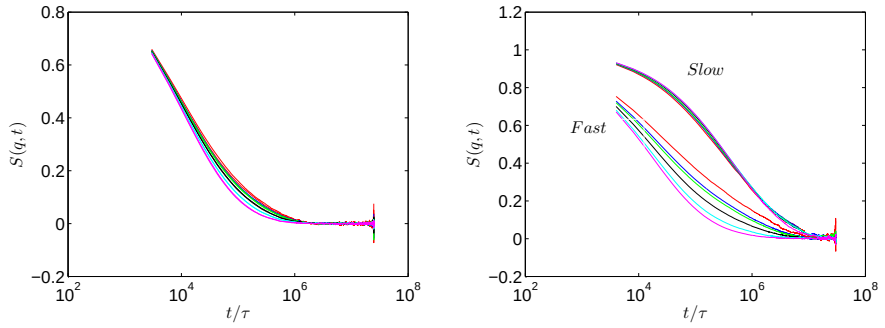

Figure 4.3: Typical relaxation curves obtained from simulations for (a) Model N (b) Model L. The arrow marks show the direction away from the interface.

$(G(r,t))$:

$$G_s(r,t) = \langle \frac{1}{N} \sum_{i=1}^{N} \delta(\mathbf{r} - (\mathbf{r}_i(t) - \mathbf{r}_i(0))) \rangle \tag{4.2}$$

where δ represents the Dirac delta function. We also calculate (locally), two different moments of $G_s(r,t)$: (i) non-Gaussianity parameter $(\alpha(r(t)))$ and (ii) mean squared displacements. Spatially resolved mean squared displacements $(\langle r_{xy}^2 \rangle)$ were calculated using,

$$\langle r_{xy}^2(z_0) \rangle = \frac{1}{2} \langle \sum_{i=x,y} [(\boldsymbol{r}_i(t,z_0) - \boldsymbol{r}_{CM}(t)) - (\boldsymbol{r}_i(0,z_0) - \boldsymbol{r}_{CM}(0))]^2 \rangle \tag{4.3}$$

where $r_i(t,z_0)$ represents the displacement of all the monomers at time t in directions parallel to the interface at a distance $z_0 = |z - z_{int}|$ at $t^* = 0$ with z_{int} representing the nearest interface position.

4.2.1.3 Non–Gaussianity Parameter

Non-Gaussian parameter $(\alpha(r(t^*)))$ is defined as the ratio between fourth and second moments of probability distribution function and is cal-

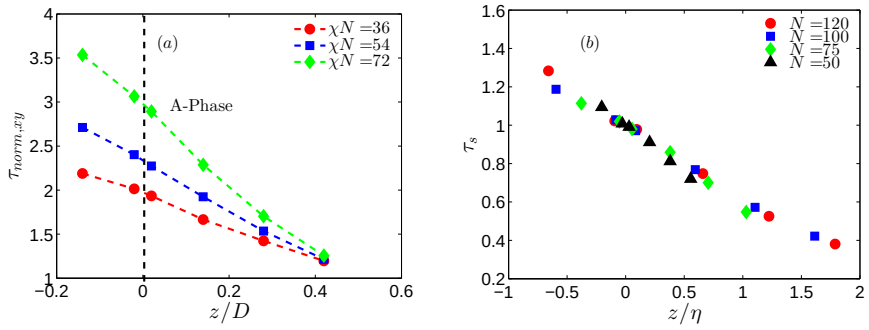

Figure 4.4: (a) Normalized relaxation times, $\tau_{norm,xy} = \tau^s_{xy}/\tau_h$ for lamellar blocks with identical mobility for different values of χN with $N = 100$ (b) relaxation times renormalized with the relaxation time of monomers near the interface for different values of N with $\chi = 0.72$.

culated for a two dimensional case using: [220]

$$\alpha(r(t^*)) = \frac{1}{2}\frac{\langle \boldsymbol{r}^4(t^*)\rangle}{\langle \boldsymbol{r}^2(t^*)\rangle^2} - 1 \tag{4.4}$$

where the $\boldsymbol{r}$ is computed using the positional vectors in the direction parallel to the lamellar plane.

4.3 Results and Discussion

4.3.1 Influence of Degree of Segregation on Local Relaxation Times

In Figure 4.4(a), the normalized relaxation times ($\tau_{norm,xy}$) for Model N are displayed for different values of χN as a function of distance from the interface z normalized by the domain width D. It can be observed that, the monomers in the proximity to the interface ($z = 0$) exhibit slower dynamics relative to the bulk of the lamella and that the retardation of the dynamics

become more pronounced with increasing χN. We recall that this case corresponds to a situation in which the mobility of A and B blocks are identical, and hence the dynamical effects observed herein can be attributed exclusively to those arising from the self-assembly of the block copolymer and the unfavorable interactions accompanying the interfacial region.

In Fig. 4.4(a) we observe that the regions of perturbations in the relaxation times correspond approximately to about 25 % of the domain width. This observation is consistent with the results presented in Slimani *et. al.* [34] who showed that the relaxation times also decay within 15 % of the domain width for their simulations. To quantitatively identify the length scale of inhomogeneities, we effected simulations in which the degree of segregation (χ) was fixed, and varied the molecular weight of the block copolymer. In Figure 4.4(b), we display the relaxation times (normalized with the relaxation times of the monomers near the interface) as a function of distance from the interface (explicit results for the interfacial width are displayed in Figure 4.5) scaled with interfacial width ($z^* = z/\eta$) for different chain lengths (N) for the same degree of segregation χ (Figure 4.4(b)). In this representation, the normalized relaxation times are seen to be independent of the chain length and collapse onto a single curve. This indicates that for the system wherein the A and B monomers possess identical mobilities, the length scale underlying dynamical inhomogeneities of lamellar block copolymers corresponds to the interfacial width in such phases.

Figure 4.6(a) displays the spatial dependence of relaxation times for

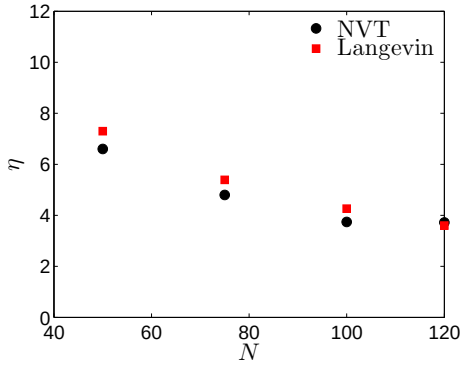

Figure 4.5: Interface values for $\chi = 0.72$ for the models considered in the main text.

Model L for different degrees of segregation at a fixed chain length ($N = 100$). For the fast (B) block, the dynamics is again seen to be slowed near the interfacial regions. In comparing the results of Figure 4.6(a) and Figure 4.4(a), we observe that the dynamics of the B segments are more significantly slowed in the interfacial region and in the A phase for model L. Such a result demonstrates that the reduction in the mobility of the fast monomers depends not only on the distance from the interface but also on the mobility of the local environment [34]. Similarly, slower monomers present in the faster domain are seen to exhibit smaller relaxation times compared to their counterparts in the slower domain (see Figure 4.7 for a more clearer depiction of the dynamics of slow monomers). Interestingly, the influence of the interface upon dynamics is seen to be considerably less pronounced for slow monomers when compared to that of the faster block segments.

In Figure 4.6(b), we display the results for model L in simulations

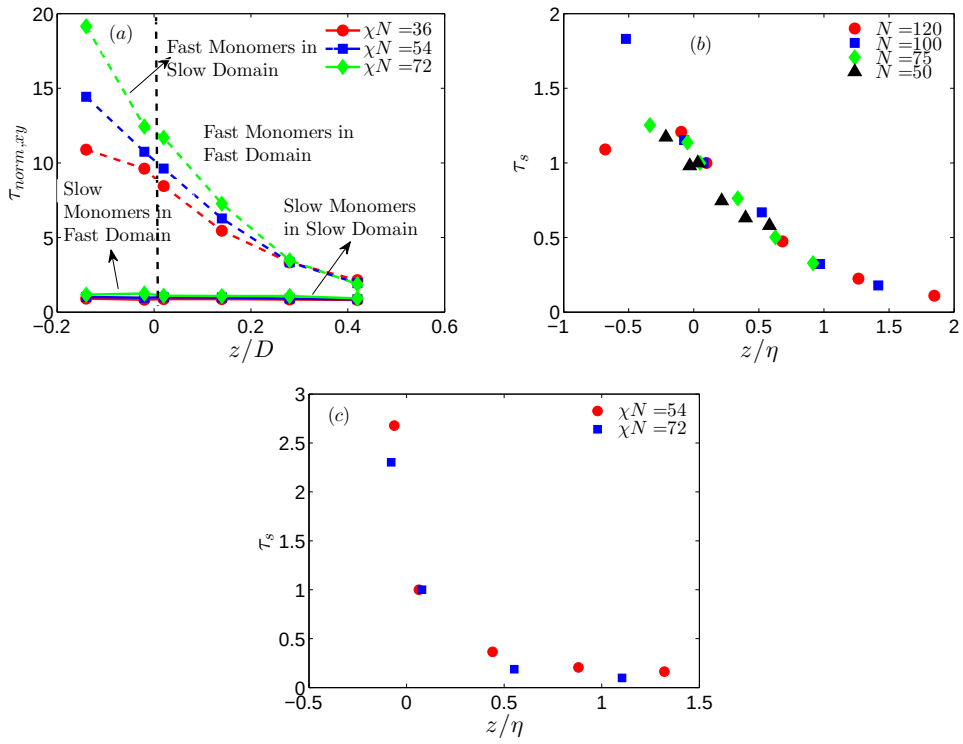

Figure 4.6: Normalized relaxation times, $\tau_{norm,xy} = \tau^s_{xy}/\tau_h$ for lamellar blocks for: (a) different values of χ with $N = 100$ for Model L. The solid and dotted lines show the relaxation times of slow and fast monomers respectively; (b) different values of N with $\chi = 0.72$ for fast monomers and $\zeta_A/\zeta_B = 50$; (c) different values of χ with $N = 100$ and $\zeta_A/\zeta_B = \infty$.

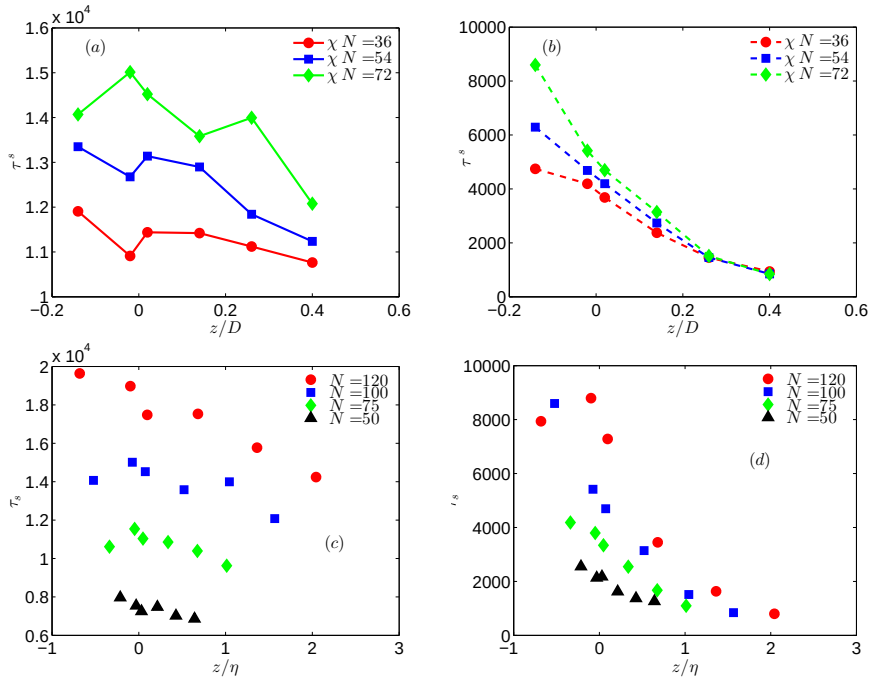

Figure 4.7: (a) Individual relaxation time curves for Model L for slow (a)/(c) and fast monomers (b)/(d). Relaxation curves as a shown as a function of χN in (a)/(b) and as a function of N for $\chi = 0.72$ in (c)/(d). Abscissa are scaled with respect to domain width D in (a)/(b) and with respect to interfacial width η in (c)/(d).

where χ was kept the same while N is varied. Overall, the results are seen to be qualitatively similar to those obtained in Model N. Explicitly, the changes in the relaxation times are seen to be independent of the chain length for both the fast and slow blocks. Moreover, the length scale over which the relaxation time is perturbed is again seen to be correlated to the interfacial width of the block copolymer lamella.

In Figure 4.6(c), we present the results for diblock copolymer systems for Model L_∞. Due to computational issues, we restricted our investigations to

different χ values for fixed $N = 100$. Moreover, due to the significant heterogeneity in dynamics of the different monomers, the stretching parameters β^s obtained by fitting $S(q, t, z)$ for these systems were extremely low and hence we display the values τ_p instead of $\bar{\tau}$. It can again be seen that the spatial variations of the relaxation times collapse for different compositional segregations when considered as a function of interfacial widths. Together, the results of Figure 4.4(b), Figure 4.6(b) and Figure 4.6(c), unequivocally confirms that the interfacial width controls the length scale of perturbation of inhomogeneities in the dynamics in ordered phases of block copolymers.

The results presented above relate to the average dynamics of segments at different locations relative to the interface. However, such quantities do not completely characterize the nature of the heterogeneities in the dynamics of the monomers present at a given spatial location.

4.3.1.1 Stretching (β) Parameter

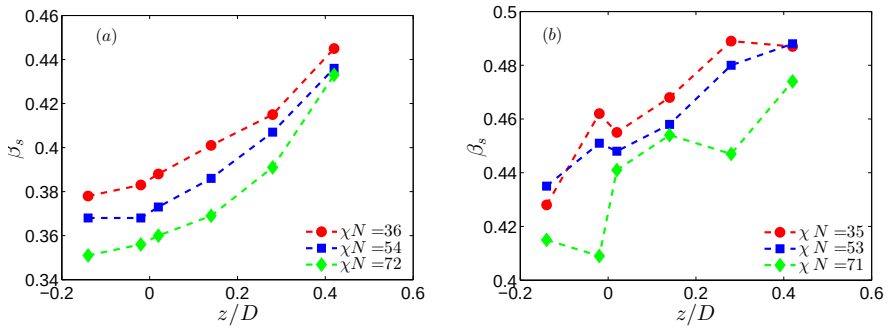

Figure 4.8: Stretching parameter β_s obtained for (a) Model N (b) fast monomers of Model L. Lines are guidelines for the eye

The results presented in the main text for $S(q,t,z)$ relate to the average dynamics of segments at different locations relative to the interface. However, such a characterization does not provide any insight into the heterogeneities in the dynamics of the monomers present at a given spatial location. To illustrate such effects, in Fig. 4.8, we present the stretching parameter (β_s) corresponding to the fits of $S(q,t)$ as a function of the distance from the interface as discussed in the previous section. We observe that β_s increases with increasing distance from the interface for both model N and for the fast monomers of model L (slow monomers did not show any appreciable change in β_s in the time scales of simulation). These results suggest that the local heterogeneities in dynamics increases with increasing proximity to the interface. Further, such characteristics become more pronounced with increasing mobility disparity and degree of segregation between the A and B blocks. These results broadly mirror the trends reported by Slimani *et. al.* [34]

4.3.2 Moments of Probability Distribution Functions

Local relaxation times obtained in previous section showed significant heterogeneity in the time scales at which segments relaxed. Stretching parameter, (β_s) obtained in from the previous section showed that non-exponential decay behavior of polymeric segments becomes predominant with proximity to the interface as well as with increases compositional interactions. This suggests that the local dynamics of polymers near the interface are different from that away from the interface. To understand such dynamics at a finer

resolution, we calculate the moments of the probability distribution function of displacements of different segments and its moments using the self part of the van Hove function [36] ($G(r,t)$) given by Eq (4.2) which quantifies the probability distribution for particles which have moved a distance $|r|$ in time t

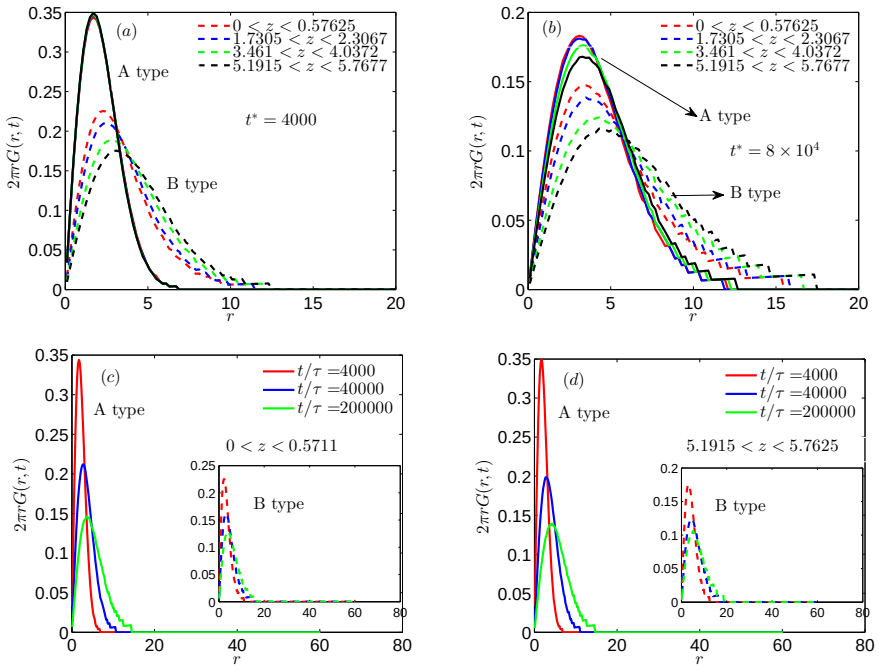

Figure 4.9: van Hove functions plotted for various segments in the block copolymer as a function of displacement at (a) $t^* = 4000$ and (b) $t^* = 2 \times 10^5$. van Hove functions plotted for various segments in the block copolymer as a function of time for (c) near interface and (d) away from interface. All simulations are performed at $\chi N = 53$

For the case of block copolymers with asymmetric mobilities, $G_s(r,t)$ serves as a useful tool to characterize "caging" [221–224] effects wherein the

diffusion of monomers are hindered by the local environment. Such effects, *if any*, are expected to be higher for fast monomers near the interface due to the presence of chemical linkage to the slow monomers ("correlation-hole" effect). Here, we investigate $G_s(r,t)$ to quantify the effect of the friction associated with slow (A) monomers for Model L upon the caging on fast (B) monomers. Figures (4.9)(a) and (b) show $G_s(r,t)$ for different segments of the block copolymer at $t^* = 4000$ and $t^* = 8 \times 10^4$ respectively. The fast (B) monomers show a heterogeneity in their distribution at both short and long times. At short times, due to the large friction associated with the slow A monomers, the distribution of displacements of various A segments is hardly discernible at short time scales ($t^* = 4000$). In contrast, at longer time scales ($t^* = 2 \times 10^5$), both the slow and fast monomers are observed to have heterogeneity in their displacements, with slow monomers showing heterogeneity to a lesser extend compared to that of the fast monomers. This is consistent with the larger relaxation times obtained for slow monomers from the previous $S(q,t)$ calculations.

Figs. 4.9(c) and (d) show $G_s(r,t)$ for higher compositional interaction as a function of time for monomers near the interface and away from the interface respectively. It can be seen that similar trends can be observed for monomers irrespective of the positions thus suggesting that the monomers of the fast B monomers near the interface has considerable mobility despite them being attached to the slow A monomers. This suggests that although compositional interactions create a heterogeneity in the displacement distribution as

a function of distance from the interface, none of the segments are pinned to the interface for the range of χN and mobility ratios investigated here.

4.3.3 Non-Gaussianity (α) Parameter

To understand the above results, we consider the displacement characteristics of the different monomers and its depdence on the distance from the interface. To quantify the heterogeneitis associated with the dynamics of the monomers as a function of distance from the interface, we probed the probablity distribution of the monomers of different identities as a function of distance from the interface. Instead of displaying the probablity distributions themselves, we present results for the heterogeneities in the probablity distributions characterized by the non-Gaussian parameter defined using Eq. 4.4.

The magnitude of deviations of α from unity indicate hetereogeneities in the displacement characteristics of the monomers. We display the α results as a parametric dependence on the average mean-squared displacements. This representation also provides a compact measure of the degree of heterogeneity in the motion and the length scale over which such heterogeneities persist in the motion of the monomers.

Fig. 4.10(a) shows $\alpha(r(t^*))$ between A and B monomers ($\chi N = 54$) as a function of distance from the interface for Model N. It can be seen that the such effecs becomes negligible for segments that are near the bulk of each lamella. Moreover, the magnitude of the maximum of $\alpha(r(t^*))$ parameter increases for increasing χN suggesting that the degree of segregation impacts

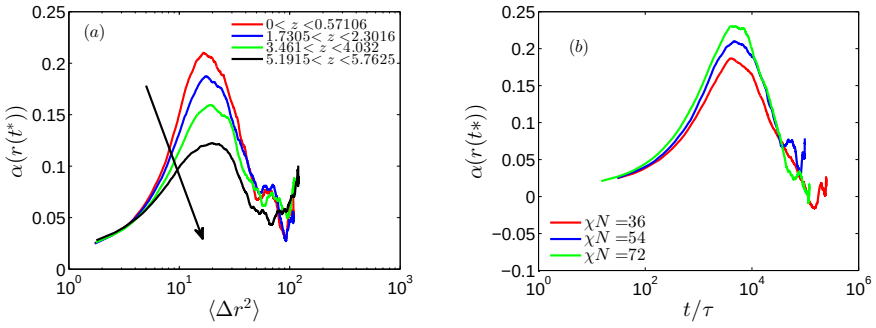

Figure 4.10: (a) Non-Gaussian parameter ($\alpha(r(t^*))$) is plotted as a function of the total segmental MSD for each segment in the lamellar phase (see legends) for $\chi N = 54$. The arrow mark denotes increasing distance from the interface to the layer under consideration. (b) Variation of $\alpha(r(t^*))$ as a function of the interaction parameter χN.

magnitude of heterogeneities. However, the value of the maximum exhibited for monomers that are away from the interface are seen to be independent of the degree of segregation between the blocks. Mean squared displacements also showed heterogeneities when such functions were plotted as a function of distance from the interface.

In Fig. 4.11(a), we display the corresponding results for Model L. In this case, the motion of the fast monomers are seen to exhibit a distinctly higher peak for $\alpha(r(t^*))$ compared to the slow monomers (and also compared to the results for the model N). Near the interface, the segments of a given type (A or B) encounters segments with different chemical identity as well as with different mobility. Such differences lead to a pronounced peak in $\alpha(r(t^*))$ for segments near the interface. Interestingly, the motion of the slow monomers is relatively unaffected by the presence of the fast monomers and we observe

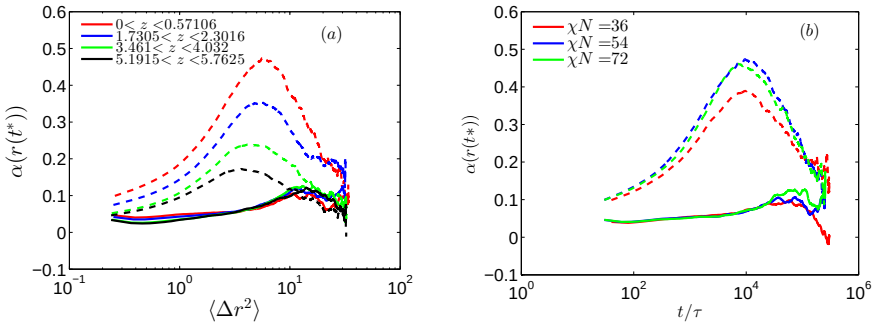

Figure 4.11: (a) Non-Gaussian parameter ($\alpha(r(t^*))$) is plotted as a function of the segmental MSD for each segment in the lamellar phase for Model L at ($\chi N = 54$). Dotted lines show the variation of $\alpha(r(t^*))$ for B (fast) monomers and solid lines show the variation of $\alpha(r(t^*))$ for A (slow) monomers (b) Variation of $\alpha(r(t^*))$ of B (fast) monomers as a function of the interaction parameter χN.

that heterogeneities are lowered relative to model N. These results can be understood by observing that because of the differences in mobilities of A and B monomers, the fast B monomers surrounding the A monomers have already relaxed on the time scale of motion of the B monomers. Thus, the A monomers encounter an environment with reduced heterogeneities relative to the model N.

4.4 Relationship between Local Segmental Dynamics, Tagged Monomer Dynamics and Distribution of Monomers in Lamellar Phases of Diblock Copolymers

In this section, we report the results of coarse-grained simulations which probed the relationship between the spatial variations of segmental dynamics

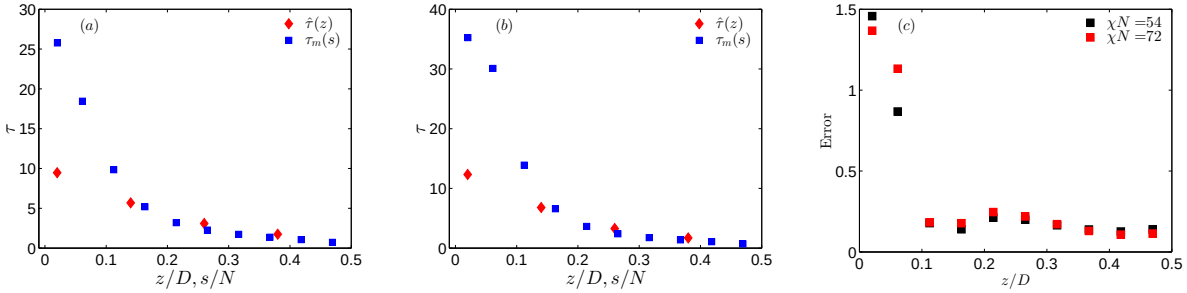

Figure 4.12: (a) Comparison between the dynamics reported by the tagged monomers, $\tau_m(s)$ (index s normalized by N) with the spatial variation of average relaxation times, $\hat{\tau}(z)$ (z denotes the distance from the interface and D the lamellar width). The relaxation times are normalized by their values in the homopolymeric state; (b) Comparison between $\tau_m(s)$ and $\hat{\tau}(z)$ for two different degrees of segregation χN: Black ($\chi N = 54$); Red ($\chi N = 72$); (c) The error between the relaxation times quantified by the two measures defined as: $|\tau_m(s) - \hat{\tau}(z)|/\hat{\tau}(z)$.

of block copolymers in lamellar phases and their correspondence to the relaxation times reported by tagged monomers identified by their position along the polymer chain. We note that the experiments themselves concern with fluorescence intensities of dyes, and not the segmental dynamics of polymers. However, a number of earlier studies have used the relaxation times arising from the segmental dynamics as a surrogate to quantify T_g in polymeric systems.[225–229] Inspired by such findings, we use the spatial and tagged monomer segmental dynamics of the polymers as substitute measures for characterizing the T_gs measured in experiments.

In Figure 4.12(a), we compare the average relaxation times of the tagged monomers (as a function of its position along the backbone normalized

by the degree of polymerization N) against the local segmental relaxation times at a given distance from the interface. It is seen that both the tagged monomer relaxations and the spatially averaged segmental times exhibit similar qualitative behavior with slower relaxations near the link position/interfaces, and a bulk polymer like behavior towards the end of the chain/the bulk of the lamella. However, despite the qualitative agreement, at a quantitative level there are seen to be discrepancies in the relaxation times arising from the two measures. Such discrepancies are seen to most pronounced near the interfaces of the lamella, and become mitigated near the bulk of the lamella.

Figures 4.12(b) and (c) present results depicting the effect of segregation strength on the differences between the tagged relaxations and the spatial variations of the relaxation times. Within the range of segregation strengths probed, we observe that the discrepancies (portrayed more explicitly in Figures 4.12(c)) are relatively insensitive to the degree of segregation. Together, the results of Figs. 4.12(a) - (c) demonstrate that tagged monomer relaxation times do not provide a quantitatively accurate measure of the spatial variations in segmental dynamics.

The discrepancies between the two relaxation times displayed in Figure 4.12, can be understood to be a consequence of the distribution of tagged monomers in the lamella. Indeed, as discussed in the introduction, in microphase separated morphologies, monomers which are located at the same position along the polymer backbone are nevertheless expected to have a spatial distribution in the morphology. To depict this in a quantitative manner,

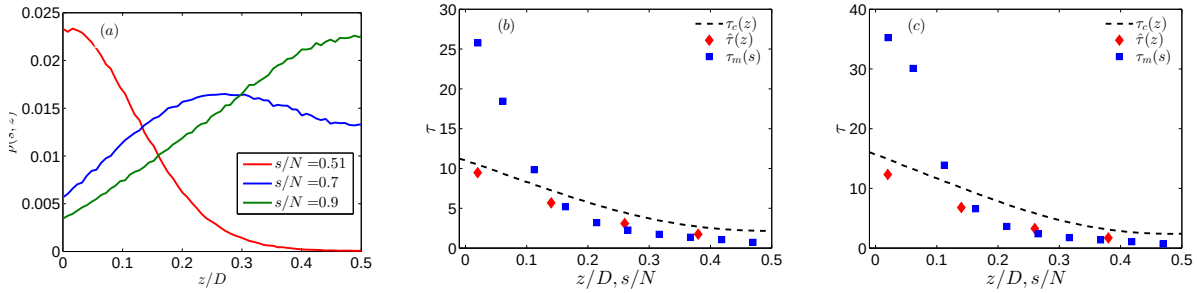

Figure 4.13: (a) Spatial distribution of tagged monomers in the lamella depicted for three different monomer indices ($s/N = 0.5$ corresponds to the link position between the A and B blocks). The degree of segregation corresponds to $\chi N = 54.0$;(b) and (c) Comparison between tagged monomer dynamics, $\tau_m(s)$, local segmental relaxation times $\hat{\tau}(z)$ and those obtained by a convolution of tagged monomer dynamics and the spatial distribution of tagged monomers $\tau_c(z)$. The relaxation times are normalized by their values in the homopolymeric state. The results correspond to a segregation strength of (b) $\chi N = 54.0$; and (c) $\chi N = 72.0$.

we characterized the density distribution of monomers ($p(s, z)$) computed as $p(s, z) = n(s, z)/(L_x L_y \delta_z)$, where $n(s, z)$ represents the average number of particles of monomer index s at a distance z along the box direction and L_x, L_y and δ_z represent the box dimensions in the directions parallel to the interface (L_x, L_y) and the bin spacing (δ_z) in the direction perpendicular to the interface.

The results displayed (for three different monomer indices) in Figure 4.13(a) demonstrates that there exists a probability distribution for the location of the tagged monomers along the lamella. Based on such a result, we can rationalize that the dynamics reported by a specific tagged monomer is not expected to correspond to the dynamics at a spatial location along lamella,

but is instead expected to embody a probabilistic weighting of the dynamical characteristics at the different spatial locations.

An interesting question is whether the data reported by the tagged monomers can be used, at least indirectly, to extract the spatial variations of segmental dynamics in inhomogeneous morphologies. Towards such a goal, we hypothesized that the averaged spatial distribution of tagged monomers ($p(s,z)$) when convoluted with the average relaxation times reported by the tagged monomers ($\tau_m(s)$), may serve to provide an approximate measure of the spatial distribution of dynamics in inhomogeneous morphologies. Such a measure is expected to necessarily be only approximate (and not exact) since the spatial variation of dynamics results from an averaging of the instantaneous monomers present in a specified location and their dynamics.

To probe the validity of the above hypothesis, we computed the spatial variation of relaxation times (denoted as $\tau_c(z)$ to distinguish from the true, local segmental relaxations $\hat{\tau}(z)$) using the monomer densities $p(s,z)$, and the the tagged monomer relaxation times $\tau_m(s)$ using

$$\tau_c(z) = \frac{\int p(s,z)\tau_m(s)ds}{\int p(s,z)ds}. \tag{4.5}$$

We effected a numerical integration to implement Eq. 4.5 using a trapezoidal rule with a Δs of 5.0.

In Figs. 4.13(b) and (c), we demonstrate that the relaxation times $\tau_c(z)$ resulting from our hypothesis indeed provides an excellent quantitative approximation to the spatially heterogeneous dynamics in block copolymer lamella.

Specifically, the $\tau_c(z)$ is seen to capture the spatial variations evident in $\hat{\tau}(z)$ both near the interface and in the bulk of the lamella. Moreover, the effect of degree of segregation is also seen to be well captured within $\tau_c(z)$.

The significance of the above result lies in the fact that the averaged spatial distribution of tagged monomers represents an equilibrium property, which can be determined by a simple theoretical framework such as polymer self-consistent field theory.[61] Our results in Fig. 4.13(b) and (c) demonstrate that such equilibrium characteristics can be used in conjunction with the experimental data for the dynamics reported by the tagged monomers to discern a quantitatively accurate representation of the spatial variations in the segmental dynamics in inhomogeneous self-assembled phases of multicomponent polymers.

4.5 Summary

In summary, the dynamical properties of block copolymers in lamellar phases were investigated using molecular dynamics simulations. We simulated systems with blocks having different mobility by adapting the thermostat underlying the dynamics. Spatially resolved relaxation dynamics of the segments showed that the length scale over which dynamical inhomogeneities propagate is controlled by the interfacial width. Since the interfacial width in block copolymer systems is controlled by the degree of segregation alone and not by the molecular weight of the block copolymer (for large enough molecular weights), such results suggest that glassy blocks has a finite range of influence

upon the dynamics of rubbery segments.

Ion conductivities in block copolymer phases are expected to be related to the local dynamics of the conducting (rubbery) phase in ordered morphologies. Since the above results indicate that the perturbations in the dynamics of rubbery segments are within a finite range which is independent of the molecular weight, such findings serve to rationalize the plateauing of the conductivity observed in experiments for large molecular weights of block copolymers. Moreover, such results also suggest that use of block copolymer electrolytes with large enough molecular weights may serve to minimize the effects arising from the slow dynamics of the glassy block and the interfacial regions.

Further, we presented results from coarse-grained molecular dynamics simulations which probed the relationship between the local segmental dynamics and the single monomer dynamics in lamellar phases of diblock copolymers. Our results demonstrate that monomer relaxation times *do not* provide directly a quantitatively accurate measure of the spatial variations in segmental dynamics. However, a convolution of the monomer density distribution with their corresponding relaxation times is shown to provide an approximate, but accurate quantitative characterization of the average local segmental dynamics.

Finally, we would like to remind that our present work was specifically concerned on the influence of the MW and the effect of segregation upon the polymer segmental dynamics which can potentially affect the ion conductivities. Although, parameters such as solubility of ions, spatial concentration of

ions etc., can influence the ion conductivity in block copolymer electrolytes, we did not embark upon identifying the influence of such parameters in this work.

Chapter 5

Segmental Dynamics in Lamellar Phases of Tapered Copolymers

5.1 Introduction

Recently, significant interest has arisen in the development of electrolyte materials which simultaneously possess both high conductivities and mechanical strengths [7, 12]. In this regard, self-assembled morphologies of large molecular weight (MW) block copolymers combining conducting and nonconducting blocks have emerged as attractive candidates [21, 24, 230]. Typically, the conducting block is more mobile and acts as a pathway for the conduction of ions, whereas, the other (relatively) immobile block serves to provide mechanical strength [12, 21, 24]. [1]

In block copolymers, the formation of different microstructures is governed by the segregation strength, χN (where χ is the Flory Huggins interaction parameter and N is the degree of polymerization) and the compositional fraction, f of the blocks. Early studies in the context of electrolyte applications mainly explored linear di- and triblock copolymers which suffer from the

[1] Citations: Vaidyanathan Sethuraman, Victor Pryamitsyn, Venkat Ganesan, "Normal Modes and Dielectric Spectra of Diblock Copolymers in Lamellar Phases", *Macromolecules*, **49** (7), 2821-2831 (2016). Victor Pryamitsyn wrote the normal modes codes and Venkat Ganesan guided the project.

limitation that there exists only a small range of compositional fractions (especially at high χN) that can form percolating morphologies (such as gyroids) suitable for conduction [231]. More recently however, Epps and coworkers demonstrated that by creating a gradient in the composition profile of diblock copolymers to create tapered copolymers, the parametric window of forming percolating morphologies can be considerably expanded when compared to pure diblock copolymers [230, 232, 233]. As a consequence there has arisen an interest on the exploration of tapered and gradient copolymers for electrolyte applications.

Two sets of earlier results and their relationship to recent experimental observations motivate the study presented in this article: (i) Computer simulations and experiments have shown that the interfacial width between the conducting and nonconducting phases exert a significant influence on the overall conductivity of self-assembled morphologies of block copolymers [29, 234]. Explicitly, the interfacial regions of conducting and nonconducting phases were suggested to possess lower mobilities and thereby hinder the transport of ions; [21] (ii) A number of experimental and simulation works have shown that the interfacial width of tapered copolymers are usually broader compared to its diblock counterparts [232, 235–238]. Combining the results (i) and (ii), it would be expected that for a specified morphology, tapered copolymers are likely to possess conductivities which are inferior to diblock copolymers. However, recent experimental results by Epps and coworkers [230, 233] have challenged such an expectation by demonstrating that the conductivity of ta-

pered copolymers assembled in lamellar phases can be higher compared to its diblock counterparts (at the same temperature). Such intriguing results motivate the question considered in this article *viz.,* "what are the mechanisms underlying conductivities in tapered copolymers and their magnitudes relative to diblock copolymers?"

We note that the ionic conductivities of block copolymer electrolytes are expected to depend on a complex interplay of factors such as local polymer segmental dynamics, ion solvation [239], distribution of ions in the conducting and nonconducting domain of the copolymer [201], the influence of the ions on the polymer dynamics[240] etc. However, a striking result which emerged from the work of Epps and coworkers was that the relative ionic conductivities of tapered and diblock copolymers were found to be primarily correlated to the glass transition temperature of the conducting block in the salt-doped lamellar phase. Based on this observation, in this study we focused on a narrower question, *viz.,* "what are the mechanisms underlying the segmental dynamics of the conducting block in the *salt-free* lamellar phases of tapered and diblock copolymers?"

In our recent work [234], we studied the influence of molecular weight (MW) and the strength of segregation upon the relaxation dynamics of non-tapered diblock copolymer melts and characterized the local heterogeneity in segmental relaxation times of the polymers as a function of distance from the lamellar interface. It was shown that the local segmental relaxation times depend on two factors: (a) the degree of segregation between the conducting

and the nonconducting phases; and (b) the ratio of mobilities between the two blocks. Based on such findings, for this study, we propose the hypothesis that in comparing the segmental dynamics of tapered diblock to linear diblock copolymers, two factors may compete with each other to modulate the polymer segmental relaxation dynamics:

1. With increase in tapering, the segregation strength required for order-disorder transition (ODT) increases (in χ units), and hence the segregation relative to ODT (at a specified χ or temperature) is expected to be lower for tapered copolymers compared to diblocks. Such effects are likely to lead to a faster local dynamics in the interfacial region of tapered copolymers.

2. The tapering of the copolymers results in increased interfacial width and an enhanced "mixing" of the conducting and nonconducting (typically less mobile) segments. Such an effect will result in slower local dynamics in tapered copolymers relative to diblock copolymers.

We hypothesize that depending on the relative mobilities of the blocks and the actual degree of segregation, either (i) or (ii) may prevail. If (i) dominates, we expect the segmental dynamics of the conducting block to be faster for tapered copolymers.

To validate the above hypothesis, in this work, we employ coarse-grained molecular dynamics simulations (CGMD) to investigate the combined influences of the degree of segregation (relative to ODT) and the mobility

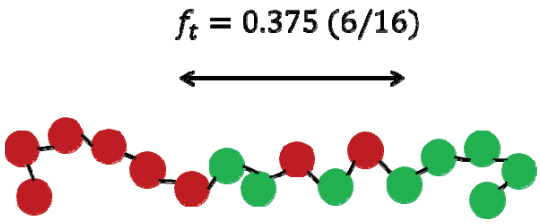

Figure 5.1: Schematic of a tapered copolymer. Tapering fraction of $f_t = 0.375$ is shown. The first and the last $N(1 - f_t/2)$ monomers are of type A and B respectively. The monomers in the central Nf_t are chosen statistically based on a linear tapering profile.

ratios between the blocks comprising the copolymer upon the average local segmental dynamics in the lamellar phase of the tapered copolymers. Our results serve to confirm our proposal and provides a qualitative rationale for the experimental results.

The rest of the Chapter is organized as follows. The details of the simulation methodology are provided in Section 5.2. In Sections 5.3.1 and 5.3.2, we present results which individually characterize the influence of the segregation strength (relative to ODT) and mobility asymmetry upon the local relaxation dynamics of tapered copolymers. Subsequently, in Section 5.3.3, we recast the results within the framework typically used in experiments and comment on the correspondence to the observations in this regard. The main findings and their implications are summarized in Section 5.4.

5.2 Simulation Details

The simulation methodology and the interaction potentials used in this work is very similar to that employed and discussed in the context of our earlier study [234]. To maintain brevity, we present only the salient features of the setup of simulation details here and refer the reader to previous works for more details [83, 84, 193]. We used CGMD simulations to study melts of tapered copolymers (and for comparison, linear diblock copolymers). The nonbonded interactions were described using shifted Lennard-Jones (LJ) intermolecular potential [40] and the bonded interactions were represented using a harmonic intramolecular potential. To generate ordered copolymer morphologies we resorted to a strategy wherein a soft coarse-grained potential was employed initially to generate long range order [83, 84, 193]. Subsequently the target (Lennard Jones) potential is introduced and the system is re-equilibrated. For all the systems studied in this work, the number of beads in the block copolymer was fixed at $N = 100$. The density of the systems simulated were $0.705 \pm 0.01\sigma^{-3}$. Along the lines of the procedure adopted in our prior work ,[193, 234] the χ parameter was deduced by fitting the structure factors obtained from the disordered phase in both DPD and shifted LJ to the renormalized one loop theory [84].

Different degrees of tapering and tapering architecture were modeled by adopting the framework suggested by Hall and coworkers which was shown in earlier work to lead to phase diagrams consistent with the experiments [232]. We studied two different degrees of tapering as quantified by the tapering

fraction, f_t, which is defined as the number of copolymer segments (relative to the degree of polymerization) over which tapering is implemented (cf. Figure 5.1). We also compare our results with those of diblock copolymers, which corresponds to $f_t = 0.0$.

Denoting the mobility of the nonconducting A segments as ζ_A and the conducting B segments as ζ_B, we probed four different values for the parameter $\eta = \zeta_A/\zeta_B$. To implement the difference in mobilities, the preequilibrated and segregated system was evolved in the presence of a Langevin thermostat in which the friction coefficient associated with the slow monomers (A) was varied while maintaining those of the fast monomers (B) constant. For $\eta = 1$, a Nóse-Hoover thermostat [94, 241, 242] was implemented with identical thermostat coefficients for A and B monomers.

To characterize the *local* relaxation dynamics, we used the intermediate structure factor, $S(q,t,z) = \langle \cos(\mathbf{q} \cdot \mathbf{r}(t,z)) \rangle$, where $\mathbf{q}$ is the wave vector and $\mathbf{r}(t,z)$ represents the monomer displacement vector at time t and at a given distance, z from the nearest interface. The values of the components of $\mathbf{q}$ chosen in the plane parallel to the interface were $q_x = q_y = 0.5\sigma^{-1}$ ($|q| = 0.71\sigma^{-1}$). The relaxation times of the fast monomers were then extracted by fitting $S(q,t,z)$ curves to a stretched exponential function of the form $\exp\left(-(t/\tau_s)^{\beta}\right)$ where τ_s and β represents respectively the relaxation time and the degree of stretching of the relaxation. Local average relaxation times (τ) were calculated using $\tau = \tau_s \Gamma(1+1/\beta)$ and constitute the quantities of interest for our study.

5.3 Results and Discussion

5.3.1 Influence of segregation strength upon local segmental dynamics (F1)

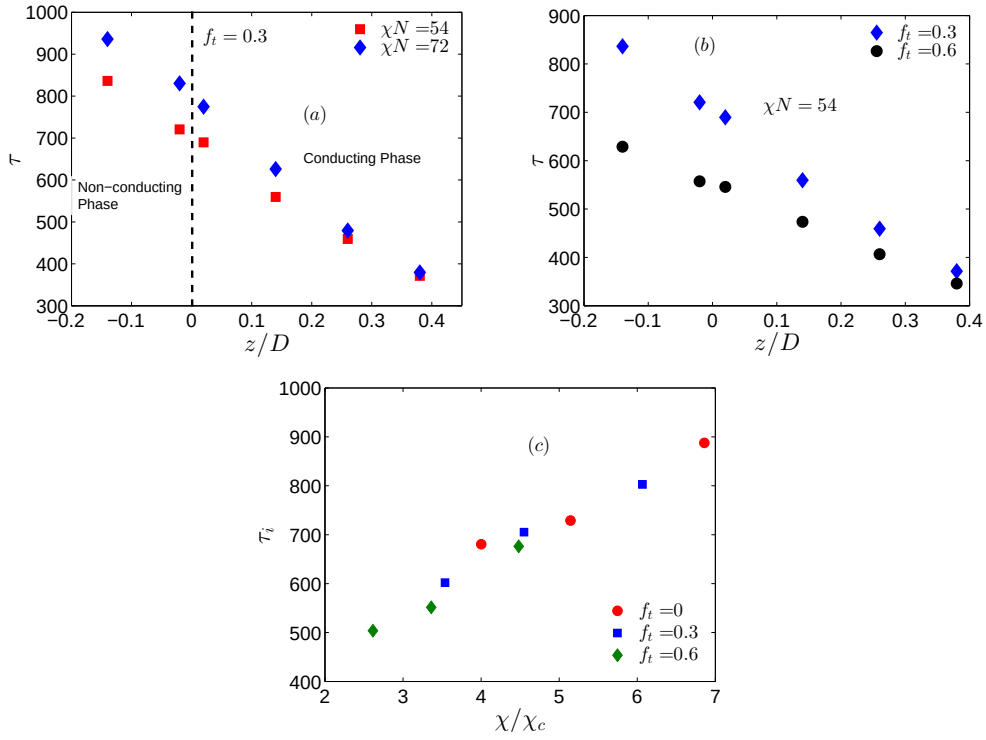

Figure 5.2: (a) Local relaxation times of B segments at different segregation strengths for $f_t = 0.3$ and $\eta = 1$. Black dotted lines represent the interface and the conducting phase refers to the B domain. The positions z are in the plane normal to the interface and D denotes the domain width.; (b) Local relaxation times of polymers for different tapering at $\eta = 1$.; (c) Relaxation times near the interface plotted as a function of χ/χ_c at $\eta = 1$.

We first consider a situation in which the segmental mobility of A and B blocks are the same (corresponding to $\eta = 1$ in our notation) and consider the influence of the degree of segregation. Figure 5.2(a) presents results com-

paring the local relaxation times of the B segments in the lamellar phase of tapered copolymer ($f_t = 0.3$) for $\eta = 1$ for two different χN. Despite the fact there is no disparity in the mobility of the blocks, the local segmental relaxation times in the vicinity of the interface are seen to be higher than those in the bulk of the domains. Similar trends were observed in our earlier work on diblock copolymers [234] and were suggested to arise as a consequence of the microphase separation induced effective potential acting on the segments. Consistent with such a hypothesis, it can be seen that an increase in degree of segregation results in an increase in segmental relaxation times near the interface.

A more interesting result is seen by comparing the local relaxation dynamics of segments for the lamellar phase of two different tapering fractions ($f_t = 0.3$ and $f_t = 0.6$) at the same χN (Figure 5.2(b)). It can be observed that the local relaxation times for the case of $f_t = 0.3$ are larger in magnitudes than those observed for $f_t = 0.6$. To reconcile these trends, we note that the *mean-field* value of ODT for $f_t = 0.3$ corresponds to $(\chi N)_c = 11.87$, whereas, for $f_t = 0.6$ we have $(\chi N)_c = 16.06$ [238]. These results suggest that the ordering-induced retardation of the polymer segments, depends on the degree of segregation *relative to the ODT*.

To provide quantitative evidence for the above proposal, in Figure 5.2(c) we display the relaxation time of the B segments at the interface (corresponding to the location $z/D = 0$ in Figures 5.2(a) and (b)) as a function of χ/χ_c (where χ_c corresponds to the mean-field value for ODT) for diblock copoly-

mers ($f_t = 0.0$) and tapered copolymers ($f_t = 0.3$ and $f_t = 0.6$). Confirming our hypothesis above, we observe that the interfacial relaxation times collapse onto a single function when displayed in this representation.

Together, the results presented in Figures 5.2(a)-(c) confirm the first portion of our hypothesis regarding the relative segmental dynamics in lamellar phases of tapered and diblock copolymers. Specifically, for a specified temperature (χ), we observe that copolymers possessing a larger degree of tapering exhibit faster relaxation times as a consequence of their higher (in χ) ODT. In our later discussion, we term this observation as a **F1**.

5.3.2 Influence of mobility disparity between the blocks (F2)

As discussed in the introduction, copolymers explored for electrolyte applications typically possess disparate segmental mobilities which arise as a consequence of the differences in their glass transition temperatures. In this section, we specifically consider the influence of such mobility disparities upon the local segmental relaxation times in the lamellar phase of tapered copolymers.

In Figure 5.3 we display the local relaxation times of the B segments (the faster, conducting block) in the lamellar phase of tapered copolymers ($f_t = 0.3$) for different values of mobility ratio. From the results displayed, we observe that the local relaxation dynamics in the mobile (conducting) phase decreases monotonically with increasing η values. These results can be understood by noting that the B monomers in the interfacial zone and its vicinity

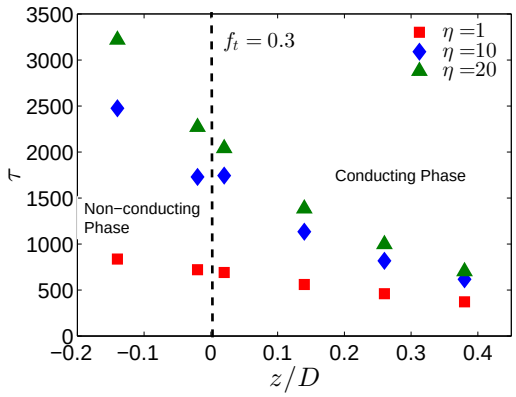

Figure 5.3: Local relaxation times of tapered copolymers for different mobility ratios and $f_t = 0.3$. The positions z are in the plane normal to the interface and D denotes the domain width, and $z = 0$ corresponds to the interfacial location.

are slowed as a consequence of being in an environment occupied by the slower A monomers. Increasing the mobility disparity between the blocks leads to an overall reduction in the mobility of such an environment and a corresponding increase in the local relaxation times of the B segments.

In Figure 5.4(a) we compare the mobility effects for different degrees of tapering of the copolymers. For this purpose, we consider systems in which the degree of segregation relative to ODT (χ/χ_c) were kept identical. In accord with the discussion of the previous section (**F1**), for $\eta = 1$ the behaviors of the local relaxation times are seen to be very similar for different tapering fractions. With an increase in the mobility disparity between the blocks, we observe that the relaxation times are slowed to a greater extent in the systems with larger degree of tapering. These results suggest that at the same degree of segregation relative to ODT, mobility effects have a more significant influence

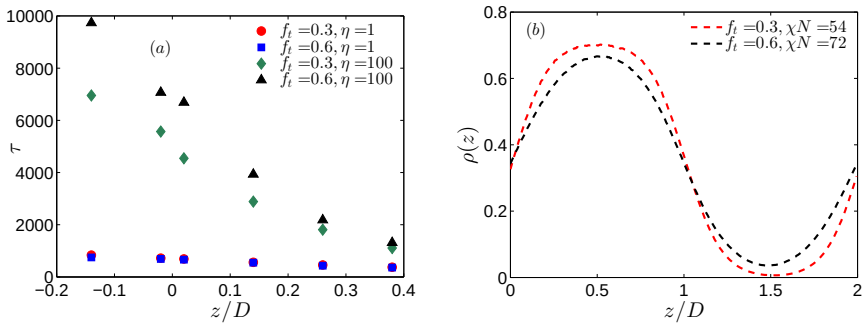

Figure 5.4: Local relaxation times plotted as a function of z/D for two different tapering fractions and two different η; (b) Density profiles at two different tapering fractions and two different χN. The positions z are in the plane normal to the interface and D denotes the domain width, and $z = 0$ corresponds to the interfacial location.

in copolymers with a larger degree of tapering. We term this observation as **F2** in the later discussion.

The results of Figure 5.4(a) can be understood by considering the degree of intermixing between A and B segments in lamellar phases of tapered copolymers. A number of earlier studies have suggested that an increase in tapering leads to broader interfacial widths [235, 238]. Such trends are also evident in the volume profile results obtained in our simulations and displayed in Figure 5.4(b). As a consequence of this broader interfacial width, a larger degree of intermixing between the slower and faster segments in the lamella is to be expected. Such mixing leads to a slower environment for B monomers and a more significant reduction in the local mobilities as seen in Figure 5.4(a).

Finally, in Figure 5.5, we characterize the effects arising from the combined influence of the degree of segregation and the segmental mobility disparities. Explicitly, we display the relaxation times at the interface for different degrees of tapering as a function of χ/χ_c for a mobility disparity of $\eta = 100$. Consistent with the results underlying our observation **F2**, we observe that at a specified χ/χ_c, copolymers possessing a larger degree of tapering exhibit slower relaxation times.

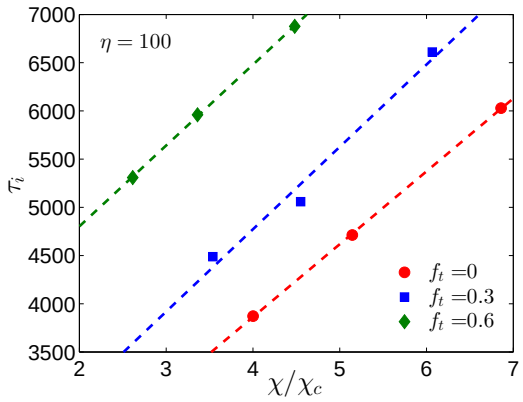

Figure 5.5: Interfacial relaxation times as a function of χ/χ_c for different tapering fractions. The lines represent a guide to the eye.

5.3.3 Comparing the relaxation dynamics in diblock and tapered copolymers

In this section, we focus on the behaviors that may result when comparing diblock and tapered copolymers arising as a consequence of the interplay of the factors discussed in the preceding sections. For this purpose, we adopt a framework similar in setup to experiments, in which we consider a *specified*

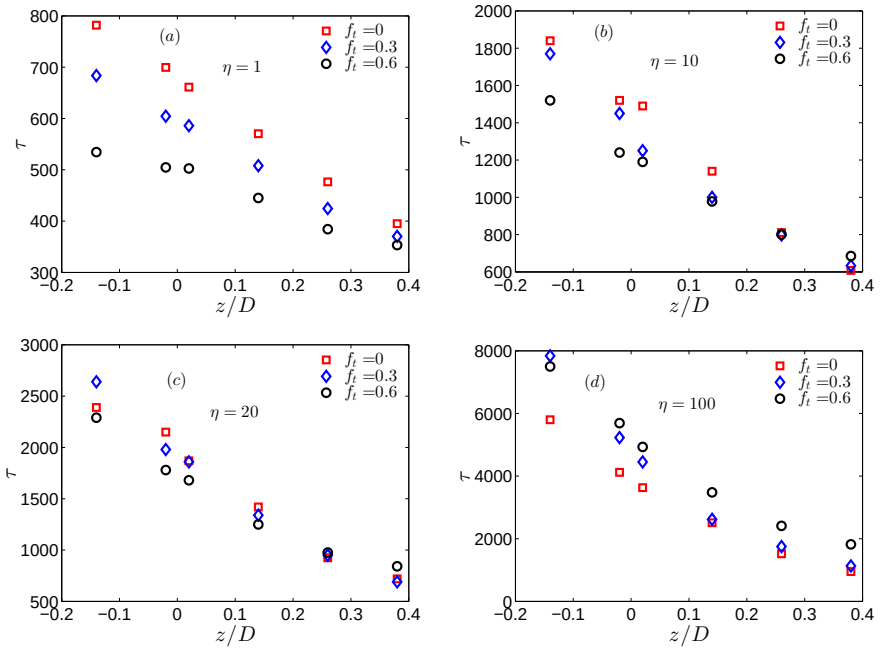

Figure 5.6: Relaxation times of polymers for different tapering fractions at (a) $\eta = 1$ (symmetric mobility); (b) $\eta = 10$; (c) $\eta = 20$; (d) $\eta = 100$. All simulations were performed at $\chi N = 42$. The positions z are in the plane normal to the interface and D denotes the domain width, and $z = 0$ corresponds to the interfacial location.

temperature or χ value, and compare the local segmental relaxation times of the conducting (B) segments as a representative of the glass transition temperature (T_g) in such phases.

In Figure 5.6, the degree of segregation is fixed at $\chi N = 42$ and the local relaxation times are compared for different tapering fractions and mobility ratios. Figure 5.6(a) displays the average local relaxation times for different tapering fractions with blocks possessing symmetric mobilities ($\eta = 1$). It can

be seen that diblock copolymers ($f_t = 0$) exhibit the slowest dynamics (largest relaxation times). Such results can be understood as arising from the effect of the degree of segregation relative to the ODT (**F1**).

Upon increasing the mobility ratio between blocks, the influence of the mobility disparity (**F2**) starts to manifest in influencing the local relaxation times. For a mobility ratio of $\eta = 10$, we observe that the diblock copolymer still has lower mobility compared to the tapered copolymer. This result suggests that even with mobility disparity, there exists parametric regimes wherein tapered copolymers possess higher mobility compared to the diblock copolymers. For a moderate mobility ratio ($\eta = 20$, Figure 5.6(c)), the effects arising from the mobility disparity almost balances the effects arising from the higher χ_c for tapered copolymers, and it is seen that the local relaxation dynamics of diblock and tapered copolymers become quantitatively similar. Finally, for very large mobility ratio between the blocks ($\eta = 100$), the effect of the mobility disparities on local dynamics becomes the dominant factor. Therefore, copolymers with a larger degree of tapering exhibit the slowest relaxation times.

Overall, the results presented above serves to confirm that diblock copolymers can indeed exhibit slower dynamics compared to tapered copolymers even in the presence of a mobility disparity between the blocks. We note that such results accord at a qualitative level with the experimental observations of Epps and coworkers[230] of salt doped electrolytes in which they observed that the T_gs of the conducting block in lamellar phases of tapered

copolymers were lower than those of the diblock copolymers. However, as noted in the introduction, ionic conductivities of block copolymer electrolytes involves a complex interplay of a number of others factors beyond the local polymer segmental dynamics, such as the ion solvation ,[239] distribution of ions in the conducting and nonconducting domain of the copolymer [201], and the influence of the ions itself on the polymer segmental dynamics.[240] The present work was concerned with only one of the underlying factors and does not account for the presence of ions and its influence on the polymer dynamics. In a future study, we plan to present results for such effects within the framework of atomistic simulations.

5.4 Summary

In summary, we reported the results of coarse-grained MD simulations which sought to understand the combined influence of mobility disparity and the degree of segregation of block copolymers upon the spatially averaged relaxation dynamics of block copolymers. Diblock copolymers were found to have slower relaxations compared to tapered copolymers at weaker to moderate degree of segregation. At a specified value of relative degree of segregation, the mobility disparity between the blocks was found to influence more significantly the dynamics of tapered copolymers as a consequence of larger interfacial widths and degree of intermixing between the slow and fast monomers.

Our results did observe parametric conditions in which diblock copolymers exhibited slower relaxation dynamics compared to tapered copolymers.

Such results are in qualitative accord with recent experimental observations on the glass transition temperature in copolymer electrolytes. While our analysis does not consider several other factors such as ion solvation etc., which can impact conductivity, nevertheless, our results serve to highlight the non-trivial interplay between mobility asymmetry and degree of segregation upon polymer dynamics in self-assembled morphologies.

Chapter 6

Normal Modes and Dielectric Spectra of Diblock Copolymers in Lamellar Phases

6.1 Introduction

The conformations and dynamics of polymer chains upon confinement, grafting to surfaces, ordering into self-assembled morphologies etc. are altered from their "bulk" behavior. Understanding such changes prove important for the use of polymeric materials in applications such as organic photovoltaics [28], semiconductors [9, 11, 243], biomedical devices [8, 15, 244, 245] etc. While substantial work has characterized such features for homopolymers [40, 246, 247], comparatively less knowledge exists for block copolymers, especially in ordered microphases. [1]

Our present study focuses on issues related to chain level dynamics of block copolymers in ordered phases and on issues relating to dielectric relaxation spectroscopy (DS) measurements.[248–252] Motivated by the sensitivity of DS in characterizing the dynamics of polymer chains, a number of experiments have used such a probe to study ordered block copolymer

[1] Citations: Vaidyanathan Sethuraman, Venkat Ganesan, "Segmental Dynamics in Lamellar Phases of Tapered Copolymers", *Soft Matter*, **12**, 7818-7823 (2016). Venkat Ganesan guided the project.

phases.[250, 252–255] Such experiments have observed a variety of different features, such as a shift of DS to lower frequencies [249, 253, 256], a considerable broadening of the DS relative to their homopolymer counterparts [252, 256], and in some cases, emergence of additional peaks in the DS [251]. Unfortunately, many of the experimentally accessible systems relate to block copolymers in which the segments of dissimilar polymer possess significantly disparate mobilities. As a result, it is has been a challenge to decouple the dynamical effects arising specifically from (i) the "tethering" of the mobile chains in the ordered phases to the glassy blocks; and (ii) the influence of microphase separation and ordering of the block copolymer. In sum, there is still a lack of clarity on the mechanisms underlying the experimental observations, and more broadly, the influence of microphase separation upon the dynamics of internal degrees of the polymer molecules.

In the last two decades, there has been an explosion of activity in the use of computer simulations to study various properties of polymeric systems [20, 61, 257]. However, despite such advances there have been only relatively few studies of the dynamical properties of block copolymer melts [30, 34–36]. For instance, Murat *et. al* used molecular dynamics simulations to study dynamics in lamellar phases of block copolymers and showed that the COM motion of ordered block copolymers was slower than their homopolymer counterparts.[30] Similar results have also been reported by others who used lattice Monte Carlo simulations and single-chain in mean field (SCMF) simulations [258, 259]. Recent work by Slimani *et. al*[34–36] studied the spatial

dependence of segmental dynamics of block copolymers and elucidated the perturbations arising as a consequence of microphase segregation.

Despite the considerable insights which have resulted from the above studies, very few models and computational studies have specifically concerned with the issues relating to chain level dynamics and DS experiments in the context of ordered block copolymers [39, 247, 260, 261]. Some unresolved questions in this regard include, "what is the influence of microphase separation upon the dynamics of internal degrees of freedom of the polymer molecules?," "what is the influence of the degree of segregation and the mobility disparity between the blocks upon such characteristics?" "do the non center-of-mass degrees of freedom also exhibit anisotropic dynamical characteristics as a consequence of microphase separation?," "In systems characterized by significant dynamical asymmetry between the blocks [262], does the dynamics of the mobile block indeed resemble the features characteristic of tethered polymer chains?"

Motivated by the above unresolved issues, in this work we used molecular dynamics simulations to study the chain level dynamics in ordered lamellar phases of block copolymers. Towards this objective, we employed methodologies that were recently developed in our group [193] to achieve equilibrated morphologies in multicomponent polymeric systems possessing realistic hard-core interactions. Using morphologies generated from such a procedure, we effected an explicit normal mode analysis of the dynamics of the chains in block copolymer phases [40, 246, 263]. We use two distinct models to isolate the specific dynamical effects arising from microphase separation and mobility

disparities between the blocks. Subsequently, the dielectric loss spectra were computed for type A polymers using the dynamics of normal modes arising from the results of such models. Together, our results identify several new features underlying the normal modes and their relaxations in ordered block copolymer phases.

The rest of the article is organized as follows. The details of simulation method and the methodology employed to obtain the relaxation and dielectric spectra are presented in Section 6.2. The results for the normal modes are discussed in Sections 6.3.1 and 6.3.2. The results obtained for dielectric spectra based on normal modes are discussed in Section 6.3.3. The article is concluded with a short summary in Section 6.4.

6.2 Simulation Details

6.2.1 Generation of Morphology

To obtain equilibrated ordered lamellar phases of diblock copolymers, we employed a molecular dynamics simulation framework presented in our earlier article [193]. Explicitly, the methodology entails a two-step procedure wherein, soft (coarse-grained) intermolecular potentials are initially used to facilitate rapid equilibration and to generate configurations of the ordered block copolymer system. Subsequently, the target potential is introduced and the "pre-equilibrated" configurations are annealed further to obtain the final equilibrated morphologies. A key aspect of our framework is the use of a rigorous mapping between the parameters of the target potential and the soft potential

which ensures that the long range structural aspects are maintained identical between the two sets of interactions [83, 84, 264]. As a result, introduction of the target potential and the final equilibration steps involve mainly a relaxation of the short-range structure.

For our target potential, we chose a modified form of the Kremer-Grest model [40], in which the intermolecular potentials (U_{ij}) between the non-bonded particles as modeled via a shifted Lennard-Jones potential of the form:

$$U_{ij}^{h} = \begin{cases} 4\epsilon_{ij}\left[\left(\frac{\sigma}{r_{ij}}\right)^{12} - \left(\frac{\sigma}{r_{ij}}\right)^{6} + \frac{1}{4}\right] & , r \leq 2^{1/6}\sigma \\ 0 & , r > 2^{1/6}\sigma \end{cases} \tag{6.1}$$

where ϵ_{ij} represents the interaction parameter between monomers i and j, σ represents the diameter of a monomer and r_{ij} represents the distance between the monomers. The bonded monomers were assumed to interact via a harmonic potential of the form:

$$U_{b}^{s} = \kappa_K (r - \sigma)^2 \tag{6.2}$$

where $\kappa_K = 200\ k_B T/\sigma^2$ represents the bond constant between the bonded monomers and k_B and T represents the Boltzmann constant and temperature respectively. Without loss of generality, we set $\epsilon_{AA} = \epsilon_{BB} = k_B T = 1.0$.

The soft intermolecular potential used in our studies is similar to those used in dissipative particle dynamics (DPD) [58] simulations:

$$U_{ij}^{s} = \begin{cases} \frac{1}{2} a_{ij} \left(r - r_c\right)^2 & , r \leq r_c \\ 0 & , r > r_c \end{cases} \tag{6.3}$$

where a_{ij} represents the interaction parameter between monomers i and j, r_c represents the cut-off radius and r represents the distance between the i and j monomers. We chose $a_{ii} = a_{jj} = 25.0$ in all the simulations performed. The bonded monomers experienced an additional harmonic potential of the form,

$$U_b^s = \kappa_D r^2 \tag{6.4}$$

where $\kappa_D = 5.0\ k_B T/\sigma^2$ represents the bond constant.

The simulations were started with a random initial configuration of the polymer segments at a density of $3.0\ r_c^{-3}$ which was then evolved with the soft potential (eq (6.3)) in a NPT ensemble at a pressure of $\approx 19.3\ r_c^{-3}$. During such a stage, two of the box directions were coupled and the box size in the third direction was allowed to vary independently. The system was evolved with a Nosé-Hoover thermostat [94, 241] with a thermostat coupling constant of $0.5\ \tau^{-1}$ and a barostat coupling constant of $5.0\ \tau^{-1}$. A timestep of 0.01 τ was used in all simulations using DPD potential. The total length of the equilibration run using the soft potential varied between 7×10^6 – 10×10^6 timesteps. In the results below, the axis perpendicular to the plane of the resulting lamella is referred to as the z-direction.

Subsequent to equilibration with the soft potential, the overlaps between the monomers, if any, is removed by evolving the system in a NVE ensemble and restricting the maximum distance moved to $0.05\ \sigma$ for about 100 – 500 steps [62]. The system was then evolved using a constant temperature ensemble at a density of 0.705 ± 0.005 with a Nosé-Hoover thermo-

stat [94, 241] and the equations of motion were integrated using Velocity-Verlet algorithm [95]. All the systems were equilibrated for 30 - 45 million time steps before the results were collected. The time step used for equilibration and production runs were 0.005 τ and 0.01 τ respectively. All simulations were performed using LAMMPS software [96].

The degree of segregation of the copolymers were varied through the control parameters, $\alpha_D = a_{AB} - a_{AA}$ and $\alpha_K = \epsilon_{AB} - \epsilon_{AA}$. As discussed above, we chose α_D and α_K in such a manner that the long-range structural details of the block copolymers are preserved between the soft potential and the target potential simulations. Such a feature is in-turn ensured by choosing α_D and α_K to map to the same effective Flory-Huggins parameter χ quantifying the interactions between A and B monomers.[83, 84, 264] The values of χ chosen in this article are in the weak-moderate segregation limits and we report our results in terms of the χ parameter. The ratio between interfacial and domain width varied between 0.2-0.35 for the range of χN investigated (see supplementary information Figure S1 for density profiles). In all the simulations performed in this article, the degree of polymerization was kept at $N = 100$.

To isolate the effects specific to microphase segregation and mobility disparities in the normal mode and DS results, we considered two distinct models: (a) Model S: In which the segmental mobilities of the two blocks are identical in their homopolymer state. This enables us to focus specifically on the effects arising from the microphase segregation of the block copolymers; (b) Model F: In which the segmental mobility of one of the blocks is frozen

after equilibration of the lamellar phases, and allows us to study the combined influence of microphase separation and the "tethering" of the dielectrically active chain to a glassy phase. The mobile block in Model F was evolved in the presence of a Langevin thermostat with a time constant of 0.5 τ^{-1}, where τ represents the monomeric relaxation time. For model S, the normal modes pertain to the monomers of the entire chain (i. e. $i = 1 \cdots N$). In contrast, for model F, the normal modes pertain to the monomers of the mobile section of the chain (i. e. $i = 1 \cdots N/2$). We note that experimentally studied systems are likely to fall in-between models S and F. However, by studying these extreme conditions, it is easier to clarify the specific effects arising from microphase segregation and mobility disparities.

6.2.2 Computation of Normal Modes

In this section, we delineate the methodology adopted in this work to compute the normal modes. Symbolically, in a normal mode representation, the chain coordinates $\mathbf{r}_i(t)$ ($i = 1 \cdots N$, where N denotes the number of beads in a chain) are expressed in terms of the normal mode coordinates $\mathbf{X}_p(t)$ as:

$$\boldsymbol{X}_p(t) = \sum_{i=1}^{N} \Phi(p, i) \boldsymbol{r}_i(t), \tag{6.5}$$

where $\Phi(p, i)$ ($p = 1 \cdots N$) represent the eigenfunctions corresponding to a diagonalization of static correlation function of the chain coordinates $\mathbf{r}_i(t)$.

For a melt of unentangled homopolymer chains, the normal modes are referred to as the Rouse modes [40, 138], and the corresponding eigenfunctions

are of the form:

$$\Phi(p,i) = \sqrt{\frac{2}{N}} \cos\left(p\pi \frac{i-1/2}{N}\right). \tag{6.6}$$

Moreover, the autocorrelation function of the Rouse modes decay exponentially: $\langle \mathbf{X}_p(t)\mathbf{X}_p(0)\rangle \approx \exp(-t/\tau_p^R)$, where the Rouse relaxation time, τ_p^R is given by[40, 138]

$$\left(\tau_p^R\right)^{-1} = \frac{12}{\zeta b^2} \sin^2\left(\frac{\pi p}{2N}\right),\ p = 1,\ \ldots\ N \tag{6.7}$$

where ζ represents the segmental friction coefficient and b represents the statistical segment length.

In many earlier studies which have considered normal modes or modeled DS measurements in microphase separated morphologies, it has been assumed that the chain dynamics in block copolymers follow the Rouse normal modes (eq 6.6) with however modified relaxation times reflecting the ordering of the chains [39, 40, 138, 246]. In contrast, in the present work, we obtain the normal modes for block copolymers by explicitly diagonalizing the matrix of the chain coordinates (relative to their center-of-mass) in our trajectories [265]. Below, we explain the explicit procedures adopted for both model S and for model F.

For Model S, the center of mass (COM) positions $\boldsymbol{r_{CM}}$ were computed from the equilibrated trajectories obtained from MD simulations. A symmetric matrix $\mathbb{R}^S$ was then constructed by subtracting the COM coordinates from the monomer coordinates such that the elements of such a matrix are given as,

$$\begin{aligned}
\mathbb{R}^S_{\alpha\alpha ij} &= \langle (r_i^\alpha - r_{CM}^\alpha)(r_j^\alpha - r_{CM}^\alpha)\rangle \\
\mathbb{R}^S_{\beta\beta ij} &= \langle (r_i^\beta - \bar{r}_{CM}^\beta)(r_j^\beta - \bar{r}_{CM}^\beta)\rangle
\end{aligned} \tag{6.8}$$

using $\boldsymbol{r_{CM}} = (\sum_{i=1}^{N} \boldsymbol{r_i})/N$, where r_i represents the coordinates of the particles in any given chain, with i and j representing the monomer indices and α and β the x, y, z directions respectively. Owing to the anisotropy arising from the microphase segregation in the system, $\mathbb{R}^S$ is calculated independently for the three spatial directions. For the directions parallel to the lamellar plane, the *instantaneous* center of mass position for each chain is subtracted from all the monomer coordinates belonging to that given chain. In contrast, for the perpendicular direction, the *time averaged* COM positions of each chain in the system was subtracted to reflect the fact that in the time scales of the simulation there is very little diffusion of the monomers in the perpendicular direction. The normal modes corresponding to each spatial coordinate ($\boldsymbol{X}_{p\alpha}$, $\alpha \in \{x, y, z\}$) were then determined as the eigenvectors of $\mathbb{R}^S$. The autocorrelation functions of such modes were then employed to determine the relaxation spectra of the normal modes.

For computing the normal modes in Model F, we chose a framework wherein the mobile block of the block copolymer is tethered to the frozen block. The elements for the symmetric matrix for Model F ($\mathbb{R}^F$) were constructed using,

$$\mathbb{R}^F_{\alpha\alpha ij} = \langle (r_i^\alpha - r_{im}^\alpha)(r_j^\alpha - r_{im}^\alpha) \rangle \tag{6.9}$$

where r_{im} represents the coordinate of the immobile monomer attached to the mobile block (which serves as an effective "grafting" location for the mobile block). Similar to Model S, the normal modes corresponding to each spatial coordinate $X_{p\alpha}, \alpha = \{x, y, z\}$ were determined as the eigenvectors of $\mathbb{R}^F$.

The above analyses avoids any assumptions regarding the applicability of Rouse modes for ordered phases, and to our knowledge, such an analysis has never been effected previously in the context of ordered block copolymer morphologies. Independent normal mode analyses were performed on the chain coordinates resolved in the three spatial directions to probe the components parallel and perpendicular to the interface of the lamella. The relaxation of normal modes were then fit to a stretched exponential of the form, $(1-\alpha)\exp[-(t/\tau^*)^\beta]+\alpha$ to extract the average relaxation times ($\tau = \tau^*\Gamma(1+\beta^{-1})$, where Γ denotes the gamma function), for modes both parallel (τ_{xy}) and perpendicular (τ_z) to the interface and α denotes the long time decay.

6.2.3 Calculation of Dielectric Spectra

We followed the approach suggested by Peter *et. al.* [266, 267] for type A polymers to calculate the dielectric loss spectra. Such a model is appropriate for polymers possessing a nonzero dipole component which is parallel to the chain backbone. Such polymers possess a "normal-mode" dielectric relaxation, $P_{norm}(t)$, related to the overall dipole parallel to the chain backbone (i. e. reorientation of the end-to-end vector), and a "segmental" dielectric relaxation, $P_{seg}(t)$, relating to the overall perpendicular dipole. In our work, we assumed that the contributions to $P_{seg}(t)$ and $P_{norm}(t)$ arose only from one of the blocks and hence the normalized normal dielectric loss (parallel to the chain) was defined in terms of the correlation of the vector joining the end of the chain to the point of linkage between the blocks: $\mathbf{R}_1(t) - \mathbf{R}_{N/2}(t)$. In

the following, we furnish the final expressions for the autocorrelation functions and the corresponding dielectric spectra (see Appendix A for derivation).

The autocorrelation function of the normal mode dielectric relaxation ($\rho_m(t)$) can be expressed in terms of normal modes as:

$$\begin{aligned}\rho_n(t) &= \frac{\langle \boldsymbol{P}_{norm}(t) \cdot \boldsymbol{P}_{norm}(0) \rangle}{\langle |\mathbf{P_{norm}(0)}|^{\mathbf{2}} \rangle} \\ &= \frac{\sum_{p=0}^{N-1} \langle \boldsymbol{X}_p^2(0) \rangle \left[\Phi(p, N/2) - \Phi(p,1)\right]^2 \exp\left(-\left(t/\tau_p^*\right)^{\beta_p}\right)}{\sum_{p=0}^{N-1} \langle \boldsymbol{X}_p^2(0) \rangle \left[\Phi(p, N/2) - \Phi(p,1)\right]^2}\end{aligned} \tag{6.10}$$

and the autocorrelation function corresponding to the segmental mode dielectric relaxation ($\rho_s(t)$) can be expressed in terms of normal modes as:

$$\begin{aligned}\rho_s(t) &= \frac{\langle \boldsymbol{P}_{seg}(t) \cdot \boldsymbol{P}_{seg}(0) \rangle}{\langle |\boldsymbol{P}_{seg}(0)|^2 \rangle} \\ &= \frac{\sum_{p=0}^{N-1} \sum_{j=2}^{N/2-1} (-1)^j \langle \boldsymbol{X}_p^2(0) \rangle \left[\Phi(p, j-1) - 2\Phi(p,j) + \Phi(p,j+1)\right]^2 \exp\left(-\left(t/\tau_p^*\right)^{\beta_p}\right)}{\sum_{p=0}^{N-1} \sum_{j=2}^{N-1} (-1)^j \langle \boldsymbol{X}_p^2(0) \rangle \left[\Phi(p, j-1) - 2\Phi(p,j) + \Phi(p,j+1)\right]^2}\end{aligned} \tag{6.11}$$

where τ_p^* is the relaxation time of the p^{th} mode. The average relaxation time of the p^{th} mode can then obtained using $\tau_p = \tau_p^* \Gamma(1+\beta^{-1})$, where $\Gamma(n)$ represents the Gamma function.

The dielectric loss $\epsilon^{''}(\omega)$, is then defined through the imaginary part of the Fourier transform of the time derivative of the corresponding autocorrela-

tion functions,

$$\epsilon''(\omega) = \kappa\Im\left[\int_0^\infty \exp(-i\omega t)\left(-\frac{d}{dt}\rho_m(t)\right)dt\right]$$
$$= \kappa\Im\left[i\omega\int_0^\infty \exp(-i\omega t)\rho_m(t)dt\right] \tag{6.12}$$

where κ is a constant which depends on the conductivity of the material and $\Im$ represents the imaginary part. Following eqs 6.10, 6.11 and 6.12, the normal dielectric loss ($\epsilon_n^{''}$) and the segmental dielectric loss ($\epsilon_s^{''}$) can be written in terms of the normal modes as,

$$\epsilon_n''(\omega) = \kappa\rho_n^p\Im\left[i\omega\int_0^\infty \exp(-i\omega t)\exp\left((-t/\tau)^{\beta_p}\right)dt\right]$$
$$\epsilon_s''(\omega) = \kappa\rho_s^p\Im\left[i\omega\int_0^\infty \exp(-i\omega t)\exp\left((-t/\tau)^{\beta_p}\right)dt\right] \tag{6.13}$$

where ρ_n^p and ρ_s^p represents the time independent part of $\rho_n(t)$ (eq (6.10)) and $\rho_s(t)$ (eq 6.11) respectively. For $\beta_p = 1$, the above equations reduce to;

$$\epsilon_n'' = \frac{\sum_{p=0}^{N-1}\langle \boldsymbol{X}_p^2(0)\rangle\left[\Phi(p,N/2)-\Phi(p,1)\right]^2\frac{\omega\tau_p}{1+\omega^2\tau_p^2}}{\sum_{p=0}^{N-1}\langle \boldsymbol{X}_p^2(0)\rangle\left[\Phi(p,N/2)-\Phi(p,1)=\right]^2}$$
$$\epsilon_s'' = \frac{\sum_{p=0}^{N-1}\sum_{i=2}^{N/2-1}\langle \boldsymbol{X}_p^2(0)\rangle\left[(-1)^i\Phi(p,i+1)-2\Phi(p,i)+\Phi(p,i-1)\right]^2\frac{\omega\tau_p}{1+\omega^2\tau_p^2}}{\sum_{p=0}^{N-1}\sum_{i=2}^{N/2-1}\langle \boldsymbol{X}_p^2(0)\rangle\left[(-1)^i\Phi(p,i+1)-2\Phi(p,i)+\Phi(p,i-1)\right]^2} \tag{6.14}$$

For our results, β_p was in the range $0.7 - 0.9$ (cf. SI Figure S2), and eq 6.14 provided an excellent approximation for the numerical values resulting in eq 6.13. From a computational point of view, the dielectric spectra were very sensitive to the exact values of the normal modes that were used and hence to avoid numerical errors, in many places we have utilized Rouse modes while computing the spectra.

6.3 Results and Discussion

6.3.1 Normal Modes: Model S

In Figure 6.1, we present the simulation results for the normal modes of ordered diblock copolymer melts based on Model S. Figure 6.1(a) displays the normal modes in the direction parallel to the interface. It can be seen that such normal modes exhibit a shape identical to the unperturbed Rouse modes (eq 6.6, displayed as dotted lines in Figure 6.1(a)). Such results are consistent with the expectation that the dynamical features in the direction parallel to the interface are likely to be unaffected due to the assembly of the chains into the lamellar morphology. However, as we demonstrate later, there are still significant quantitative differences between the relaxation dynamics of such parallel modes and the behavior expected for unperturbed Rouse modes.

Figure 6.1(b) displays the normal modes in the direction perpendicular to the lamellar interface. The computed eigenfunctions for the odd numbered modes are seen to match closely with the unperturbed Rouse modes. In contrast, the even numbered modes are seen to exhibit deviations from the cosine

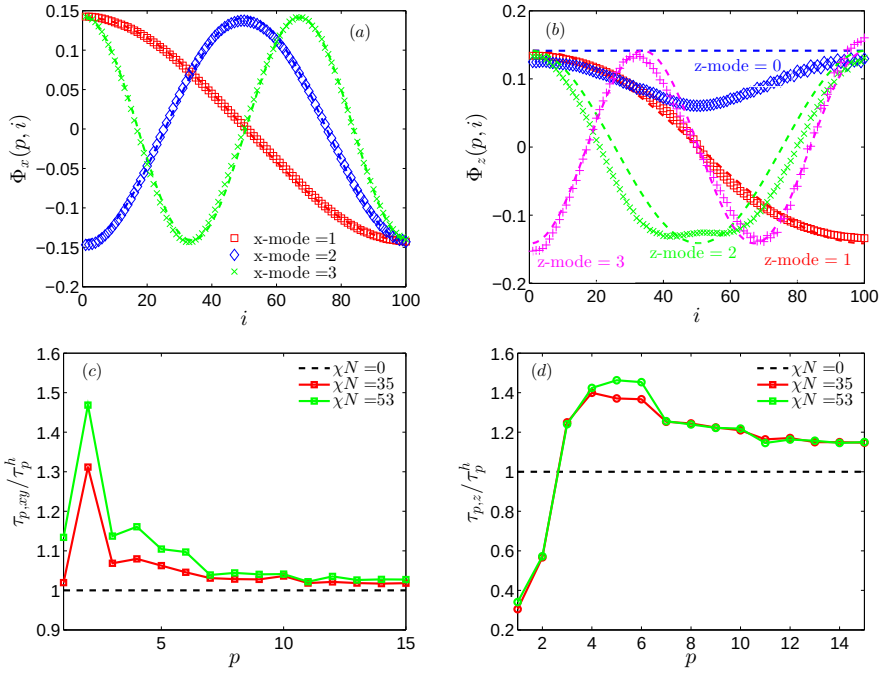

Figure 6.1: (a) Eigenfunctions (ϕ_p) of mode p in the direction parallel (a) and perpendicular (b) to the interface for $\chi N = 53$. Legends represent the value of p. Computed eigenfunctions are shown using different markers (see legends) and the corresponding Rouse modes in dotted lines. The relaxation times resolved (c) parallel ($\tau_{p,x}$) to the interface and; (d) perpendicular to the interface ($\tau_{p,z}$). All relaxation times are normalized with the homopolymer relaxation time.

shape characteristic of the unperturbed Rouse modes. Interestingly, the functional form of the $p = 0$ mode is no longer identically zero suggesting that the zeroth mode now differs from the center of mass (COM) of the chain.

To understand the above results for the perpendicular modes, we recall that the eigenfunction $\Phi(p, i)$ quantifies the weight arising from the dynamics

of i^{th} monomer to the p^{th} mode. Further, we note that the assembly of the block copolymer is likely to have the strongest effect on the dynamics of segments near the AB links. The unperturbed Rouse modes for odd p ascribe only a small weight to the monomers near the AB links (see for instance, the x modes for $p = 1, 3$), and hence the assembly of the block copolymer and the accompanying localization of the link segments to interfacial region has only a small impact on the shape of such modes. In contrast, the unperturbed Rouse modes for even values of p ascribe a significant weightage to the monomers near the link segment of the block copolymer. Due to the segregation of the block copolymer, the motion of the monomers near the link segments (near $i = 50$ in the notation of Figure 6.1(b)) are significantly impacted. Such an effect manifests as deviations of the even numbered p modes from the unperturbed Rouse modes.

Figures 6.1(c) and (d) displays the normalized relaxation times (τ_{xy}, τ_z) as a function of p for parallel (open squares) and perpendicular (open circles) modes normalized by the corresponding relaxation times for a *homopolymer melt* possessing the same number of segments as the diblock copolymer. For $p \gtrsim 5$, the relaxation times of the parallel modes (Figure 6.1(c)) are seen to follow the behavior expected for the homopolymers (eq (6.7)). Surprisingly, it can be seen that the relaxation times for longer wavelength modes ($p \leq 5$) are larger than the corresponding homopolymer values, and moreover, the magnitudes (relative to the hompolymer dynamics) are seen to increase with increasing degree of segregation between the polymers. These results suggest

that the dynamics of the chain segments in the direction parallel to the interface is slowed as a consequence of the self-assembly of the block copolymer. Such trends *contrast* with the expectation that the dynamics in the directions parallel to the interface are likely to unaffected by the ordering of the block copolymers.

For the normal modes in the perpendicular direction (Figure 6.1(d)), the mode $p = 0$ now possesses a non-zero relaxation time due to the fact that such a mode no longer represents the center-of-mass coordinate (we do not display the explicit value in the figure since there is no corresponding homopolymer relaxation time to serve as the normalization factor). More surprisingly, the relaxation dynamics of modes $p \lesssim 3$ are seen to exhibit lower relaxation times than the homopolymer (Figure 6.1(d)). This indicates a faster motion of the segments along the normal direction for longer wavelength modes. For $p \gtrsim 3$, the dynamics of the normal modes in the perpendicular direction are however seen to become slower than the corresponding hompolymer values.

To understand the results of Figures 6.1(c) and (d), we extract two distinct contributions to the relaxation time of the different modes. The first of these is the eigenvalues λ corresponding to the normal modes and quantifies the strength of the "harmonic potential" influencing the dynamics of such a mode. Figures 6.2(a) and (b) display the eigenvalues as a function of the mode number for the parallel ($\lambda_{p,x}$) and perpendicular modes ($\lambda_{p,z}$) respectively. Therein, we observe that the results for the parallel modes are unaffected by the microphase separation and match with the corresponding values for

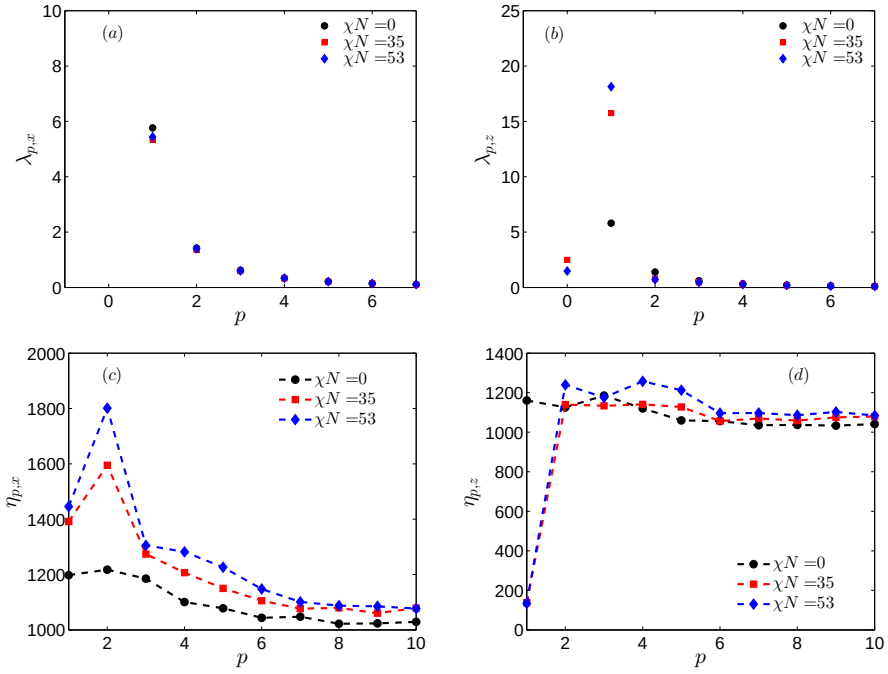

Figure 6.2: Eigenvalues, for directions (a) parallel ($\lambda_{p,x}$) and (b) perpendicular ($\lambda_{p,z}$) to the interface. Friction coefficients as a function of mode number in directions (c) parallel ($\eta_{p,x}$) and (d) perpendicular ($\eta_{p,z}$) to the interface. Dotted lines are guidelines for the eyes.

the homopolymer ($\chi N = 0$). Such trends are consistent with the absence of influence of the ordering-induced potential on the dynamics of the monomers in the plane *parallel* to the interface. In contrast, we observe that the magnitude of the eigenvalues in the Z direction are enhanced for the smaller p. Moreover, such an effect is seen to become more pronounced with increasing degree of

segregation. Such results are consistent with the strength of the segregation-induced potential influencing the dynamics in the direction normal to the lamella interface. Zeroth eigenvalue is shown in Figure 6.2 for providing a complete picture of the eigenvalues in the perpendicular direction.

The results presented in Figures 6.2(a) and (b) are broadly consistent with the expectations for dynamics in the directions parallel and perpendicular to the interface, and hence does not serve to explain the nontrivial features noted in Figure 6.1(b). Towards this objective, we note that a second contribution to the relaxation times corresponds to the friction coefficient η experienced by the modes. The latter cannot be independently characterized and for discussion purposes we deduce $\eta = \tau/\lambda$ to understand the underlying mechanisms. The corresponding results for the friction coefficient η are displayed in Figures 6.2(c) and (d).

It can be seen that the friction coefficient experienced by the chains in the parallel direction (Figure 6.2(c)) is higher than the homopolymer values. While such results may appear surprising, we note that such findings are consistent with recent results which indicated that ordering of polymers in lamellar morphologies leads to an increase in the number of constraints experienced by the chains in the direction parallel to the lamellar interface [268]. Moreover, the number of constraints were reported [268] to increase with increasing χN, a trend which is consistent with our results for the friction coefficient.

With regard to the perpendicular modes (Figure 6.2(d)), we observe an equally surprising result that the long wavelength modes experience substan-

tially less friction than the homopolymer chains. We do not have a conclusive explanation for the latter and speculate that such reduced friction and accelerated dynamics are likely a consequence of the pseudo one-dimensional nature of dynamics in segregated, stretched chains. These results however serve to indicate the nontrivialities in the dynamics of chains in ordered phases which manifest not only in the influence of the ordering induced potential but also on the friction coefficient influencing the dynamics.

In summary, for Model S, the normal mode dynamics were seen to behave very differently in the directions parallel and perpendicular to the interface. While the normal modes in the direction parallel to the interface closely followed unperturbed Rouse modes, the zeroth and even normal modes in the direction perpendicular to the interface showed deviations from unperturbed Rouse modes. Such difference were attributed to the presence of an external confining potential in the perpendicular direction arising from the self-assembly of the block copolymer. Additionally, the long wavelength relaxation times were larger in the direction parallel to interface, whereas an accelerated dynamics (smaller relaxation times) were observed in the direction perpendicular to the interface.

6.3.2 Normal Modes: Model F

In situations in which the dielectrically inactive block possesses significantly lower mobility compared to the dielectrically active block, it has been common to assume that the normal modes (and the dielectric spectra) of the

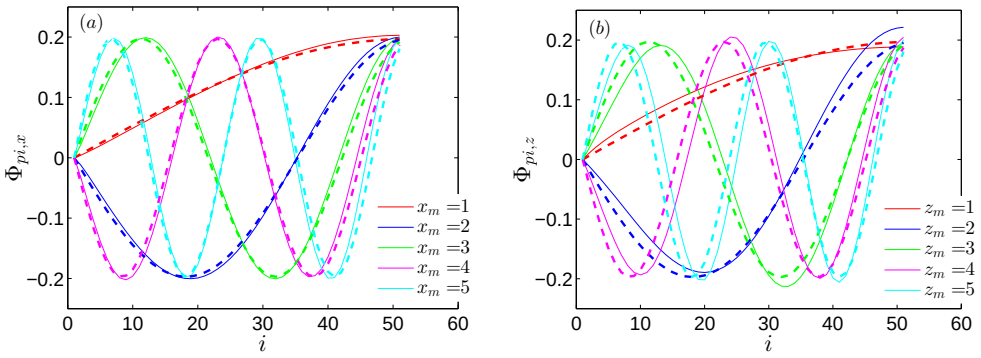

Figure 6.3: (a) Eigenfunctions parallel to the interface (x modes). (b) Eigenfunctions perpendicular to the interface (z modes)

polymer map to those of a polymer chain tethered to a surface [256, 262]. In such a picture, the normal modes are modeled as the unperturbed Rouse modes for odd values of p corresponding to a polymer chain tethered to a point in space [260]. While physically appealing, such a model relies on several unverified assumptions. On the one hand, the tethering of a polymer chain to a surface (in contrast to a point tether) is expected to render the normal modes anisotropic [261]. Further, the influence, if any, of the interactions with the other polymer chains are not addressed in such a picture. Motivated by such considerations, we studied the explicit normal mode and DS results for the model F in which the dielectrically inactive block was frozen after equilibration into lamellar phases. We compare the results for the normal modes and its dynamics with the predictions for a chain tethered to point (i. e. the odd numbered Rouse modes) — a model which is referred to henceforth as "tethered Rouse model."

Figures 6.3(a) and (b) display the normal modes in the directions parallel and perpendicular to the interface respectively. Solid lines depict our numerical results and the dotted lines display the tethered Rouse model predictions. The eigenfunctions parallel to the interface are seen to resemble the Rouse modes expected for odd p and are in accordance with the spectrum for the tethered Rouse model [253, 256, 260, 261]. In contrast, the eigenfunctions perpendicular to the interface, while qualitatively similar to the modes parallel to the interface, do exhibit small, quantitative deviations from such Rouse modes. Such results are indicative of the anisotropy in dynamics arising due to the ordering of the block copolymer. However, such deviations are seen to be relatively small, and suggest that the tethered Rouse model serves as an excellent approximation to the normal modes in the present situation.

Figures 6.4(a) and (b) display the corresponding relaxation times in the directions parallel and perpendicular to the interface. The relaxation times of the long wavelength parallel modes for microphase segregated cases are seen to be significant slowed and the absolute relaxation times are significantly slower than those of homopolymers of length $N = 50$ (Figure 6.4(a)). In contrast to the tethered Rouse model, which predicts that the longest relaxation time is four times that of the corresponding homopolymer, the results for microphase segregated systems show almost an order of magnitude slower relaxation times. Such differences show that while using tethered Rouse model yield approximately correct shape for the normal modes, the relaxation dynamics by themselves are very different from such predictions.

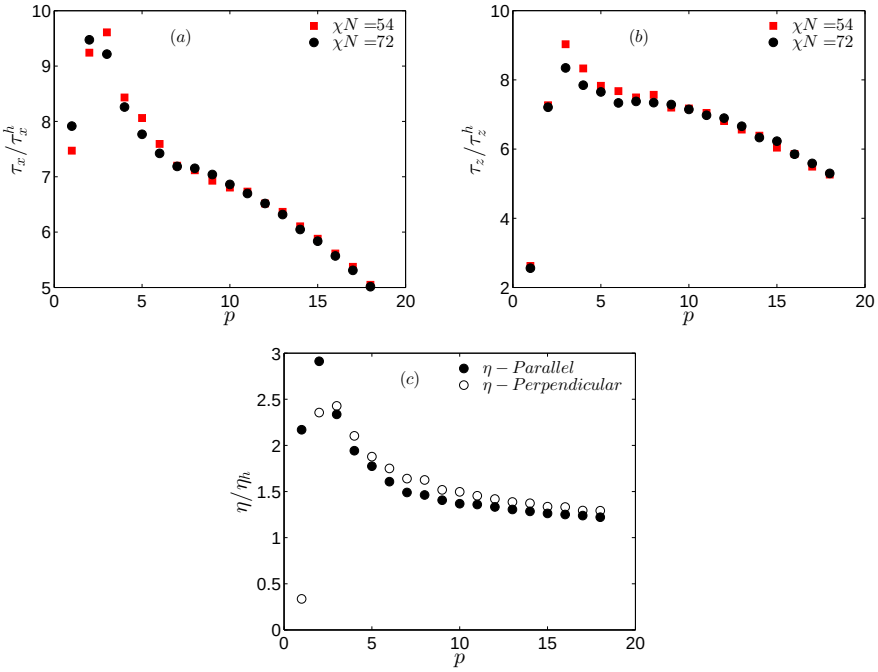

Figure 6.4: Relaxation times (a) parallel to interface and (b) perpendicular to interface for Model F.(c) Friction coefficient $\eta = \tau/\lambda$ for $\chi N = 72$ in the directions parallel and perpendicular to the interface. All values are normalized with the corresponding homopolymer for $N = 50$.

Similar to the observations in the context of Model S, we observe that the relaxation times of the long wavelength perpendicular to the lamellar interface to be smaller than those in the direction parallel to the interface. In Figure S4 (Supplementary Info), we present the eigenvalues corresponding to the normal modes and demonstrate that the magnitude of the eigenvalues

in the parallel direction are unaffected by microphase separation. In contrast, the eigenvalues corresponding to the perpendicular modes are seen to be larger than the homopolymer values and are consistent with the influence of the ordering induced potential arising from microphase separation. To rationalize the behavior of the relaxation times seen in Figures 6.4(a) and (b), we again invoke the behavior of the friction coefficient ($\eta = \tau/\lambda$, where λ denotes the corresponding eigenvalues). In Figure 6.4(c), we observe that the friction coefficient for tethered polymers are higher than that of the corresponding homopolymer ($\eta/\eta_h > 1.0$) for all modes. This is directly manifested as larger time constants for the tethered monomers. Moreover, similar to Model S, friction coefficient accompanying the dynamics of perpendicular modes to be smaller in comparison to those modulating the dynamics of parallel modes. Such observations can be reconciled in a similar manner to the reasoning suggested for Model S, wherein the increase in the constraints parallel to the interface manifests as higher friction coefficient accompanying the dynamics.

6.3.3 Dielectric Spectra

The output from the normal mode analysis was used within the framework suggested by Peter *et. al.* [266, 267] for type A polymers to calculate the dielectric loss spectra. As discussed earlier, in this work, we assumed that the contributions to $P_{seg}(t)$ and $P_{norm}(t)$ arose only from one of the blocks and hence the normalized normal dielectric loss (parallel to the chain) was defined in terms of the correlation of the vector joining the end of the chain to the

point of linkage between the blocks: $\mathbf{R}_1(t) - \mathbf{R}_{N/2}(t)$.

6.3.3.1 Segmental Dielectric Spectra

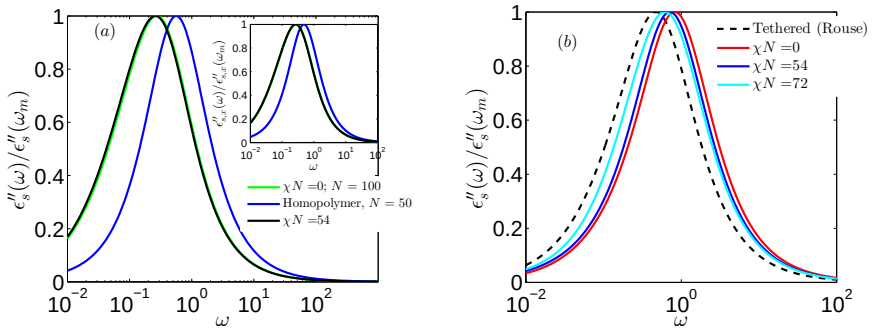

Figure 6.5: Overall normalized segmental dielectric spectra: (a) Model S; (b) Model F. Inset of the left panel represent the segmental dielectric spectra resolved parallel to the interface.

Figure 6.5(a) displays the results for segmental dielectric spectra (eq (6.14)) for Model S for different χN. We compare our simulation results with two other cases: (i) $\chi N = 0$ *system*: The block copolymer case of length N, in which χN was set to zero; and (ii) *Homopolymer system*: A melt of homopolymers with $N/2$ segments each. In comparing the results for the block copolymer with those of the homopolymer, we observe a shift in the spectra towards lower frequencies — a result which is consistent with the slowing of relaxations arising from linking the homopolymer to another block. In comparing the results for $\chi N = 54$ and $\chi N = 0$, we observe that the shape of the segmental DS is independent of the degree of segregation suggesting that the segmental DS to be unaffected by the self-assembly of block copolymers. Results for dielectric spectra resolved parallel to the interface (inset of Figure 6.5(a)) shows

characteristics similar to those observed for the overall segmental dielectric spectra. Similar trends were also observed in the DS resolved perpendicular to the interface and is presented in the SI (Figure S3(a)).

Figure 6.5(b) depicts the corresponding segmental dielectric spectra for Model F. Here we compare the segmental DS obtained for self-assembled block copolymers with that arising from (i) Homopolymers with chain length of $N = 50$; and (ii) Tethered Rouse model (for the tethered Rouse model, we used a friction coefficient of 1.2 obtained by fitting the simulation results for untethered homopolymer melts). In contrast to the results seen for Model S, with increasing degree of segregation a very weak shift is observed in the case of Model F relative to both the homopolymer and the tethered model. This suggests that the segregation of block copolymers weakly does affect the segmental dielectric spectra for copolymers possessing asymmetric mobilities.

To understand the above results, we note that segmental dielectric spectra probes the relaxation dynamics at short length scales corresponding to three or four monomers of the polymer chain, or equivalently, one or two beads in the coarse-grained model. Such a length scale corresponds to the short wavelength normal modes, the relaxation times of which were found to be practically unaffected in model S. In the context of model F, the relaxation times of small wavelength modes were seen to be affected (albeit, to a lesser extent than the long wavelength modes) due to the tethering of the dielectrically active block to the immobile phase. Such modifications underlie the shifts seen in the DS as shown in Figure 6.5(b).

In summary, from our results presented for Models S and F, it is evident that microphase separation and the degree of segregation has only a small influence on the segmental dielectric spectra of the polymers. In comparison to the homopolymer containing $N/2$ segments, the spectra was seen to shift to lower frequencies. Such findings were seen to hold independent of the mobility disparity between the blocks.

6.3.3.2 Normal Dielectric Spectra

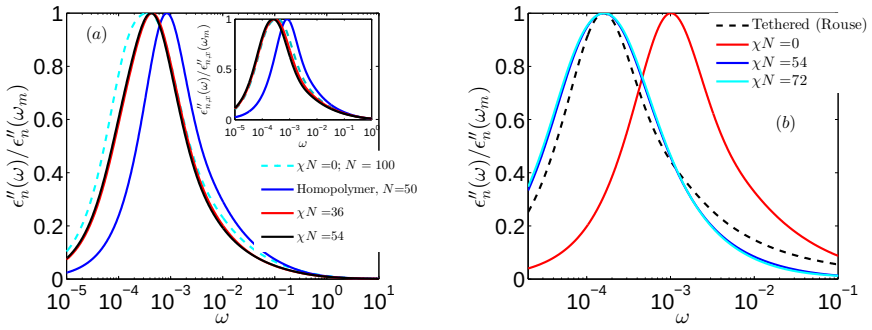

Figure 6.6: Overall normalized normal dielectric spectra: (a) Model S; (b) Model F. Inset of the left panel represent the normal dielectric spectra resolved parallel to the interface. For Model F, full width at half maximum (FWHM) defined as $\log(\omega_{max}(\epsilon_s'' = 0.5)/\omega_{min}(\epsilon_s'' = 0.5))$ are 2.929 (Tethered Rouse Model); 2.936 (Homopolymer); 3.334 ($\chi N = 54$) and 3.391 ($\chi N = 72$)

Figure 6.6(a) displays the overall normal dielectric spectra for Model S. In comparison to homopolymers, it can be seen that the block copolymers exhibit a weak shift to higher frequencies, and moreover, the extent of shift is seen to increase with χN. To decouple the different contributions to such a result, we resolved the dielectric spectra based on the dynamics parallel and

perpendicular to the lamellar plane (inset of Figure 6.6(a)). It is seen that the spectra calculated based on the dynamics in the plane parallel to the lamella shifts to lower frequencies, whereas, the results for the spectra calculated based on the dynamics in the direction perpendicular to the lamella (Figure S3(b) of SI) displays a shift to higher frequencies.

To rationalize the above trends, we first note that normal dielectric spectra probes the long wavelength relaxations of the polymer chains. The results presented in Figure 6.1(b) indicated that the longer wavelength modes the dynamics of the chain were slowed in the direction parallel to the interface. The results depicted in the inset to Figure 6.6(a) mirror such trends and reflect a shift in the spectra based on parallel modes to lower frequencies. In contrast, the normal modes perpendicular to the interface for long wavelength modes $p \leq 3$ were accelerated relative to the homopolymer time scales. The results presented in the inset to Figure 6.6(a) are consistent with such changes.

In Figure 6.6(b), we display the normal dielectric spectra for model F and compare with that of the reference homopolymer system ($N = 50$) and the tethered Rouse model. Consistent with the presence of only odd numbered Rouse modes in models for tethered systems, the simulation results for the homopolymer system is seen to have a peak frequency ($\omega_m = 0.01$) which is approximately four times that of the peak frequency predicted for the tethered systems [247]. The simulated block copolymers systems are however seen to exhibit shifts to even much lower frequencies relative to the tethered systems. In addition, the extracted width at the half maximum (FWHM) shows that

there is a broadening of the spectra seen relative to the homopolymers (see caption of Figure 6.6 for values of FWHM). On increasing the strength of segregation between the blocks, the spectra exhibits a small shift to further lower frequencies (imperceptible in the scale of Figure 6.6(b)).

To explain the above results, we again invoke the relaxation spectra of the normal models for Model F discussed in the context of Figure 6.4(b). Therein, we observed that the relaxation times for model F were much longer than relaxation times based on the Rouse predictions for tethered polymers. We suggest that such differences underlie the shift in the peak frequency in model F (relative to both homopolymers and tethered model predictions) seen in Figure 6.4(b).

In summary, from our results presented for Models S and F, it is evident that microphase separation leads to a shift of the normal dielectric spectra of the polymers. While such effects were observed in both models, the magnitudes of the effects were found to depend on the mobility disparity between the blocks. Moreover, the differences seen between the results for model F and tethered Rouse chain predictions indicate that the dynamics of chains in microphase separated morphologies (even with a relatively immobile block) exhibit important differences from the behavior expected for chains tethered to a point.

6.3.3.3 Relationship of our results to experimental observations

A number of experiments which have studied dielectric spectra of type-A polymers in ordered block copolymer morphologies have reported shifts in either or both the normal and segmental spectra relative to their homopolymer counterparts [39, 251–253, 256, 262, 269, 270]. Additionally, a few other experiments [251, 256] have also shown the emergence of an additional peak at a frequency in between the segmental and normal peak frequency. In comparing our results with those reported in experiments, the trends we observed for normal dielectric spectra are seen to broadly agree with those seen in the experiments. This suggests that a coarse-grained model like ours, in conjunction with the normal mode analysis, captures the essential physics at the long wavelength modes. In contrast, our results displayed much less changes in the segmental DS, which is consistent with the lack of ability of our coarse-grained model to capture the dynamical effects arising at the scale of short wavelength segmental modes.

6.4 Summary

To summarize, the dynamical properties of block copolymers in lamellar phases were investigated using molecular dynamics simulations. Motivated by dielectric spectroscopic studies, we performed normal mode analysis on the chains in directions both parallel and perpendicular to the interface. We employed two distinct models to clarify the specific effects arising from the self-assembly and the disparities in mobilities of the blocks.

In the absence of mobility disparities, the microphase separation of the block copolymer was seen to most drastically affect the shape of long wavelength normal modes of the system. Within such a context, the even normal modes displayed the most distinct deviations from the unperturbed Rouse modes. The relaxation dynamics of such normal modes resolved in the direction parallel to the interface displayed a slowing of the dynamics compared to their homopolymer counterparts with the relaxation times increasing with increasing degree of segregation. in contrast, an acceleration in dynamics was observed for the long wavelength normal models in the direction perpendicular to the interface. Such changes were explained by invoking both the influence of the confinement potential and the friction coefficients accompanying the dynamics. For systems with mobility disparities, the normal modes were qualitatively similar to the tethered Rouse model predictions. However, the magnitudes of the relaxation times of the normal modes were much larger relative to the homopolymer counterparts and those predicted by the tethered Rouse model.

We also computed the dielectric spectra using the results obtained for normal modes. It was observed that the normal mode dielectric spectra showed deviations from its homopolymer counterpart and such deviations were stronger for the case of systems possessing asymmetric mobilities. In contrast, the segmental spectra showed only much smaller deviations from its homopolymer counterparts. The results of both normal and segmental spectra were rationalized from the results obtained for the dynamics of the normal

modes.

The models adopted in this work constitute two extreme cases of mobility ratios experimental situations. Despite such assumptions, our results are still expected to be useful to disentangle the effects arising from the microphase segregation and mobility differences upon the normal modes and DS spectra.

Chapter 7

Multiscale Simulations of Lamellar PS-PEO Block Copolymers doped with $LiPF_6$ Ions

7.1 Introduction

There has arisen significant interest and a concomitant number of studies related to renewable energy sources such as lithium ion batteries and fuel cells [5, 7, 10, 12, 37, 271, 272]. A key component that affects the performance of materials is the electrolyte that facilitates ion transport between electrodes. In this regard, solid polymer electrolytes (SPE) have emerged as attractive candidates for such a function owing to its nonflammability and mechanical strength characteristics [4, 5, 12, 273, 274]. Unfortunately, while SPEs possess high mechanical strength, they often possess lower room temperature ionic conductivity. Hence, the development of polymer membranes with both high conductivity and mechanical strength has emerged as an objective of significant interest in this field. [1]

In the above context, block copolymer electrolytes have emerged as an attractive option for polymer electrolytes [12, 21, 24, 273]. For instance, re-

[1]Citations: Vaidyanathan Sethuraman, Santosh Mogurampelly, Venkat Ganesan, Multiscale Simulations of Lamellar PS PEO doped with LiPF6 ions, *Macromolecules*, **50** (11), pp 45424554, 2017. Santosh Mogurampelly helped in setting up simulations and Venkat Ganesan guided the project.

cent experiments on copolymer systems with blocks made up of conducting and non-conducting segments have shown that both the conductivity and the mechanical strength of segregated morphologies can increase with increasing molecular weight (MW) [24, 201, 275]. Such a result contrasts with its homopolymer counterparts in which the conductivity decreases with increasing MW, thereby leading to a trade-off between the mechanical and transport properties in such cases [25] Such results have piqued significant interest in BCP based polymer electrolytes [7, 12]..

Despite the significant insights which have emerged from experimental studies in BCP electrolytes [2, 12, 24, 28], there still exists a lack of fundamental understanding of the mechanisms underlying the ion coordination, segregation and transport characteristics of salt-doped block copolymer electrolytes, and especially the differences from the corresponding homopolymer systems and the influence of microphase segregation and ordering. While some preliminary results have emerged from coarse-grained models [28, 29, 276] information, especially at an atomistic level of resolution of such systems, is still lacking.

In pursuing a computational strategy to address the above questions, a major impediment confronting the simulations of microphase separated polymers at an atomistic resolution is that equilibrating self-assembled morphologies within such a framework proves to be computationally expensive due to the time scales involved in phase separation [20]. Commonly, in studies concerned with phase-separated systems, such an issue is circumvented by use of

less resolved/coarse-grained models which utilize soft intermolecular interaction potentials that can facilitate rapid equilibration [31, 32]. However, since such approaches coarse-grain over many degrees of freedom, they eliminate the possibility to study many of the interesting static and dynamical properties of the polymer chains which are expected to prove relevant for addressing the physics of polymer electrolytes.

Motivated by the above issues, in this work, we pursue a multiscale simulation strategy [62, 193] to equilibrate and study at an *atomistic level*, self-assembled lamellar morphologies of polystyrene-polyethylene oxide (PS-PEO) block copolymers doped with Lithium-hexaflurophosphate ($LiPF_6$) salts. Using the configurations resulting from our simulation approach, we study the static conformational properties of the system and specifically seek to clarify: (i) The manner in which ion-polymer coordinations differ between self-assembled morphologies and the corresponding homopolymer systems; (ii) The local distribution and the coordination of ions in the self-assembled phase and; (iii) The effect of salt concentration on such characteristics.

The rest of the Chapter is organized as follows. The multiscale simulation strategy which is employed to generate the ordered morphologies is discussed in Section 7.2.1 and the measures that are used to characterize the structural properties of the electrolyte are presented in Section 7.2.2. The results and discussion pertaining to the mass density profiles and the distribution of ions in the BCP system are presented in Section 7.3.1. A comparison of cation–polymer chain coordinations in BCP and homopolymers are presented

in Section 7.3.3. The comparisons in structural properties of homopolymer and block copolymer electrolytes are discussed in Section 7.3.4. The local characteristics of the coordination behavior in block copolymer electrolytes are discussed in Section 7.3.5.1. Influence of microphase segregation and salt concentration on ionic aggregates are presented in Section 7.3.6. The findings of our study are summarized in Section 7.4.

7.2 Simulation Methods and Characterization Measures

7.2.1 Generation of Ordered Morphology

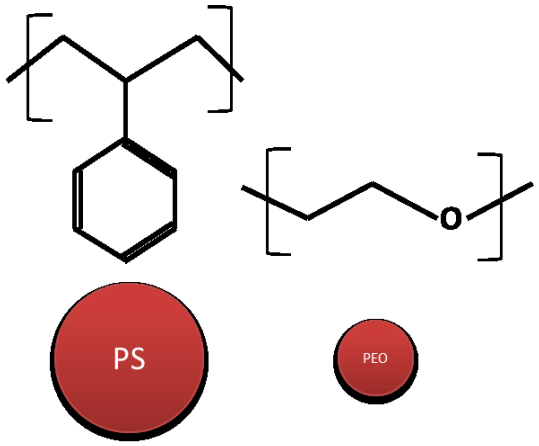

Figure 7.1: Schematic for coarse-graining of PS-PEO block copolymer.

The computer simulation methodology we use to generate BCP morphologies involves three major steps: (i) Coarse-graining of atomistic potentials; (ii) Simulations using such coarse-grained potentials to generate the long range ordered morphologies; and (iii) Reintroduction and equilibration

of atomistic details into the coarse-grained ordered morphologies. For the atomistic level of description we chose a United Atom (UA) resolution of the PS-PEO systems. Specifically, TraPPe force fields were utilized to describe the salt-doped PS-PEO melt at the atomistic level, and an explicit atom model was used for PF_6 anions. The dielectric constants for the pure PEO and PS homopolymer system (in the absence of ions) for the specified force field were computed [277] to be 4.71 and 1.0 respectively. The resulting ratio between the dielectric constants of pure PEO and PS homopolymer melts is close to the experimentally reported values [278]. The chemical structure of the PS and PEO monomeric units chosen in this work and the corresponding coarse-grained monomeric units are shown in Figure 7.1. The steps accompanying our multiscale simulation approach are discussed below:

1. *Coarse-Graining of PS-PEO chains:* The first step of our procedure involved coarse-graining the atomistic description to a less detailed representation which can facilitate simulations of microphase separation. For the coarse-grained simulations described below, we used a CG representation of the molecules and their interactions. Explicitly, the PS monomer was coarse-grained into one single bead (type A) and the PEO monomer was coarse-grained into a second bead (type B).

   To obtain the coarse-grained intramolecular potentials, we simulated a PS-PEO melt atomistic system (without ions) consisting of 100 block copolymer chains at $T = 600$ K. At this temperature, the system exists in a disordered state. The interaction parameters [279–284] used

for the atomistic simulations are summarized in Table 7.1. Each chain consisted of 151 UA monomers with 10 PS monomeric units and 23 PEO monomeric units. Such a choice ensures a 50:50 composition for the di-block copolymer. NPT simulations were employed at a pressure of 1 atm. Nóse-Hoover thermostat with a thermostat coupling coefficient of 0.1 ps and a barostat coupling coefficient of 1 ps were employed in such simulations. Prior to computing different intramolecular interactions, the systems were equilibrated for 7 ns.

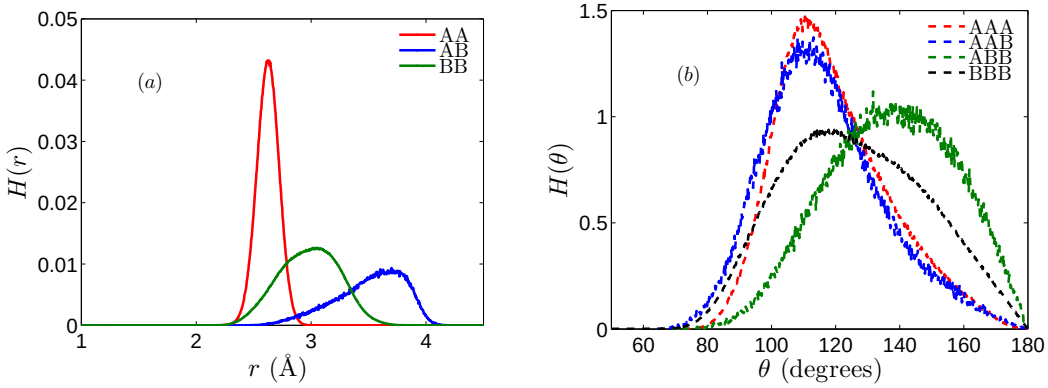

Figure 7.2: Histograms obtained from (a) bond distribution; and (b) angle distribution.

Table 7.1: Interaction parameters for PS-PEO united atom model.

Bonding Potential: $V_b = k_b(r - r_0)^2$				
Type	k_b $(kcal/mol/(\text{Å})^2)$	r_0 (Å)		
CH_2-CH_2	250	1.54		
CH-CH_2	250	1.54		
CH-CH_3	250	1.51		
CH(ring)-CH(ring)	250	1.40		
C(ring)-CH(ring)	250	1.40		
C(ring)-CH_2	250	1.51		
O-CH	250	1.41		
P-F	190	1.6		
Angle Potential: $V_\theta = k_\theta(\theta - \theta_0)^2$				
Type	k_θ $(kcal/mol/rad^2)$	θ_0 (deg)		
CH_2-CH_2-CH_2	120	114		
CH(ring)-CH(ring)-CH(ring)	120	120		
CH-CH_2-CH	62	114		
C(ring) - CH(ring)-CH(ring)	120	120		
CH(ring)- C(ring) -CH	120	120		
CH_2- C(ring) - CH_2	120	120		
CH_2-O -CH_2	60	114		
CH_2-CH_2- O	50	112		
Dihedral Potential: $V_\phi = \sum_{i=1}^{4} \frac{1}{2} k_{i\phi} \left(1 + (-1)^{(i+1)}\right) \cos(i\phi)$				
Type	$k_{1\phi}$ $(kcal/mol)$	$k_{2\phi}$	$k_{3\phi}$	$k_{4\phi}$
O-CH_2-CH_2-CH_2	0.7020	-0.2120	0.30600	0
CH_2-CH_2-O-CH_2	2.8828	-0.6508	2.2184	0
CH_2-CH_2-O-CH_3	2.8828	-0.6508	2.2184	0
CH_2-C(ring) -CH_2-C(ring)	1.4112	-0.2712	3.1452	0
CH_3-C(ring) -CH_2-C(ring)	1.4112	-0.2712	3.1452	0
Non-bonded Potential: $V_{ij} = 4\epsilon_{ij}\left[\left(\frac{\sigma_{ij}}{r_{ij}}\right)^{12} - \left(\frac{\sigma_{ij}}{r_{ij}}\right)^{6}\right] + \frac{q_i q_j}{r_{ij}}$; $\epsilon_{ij} = \sqrt{\epsilon_i \epsilon_j}$; $\sigma_{ij} = \frac{\sigma_i + \sigma_j}{2}$				
Type	ϵ $(kcal/mol)$	σ (Å)	q (e)	
C(ring)	0.0596	3.700	0.0	
CH(ring)	0.1003	3.695	0.0	
CH	0.0199	4.650	0.0	

CH_2(PS)	0.0914	3.950	0.0
CH_3	0.1947	3.750	0.0
CH_2(PEO)	0.0914	3.950	0.25
O	0.1093	2.800	-0.5
Li	0.4000	1.400	1.0
P	0.2000	3.742	0.7562
F	0.0610	3.118	-0.2927

Table 7.1: Interaction parameters for PS-PEO united atom model.

Subsequently, the intramolecular interactions between the A and B beads were obtained by coarse-graining the atomistic interactions. Explicitly, three types of bond distributions (AA, AB and BB) and four types of angle distributions (AAA, AAB, ABB and BBB) were quantified. The histograms obtained ($H(r)$ and $H(\theta)$) from such distributions are displayed in Figure 7.2. The intramolecular potentials (V_{cg}) were then obtained using inverse Boltzmann technique [285, 286] designed to reproduce such distributions and were then fit to a sum of Gaussian distributions of the form: [69, 70]

$$V_{cg}(\theta) = -kT \log \left(\sum_{i=1}^{n} g_i(\theta) \right),$$
$$g_i(\theta) = \frac{A_i}{w_i \sqrt{\pi/2}} e^{\frac{-2(\theta-\theta_{ci})^2}{w_i^2}}, \tag{7.1}$$

where g_i represents the i^{th} Gaussian distribution and n represents the number of distributions chosen to fit the potentials. A_i, w_i and θ_{ci} represent the amplitude, variance and mean of the Gaussian distributions. The parameters obtained using Eq. 7.1 for bending and bonding potentials were too strong to be employed in a coarse-grained simulation. Since our earlier works demonstrated that the morphologies obtained are relatively insensitive to the strength of such interactions (beyond a critical extent of rigidity) [287], the potentials were softened by multiplying the variance w_i by a factor of 10.0 to render the potentials more amenable for the simulations using the coarse-grained model. Moreover, as we detail below, the final step of our strategy involves reintroduction

of the accurate atomistic configurations and potentials followed by a re-equilibration procedure. Hence, any small inaccuracies in the coarse-grained intramolecular interactions are expected to equilibrate eventually to the accurate distribution. Table 7.2 lists the intramolecular interaction parameters obtained from inverse Boltzmann technique which were then used for CG simulations.

Bonding Parameters		
Type	r_0/b	
A-A	1.0	
A-B	0.872	
B-B	1.242	
Angle Potential: $V_\theta = k_{\theta,cg}\left(\cos(\theta) - \cos(\theta_0)\right)^2$		
Type	k_{cg}	θ_0 (degrees)
AAA	2.06	109
AAB	1.989	109
ABB	1.989	130
BBB	1.528	109

Table 7.2: Interaction parameters for PS-PEO coarse-grained SCMF model.

In this work, we have fitted the histograms in Figures 2(a) and (b) to single Gaussian curve. Such procedure is expected to work for single modal curves. There can be slight error in the case of BBB angles since the distribution is asymmetric. However, we expect that any discrepancies between the coarse-grained potential vs atomistics configurations

will not prove significant due to the period of equilibration at at the atomistic level, which is enforced in the third stage of our strategy (see text below).

2. *Single Chain in Mean Field (SCMF) Simulations* The second step of our multiscale simulation strategy involves the use of the above-deduced coarse-grained potentials to simulate the microphase separation in the PS-PEO block copolymer system. In this work, single chain in mean field simulations [32] (SCMF) were utilized for effecting the CG simulations. The details of single chain in mean field theory approach have been expounded in a number of previous works [32, 288–292] and hence, we present only the salient details here. In SCMF the polymers are explicitly modeled through a bead-spring like model. The intramolecular interactions consisted of bending potential (H_θ) between the coarse-grained beads were adopted to be of the form,

$$H_\theta = k_{\theta,cg} \left(\cos\left(\theta\right) - \cos\left(\theta_{0,cg}\right)\right)^2 \tag{7.2}$$

where, $k_{\theta,cg}$ and $\theta_{0,cg}$ represent the bending constant and the equilibrium angle between three consecutive neighboring blobs. The parameters accompanying the above potential function were obtained as an outcome of the coarse-graining step discussed in the context of step 1.

With regard to the intermolecular interactions between the beads, SCMF borrows the framework of self-consistent field theory (SCFT) wherein

such interactions are replaced by pseudo chemical potential fields $w(r)$ and $\pi(r)$ which account for the driving forces for segregation and incompressibility respectively. The incompatibility and incompressibility fields are in turn characterized by Flory Huggins parameter (χ) and the compressibility parameter (κ), respectively. Recent works by Morse *et. al.,* [83, 264] and ours [193] have shown that an accurate way to obtain the χ parameter for such CG simulations is by matching the structure factor peaks obtained in the disordered phases of both hard and soft potentials. However, implementing such a procedure in the present context proves cumbersome due to the large number of atomistic simulations involved required to determine such a mapping. As an alternative, in our work, we adopt a value of $\chi N = 55$. Such a choice is based on the expectation that while accounting for the fluctuation effects (the Fredrickson-Helfand fluctuation corrected ODT [32] corresponds to 36 for our MWs), such a system still will be in an intermediate degree of segregation.

We chose a block copolymer system with 700 chains having a degree of polymerization $N = 33$ in the SCMF simulations. To obtain a 50:50 composition, the first 10 monomers were labelled as PS monomers and the ratio between the sizes of PS and PEO were made proportional to their masses (since densities of PS and PEO at the temperatures of interest are comparable). Such systems correspond to an experimental MW of approximately 2.1 kDa. Further, all dimensions were scaled by the average diameter of the coarse-grained bead ($\sigma_b = 3$ Å). Simulation

box in each spatial direction was divided into $16 \times 16 \times 16$ grid points, thus ensuring approximately 5.6 particles in each cell.

The above model was evolved within a Metropolis Monte Carlo approach. The bond lengths were fixed and for Monte Carlo moves for bending, we employed local pivot moves. The acceptance rule for Monte Carlo simulations is given by, $p_{acc} \rightarrow min\,(1, \exp(-\Delta H_\theta - \Delta w - \Delta\pi)$, where Δ represents the difference in energies between new and old configurations. Simulations were done for 2.5×10^5 equilibration cycles and 1×10^4 production cycles at the end of which an ordered morphology is obtained.

We performed several simulations with varying cuboid box dimensions at the same density to obtain equilibrated lamellar phases which lack defects. The ordered morphology obtained using such box dimensions were however not necessarily parallel to any of the three coordinate axes. However, for the purpose of characterization of the coordination characteristics, it is desirable to have morphologies for which the normal to the lamellar plane lies parallel to one of the box dimensions. Towards such an objective, we employed the principal component analysis (PCA) approach which involved computing the normal vector at each grid point defined by $\hat{\mathbf{n}} = \frac{\nabla\phi}{|\nabla\phi|}$, where ϕ denotes composition field acting at every grid point. Such a normal vector is used to compute a tensor, $\mathbf{S} = \hat{\mathbf{n}}\hat{\mathbf{n}}$ at every grid point. Subsequently PCA is employed to identify the normal of the lamellar plane using an average of $\underline{\underline{S}}$ tensor. Once the coordinates are rotated using the angle obtained from PCA, the box is re-sized in

such a way that the new box direction perpendicular to the lamellar is made commensurate with the domain spacing. Other sides were adjusted in such a way that the volume of the system remains the same.

3. *Reintroduction of United Atom Potentials* The third step of our multi-scale simulation strategy entails the reintroduction and re-equilibration of atomistic details into the microphase separated morphologies resulting as outcomes of step 2 above. For the PEO monomers, the geometric centers of the blobs were assumed as the oxygen centers and carbon atoms were reintroduced at random keeping the bond length prescribed at the CH_2-O bond length. For the PS monomers, the geometric centers were assumed to coincide with the carbon atom above the phenyl ring. Subsequently the backbone atoms were reintroduced in the system. Finally, the phenyl ring was introduced perpendicular to the backbone. The terminal atoms were introduced as CH_3 for symmetry purposes.

   The equilibration step consisted of the following steps: (i) While reintroduction, care was taken such that the global packing of the system did not change. To this end, the geometric centers during the reintroduction step (oxygens for PEO and phenylene carbon for PS) were tethered to its initial position using a harmonic potential of the form $U_t = \frac{1}{2}k_t(r - r_i)^2$. The tethering spring constant (k_t) was chosen as a high value of 1500 kcal/mol/Å^2 [293]. This ensures a minimum change in the global structure of the system. Under such conditions, a small energy minimization using conjugate-gradient method was performed; (ii) Sub-

sequent to energy minimization, a short NVT run of 30 ps is performed with a Nóse-Hoover theromostat with a coupling coefficient of 100 fs and at a temperature of 350 K. The choice of temperature was motivated by the experimental findings that block copolymers (possessing the MW close to those used in simulations) were found to undergo ODT at $\approx 90^{\circ}$ C; [275](iii) Further to the short period of equilibration using NVT, the system is re-equilibrated for a long run using a NPT ensemble with a barostat coefficient of 1 ps. Particle-particle-particle-mesh solver [294] was used to compute the electrostatic interactions in all the above steps. The cut-off used for both long-ranged and pair interactions was 14 Å. Prior to the introduction of ions, the block copolymer melt was equilibrated for 2-4 ns. Tail corrections were incorporated to correct for the error in long ranged pressure and energy. In accordance with the TraPPe force-field, the 1-4 electrostatic interactions were scaled by a factor of 0.5 and all the UA simulations were carried out using LAMMPS [96].

Subsequent to the equilibration of block copolymer melts, the Li^+ cations and $PF_6{}^-$ anions are introduced at random into the system and their distribution are re-equilibrated. In this work, we studied block copolymers at three salt concentrations (EO:Li= {10:1,20:1,30:1}) which correspond to 1610, 805 and 540 Li^+ ions respectively. The ions were doped into the equilibrated block copolymer using PACKMOL software at random with equal probabilities on any site in the box. The initial distribution of the ions is depicted in Figure 7.3. Further to the introduction of ions, the

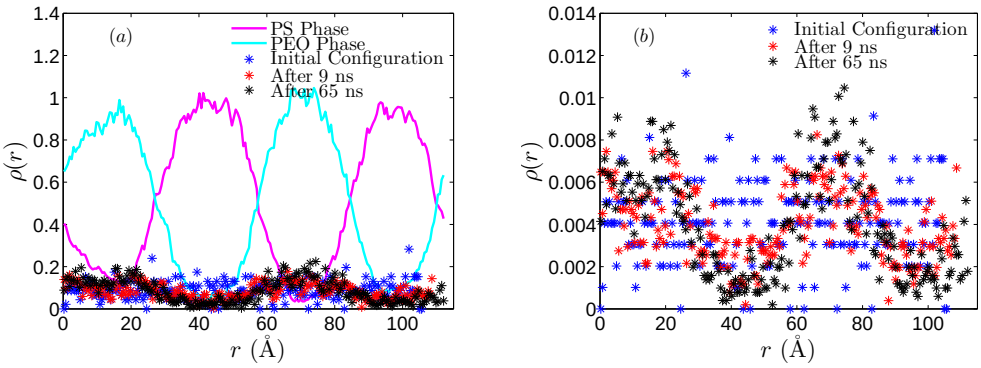

Figure 7.3: Evolution of density profiles of (a) Lithium ions along with the initial density profile for PS and PEO; (b) Only Lithium ions

EO:Li	BCP Density (g/cm^3)	Homopolymer Density (g/cm^3)
10:1	1.180	1.33
20:1	1.130	1.22
30:1	1.113	1.19

Table 7.3: Densities for the investigated set of salt concentrations.

systems were re-equilibrated, at the end of which a redistribution of ions was observed. Consistent with the experimental observations, the system densities were observed to increase with increasing salt concentration for both homopolymers and block copolymers (cf. Table 7.3).

The system comprising of ions and melt was again energy minimized and a short NVT run was performed for 100 ps, following which a long NPT run ($\approx$ 40 ns) was conducted. During the NPT phase, the barostat in the directions parallel to the lamellar phase was coupled together

whereas the one in the perpendicular direction was allowed to vary freely. The timestep used for the equilibration cycles was 1 fs whereas that for production cycles was 1.5 – 2 fs. Velocity Verlet algorithm was used to integrate the equations of motion [95]. Structural quantities were saved every 2 ps intervals and the results reported in this Chapter are averaged over 4 – 8 ns. Our BCP results were compared with simulations performed on homopolymer systems with the same set of EO:Li ratios. For such cases, the simulation strategy consisted of quenching at 600 K using NVT simulation followed by annealing to 350 K and NPT runs at 350 K.

7.2.2 Quantification of Structural Properties

We analyze the structural properties of the block copolymer melt at both the global (averaged over the entire system) level as well as at the spatially local level. Below, we provide a brief description of the global and local structural quantities that were probed:

7.2.2.1 Global Structural Quantities

1. *Structural Coordination*: Coordination behavior between any two types of atoms (α and β) were quantified as a function of distance between the atoms using the radial distribution functions ($g_{\alpha\beta}(r)$). To identify the influence of type of domain in the BCP melt (PS/PEO) on the coordination, RDFs between different types of atoms were also computed

in the PS and PEO domains separately. For computing the RDF in the individual domain, the volume of the bin was calculated separately for each reference atom, since periodic boundary conditions are not imposed in the z-direction. The elemental "ideal" volume of the spherical cap ($dV(r)$) at a distance r from each reference atom is then computed using $dV(r) = (2\pi r\,(r + |z_{int} - z_i|)dr)$, where z_{int} and z_i represent the z coordinates of the nearest interface and the reference particle respectively. We cut-off the RDF at a distance equal to half the domain width. Further, the average number of neighbors of β around any species α, at a specific distance was quantified using the coordination number ($n_\beta(r)$):

$$n_\beta(r) = \rho_\beta \int_0^r 4\pi \bar{r}^2 g_{\alpha\beta}(\bar{r}) d\bar{r}, \tag{7.3}$$

where ρ_β denotes the density of particles of type β.

2. *Li-PF_6 Aggregates*: Prior experiments and simulations [240, 295] have studied salt doped polymer electrolytes, and have reported the formation of anion–cation aggregates of different net charges which influence the transport properties and net conductivity in such systems. To identify the influence of microphase segregation on such features, we quantified the ion aggregates through two related measures. For this purpose, we identify a Li^+-PF_6^- ion pair to be connected if they are present in the first coordination shell ($r \leq r_c = 4.5$ Å based on the RDFs in homopolymer melts). Subsequently, we quantified the resulting aggregates through the following measures: (i) An *aggregate* of size $N(s)$ is identi-

fied as containing exactly $s-1$ anions (cations) around any given Li^+ ($PF_6{}^-$) ion. Within such a classification, we further characterize two types of ion aggregates: (a) Those formed by the coordination of different number of anions around any given cation such as: Li^+, $Li(PF_6)$, $Li(PF_6)_2^-$, $Li(PF_6)_3^{2-}$ etc.; and (b) Those formed by the coordination of different number of cations around any given anion: $PF_6{}^-$, $Li(PF_6)$, $Li_2^+PF_6$, $Li_3^{2+}PF_6$ etc. Explicitly, we use the notation, $N(s)$ to denote ion aggregates of the form $Li(PF_6)_{s-1}$ and $Li_{s-1}PF_6$which contain exactly $(s-1)$ $PF_6{}^-$ (or Li^+) centers within the prescribed cutoff distance ($r_c \leq 4.5$ Å) on an average around the Li^+ cation ($PF_6{}^-$ anion). In this notation, $s=1$ quantifies the number of lithium cations ($PF_6{}^-$ anions) which are devoid of any counterion within its first coordination shell; (ii) To supplement the "aggregate" results, we also effected an alternate analysis which sought to identify connected structures which do not isolate a single ion. The resulting aggregates are termed as "clusters," and the corresponding definition and results for such quantities are also presented.

7.2.2.2 Local Structural Quantities

As a consequence of microphase separation of BCPs, the coordination and ion distribution characteristics are expected to exhibit an inhomogeneity. To quantify such details, the local properties of the BCP electrolyte were analyzed as a function of the distance ($|z-z_i|$) from the interface, where

z_i denotes the interfacial positions and z denotes the distance in the plane normal to the interface. For such analysis, three separate regions of equal volume were defined: (i) "Near the interface", defined by coordinates $\{0 \leq |z - z_i|/D \leq 0.05\}$; (ii) In the "bulk of the domain" defined as $\{0.30D \leq |z - z_i|/D \leq 0.35D\}$ and; (iii) "Between the bulk and interface" defined as $\{0.15D \leq |z - z_i|/D \leq 0.20D\}$, where D represents the average domain width. For such local quantities, we present the results obtained individually in the PEO and PS domains along with those averaged over both the domains.

7.3 Results and Discussion

7.3.1 Mass Density Profiles

In this section, we discuss the results for the overall structural characteristics arising in our simulations for ion containing phase-separated BCP system. Figure 7.4(a) displays a snapshot of the equilibrated Li-PF_6 doped PS-PEO system (see caption of Figure 7.4 for legends), wherein both the lamellar structure of the BCP and the preferential segregation of the ions to the PEO domain are evident. Figure 7.4(b) displays the corresponding mass density profiles of various components of the block copolymer as a function of distance along the box. It is seen that the density profiles for both PS and PEO exhibit a sinusoidal nature consistent with the expectations for phase-separated block copolymer melts, and moreover the Li^+ ions are seen to be localized in the PEO domain. Explicitly, for the depicted case of EO:Li=20:1, the total fraction of Li^+ ions in PEO and PS phases were found to be 0.75

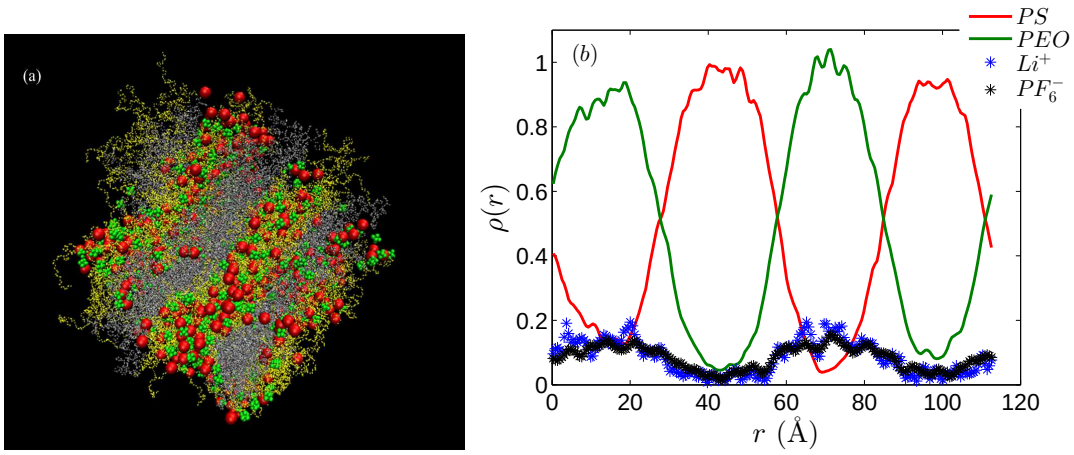

Figure 7.4: (a) Snapshot of the equilibrated block copolymer system. The mass densities of Lithium ions are scaled by the ratio of masses between Li and PF_6 . Yellow represents PEO domain, Silver represents PS domain, Red represents $PF_6{}^-$ ions and Green represents Li^+ ions; (b) Mass density profiles as a function of distance along the box. The results presented correspond to a salt concentration of EO:Li=20:1.

and 0.25 respectively, whereas the fraction of $PF_6{}^-$ centers in PEO and PS phases were found to be 0.68 and 0.32. Such a preferential segregation of Li^+ ions to PEO domains can be attributed to the partial negative charges of the oxygen atoms which attracts the cation. The counterions ($PF_6{}^-$) closely follow the density profile of the Li^+ ions as a consequence of the strong electrostatic interactions between the cations and anions in the system.

Figure 7.5 displays the fraction of cations and anions residing in the PEO and PS phases for different salt concentrations. It can be observed from Figure 7.5(a) that the fraction of Li^+ residing in the PEO phase decreases and correspondingly the fraction of Li^+ residing in the PS phase increases

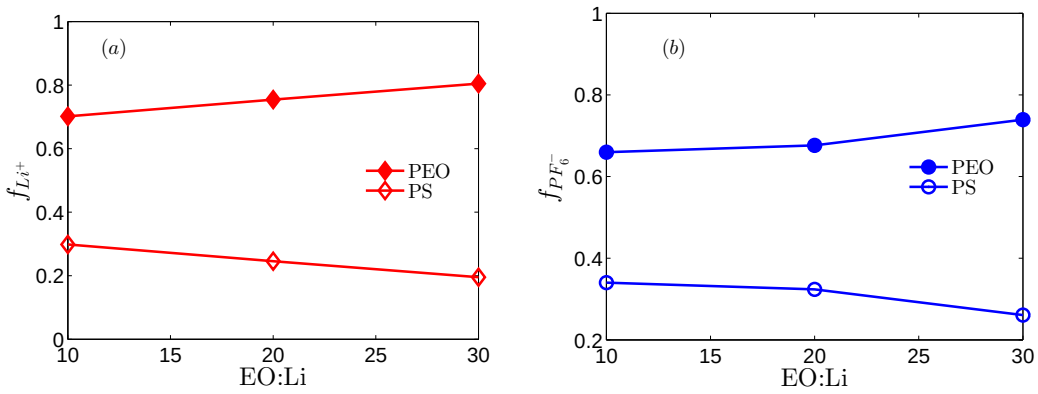

Figure 7.5: Fraction of (a) cations; and (b) anions, residing in the PEO and PS respectively.

with increasing salt concentration. Such trends can be understood to be a consequence of the competition arising, at higher salt concentrations, from the same fixed number of coordinating EO groups available for ions in the PEO phase. We also observe that the anions follow a trend similar to that of the cations (displayed in Figure 7.5(b)), a behavior which can be rationalized based on the cation-anion electrostatic interactions.

From the above discussion it is clear that while the ions reside predominantly in the conducting phase, at the highest salt concentration almost 25 % of the ions do segregate to the nonconducting phase. Previous experiments [296–298] which investigated the effects of alignment of conducting domains in BCPs have measured the lithium ion concentration in both the conducting and non-conducting domains using Fourier Transform Infrared (FTIR) spectra. Such

measurements for salt doped copolymers showed a shift in the high wavenumber peaks to even higher wavenumbers with increasing salt concentration. Such a shift in peak was speculated to originate from the segregation of salt to the nonconducting domain at high salt concentrations. The results of Figure 7.5, lend support to such a hypothesis.

7.3.2 Salt-induced Changes in Domain Spacing

A number of previous experiments [2, 12] and theoretical models [299, 300] have concerned with the influence of salt on the the domain spacing of block copolymers. Whilst, some experiments have shown that the domain spacing can increase significantly with salt concentration [2, 12], other experiments have reported smaller magnitudes of such variations [301], and in some cases, a non-monotonic trend [302] in domain spacing with increasing salt concentration. Motivated by such observations, in this section we present our simulation results for the lamellar domain spacing as a function of salt concentration.

Figure 7.6 displays the salt concentration dependence of the ratio of the domain width of the salt doped block copolymer system, d, to that of the pure PS-PEO block copolymer system, d_0. For low salt concentrations, it is observed that there is an increase in the domain spacing with increasing salt concentrations. The magnitude of the change in domain spacing ($\approx 6\%$) is however smaller relative to those observed in the experiments of Young *et al.* [12], but is comparable to the effects seen in Chintappalli *et al.*[2] for low

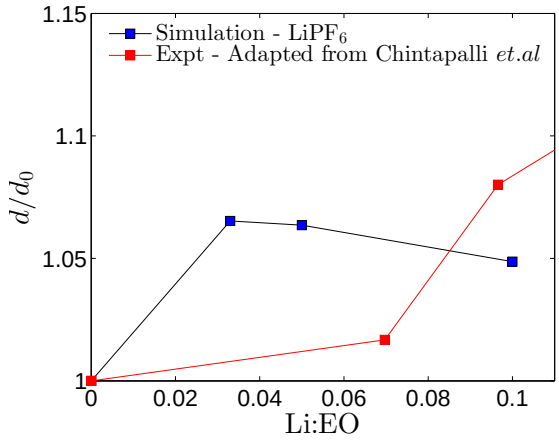

Figure 7.6: Domain spacing relative to the pure PS-PEO block copolymer. The experimental results are adapted from Chintapalli *et. al.*[2] for a low molecular weight PS-PEO block copolymer (4.9-5.5 kg mol^{-1}) doped with LiTFSI salt.

MW block copolymers. For higher salt concentrations, however, there is seen to be a nonmonotonic variation in domain spacings. Such results are qualitatively consistent with the experimental observations of Huang *et. al.* [302] for poly(a-caprolactone)-b-poly(ethylene oxide) (PCL-b-PEO) block copolymer doped with $LiClO_4$ salt. Such experimental observations were rationalized as a consequence of the enhanced segregation of the salt into the PCL phase of the block copolymer [302] — a hypothesis which is consistent with the results presented in Figure 7.5. In addition, theoretical models [300] have suggested that an enhanced propensity for ion-pairing can also lead to such nonmonotonic dependence of domain spacing on the salt loading. In a later section (Section 7.3.6) we present results which demonstrate the occurrence of significant ion pairing, especially at high salt concentrations, which may additionally contribute to the observed variations in domain spacing.

In summary, the above results serve to confirm that the introduction of salt does increase the domain spacing of the lamella of the block copolymer. However, due to the low MWs probed in our simulations, and the resulting ion segregation to the nonconducting phase and the ion pairing effects, the magnitudes of the changes in domain spacings were smaller than some of the experimental observations, and moreover, the domain spacings themselves were seen to exhibit a nonmonotonic variation as a function of salt loadings.

7.3.3 Lithium coordination with PEO molecules

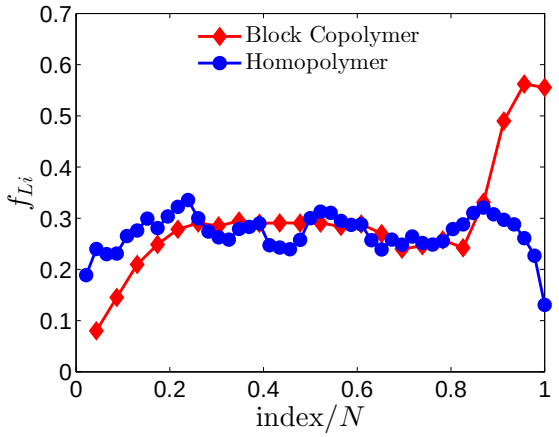

Figure 7.7: Normalized fraction of lithium ions bound to each oxygen atom of the chain relative to the total number of lithium ions in the PEO phase.

The preceding section which presented results on the density distribution of ions and polymers, demonstrated that the ions preferentially segregate into the PEO phase. However, the conformations of PEO chains in the homopolymer and BCP melt are expected to be different. Thus, it is of interest to characterize the coordination of Li^+ ions with the specific EO atoms based

on the placement of the latter groups along the chain and contrast the results for BCP with homopolymers.

Towards the above objective, we computed the fraction of the number of cations (f_{Li}), defined as the number of cations that are within the first co-ordination shell of each EO atom ($r \leq 2.4$ Å) relative to the number of cations in the copolymer (or homopolymer) system, as a function of EO monomer index along the chain. We indexed EO atoms starting at the link position, with the terminal oxygen having an index of 23 for block copolymers and 46 for homopolymers.

In Figure 7.7, we display f_{Li} as a function of the EO atom positions along the chain. For the case of homopolymers, the distribution of lithium ions across different oxygens are seen to be almost uniform, with a slight dip near the end of the chains arising from end-effects accompanying the small MW chain [295]. In contrast, in the case of block copolymers a stronger heterogeneity can be seen, with a larger fraction of Lithium ions binding with the EO segments towards the end of the PEO chain accompanied by a depletion in binding characteristics with the EO monomers in proximity to the PS-PEO link positions. Such differences arise because the oxygen atoms corresponding to the EO units near the link position are localized near the interfacial region of the lamella accompanied by a lower density of lithium ions (Figure 7.4). In contrast, the oxygen atoms towards the end of the chain are concentrated towards the bulk of the PEO domain which is characterized by a higher density of lithium ions (Figure 7.4).

7.3.4 Ion-Ion and Ion-Polymer Coordination

7.3.4.1 Comparisons between PEO homopolymers and PS-PEO Block Copolymers

In this section, we present results comparing the radial distribution functions (RDF) in the self-assembled PS-PEO block copolymer system with that of the PEO homopolymer system. For all the results discussed herein, the salt concentration is fixed at EO:Li = 20:1.

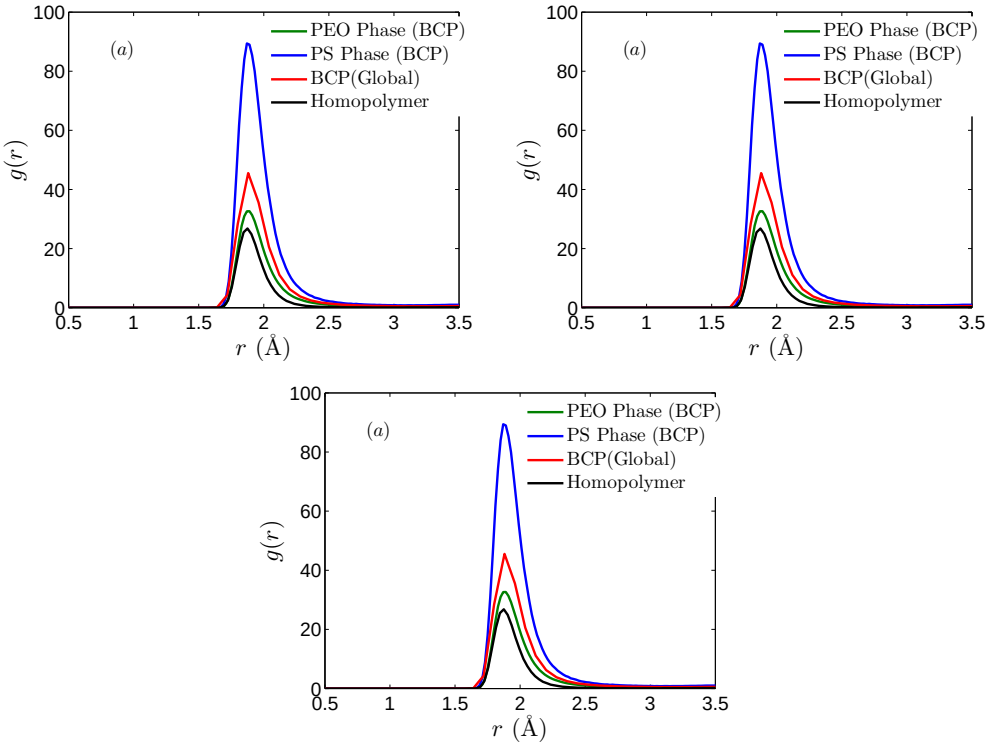

Figure 7.8: Radial distribution functions for (a) Li–O; (b) Li-PF_6 and (c) P-O in PEO and PS domain separately. For comparison, the global averaged RDF in BCP and homopolymer are also shown.

Figures 7.8(a) – (c) display the RDFs between ions and the oxygen

atoms of the ethyl oxygen (EO) groups. We present such results individually for the PS and PEO domains alongside the averaged RDF (termed "global"), and compare with the results for the PEO homopolymer (labelled "homopolymer").

Figure 7.8(a) presents the RDF for the coordination between EO atoms and the Li^+ cations, wherein a peak, corresponding to the averaged van der Waals radii of the lithium-oxygen atoms ($r_{Li–O}$ = 2.1 Å) is seen at r = 1.9 Å in both homopolymers and block copolymers. Interestingly, the *averaged* strength of coordination of Li–EO is seen to be larger in the BCPs compared to pure PEO homopolymer melts. However, upon closer examination, the intensity of Li–EO peak in the PEO domain is seen to be almost identical to the results for pure PEO homopolymer melt. In contrast, the strength of Li–EO coordination is found to be much higher in the PS domain. Such trends can be rationalized by identifying that there exists a smaller number of EO atoms in the PS domain compared to that in the PEO domain. Hence, the cations in the PS domain are more strongly bound to the available EO atoms whereas such association is more evenly distributed in the PEO domain owing to the larger number of EO atoms.

Together, the above results indicate that the coordination between the EO and Li^+ ions in the PEO domains are not influenced by the microphase segregation of the PS-PEO block copolymers. However, the averaged coordination characteristics are seen to be influenced by the interaction between EO and Li^+ ions in the PS phase.

Figure 7.8(b) displays the global and domain specific RDFs between cations and anions. In all the cases, two distinct peaks can be observed at $r = 2.9$ Å and at $r = 7$ Å. Similar to the lithium-oxygen RDF displayed in Figure 7.8(a), the cation-anion coordination is also seen to be enhanced in the PS domain compared to that in the PEO domain. To understand such results, we note that in the PS domain, the potential partners for the Li^+ ions constitute the PF_6^- ions and the smaller number of EO atoms present therein. In contrast, in PEO domain, there is a larger concentration of EO atoms, and therefore, the binding of cations is expected to be stronger with the anions in the PS domain compared to that in the PEO domain. Such a coordination behavior causes the averaged (global) cation-anion RDF of BCPs to display a stronger peak compared to its homopolymer counterparts. Moreover, the peak of second shell is seen to occur at ≈ 7 Å for both the homopolymers and BCPs. The distance at which the second coordination shell occurs is approximately twice at the distance at which the first shell occurs and is seen to be uninfluenced by the microphase segregation.

In Figure 7.8(c), we display the RDFs between anions and the EO atoms. Similar to the trends observed above for cation-EO distribution, a stronger coordination between the anions and EO atoms is seen in the PS domain compared to the PEO domain. Similarly, at $r = 4$ Å, a strong coordination is seen between the anions and EO oxygens in the PS phase, whereas a very weak coordination is seen in the PEO phase. Such trends can again be attributed to the "localized," but strong P–O coordination between the

PF_6 and EO groups the PS phase in contrast to the more distributed P–O pairs in the PEO phase. As observed in the previous cases, due to the presence of strong P–O coordination in the PS phase of the BCP, the strength of the peak as seen in the averaged BCP $g(r)$ is seen to be stronger compared to the homopolymer PEO counterparts.

7.3.4.2 Effect of Salt Concentration

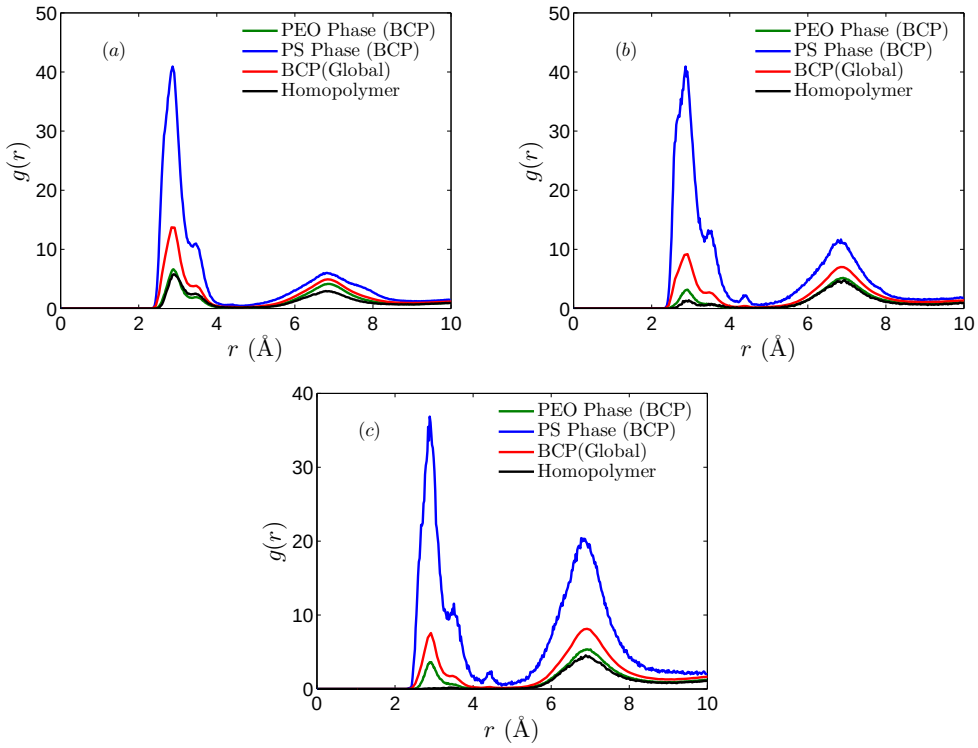

Figure 7.9: Anion-cation RDFs as a function of salt concentration for EO:Li: (a) 10:1; (b) 20:1; and (c) 30:1.

Figures 7.9(a) – (c) compares the salt concentration dependence of the cation-anion RDFs in the block copolymer melt with the corresponding ho-

mopolymer melt. While a number of features discussed in the preceding section are seen to apply, a few qualitative aspects are seen to be sensitive to the salt concentration. Explicitly, at the highest salt concentration (Figure 7.9(a)), the first peak in the Li-PF_6averaged RDF for BCPs is found to be higher than that in the homopolymer. In contrast, for the lowest salt concentration, the first peak in the Li-PF_6averaged RDF is seen to be higher in the homopolymers compared to the BCPs. In more quantitative terms, the ratio between the intensity of the first peak of the anion-cation RDF in BCP melt and homopolymer is seen to increase monotonically from a value of ≈ 0.5 at EO:Li = 30:1 to 1.4 for EO:Li = 10:1.

We rationalize the above observations as a consequence of an interplay of two factors: (a) The fraction of total salt segregated in the PS phase of the BCP; and (b) The ratio of peak heights in the Li-PF_6 RDF between the PEO phase of the BCP and the homopolymer melt. From Figure 7.5, it is seen that the fraction of cations and anions that segregate to the PS domain of the BCP increases with increasing salt concentration, suggesting that the contribution to the Li-PF_6 RDF from the PS phase increases with increasing salt concentration. Further, on comparing the Li-PF_6 RDF peaks in the PEO phase of the BCP and the homopolymer melt, it can be seen that, the peak heights for the homopolymer are either equal to or slightly greater than that in the BCP melt. Therefore, at the lowest salt concentration, since a larger fraction of cations/anions segregate into the PEO phase, and since the Li-PF_6 peak heights of the PEO phase of the BCP are slightly lower than the

corresponding values in homopolymer, the overall BCP peak is found to be lower than that of the homopolymer peak. In contrast, at the highest salt concentration, since the fraction of anions/cations that segregate into the PEO phase is lower, Li-PF_6 RDF in PS phase contributes more to the average, and renders the overall averaged BCP peak higher.

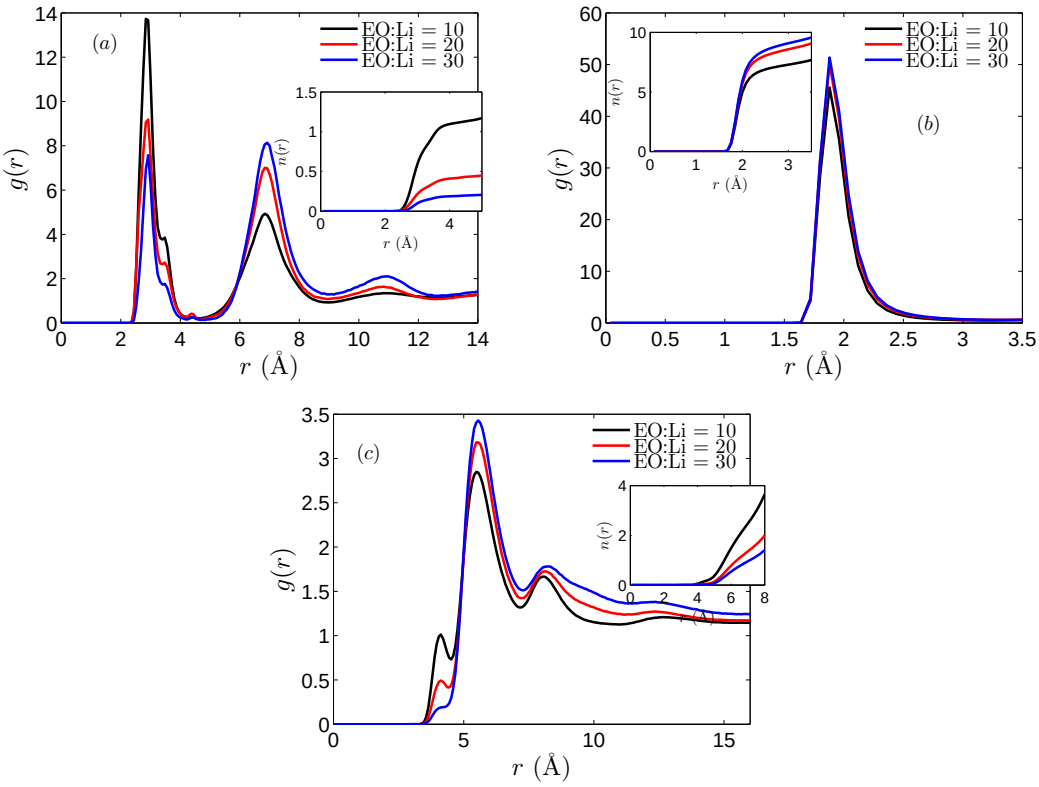

Figure 7.10: Global RDF as a function of salt concentration for (a) Li-P; (b) Li–O; and (c) P-O. Inset represents the corresponding coordination numbers, $n(r)$.

Figure 7.10 compares the cation-anion, cation-oxygen and anion-oxygen

RDFs and the corresponding coordination numbers for the three different salt concentrations investigated in the BCP melt. From the anion-cation RDF in Figure 7.10(a), it can be observed that the magnitude of Li-PF_6 peaks increase with increased salt concentration, a trend consistent with increase in the overall number density of Li-PF_6 pairs. Such results are in contrast to the results obtained for PEO homopolymer melt (cf. Figure S2(a)), wherein it is observed that the Li-PF_6 peaks reduce with increasing salt concentration. To rationalize such differences, we note that for both BCPs and homopolymers, the overall densities increase with increasing salt concentration (Table 7.3). Therefore, in the case of homopolymers, with increasing salt concentration, cations coordinate more with the oxygen atoms, thus causing the Li-PF_6 RDF peaks to reduce. In contrast, in the case of BCPs, with increasing salt concentration, the fraction of ions that are segregated into the PS phase increases, thus permitting the Li-PF_6 pairs within the PEO phase of the BCP to remain significant. Such results are consistent with the increase in magnitude of Li-PF_6 coordination in the PS phase (Figure 7.8). To support our arguments above, we quantified the number of anions coordinated with any given and are displayed in the inset of Figure 7.10(a). From the results displayed, it is seen that the Li-PF_6 coordination number in BCPs increases with increasing salt concentration — trends which match those found for PEO homopolymer melts.

Figure 7.10(b) displays the Li–O complexation at different salt concentrations. It can be seen that the Li–O coordination decreases with in-

creasing salt concentration, a result which is opposite to those displayed in Figure 7.10(a). Such trends can be understood to arise from the competition between PF_6^- and O atoms for pairing with Li^+ ions. Within such a framework, increase in the Li^+-PF_6^- ion coordination (Figure 7.10(a)) is expected to lead to a reduction in the Li–O pairing. Similar to the results discussed in the context of Figure 7.10(a), the coordination numbers of Li–O are similar to PEO homopolymer melts (Figure S2) and indicate an increase in the number of EO atoms around any given cation with increasing salt concentration. Such results which characterize the coordination behavior as a function of salt concentration demonstrate again that there is only a minor influence of microphase segregation itself on the Li–O complexation behavior in the PEO domains.

In Figure 7.10(c), the P–O RDFs are displayed for different salt concentrations. At higher salt concentrations, a weak peak is seen to emerge at a distance of ≈ 4 Å, corresponding to the average diameter of the phosphorous and oxygen atoms. In comparison with the homopolymer melt (cf. Supplementary Information, Figure S2(c)), the first peak is seen to be slightly more prominent in the case of BCP melt, with such peaks almost non-existent for EO:Li = 10:1 and 20:1 in the case of homopolymer melts. Such trends can again be understood to arise from the contributions of P–O coordinations in the PS domain of the BCP melt. In addition, a stronger peak is also observed at ≈ 6 Å, and the strength of such coordination decreases with increasing salt concentrations. Such results arise from the screening of P–O interaction due

to the increased Li–O and Li–PF_6 pairs with increasing salt concentration.

In summary, the results presented in this section indicate that the coordination between the ions and between the ions and EO atoms, are in general stronger in the PS phase compared to that in the PEO phase. Interestingly however, the coordination characteristics in the PEO domain of BCP are found to be similar to that in the pure PEO melt. Together, the combination of the preceding contributions manifest in general as stronger average coordination in the BCP system compared to that in the pure PEO melt. Further, with increasing salt concentration, the strength of the ion-ion coordination was found to increase, whereas the corresponding ion-EO coordination decreases (albeit to a smaller extent).

7.3.5 Local Structural Characteristics

7.3.5.1 Effect of Microphase Segregation

In this section, we present and discuss the *local* variations in the Li^+-$PF_6{}^-$, Li^+-EO and $PF_6{}^-$-EO RDFs in the PS and PEO phases arising from the microphase segregation of the BCP. For this section, we present the results for the highest salt concentration investigated (EO:Li = 10:1).

Figures 7.11(a) and (b) display the local variations in the Li^+–O RDF in the PEO phase and PS phase respectively. To enhance clarity, only the region near the peaks is shown in Figures 7.11(a) and (c). For the PEO phase, the strength of coordination of Li–O RDF is seen to be strongest near the "bulk" of PEO and weakens towards the PS-PEO interface. Such trends can

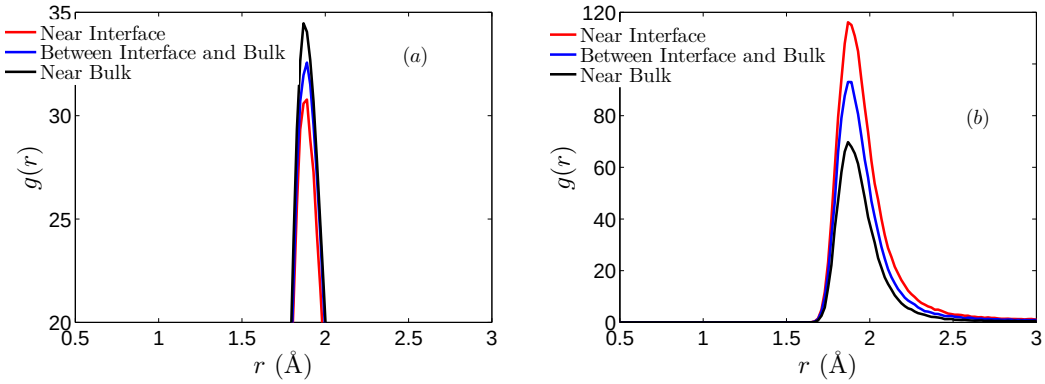

Figure 7.11: Local Li–O RDF as a function of distance from the interface for (a) PEO phase; (b) PS phase.

be rationalized based on our results and discussion presented in the context of Figure 7.7. Therein, it was observed that for BCPs the lithium ions coordinate more preferentially with the oxygen atoms in the ends of the chain. Such results are seen to be directly manifested in the Li–O coordination strength displayed in Figure 7.11(a), with the maximum coordination strength occurring near the bulk of the PEO domain and weakening progressively towards the interface. In contrast, an opposite trend is seen in the coordination between Li–O in the PS phase, with the coordination being strongest near PS-PEO interface and weakening towards the bulk of the PS domain. The number of EO group are expected to be lower in the bulk of the PS domain and hence the coordination between Li^+ and EO is also expected to be weaker in the bulk of the PS domain compared to that near the interface.

We note that at first sight, the results discussed above appear to contradict the results discussed in the context of the Li–EO coordinations in the PEO and PS phases (Section 7.3.4) wherein the peak of $g(r)$ was found to be higher in the PS phase compared to that in the PEO phase. To resolve this apparent discrepancy, we point out that two factors influence $g(r)$: the coordination numbers $n(r)$ and local density of ions or EO atoms (ρ) ($g(r)$ scaling as $n(r)/\rho$). In the context of *global* RDF between PS and PEO phase (Section 7.3.4), the overall density change in the ions between PEO and PS phases dominates that of the change in the coordination number and hence the overall $g(r)$ is higher in PS phase compared to that of the PEO phase. In contrast, the local RDFs are influenced by local ion densities and hence display behavior which appears to contradict the trends observed in global RDFs.

Figures 7.12(a) and (b) display the local RDFs for Li-P in the PEO and PS phase respectively. It is seen that the Li-PF_6 coordination strength is strongest near the interface of the PS-PEO domain, and that there is a progressive weakening towards the bulk of the PEO domain. Further, Li-PF_6 coordination strength is seen to be strongest near the bulk of PS domain and weakens towards PS-PEO interface. Overall, such trends are opposite to the Li–O RDF coordination presented in Figure 7.11(a) and can be rationalized based on the competition for coordination with Li^+ cations by both the negatively charged $PF_6{}^-$ anions and the partially negative EO atoms. A reduction in the Li–O coordination (Figure 7.11) is reflected as an increase in the Li-PF_6 coordination (Figure 7.12) and vice versa.

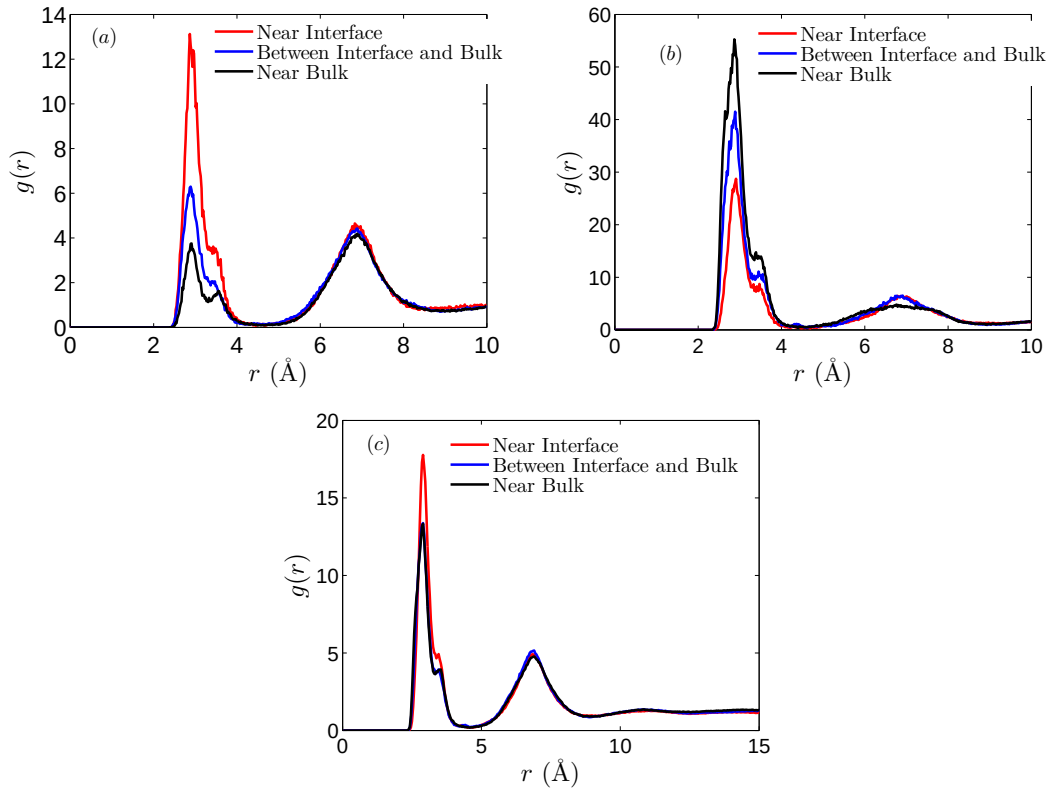

Figure 7.12: Local Li-P RDF as a function of distance from the interface for (a) PEO phase; (b) PS phase and (c) Average over both domains.

Finally, Figure 7.12(c) displays the local Li-P RDF averaged over both the domains, the results of which can be understood as a result of the weighted average of the two opposing trends in Figures 7.12(a) and (b).

In summary, the results presented in this section demonstrate that there exist a strong spatial heterogeneity in the coordination of cations with both anions and oxygen atoms. Such heterogeneities arise from the differences in coordination of lithium ions with different oxygen atoms along the chain and

the distribution of ions in the BCP. Further, the relative competition existing between oxygen and anions for the cations in both the PEO and PS phases influences the local cation-anion coordination behaviors.

7.3.5.2 Influence of salt concentration on local coordination characteristics

The local distribution of cation-anion coordination as a function of salt concentration is presented in this section. The local trends depicted by Figures 7.13(a)–(c) are seen to be qualitatively similar to those discussed in the context of overall trends (Figure 7.10). Explicitly, irrespective of the regions of consideration, the highest salt concentration (EO:Li=10:1) shows the strongest coordination. Further, by comparing Figures 7.13(a) – (c) for any given salt concentration, it can be seen that independent of the salt concentration, the magnitude of peaks decreases towards the bulk, since the lithium cations find more oxygen atoms to coordinate with and exhibits behavior consistent with the results discussed in the context of Figure 7.11.

7.3.6 Ionic Aggregates

Many earlier studies have pointed to the aggregation state of cation-anion pairs to be a quantity critical for determining the net conductivity of the polymer electrolyte. For instance, Borodin and coworkers have investigated ion aggregation in different PEO-salt complexes as a function of both temperature and salt concentration and found that the number of free cations increased with decrease in either temperature or salt concentration [295]. In this section, we

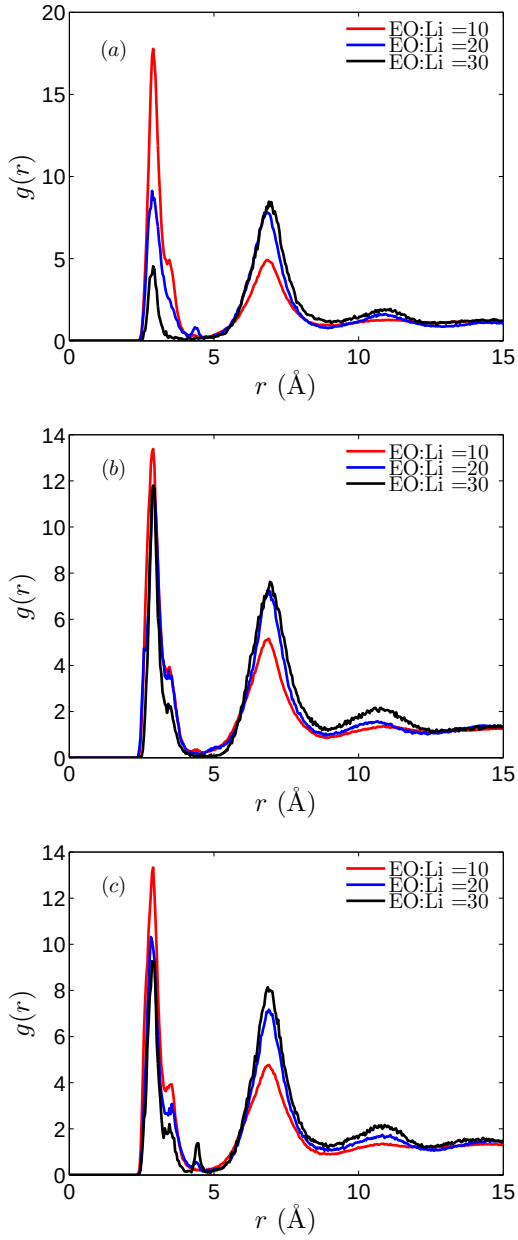

Figure 7.13: Cation-Anion RDF at (a) Near interface; (b) Middle of interface and bulk and; (c) Bulk.

characterize the influence of microphase separation upon similar features.

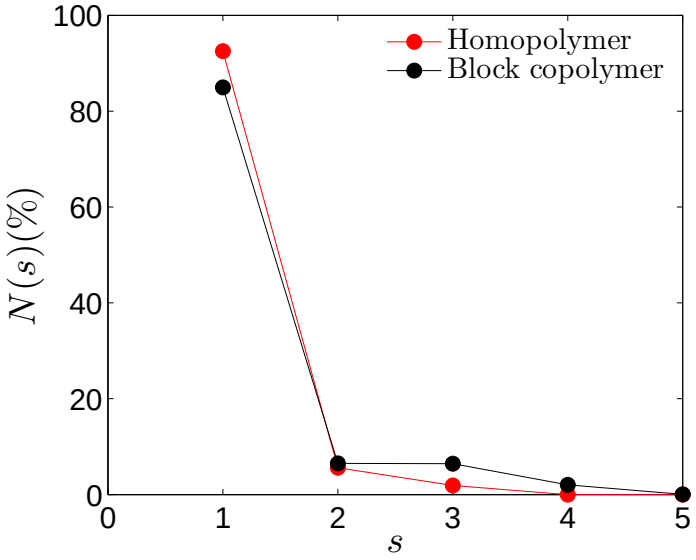

Figure 7.14: Comparison between homopolymers and BCP melts for $Li(PF_6)_{s-1}$

Figure 7.14(a) presents results comparing the fraction of PF_6 ions coordinated with cations in homopolymer and block copolymer systems. We define the latter as the ratio of number of aggregates of size s (see Section 7.2.2) to the total number of aggregates in the system. It can be seen that the fraction of free PF_6^- ions ($s = 1$) is larger in the case of block copolymers compared to that of the homopolymer. Correspondingly, a larger fraction of higher order pairs ($s > 1$) are seen in the case of homopolymers compared to that in the block copolymers. The trends observed in the above results can be rationalized based on the Li-PF_6 coordination characteristics presented in Figure 7.8(b), wherein the Li-PF_6 coordination was seen to exhibit a stronger first peak in the

BCP compared to that in the homopolymer. Consistent with such behavior, the corresponding complementary results for the $Li_{s-1}PF_6$ aggregates in homopolymer and block copolymer systems also indicate that the fraction of free ions to be higher in the block copolymer system compared to the homopolymer systems.

The above results point to a significant finding that the aggregation tendencies, and the more specifically, the fraction of free ions and charged multiplets, exhibit significant differences between BCPs and homopolymers. While experimental results for the differences between conductivities of homopolymer and BCPs have been usually explained based on polymer dynamical characteristics, our results above suggest that more detailed considerations which invoke the coordination characteristics may be necessary to obtain an accurate picture.

Figures 7.15(a) and (b) display the distribution of $Li(PF_6)_{s-1}$ and $Li_{s-1}(PF_6)$ ($s \geq 1$) pairs as a function of salt concentration in the BCP system. For all the salt concentrations investigated, free Li^+ and ${PF_6}^-$ ions are seen to dominate the aggregates. However, it can be seen that the free ions ($s = 1$) decrease with increasing salt concentration. Such results are intuitive, since increasing the number of ions is expected to lead to a stronger likelihood of forming bound pairs of cations and anions. Such reduction in free ions with increasing salt concentration is also consistent with the results of Figure 7.10(a) wherein it was showed that the Li-P coordination increased with salt concentration. While a monotonic decrease in the fraction of aggregates

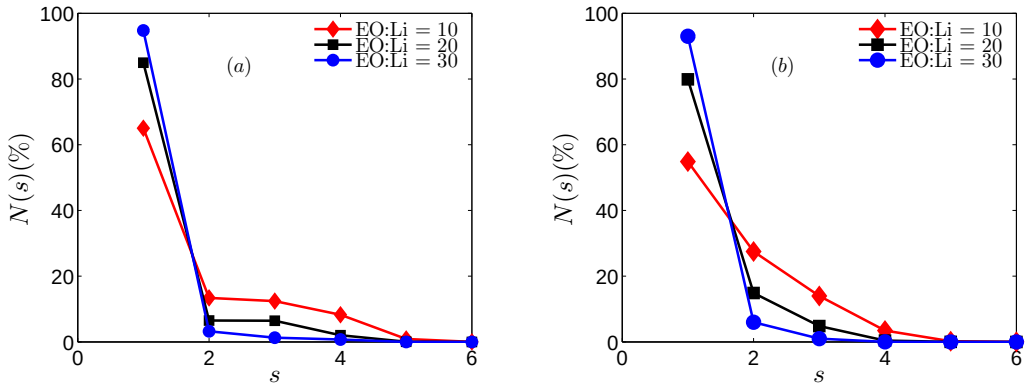

Figure 7.15: (a) Distribution of aggregates of (a) $Li(PF_6)_{s-1}$ pairs; (b) $Li_{s-1}(PF_6)$ pairs as a function of salt concentration.

with increasing aggregate size is seen for all salt concentrations investigated, the ratio between the fraction of $Li(PF_6)_2$ and $Li(PF_6)$ (and the corresponding quantities in PF_6 aggregates) are found to increase with increasing salt concentration. Such trends arise from the increase in density of the system with increasing salt concentrations, forcing the lithium cations to coordinate with more anions.

7.3.7 Cluster Analysis

An alternate characterization of aggregates were also effected through a "cluster" analysis meant to identify connected structures. For this purpose, we effected a cluster analysis using the methodology proposed by Sevick *et.al.,* [303] in which the ion pair clusters were identified through a con-

nectivity matrix. The cut-off criteria between ion-pairs was again chosen as $r_c = 4.5$ Å. Sequences Li-PF_6-Li-PF_6... and PF_6-Li-PF_6-Li... were considered as part of the same kind of clusters. Subsequently, we computed the average fractions of particles in a cluster of size s as;

$$H_s = \frac{sC_t(s)}{C_p} \tag{7.4}$$

where $C_t(s)$ and C_p represent the average number of Li-PF_6 clusters of size s and the total number of ion-pairs respectively.

We note that the quantity measured using $H(s)$ is different from Li-PF_6 aggregates or $N(s)$ as defined in Part 2 of Section 2.2.2 of main text, since $H(s)$ computes an ion-cluster (quantifying the overall aggregation) where as $N(s)$ computes the average PF_6 neighbors per Li ions (quantifying the aggregates in the first shell). To distinguish, $N(s)$ is referred to as Li–PF_6 "aggregates", whereas $H(s)$ is referred to as Li-P "clusters".

Figure 7.3.7 displays the Li-PF_6 cluster size distributions for the different salt concentrations. At the lowest salt concentration, clusters are seen to be limited to sizes less than 5 units. At larger salt concentrations, bigger clusters of the order of 10 pairs are seen to be formed in the system. However, in all cases, Li-PF_6 pair are seen to dominate the distribution. Further, at very low salt concentrations, fraction of single Li-PF_6 cluster (not shown here) dominates far more than other type of clusters. Such results can be rationalized as a direct consequence of the lower density of the system (cf. Table 1) and the smaller number of ions which reduces the number of larger aggregates.

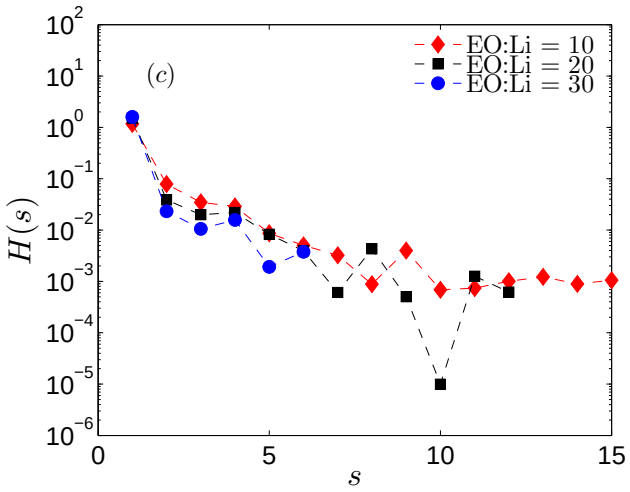

Figure 7.16: Number of clusters normalized by the total number of clusters in the system for EO:Li = 20:1.

Further, the density of the system increases with increasing salt concentration. At the largest salt concentration investigated (EO:Li=10:1), there is a larger propensity to aggregate into larger clusters owing to the crowding of ions inside the system. Such trends are reflected in the higher fraction of longer clusters (12 – 14 $LiPF_6$ pairs) for the largest ion concentration. At intermediate ion concentration, the density is not significantly larger and there does not exist sufficient ions to form larger clusters, and hence the fraction of smaller clusters (2-8) is found to be large, whereas the number of longer clusters ($\geq$ 10) is found to be small.

7.4 Summary and Outlook

In this Chapter, we reported the results of the structural characteristics of salt doped PS-PEO block copolymer. Significant changes were observed in the structural coordination of the cations in the block copolymer system due to the presence of the PS block. However, the coordination of the cations with oxygen atoms of the PEO chain was seen to be less impacted by microphase segregation. Further, the fraction of free ions was found to be smaller in the BCP compared to that of the homopolymer. Local analysis of cation-anion RDF in the PEO domain showed differences in the RDF peaks as a function of distance from the interface suggesting that there exists a spatial heterogeneity in the coordination of the lithium ions.

We also analyzed the structural properties of the block copolymer melt as a function of the salt concentration. It was observed that the cation-anion peak increased with increasing salt concentration in both the BCP and homopolymer melts. Further, the fraction of free ions reduced with increasing salt concentration in both homopolymers and block copolymers.

The above analyses give insights into the structural coordination of the ion-block copolymer system. Such structural insights are paramount in understanding the differences in the conductivity and other dynamic properties between the ion-homopolymer and ion-block copolymer systems. Analyses on the corresponding dynamical properties are discussed in the next Chapter.

Chapter 8

Ion Transport Mechanisms in Lamellar Phases of Salt–Doped PS-PEO Block Copolymer Electrolytes

8.1 Introduction

There has been a surge in the number of studies examining the properties of solid polymer electrolytes (SPEs) as membranes for lithium ions batteries [4, 5, 7, 12–14, 22, 25, 27, 275] . While many of the investigations have been concerned with homopolymer electrolytes [4, 25, 304, 305], such materials suffer from the disadvantage that properties like conductivity and mechanical strength are often inversely correlated, and hence cannot be manipulated independently [25, 305]. To overcome such a limitation, multicomponent polymers such as block copolymers [16, 17], and polymer blends [18, 19], which enable access to multifunctionality have been proposed as alternative SPEs [12, 24, 306–308]. [1]

In the above pursuit of multifunctional electrolytes, self-assembled block copolymers (BCP) consisting of alternating conducting and non-

[1]Citations: Vaidyanathan Sethuraman, Santosh Mogurampelly, Venkat Ganesan, Multiscale Simulations of Lamellar PS PEO doped with LiPF6 ions, *Soft Matter* (Under Review) 2017. Santosh Mogurampelly helped in setting up simulations and Venkat Ganesan guided the project.

conducting block(s) have emerged as especially attractive candidates [2, 12, 24, 273, 306, 308–311] . In the case of BCP electrolytes, the conducting blocks, which possess a lower glass transition temperature (T_g), act as the ion conducting pathways, whereas the nonconducting blocks, which typically possess a higher T_g, serves to provide the mechanical strength [12, 24]. A number of experiments in this regard have demonstrated that the conductivity of ions in such systems depend both on the morphology and the underlying chemistry of the conducting/nonconducting blocks [307, 312, 313]. Further, recent studies have demonstrated that ionic conductivity in block copolymers have non-trivial salt concentration dependencies [2, 307].

A number of past studies have examined the mechanisms of ion transport in homopolymer electrolytes such as PEO [295, 314–320] . Ion transport in such homopolymer electrolytes has been demonstrated to occur primarily by the motion of ions along the polymer backbone, referred commonly as "hopping motion".[295, 316] Computer simulations by Borodin *et.al.,*[240, 295] and Heuer *et.al.,* [320] have demonstrated that there primarily exist two types of hopping: (i) Intramolecular hopping wherein the ions hop along one chain; and (ii) Intermolecular hopping wherein the ions hop between chains. Further, it was shown that the hopping rates are themselves intrinsically tied to the polymer segmental dynamics.

Despite significant experimental advances in the context of BCP electrolytes, ion-transport mechanisms in BCP systems are not well understood. Coarse-grained simulations of the ion transport in BCPs have shown that there

exists a spatial heterogeneity in the polymer dynamics whose length scale is controlled by the interfacial width of the polymer [29, 311, 321]. Such heterogeneties have been argued to influence the MW dependence of conductivity of diblock and tapered copolymers [29, 234, 321]. Although, such insights have proven informative, detailed *atomistic* level studies ion transport mechanism and its relation with the morphology and structure of the BCP are still lacking. Some unresolved questions in this regard include,

1. Do ion motions in BCPs exhibit spatially heterogeneous dynamics arising as a consequence of microphase separation?

2. Is the segmental dynamics of the conducting block influenced by the microphase separation, and do such effects influence the ion dynamics?

3. How are the mechanisms of ion motion influenced by microphase separation?

4. What is the influence of salt concentration on the above-mentioned features?

Atomistic simulations of microphase separated BCPs have been largely hindered by the significant computational times involved in generating equilibrated configurations of ion-doped self-assembled BCP morphologies [30, 285, 290]. To overcome such a challenge, in a recent work [3], we presented a multiscale simulation strategy to generate equilibrium microphase segregated morphology at atomistic level. Our recent article [3] identified the influence

of microphase segregation on the equilibrium structural coordination between ions and polymers. Therein, it was shown that microphase segregation leads to stronger ion–ion and ion–oxygen backbone coordination. Further, a heterogeneity in strength of coordination between ion and atom pairs was observed as a function of distance from the lamellar interface for microphase segregated BCPs.

Motivated by the lack of understanding on ion transport mechanisms in microphase segregated BCPs, in this study, we adapted our multiscale simulation approach [3] to elucidate the ion transport mechanisms at an atomistic level in such systems. We compared such results with those observed in pure homopolymer melts, and also characterized the influence of salt concentrations. The results arising from such a study are reported in this Chapter.

The rest of the Chapter is organized as follows. Details of the simulation methodology and the different measures which are used to quantify the ion transport characteristics are presented in Section 8.2. In Section 8.3.1, the results obtained for global and local ion dynamics such as mean squared displacement and the residence time correlation of ions are compared with those obtained in the context of homopolymer melts. The mechanisms underlying ion transport in BCPs are discussed in Section 8.3.2. The effect of salt loading upon ion dynamics and the transport mechanisms are presented in Section 8.3.3. Finally, our findings are summarized in Section 8.4.

8.2 Simulation Details

In an earlier article [3], we presented a detailed exposition of the multiscale simulation technique that was employed to generate lamellar phases of ion–doped block copolymers at an atomistic level of resolution. The simulation methodology and parameters chosen for the present work are identical to our earlier work and we refer reader to Ref. 3 for more details. For completeness, we present here a short summary of the underlying ideas and elaborate on the details of the force fields in the previous Chapter.

The simulation methodology consists of three major steps: (i) Performing atomistic simulations on PS-PEO block copolymer melt (without ions) at high temperature (600 K) using TraPPE force fields [282–284] to extract the intramolecular interaction parameters for use in coarse-grained simulations; [70, 285] (ii) Performing single chain in mean field (SCMF) [287, 288, 322–324] coarse-grained simulations on diblock copolymer melts using the intramolecular interaction parameters obtained from step (i) to generate the ordered phases of block copolymers; (iii) Reintroduction of atomistic details of PS and PEO blocks and the salt ($LiPF_6$) into the microphase separated morphology [3, 62, 70, 325, 326] . Subsequently the atomistic morphology is subjected to a long NPT run (40 – 120 ns) for equilibration and analysis of ion transport properties and mechanisms.

In all the simulations, the number of chains for the BCP were fixed at 700 chains. Each chain consisted of 151 UA beads with 10 PS and 23 PEO monomeric units corresponding to a 50:50 composition of block copolymer.

Three different cases of salt concentration were studied with the ratio between the number of ethyl oxygen monomers (EO) to lithium ions (EO:Li) fixed at 10:1, 20:1 and 30:1 respectively. All the simulations were carried out at a temperature of 350K. For comparison to BCPs, pure PEO homopolymer melts were also simulated at 350K. For the latter, NPT simulation was performed on the ion-polymer system starting from random initial conditions. For comparison with the same MW PEO block, we chose PEO homopolymers consisting of 23 monomeric units. All the simulations were performed using LAMMPS [96].

A number of different measures were used to quantify the dynamics of the ions and transport mechanisms of the ions both, spatially locally, and averaged over the entire lamellar domain. We note that our simulations are effected at a low temperature of 350K to maintain the phase segregation of the BCP at the low MWs. In addition, for the sake of computational efficacy, we do not use polarizable force fields [295]. Due to these factors, the dynamics of ions in our simulations are much slower than those studied in earlier works [295], and for many of the results reported, the true long-time limit of trends are not manifest. However, despite this limitation, the influence of microphase segregation and salt concentration is evident within the time span of our simulations, and constitutes the basis of our discussion and understanding. The different measures used to quantify the ion dynamics are discussed below.

8.2.1 Mean Squared Displacements

The mobility of the ions and atoms were quantified using the mean squared displacement (MSD) of the monomers defined as:

$$\langle \mathbf{r}^2 \rangle = \sum_{i=0}^{N} \langle (\mathbf{r}_i(t) - \mathbf{r}_i(0))^2 \rangle \tag{8.1}$$

where $\mathbf{r}_i(t)$ denotes the position of the i^{th} monomer at time t and, $\langle\rangle$ denotes an ensemble average.

8.2.2 Residence Time Correlation Function

Ion transport in homopolymers has been shown to occur via ion hopping along the backbone of the conducting polymer. To characterize such transport, we quantified the ion-ethyl oxygen residence time, which is defined as the average time of coordination between the Li^+ cations and the oxygen atoms. To compute such a quantity, we consider a residence time function ($H(t)$), which is assigned a value of unity if a lithium ion is found within the first coordination shell ($r_c = 2.4$ Å) of an oxygen atom or else it is assigned a value of zero:

$$H(t) = \begin{cases} 1, & \text{if } r \leq r_c \\ 0, & \text{if } r > r_c \end{cases}$$

Subsequently, a normalized residence time autocorrelation function is obtained using:

$$A(t) = \frac{\langle H(t)H(0) \rangle}{\langle H(0)^2 \rangle}. \tag{8.2}$$

To compute the average residence time (τ_r), the above correlation function is fitted to a stretched exponential curve of the form: $\exp\left(-\left(t/\tau\right)^{\beta}\right)$, where τ

and β are fitting constants, and then, τ_r is calculated using $\tau_r = \tau\Gamma(1 + 1/\beta)$, where $\Gamma(n)$ represents the Gamma function.

8.2.3 Polymer Dynamics

As discussed in the introduction, ion transport in polymer electrolytes is believed to be tightly correlated with the dynamics of polymer segments. In this work, we consider the normalized dihedral–dihedral autocorrelation function ($C_{\phi\phi}$) to quantify the polymer segmental dynamics.

$$C_{\phi\phi} = \frac{\langle \cos(\phi(t)) \cos(\phi(0)) \rangle - \langle \cos(\phi(0)) \rangle^2}{\langle \cos(\phi(0)) \cos(\phi(0)) \rangle - \langle \cos(\phi(0)) \rangle^2} \tag{8.3}$$

where $\phi(t)$ denotes the dihedral angle of the polymer backbone. The results presented in this work correspond to the autocorrelation of CCOC dihedrals along the polymer backbone. Similar to the residence time autocorrelation function described earlier, the dihedral autocorrelation is fitted to a stretched exponential curve to extract the average segmental relaxation time, τ_ϕ.

8.2.4 Local Dynamical Characteristics

The local dynamic properties of the ions in the microphase separated BCP were analyzed as a function of the distance ($|z - z_i|$) from the interface, where z_i represents the location of the interface of the lamella and z denotes the distance in the plane normal to the interface. Interfacial positions are calculated from the PS–PEO density profiles as those locations obeying $\rho_{PS}(z) = \rho_{PEO}(z)$ (ρ_i corresponds to the normalized density of the ith component).

For the analysis of local dynamics, three separate regions of equal volume were defined: (i) "Near the interface" as defined by the region $\{0 \leq |z - z_i| \leq 0.05D\}$; (ii) In the "bulk of the domain" defined as $\{0.30D \leq |z - z_i| \leq 0.35D\}$; and (iii) "Between the bulk and interface" defined as $\{0.15 \leq |z - z_i| \leq 0.20D\}$, where D represents the average domain width. Subsequent to defining the regions of interest, the ions that are in each domain at $t = 0$ are identified. The dynamic property of the particular layer is then obtained as an ensemble average of the property of the ions that are present in the corresponding layer at $t = 0$. We present the results obtained individually in the PEO and PS domains along with those averaged over both the domains.

8.2.5 Ion–Chain Coordination

An important equilibrium feature for characterizing the mechanism of ion transport is the average number of chains to which an ion is coordinated. Ions coordinated with multiple chains during the course of simulation are expected to have slower mobilities compared to those coordinated with a single chain [295]. To quantify such characteristics, we compute the distribution of ions which are coordinated to single and multiple chains using a function $F(n)$ representing the fraction of ions which are coordinated with n number of chains and is defined as:

$$F(n) = \frac{N_{Li}(n)}{N_{Li}^t} \tag{8.4}$$

where $N_{Li}(n)$ and $N_{Li}^{t}(n)$ represent the number of ions coordinated with n chains and total number of ions. A chain is said to be coordinated with a given lithium atom, if at least one oxygen atom of the chain under consideration lies within the first coordination shell ($r < 2.4$ Å) of the given lithium atom.

8.3 Results and Discussion

8.3.1 Ion Dynamics in Block Copolymers

In this section, we present results comparing the ion transport characteristics in the lamellar phase of PS-PEO block copolymers with those in the pure PEO homopolymer.

Figure 8.1(a) compares the mean squared displacement (MSD) of lithium ions in homopolymers and block copolymers (averaged over PEO and PS domains) for a salt concentration of EO:Li = 20:1. In Figure 8.1(b) we compare the mean squared displacements of ions located respectively in PS and PEO domains to the homopolymer PEO melt. For block copolymers, the MSDs represent dynamics averaged in the directions parallel to the lamellar plane, whereas for the homopolymers, MSDs are averaged in all three spatial directions. In contrast to the previous studies on homopolymers which reported ion diffusivity values [240], in this study, we are limited by the statistics at low temperatures, and are unable to extract the long-time diffusivities (a comparison of approximate diffusivities between BCP and HP melts is presented in Section 8.3.3). However, by comparing mean squared displacements of homopolymer and BCPs, a qualitative picture of the effect of microphase

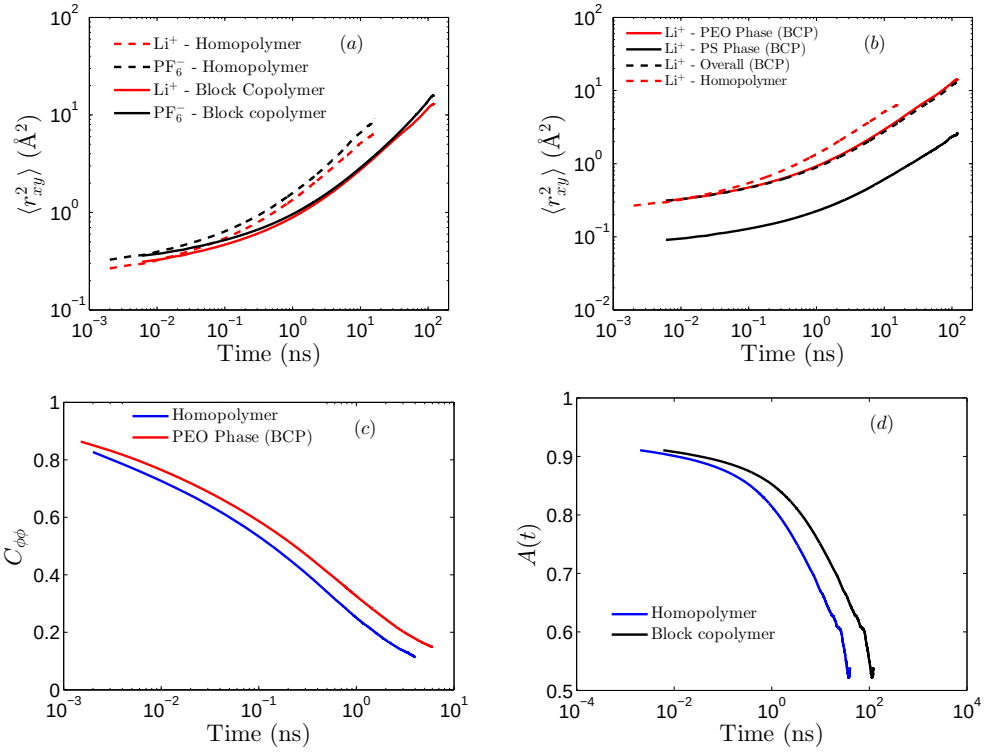

Figure 8.1: (a) Ion (Li^+) and counterion (PF_6^-) diffusivity in pure PEO melt and block copolymer. (b) Ion diffusivity in PS and PEO domains of the BCP along with that in pure PEO melt. (c) Polymer segmental dihedral-dihedral autocorrelation function. (d) Normalized residence time autocorrelation function in homopolymers and block copolymers.

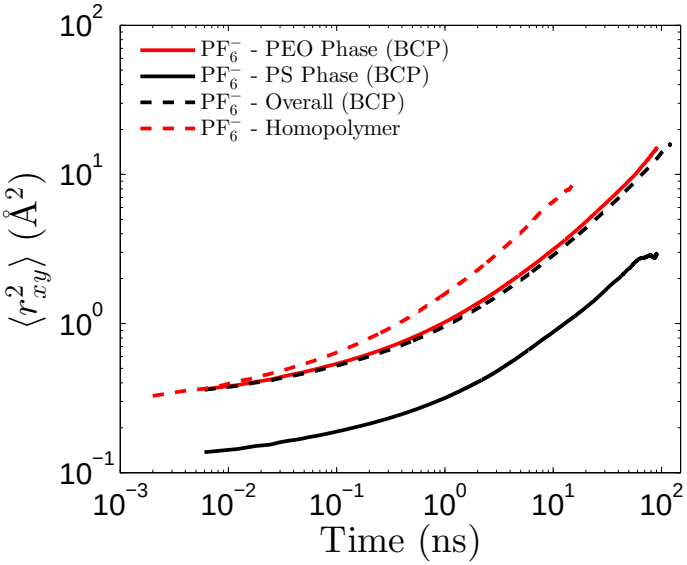

Figure 8.2: Counterion diffusion comparison.

segregation on ionic diffusivities can nevertheless be identified.

Three observations emerge from Figures 8.1(a) and (b):

(i) The MSDs of Li^+ in PS domains are seen to be significantly smaller compared to those in the PEO domain of the BCP (Figure 8.1(b)). The MSDs of PF_6^- counterions follow similar trends and are displayed in Figure 8.2. To rationalize this observation, we note that the nonconducting PS block has a higher T_g ($\approx$ 380 K) [327] compared to that of PEO ($T_g \approx$ 210 K) [328] and is hence expected to have slower dynamics. Such slower polymer dynamics is expected to lead to slower ion dynamics in the PS phase;

(ii) In both the block copolymers and homopolymers (Fig. 8.1(a)), the counterions (PF_6^-) are seen to diffuse faster compared to that of the ions (Li^+)

themselves (Figure 8.1(a)), but are slower in BCPs compared to HPs. The relative mobilities of anions and cations are consistent with earlier observations in the context of homopolymers [295]. In the context of BCPs, the coordination between lithium and PF_6^- counterions [3] coupled with the slower dynamics of Li^+ ions themselves (see (iii) below) are expected to serve as additional factors which hinder the dynamics of the anions;

(iii) Most interestingly, both the lithium ions and PF_6^- counterions are observed to diffuse slower (Figure 8.1(a)) in the block copolymer compared to that in the homopolymer. The fact that the MSDs in the PEO homopolymer melt are larger than those in the PEO domains of BCPs (Fig. 8.1(b)) demonstrates that such trends are not a result of the slow dynamics in PS phase, but instead arise as a consequence of microphase separation. Such results are broadly consistent with previous experimental observations [24] and coarse-grained simulations [29] .

To understand the origins of (iii), we note that ion transport in polymer electrolytes is expected to be intrinsically linked to the polymer segmental dynamics. Prior studies [29, 321] in this context have suggested (from coarse-grained simulations) that as a consequence of the covalent linking of the more mobile conducting block (PEO) to the slower block (PS) and the accompanying microphase separation, the dynamics of EO segments become hindered in the interfacial regions of the lamella. Such a factor has been argued in prior studies [2, 29, 234, 275, 311] to be responsible for the lower conductivities in BCP systems relative to the homopolymers.

To probe the validity of the above arguments, in Figure 8.1(c), we compare the relaxation of polymer dihedral autocorrelation function, $C_{\phi\phi}$ in the PEO phase of the block copolymer melt with those in the pure PEO homopolymer melt. From the results therein, it can be seen that the dihedral autocorrelation for the PEO phase of the BCP indeed decays much slower than that in the pure PEO melt. More explicitly, fitting a stretched exponential function yields a dihedral relaxation time (τ_ϕ) as 2.4 ns for pure PEO melt and 5.4 ns for the PEO phase in the BCP melt. Such results demonstrate polymer dynamics is indeed slower in the conductive phase in the BCP melt compared to the pure PEO homopolymer melt.

How does the slower polymer dynamics influence ion motion? Previous studies [240] have shown that ion motion in salt-doped polymer electrolytes such as PEO involves successive hops of the cations along the polymer backbone with a time scale strongly correlated to the segmental relaxation times of the polymer. To demonstrate such a correlation for our system, we consider the lithium ion–ethyl oxygen residence times, which quantifies the time over which the Li^+ cations are bound to the ethyl oxygen atom. Such residence times have been shown related directly to the time between successive ion hops, and quantifies in a direct manner the correlation between ion and polymer segmental dynamics.

Figure 8.1(d) compares the normalized residence time autocorrelation function (ACF, Equation (8.2)) for the BCP system with the corresponding results in pure homopolymer melts. Therein, it is clearly seen that the de-

cay of such correlation functions is much slower in BCP compared to the homopolymer. More explicitly, if we crudely fit the relaxation to a stretched exponential (despite the fact that ACF has not decayed sufficiently), we find that such time constant for the pure PEO melt and the BCP melt are 0.563 μs and 4.415 μs respectively, which confirms the order of magnitude slower dynamics of ions in BCPs (We note that the residence times obtained in our simulations are of the order of hundreds of nanoseconds for pure homopolymer melt in contrast to the results of the order of a few ns (10 – 50 ns) obtained by Borodin *et. al* [295]. Such differences arise as a consequence of not using any polarization interactions or charge scaling to accelerate the dynamics of the system).

Together, the results of Figs. 8.1(c) and (d) provide evidence that the slower ion dynamics in BCPs arises in turn from the slower polymer segmental dynamics and its influence on the time scale for ion hopping along the polymer backbone. As discussed above, such effects on the polymer segmental dynamics of EO segments have been argued to arise as a consequence of the covalent linking of the more mobile conducting block (PEO) to the slower block (PS) and the interfacial effects accompanying microphase separation [2, 29, 234, 275, 311] . To provide direct evidence for such a mechanism, we consider the spatial variation of ion residence correlation functions and the residence times in the PEO phase of the block copolymer melt (for EO:Li = 30:1) as a function of the distance from the interface. Explicitly, it is seen that the residence time correlation function decays slower near the interface relative to the bulk of

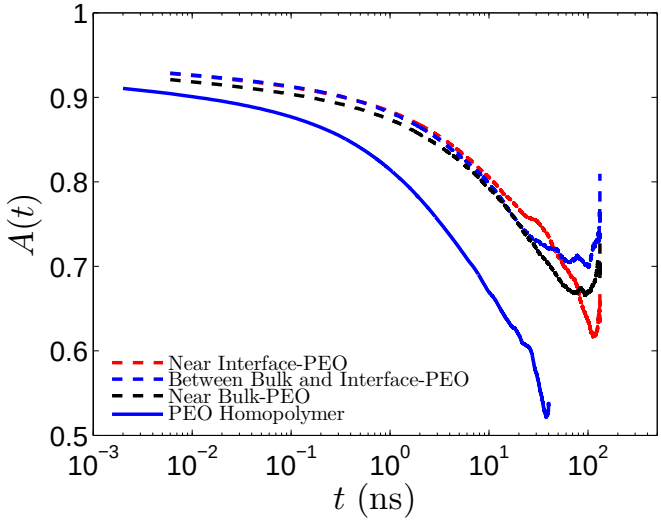

Figure 8.3: Residence time autocorrelation function as a function of time for different layers as a function of distance from interface.

the PEO phase in the BCP. Interestingly, we observe that the decay of the correlation function in the bulk of the PEO phase is still slower than that of the pure homopolymer melt. Such a result arises from the fact that the MW of the block copolymer considered in our simulations is small and the microphases correspond to moderate segregation regime. Thus, the interfacial effects arising from the glassy PS blocks are expected to be significant and extend to the bulk of the PEO phase.

Together, the results displayed in Figures 8.1(a) - (d) and Figure 8.3 demonstrate a consistent picture of ion dynamics in microphase separated block copolymers and the differences from the corresponding homopolymer systems. Explicitly, the covalent linking of the PEO blocks to the PS blocks and the accompanying microphase separation is seen to slow the dynamics

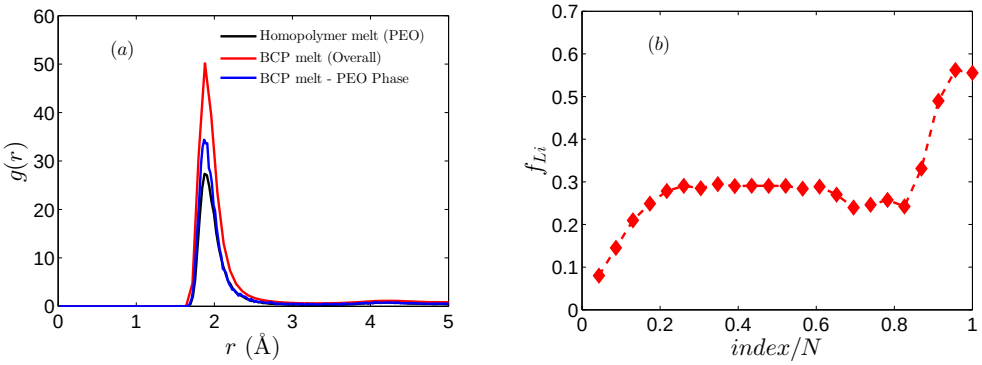

Figure 8.4: (a) Comparison of Li–O RDF in BCP melt, PEO phase of BCP melt and pure PEO melt; (b) Fraction of ions distributed as a function of the oxygen index in BCP. Both the figures are adapted with permission from Sethuraman *et.al.* (Figures 6 and 7 of original article) [3].

of EO segments in BCP phases. Such an effect is seen to directly influence ion–EO residence times underlying the hopping dynamics of the cations and the accompanying ion mobilities in BCP phases.

In concluding this section, we raise the question whether the effects noted in BCPs arise *exclusively* from the combined influence of the glassier PS block and microphase separation upon PEO segmental dynamics. To address this issue, we recall the results from our previous work on the equilibrium characteristics of ion-doped BCP melts (Figure 8.4(a)) which showed that the binding of the cations with ethyl oxygens are stronger in BCP melt compared to that in homopolymer melt. Such a stronger binding of ions with the backbone is also expected to contribute to a slower polymer dynamics and larger ion residence times. Similarly, in our previous work [3], it was shown that the number of oxygen atoms that surround lithium atoms is more near the

bulk of the PEO phase when compared to those near the PS-PEO interface (reproduced in Figure 8.4(b)). Such a higher density of oxygens near the bulk endows a higher propensity for the lithium ions to move to the neighboring oxygen atoms, thus causing lower residence times in the bulk of PEO domains. Such results suggest that the dynamics of the ions are also likely to be influenced by the changes in equilibrium cooordination characteristics arising from microphase separation in addition to changes in the PEO segmental dynamics. Unfortunately, in realistic simulations such as pursued in our study, it is not possible to decouple the effects arising from such equilibrium coordination behavior and the dynamical asymmetry inherent in the blocks.

8.3.2 Ion Transport Mechanisms in Block Copolymers

The preceding section presented results for the local and global dynamics of ions in block copolymers as quantified through the mean-squared displacements and residence time correlations. In this section, we present results which provide insights into whether the modes of ion transport are themselves influenced by the microphase separation of the BCP.

To quantify different modes of ion transport in BCPs, we adopt the methodology used by Borodin *et.al.,* [295] for homopolymers. Explicitly, during the simulations, a fraction (chosen as 10 % in our study) of the entire lithium ions are screened for the presence of an oxygen atom (or anions) in its first coordination shell every 6 ps. Such a fraction corresponds to 30 – 161 lithium atoms for the case of block copolymer salt ratios under consideration.

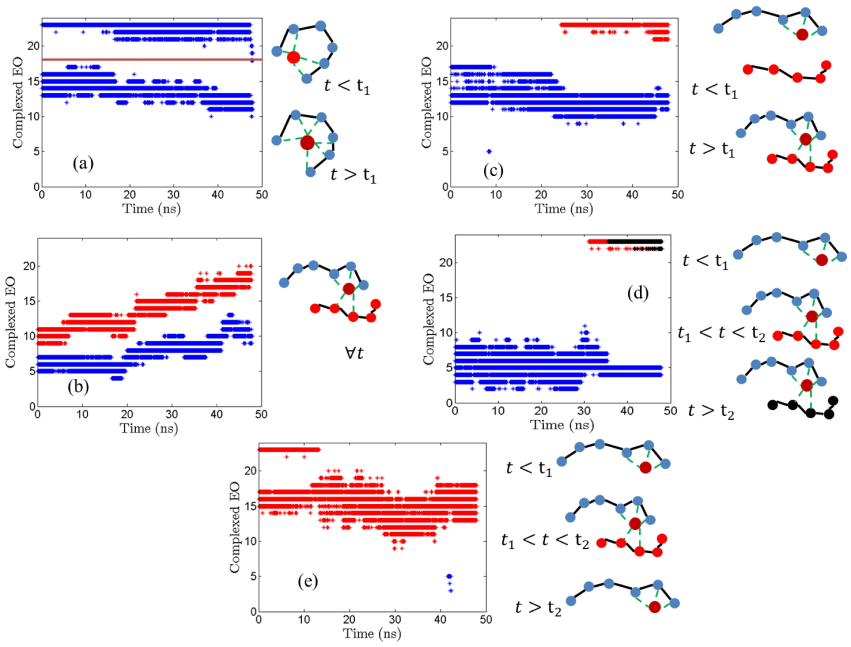

Figure 8.5: (a) Intramolecular hopping; (b) Hopping along two chains; (c) Hopping along chain one and switching to chain two while continuing its attachment with chain one; (d) Hopping to chains two and three while keeping its initial attachment with chain one; (e) Transient hopping to chain two and back to chain one. The figures to the right of the plot are cartoons depicting the respective mechanism.

An oxygen atom or PF_6^- anion is said to be in the vicinity of a lithium ion if such atoms are within the first coordination shell of the lithium ion for a period of atleast 30 ps every 60 ps window. The oxygen atoms of every chain to which a particular lithium ion is coordinated are then characterized as a function of time to identify the different modes of ion transport and hopping.

Figure 8.5 displays the different modes of ion transport that were observed in our block copolymer system in a representation that depicts the oxygen segments corresponding to different chains with different colors and con-

tiguous ethyl oxygens separated by solid lines. To maintain clarity, data only every 60 ps are shown in Figure 8.5. For ease of understanding, a schematic representation of various ion transport mechanisms is also shown alongside the corresponding results. Overall, five distinct mechanisms for ion hopping along the backbone of the chain were observed in the case of block copolymers.

- Type 1: Figure 8.5(a) displays an intramolecular transport mechanism wherein only one chain is involved in the transport of that particular ion (shown by blue color). Further, a solid line separates two contiguous sets of oxygen atoms (first oxygen set having indices between 10 and 16 and second oxygen set having indices between 19 and 23). In this case, the ions are within the coordination shell of the oxygen atoms of the same chain for the entire period of the simulation window. At short time scales ($t < t_1 \approx 20$ ns), the ion is complexed with only 4 of the contiguous oxygen segments (segments 23 and 11–14). The combined motion of the chain ends and the ions themselves change the complexation of ions from 4 oxygen segments to 6 segments of the same chain for $t > t_1$ (segments 20–23 and 14–16). Such a hopping is pictorially represented on the right side of the plot. *Such results have also been observed in the context of PEO HPs wherein the ions* [295].

- Type 2: Figure 8.5(b) displays the transport of ions wherein the ions are coordinated with the same two chains for the entire course of the simulation. In our analysis, a significant number of ions are linked to at least

two chains during the course of our simulations. Two distinct classes of motion were observed within this context. (i) The ions "hopped" along the backbone, *i.e.,* the oxygen segment to which the ions are coordinated changed over the simulation time as shown in Figure 8.5(b); (ii) The ions were coordinated to two chains, but were linked to the same set of oxygen segments for the entire duration of simulation (not shown here). *Again, in the context of homopolymers, similar ion transport mechanism wherein the ions are coordinated to two separate chains were observed* [295].

- Type 3: Figure 8.5(c) displays the case wherein the ions are initially coordinated with single chains until about 25 ns ($t < t_1$), subsequent to which the ions become complexed by multiple chains for the rest of the simulation. Such mechanisms were also observed in the context of our homopolymer systems. *However, in the case of homopolymers, the number of such events were smaller compared to those in BCP melts.* Such results indicate that the conformational arrangement of the chains in the lamellar microphases facilitate enhanced transitions from single chain to multiple chain based hopping mechanism. Such conclusions are also supported by results presented in Fig. 8.6(b) and (c) below.

- Type 4: Figure 8.5(d) displays a case wherein the ions are linked to one chain until $t = t_1 = 30$ ns. Subsequently for a short time ($t_1 < t < t_2 = 35$ ns), ions are linked to the end segments of a different

chain. However, such coordination is short lived and the ions hop on to a different chain. Here the chain ends are found to play an important role in the intersegmental hop of ions, and was found to occur (relatively) more often than homopolymers due to the proximity of different chain ends in the lamellar phase.

- Type 5: Figure 8.5(e) displays the case wherein the ions are connected with a single chain for most of the course of simulation. However, for a very small fraction of time, transient coordinations with ($t \approx 42$ ns) other chains were also observed. In both BCPs and HPs we observed that occurrences of such cases are very rare.

While the results of Figure 8.5 presented the detailed ion transport mechanism in BCP melts and indicated qualitative similarities to the behavior in homopolymers, in Figure 8.6, we quantify such ion hops and compare the trends in BCPs with homopolymers.

In Figure 8.6a, we present the fraction of ions (with respect to the total ions in the system) that are coordinated with different number of chains over the time period of simulation. It can be seen that in both homopolymers and block copolymers, the majority of the ions are attached to either one or two chains. More interestingly, the almost quantitative agreement between HPs and BCPs indicate that microphase segregation does not change the average coordination behavior of the ions with the chains at this salt concentration. Previous works on homopolymer melts demonstrated that ions which are co-

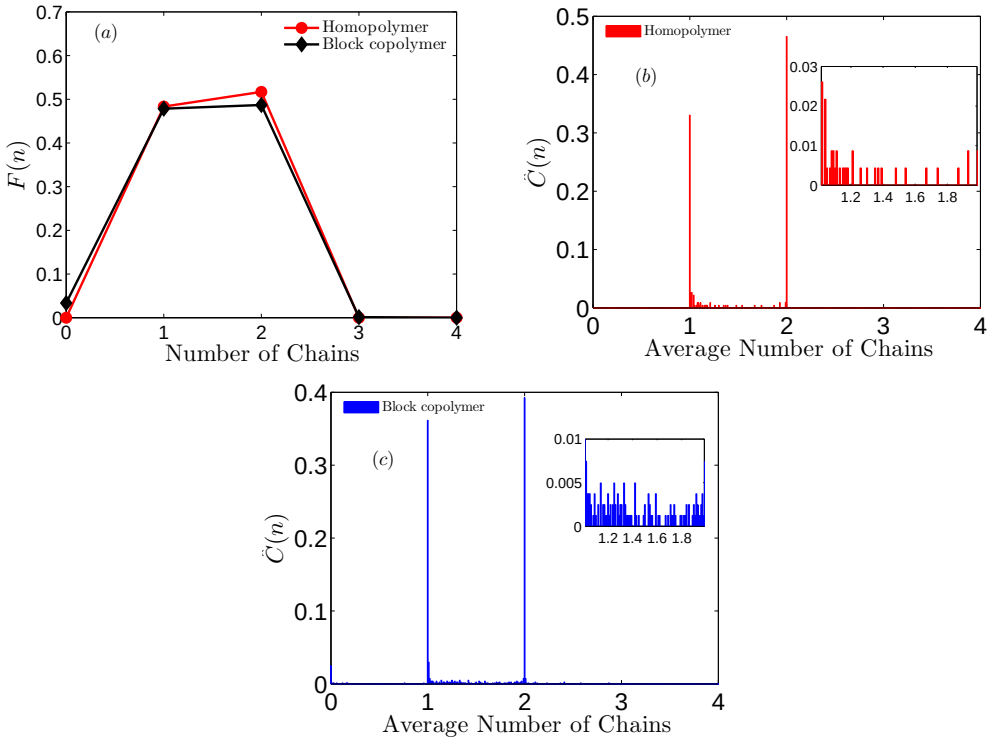

Figure 8.6: (a) Fraction of ions as a function of the number of chains to which they are coordinated. (b) Homopolymer and (c) Block Copolymer: Average based on the instantaneous state of coordination of ions. Insets to the figure shows the fraction of ions that jumped between 1 and 2 chains.

ordinated to one chain move faster compared to those coordinated with multiple chains [295]. Our results above lend support to the hypothesis that the difference in mobility of ions between HPs and BCPs do not arise from the differences in coordination of atoms with multiple chains, but by the inherently slower polymer segmental dynamics in the BCP itself as discussed in the previous section.

Figures 8.6(b) and (c) compares the coordination behaviors of HPs and BCPs based on the average of the instantaneous number of chains ($\hat{C}(n)$) an ion is coordinated. In this representation, if an ion is coordinated with 2 chains for a small period of time followed by 3 chains for the rest of the simulation, the average chain coordination will be a value between 2 and 3. In contrast, an ion which is coordinated with only one chain throughout the simulation will have a value of 1. Thus, non-integer values correspond to changes in the instantaneous number of coordination. Note that, such an analysis is different from that presented in the context of Figure 8.6(a) wherein only the fraction of ions coordinated with multiple chains are displayed.

The following observations emerge from Figures 8.6(b) and (c): (i) In both BCPs and homopolymer melts, ions which are bound to one/two chains are seen to persist in their coordination state for most of the time scale of simulation, suggesting that events leading to changes in the coordination state of the ions occur only very infrequently; (ii) Among the non-integer coordinations, the distribution of the instantaneous fraction of chains coordinated is seen to be more or less uniformly distributed between 1 and 2 chains for

BCPs (inset of Figure 8.6(c)), whereas the distribution is more biased towards the values near 1 for the case of homopolymers (inset of Figure 8.6(b)). Such results are consistent with the discussion underlying Type 3 events above and indicate that instances where ions do transform from being coordinated with single chain to becoming involved with multiple chains occur more often in BCPs relative to HPs.

The above discussion of ion hopping mechanisms pertained to the inter and intrasegmental hops along the backbone of the chain. Interestingly, in all the above five cases, the complexation of anions was rarely observed. In a few cases however, when there existed at least three anions coordinated per lithium cation, the ion motion was influenced by the motion of the complexed anion–cations. Such cases of complexation with multiple anions were not observed in the context of homopolymer melts, and likely arise as a consequence of the stronger coordination between Li and PF_6 ions in the case of BCPs when compared to homopolymer melts (Figure 4 and the results corresponding to Figure 4 in Ref 3).[3]

Overall, the above results provide a detailed description of ion hopping mechanisms in block copolymers relative to homopolymers. The mechanisms underlying ion motions were observed to exhibit similar characteristics in BCPs and HPs. However, as a consequence of the conformational effects arising from microphase separation, specific modes of transport were observed more frequently in BCP systems. Our results also indicated that in the case of block copolymer, the cations prefer to stay complexed with the backbone of

the chain rather than engaging with anions.

We note that in previous study on homopolymers [295] a mode of hopping of ions between two chains facilitated by anions was observed. However, such a mechanism was not observed in our work. In addition to the influence of microphase separation, such differences could also be a consequence (a) slower BCP dynamics in our system; and the (b) non–polarizable forcefields utilized in this study.

8.3.3 Effects of Salt Concentration

In this section, we present results characterizing the influence of salt concentration on the mobility of ions and the mechanisms accompanying ion motion in BCPs.

8.3.3.1 Dynamics of Ions and Polymers

Figure 8.7(a) compares the mean squared displacements of the lithium ions in BCP (overall) with those in pure PEO melts as a function of salt concentration. With increasing salt concentration, it can be observed that the displacement of the ions become smaller, indicating that the dynamics become slower in both block copolymers and homopolymer melts. Interestingly, the ion diffusivities in the BCP system and homopolymer PEO melts are seen to become similar for the highest salt concentrations. The latter results are broadly consistent with experimental observations which have noted that the differences in the conductivities of BCPs and homopolymers become reduced

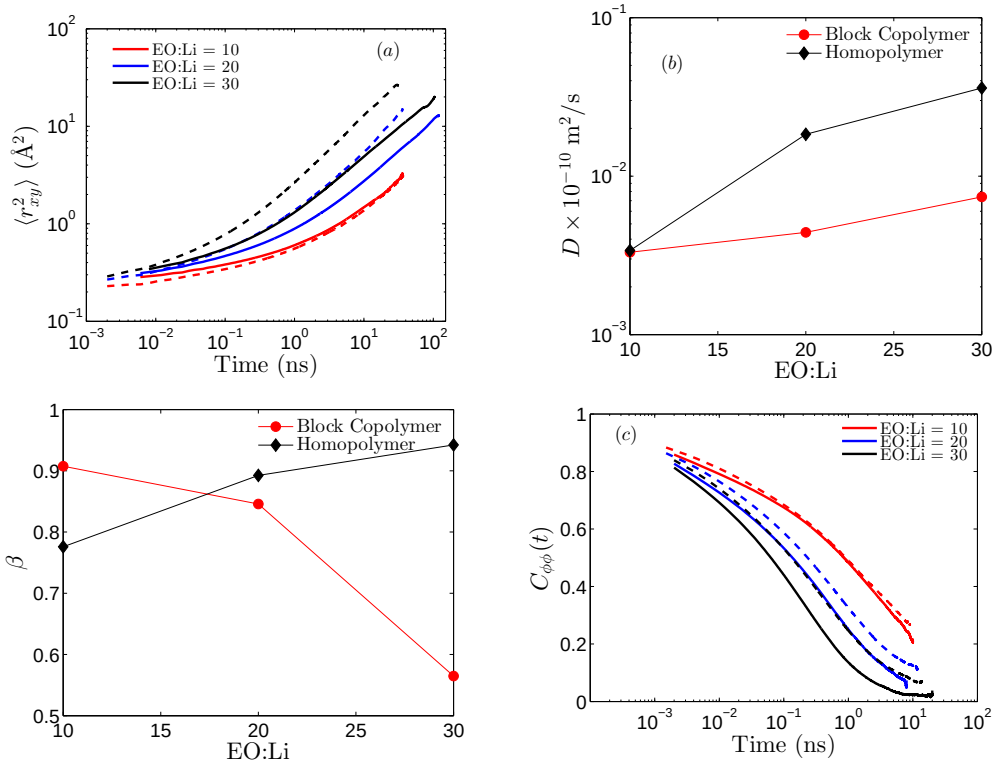

Figure 8.7: (a) Mean squared displacements as a function of salt concentration in BCP (overall) and pure homopolymer melt. Solid lines correspond to MSDs of BCP and dotted lines correspond to MSDs of PEO melt.; (b) Diffusivity values obtained from fitting to a linear plot.; (c) Slope of the MSD curves at long–time limits. (d) Dihedral–dihedral autocorrelation function as a function of salt concentration. Solid lines correspond to BCPs and dotted lines correspond to PEO homopolymer melts.

for higher salt concentrations[2].

Figure 8.7(b) compares the ion diffusivity values in homopolymer melt and BCP melt obtained from fitting the long–time MSDs to a linear function. In Figure 8.7(c), we present results which assess the approach "linearity" of the long time regime [329]. Results for the ion diffusivities of homopolymer melts are broadly in the same range as those reported in the simulations of PEO–LiTFSi melts [295]. Consistent with Figure 8.7(a), it can be seen that at lower salt concentrations, the diffusivities of homopolymers are higher than that of the BCP. In contrast, at the highest salt concentration investigated, the diffusivities of homopolymer melt and BCP becomes comparable.

To understand the above results, we again invoke the changes in polymer segmental dynamics arising as a consequence of the combined effects of microphase separation and the salt concentrations. In Figure 8.7(d), we display the polymer segmental relaxations in BCP (dotted lines) and homopolymers (solid lines) as a function of salt concentration. Therein, it can be seen that with increasing salt concentration, the polymer dynamics indeed becomes slowed in both BCP and homopolymers. Moreover, consistent with the results of Figure 8.7(a), for the highest salt concentrations, the relaxation of polymer dynamics is seen to become comparable between the homopolymer and block copolymers.

Figure 8.8 present results for the salt concentration dependence of the ion residence times. Therein can again be seen that with increasing salt concentration, the residence times of the ions with the polymer backbone increases,

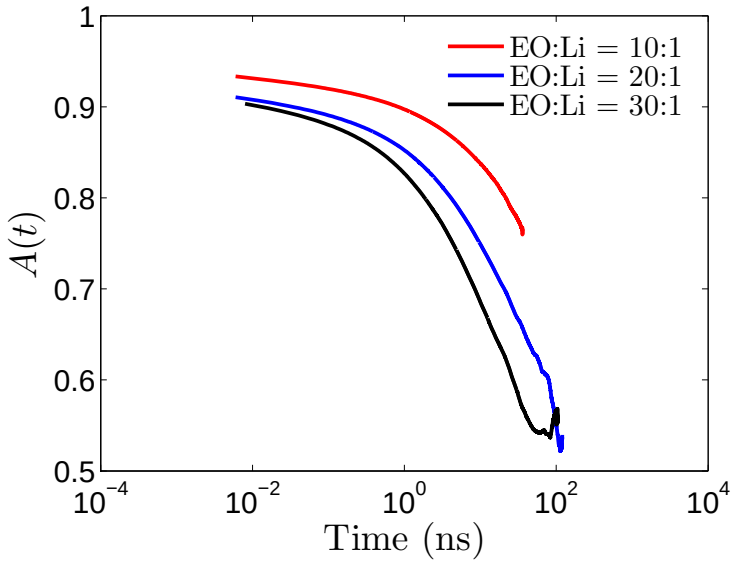

Figure 8.8: Residence time autocorrelation function as a function of salt concentration.

consistent with the slower polymer and ion dynamics.

To understand the above results, we note that with increase in salt concentrations, a larger number ions are expected to coordinate with the polymer backbone, and lead to more instances where the ions bind simultaneously to multiple polymer chains and act as a "crosslinker." Such effects are expected to manifest in both homopolymers and BCPs and hinder the dynamics of the polymer segments and correspondingly increase the relaxation times [240, 295].

Why do the differences between BCPs and HPs become mitigated at higher salt concentrations? While we do not have a conclusive resolution of this observation, based on earlier work [234, 321] we suggest that the dynamical influence of the glassy PS blocks and the microphase separation itself

becomes mitigated when the asymmetry in dynamics between the conducting and nonconducting blocks become reduced. As argued above, with increasing salt concentration the dynamics of EO segments are themselves expected to become slower, which reduces the differences in the dynamical characteristics of PS and PEO blocks, which possibly renders the influence of microphase separation less important.

In summary, in this section we presented the effects of salt concentration on ion transport in BCP lamellae. Our results indicate that an increase in the salt results in the reduction of ion mobilities. Such reduction in mobility of ions arise from the reduction in polymer segmental dynamics which in turn is arising from the cross-linking of salt with the polymer backbone. Pertinently, the ion mobilities of BCPs and homopolymers were found to be become comparable at higher salt concentrations.

8.3.3.2 Mechanisms of Ion Transport

Ion transport mechanisms were also studied as a function of salt concentration. However, for the range of salt concentrations investigated, we observe that there are no substantial differences in the ion transport mechanisms discussed in Section 8.3.2. Explicitly, with the change in salt concentration, the five distinct mechanisms that were observed in the context of the EO:Li = 20:1 (Section 8.3.2) were also observed at other concentrations. To maintain brevity, we eschew repeating the underlying features.

Figures 8.9(a)–(c) displays the instantaneous fraction of ions coordi-

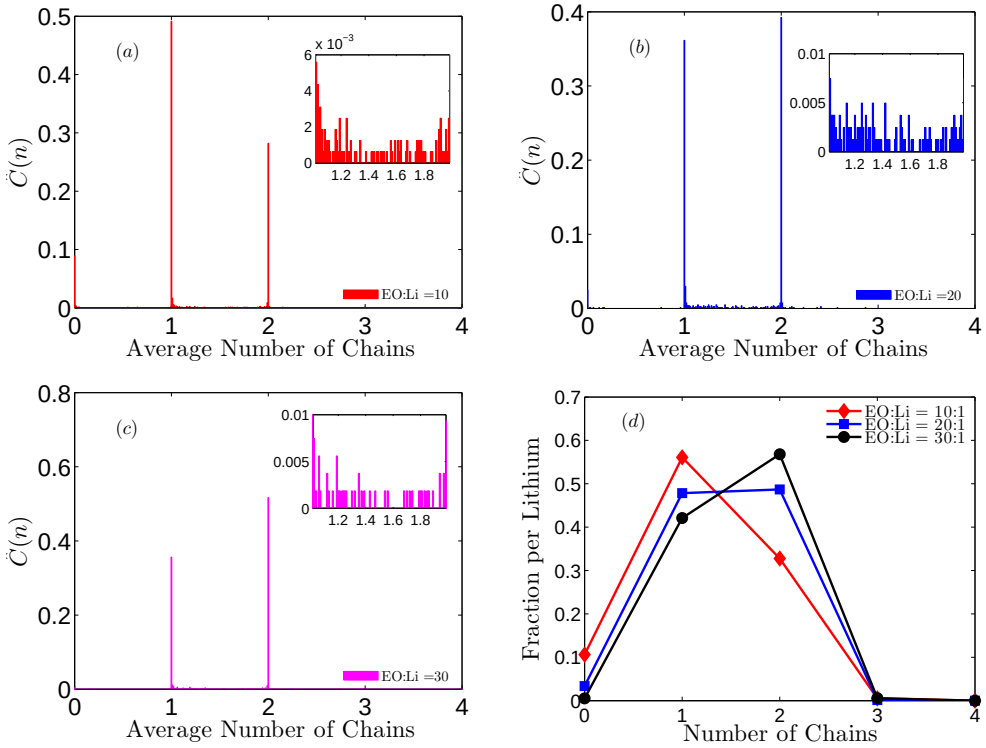

Figure 8.9: Fraction of the instantaneous number of chains coordinated for EO:Li = (a) 10:1; (b) 20:1; (c) 30:1. (d) Average fraction of ions coordinated as a function of number of chains for block copolymers.

nated with n number of chains for different salt concentrations. Therein, it can be observed that fraction of ions that are coordinated to no chains increase with increasing salt concentration. Such results indicate that with increasing salt concentration, there is an increased pairing of the cations with the anions, and can be rationalized based on the increase in strength $LiPF_6$ coordination (and the saturation of polymer backbone sites for coordination of cations) with increasing salt concentration. Accordingly, the ensemble average of the fraction of ions (Figure 8.9(d)) also shows an increase in the fraction of ions that are coordinated with no chains with increasing salt concentration. However, the distribution of jumps (insets of Figures 8.9(a)–(c)) are observed to be not sensitive to salt concentrations.

8.4 Summary

In summary, a multiscale simulation strategy was employed to understand the dynamical properties of ions in salt doped BCP melts. Specifically, we quantified the ion transport properties in the lamellar phase of block copolymer melts and compared such properties with pure PEO homopolymer melts. Our results indicate that the mean squared displacements for ions were lower in BCP melts compared to their homopolymer counterparts. Correspondingly, the ions are found to have larger residence times near the polymer backbone in BCP melts compared to homopolymer melts. Such results were rationalized based on the slower polymer segmental dynamics in BCP melts compared to homopolymer melts.

Investigations on ion transport mechanism in BCP melts revealed five different mechanisms. While the mechanisms were observed to exhibit similar characteristics in BCPs and HPs, however, as a consequence of the conformational effects arising from microphase separation, a few specific modes of transport were observed more frequently in BCP systems.

Finally, effects of salt concentrations were also studied. It was seen that increasing salt concentration leads to a reduction in the mean squared displacements and an increase in residence times. However, the differences in ion dynamics between BCPs and homopolymers were found to become reduced with increasing salt concentration.

Chapter 9

Summary and Future Work

9.1 Introduction

In this Chapter, a summary of this thesis work is presented. Subsequently, a discussion on the possible future work is also presented.

9.2 Summary and Outlook

This thesis work was mainly motivated due to the unresolved issues in the recent experimental studies on battery technology, which employed multicomponent polymers to obtain multiple desirable characteristics for the polymer electrolytes. Specifically, in the field of lithium ion batteries, an enhancement in both ionic conductivity and mechanical properties of electrolytes were observed when block copolymer membranes with asymmetric block mobilities were used as electrolytes. However, the structure-property relationships in such multicomponent block copolymer systems are poorly understood. One of the major hindrances in simulations is the significant computational time that is to required to generate equilbrated microphase segregated block copolymers at the atomistic level. In pursuit of answering the unresolved questions above, in this thesis work, we developed a multiscale simulation method which

is then employed to understand both the structure–property relationships in microphase segregated block copolymers and the ion transport mechanisms in such electrolytes.

Specifically, this thesis work explored a range of length scales (from mesoscopic to atomistic) to understand both the static structure relationships and the dynamic behavior of polymer segments and ions. To address the influence of the polymer segmental dynamics in microphase segregated block copolymer systems, we developed a coarse–grained model with non–overlapping potentials for such systems. To this end, a soft potential was initially utilized to generate the long–ranged structure. Subsequently a mapping based on renormalized one loop theory was used to map the non–bonded interaction parameters between the soft and hard potentials to generate the equilibrium self-assembled morphologies within a hard potential framework. Further, such a method was demonstrated to computationally efficient to generate self-assembled morphologies having different compositions and architectures.

The above developed coarse–grained self-assembled morphology was then utilized to understand the influence of microphase segregation on static properties such as topological entanglements and normal modes of the polymeric system in lamellar phases. It was seen that the topological entanglements increased with increasing degree of segregation. It was also seen that the number topological entanglements near the lamellar interface are higher than those near the bulk of the block copolymer phase. Further, by extend-

ing Kavassalis-Noolandi (KN) analysis within the framework of self-consistent field theory it was shown that qualitative features of the topological entanglements can indeed be identified using such analyses which is computationally less expensive compared to those obtained using molecular dynamics simulations. Normal mode analysis on microphase segregated copolymers revealed the existence of an extra confinement mode. Such a mode arises due to the link monomers at the interface.

Next, we used the coarse–grained morphology to understand the dynamics of polymer themeselves in block copolymer morphologies. Both global dynamics and spatially local dynamics as a function of the distance from the interface were characterized in such systems. Spatially resolved relaxation dynamics of the segments showed that the length scale over which dynamical inhomogeneities propagate is controlled by the interfacial width. Since the interfacial width in block copolymer systems is controlled by the degree of segregation alone and not by the molecular weight of the block copolymer (for large enough molecular weights), such results suggest that glassy blocks has a finite range of influence upon the dynamics of rubbery segments.

Further, interestingly, we saw that the local relaxation times can be modeled as a convolution of the monomer density distribution with their corresponding relaxation times is shown to provide an approximate, but accurate quantitative characterization of the average local segmental dynamics. Our results also demonstrated that monomer relaxation times is not a quantitatively accurate measure of the spatial variations in segmental dynamics. Our

results can be used in conjunction with the results from experiments on single monomer tagged dynamics which can measure the dynamics of individual monomers themselves.

From a mesoscopic perspective, it was shown that the controlling length scale for the propagation of heterogeneities is the interfacial width of the block copolymer system. However, such results do not provide a quantitative understanding of the fundamental ion transport mechanisms and its relationship with the underlying chemistry of the block copolymer system. To this end, we extended our inverse coarse–graining approach to understand such details from an atomistic perspective. A combination of coarse–graining and inverse coarse–graining techniques were employed to extract the atomistic details of the ion–doped microphase segregated block copolymer system.

We modeled a $LiPF_6$ ion doped PS–PEO block copolymer electrolyte and compared the results in such systems to those in $LiPF_6$ doped pure PEO homopolymer melt to understand the influence of microphase segregation in the structure–property relationships in polymer electrolytes. Many interesting properties were revealed at an atomistic length scale. Investigations into the structural properties of the block copolymer melt as a function of the salt concentration revealed that the cation-anion peak increased with increasing salt concentration in both the BCP and homopolymer melts. Further, the fraction of free ions reduced with increasing salt concentration in both homopolymers and block copolymers. The coordination of the cations with oxygen atoms of the PEO chain was seen to be less impacted by microphase segregation.

Further, the fraction of free ions was found to be smaller in the BCP compared to that of the homopolymer. Local analysis of cation-anion RDF in the PEO domain showed differences in the RDF peaks as a function of distance from the interface suggesting that there exists a spatial heterogeneity in the coordination of the lithium ions.

Finally, we employed a long molecular dynamics simulation to understand the ion transport mechanisms in block copolymer electrolytes and compared such results with pure PEO homopolymer electrolytes. Our results indicated that the ion diffusivity were lower in BCP melts compared to their homopolymer counterparts. Correspondingly, the ions are found to have larger residence times near the polymer backbone in BCP melts compared to homopolymer melts. Such results were rationalized based on the slower polymer segmental dynamics in BCP melts compared to homopolymer melts. Investigations on ion transport mechanism in BCP melts revealed five different mechanisms. While the mechanisms were observed to exhibit similar characteristics in BCPs and HPs, however, as a consequence of the conformational effects arising from microphase separation, a few specific modes of transport were observed more frequently in BCP systems.

Together, our results above give fundamental insights into the ion transport mechanisms in block copolymer melts. In the process, we also developed a multiscale modeling technique to generate self–assembled morphologies at multiple length scales.

9.3 Future Work

The results presented above were restricted to the lamellar phases of the block copolymer electrolyte. Further such results were applied to a specific chemistry. Below we discuss some potential directions to which the above findings can be extended. The simulation approach developed in this thesis work is very generic and can be applied to any multicomponent systems. We also discuss one such potential problem wherein the above simulation method can be applied.

9.3.1 Ion Transport Mechanisms in Block Copolymer Electrolytes with Different Morphologies and Chemistry

Very recently, experiments showed that the ionic conductivity is dependent on the morphology themselves [12]. Such results were rationalized by the changes in interfacial area between different morphologies. The techniques developed in our work for generating self–assembled phase can be easily extended to other morphologies such as cylindrical or spherical. Such analysis can shed light on the effect of curvature and interfacial area on the ion transport properties in polymer electrolytes.

A number of studies also showed that the ionic conductivity and the mechanical strength of the electrolytes are intrinsically dependent on the underlying chemical structure of the conducting and non conducting blocks [12]. The methods developed in this work can be utilized to generate self–assembled morphologies possessing different chemistry. Although, such an effort would entail

parameterizing the potentials in the coarse–grained framework, the methodology for generating the morphologies are generic enough such that transferability of the method to other underlying chemical structures will be easy. Together the above works can shed light on the influence of morphology and chemical structure on the ion transport properties in multicomponent polymeric systems.

9.3.2 Water and Salt Transport Mechanism for Water Purification Applications

Recent experimental advancements in the context of desalination, usage of sulfonated pentablock copolymer membranes showed an increase in water transport rate and high mechanical strength [271, 272, 330]. Such studies also suggested that the efficiency and the water sorption rate in the membrane is intrinsically tied to the polymer dynamics itself. The methods developed in this work can be utilized to generate the morphology which are close to equilibrium to study the water transport in such systems. Understanding such physical phenomena can then be used to "design" new materials using computer simulations which can subsequently serve as a guideline for experimental studies to formulate materials with desired transport and mechanical properties.

Appendix

Appendix 1

Derivation of Dielectric Spectra using Normal Modes

A1 Dielectric Spectra in Terms of Normal Modes

In the normal mode representation, the monomer coordinates can be expressed in terms of the normal modes [331–333] as:

$$\mathbf{R}_i(t) = \sum_{p=0}^{N-1} \Phi_{ip} \mathbf{X}_p(t) \tag{A1}$$

where R_i and X_p represent monomer and normal mode coordinates respectively. The autocorrelation of the normal modes can be generally assumed to follow a stretched exponential decay of the form:

$$\langle \boldsymbol{X}_p(t) \boldsymbol{X}_q(0) \rangle = \delta_{pq} \langle \boldsymbol{X}_p(0)^2 \rangle \exp\left(- \left(t/\tau_p\right)^{\beta_p} \right) \tag{A2}$$

where δ_{pq} represents the Kronecker delta function.

In our models we assumed that only one of the blocks of the block copolymer was dielectrically active (without loss of generality, this was assumed to be block in the segments $i = 1 \cdots N/2$. The "end-to-end" vector of the dielectrically active block, $\boldsymbol{P}_{norm}(t) = \boldsymbol{R}_{N/2}(t) - \boldsymbol{R}_1(t)$, can be expressed in terms of the normal modes using Eq. (A1) as:

$$P_{norm}(t) = \sum_{p=0}^{N-1} \boldsymbol{X}_p(t) \left[\Phi(p, N/2) - \Phi(p, 1) \right] \tag{A3}$$

Using Eqs. (A2) and (A3) the autocorrelation function of the "end-to-end" vector of the dielectrically active block ($\rho_m(t)$) can be expressed as:

$$\begin{aligned}\rho_m(t) &= \frac{\langle \boldsymbol{P}_{norm}(t)\boldsymbol{P}_{norm}(0)\rangle}{\langle |\boldsymbol{P}_{norm}(0)|^2\rangle} \\ &= \frac{\sum_{p=0}^{N-1}\langle \boldsymbol{X}_p^2(0)\rangle \left[\Phi(p,N/2)-\Phi(p,1)\right]^2 \exp\left(-\left(t/\tau_p\right)^{\beta_p}\right)}{\sum_{p=0}^{N-1}\langle \boldsymbol{X}_p^2(0)\rangle \left[\Phi(p,N/2)-\Phi(p,1)\right]^2}\end{aligned} \tag{A4}$$

To calculate the corresponding dielectric spectra, we recall that the dielectric loss $\epsilon^{''}(\omega)$ is given by the imaginary part of the Fourier transform of the time derivative of the autocorrelation function:

$$\begin{aligned}\epsilon''(\omega) &= \kappa\Im\left[\int_0^\infty \exp(-i\omega t)\left(-\frac{d}{dt}\rho_m(t)\right)dt\right] \\ &= \kappa\Im\left[i\omega\int_0^\infty \exp(-i\omega t)\rho_m(t)dt\right]\end{aligned} \tag{A5}$$

where κ represents a constant which depends on the conductivity of the material, ω represents the frequency and $\Im$ represents the complex part.

Using Eqs. (A4) and (A5), we can write the parallel (normal) dielectric loss, ($\epsilon_n''(\omega)$) as:

$$\epsilon_n''(\omega) = \kappa\frac{\sum_{p=0}^{N-1}\rho^n(p)\Im\left[i\omega\int_0^\infty \exp(-i\omega t)\exp\left((-t/\tau)^{\beta_p}\right)dt\right]}{\sum_{p=0}^{N-1}\langle \boldsymbol{X}_p^2(0)\rangle \left[\Phi(p,N/2)-\Phi(p,1)\right]^2} \tag{A6}$$

where $\rho_p^n(t)$ denotes the time independent part of the numerator in Eq. (A4) given by,

$$\rho^n(p) = \langle \boldsymbol{X}_p^2(0) \rangle \left[\Phi(p, N/2) - \Phi(p, 1)\right]^2 \tag{A7}$$

The correlation of sum of tangent vectors of the monomers in the dielectrically active block constitute the segmental autocorrelation function. The segmental autocorrelation function can thus be defined as,

$$\boldsymbol{P}_{seg} = \sum_{p=0}^{N-1} \sum_{j=2}^{N/2-1} (-1)^j \langle \boldsymbol{X}_p(t) \rangle \left[\Phi(p, j-1) - 2\Phi(p, j) + \Phi(p, j+1)\right] \tag{A8}$$

Similarly, following the derivation of normal dielectric loss (Eqs. (A4) – (A6)), the segmental autocorrelation function can be defined as:

$$\begin{aligned}\rho_s(t) &= \frac{\langle \boldsymbol{P}_{seg}(t) \boldsymbol{P}_{seg}(0) \rangle}{\langle |\boldsymbol{P}_{seg}(0)|^2 \rangle} \\ &= \frac{\sum_{p=0}^{N-1} \sum_{j=2}^{N/2-1} \langle \boldsymbol{X}_p^2(0) \rangle \left[\Phi(p, j-1) - 2\Phi(p, j) + \Phi(p, j+1)\right]^2 \exp\left(-(t/\tau_p)^{\beta_p}\right)}{\sum_{p=0}^{N/2-1} \sum_{j=2}^{N-1} \langle \boldsymbol{X}_p^2(0) \rangle \left[\Phi(p, j-1) - 2\Phi(p, j) + \Phi(p, j+1)\right]^2}\end{aligned} \tag{A9}$$

and the corresponding segmental dielectric loss ($\epsilon_s''(\omega)$) as

$$\epsilon_s''(\omega) = \kappa \frac{\sum_{p=0}^{N-1} \rho^s(p) \Im \left[i\omega \int_0^\infty \exp(-i\omega t) \exp\left((-t/\tau)^{\beta_p}\right) dt \right]}{\sum_{p=0}^{N/2-1} \sum_{j=2}^{N-1} \langle \boldsymbol{X}_p^2(0) \rangle \left[\Phi(p, j-1) - 2\Phi(p, j) + \Phi(p, j+1)\right]^2} \tag{A10}$$

where ρ_p^s represents the time independent part of Eq. (A10) given by,

$$\rho^s(p) = \sum_{j=2}^{N/2-1} \langle \boldsymbol{X}_p^2(0) \rangle \left[\Phi(p, j-1) - 2\Phi(p, j) + \Phi(p, j+1)\right]^2 \tag{A11}$$

For $\beta_p = 1$, one may use the following identity:

$$\Im\left[\int_0^\infty \exp(-i\omega t)\exp\left(-t/\tau\right)dt\right] = \frac{\omega\tau}{1+\omega^2\tau^2} \tag{A12}$$

In our simulations, we obtain β values between 0.7 – 0.9 and thus Eq. A12 in conjunction with Eqs. (A5) – (A12) served as an excellent approximation to calculate the normal and segmental dielectric spectra.

$$\epsilon_n'' = \frac{\sum_{p=0}^{N-1}\langle \boldsymbol{X}_p^2(0)\rangle \left[\Phi(p,N/2)-\Phi(p,1)\right]^2 \frac{\omega\tau_p}{1+\omega^2\tau_p^2}}{\sum_{p=0}^{N-1}\langle \boldsymbol{X}_p^2(0)\rangle \left[\Phi(p,N/2)-\Phi(p,1)\right]^2} \tag{A13}$$

and the segmental dielectric loss ϵ_s'' can be obtained using,

$$\epsilon_s'' = \frac{\sum_{i=2}^{N-1}\sum_{p=0}^{N-1}\langle \boldsymbol{X}_p^2(0)\rangle \left[(-1)^i\Phi(p,i+1)-2\Phi(p,i)+\Phi(p,i-1)\right]^2 \frac{\omega\tau_p}{1+\omega^2\tau_p^2}}{\sum_{i=2}^{N-1}\sum_{p=0}^{N-1}\langle \boldsymbol{X}_p^2(0)\rangle \left[(-1)^i\Phi(p,i+1)-2\Phi(p,i)+\Phi(p,i-1)\right]^2} \tag{A14}$$

where $\langle \boldsymbol{X}_p^2(0)\rangle$ represents the eigenvalue of the p^{th} mode.

If the unperturbed Rouse modes were employed as the normal modes, then Eqs. (A13) and (A14) become:

$$\epsilon_n'' = \frac{\sum_{p=1}^{N-1}\csc^2(\frac{p\pi}{2N})\sin^2(\frac{p\pi}{4})\sin^2\left[\frac{1}{2}\left(\frac{p\pi}{2}-\frac{p\pi}{2N}\right)\right]\frac{\omega\tau_p}{1+\omega^2\tau_p^2}}{\sum_{p=1}^{N-1}\csc^2(\frac{p\pi}{2N})\sin^2(\frac{p\pi}{4})\sin^2\left[\frac{1}{2}\left(\frac{p\pi}{2}-\frac{p\pi}{2N}\right)\right]} \tag{A15}$$

where τ_p represents the relaxation time of the p^{th} mode. Similarly, the segmental dielectric loss is given by

$$\epsilon_s'' = \frac{\sum_{p=1}^{N-1} \tan^2(\frac{p\pi}{4}) \sin^2\left(\frac{p\pi}{N}\right) \left[\cos\left(\frac{(N-2)(N-p)\pi}{N}\right) + \cos\left(\frac{p\pi}{N}\right)\right]^2 \frac{\omega\tau_p}{1+\omega^2\tau_p^2}}{\sum_{p=1}^{N-1} \tan^2(\frac{p\pi}{4}) \sin^2\left(\frac{p\pi}{N}\right) \left[\cos\left(\frac{(N-2)(N-p)\pi}{N}\right) + \cos\left(\frac{p\pi}{N}\right)\right]^2} \quad \text{(A16)}$$

Bibliography

[1] William Humphrey, Andrew Dalke, and Klaus Schulten. VMD – Visual Molecular Dynamics. *J. Mol. Graphics Modell.*, 14:33–38, 1996.

[2] Mahati Chintapalli, Thao N. P. Le, Naveen R. Venkatesan, Nikolaus G. Mackay, Adriana A. Rojas, Jacob L. Thelen, X. Chelsea Chen, Didier Devaux, and Nitash P. Balsara. Structure and ionic conductivity of polystyrene-block-poly(ethylene oxide) electrolytes in the high salt concentration limit. *Macromolecules*, 49(5):1770–1780, 2016.

[3] Vaidyanathan Sethuraman, Santosh Mogurampelly, and Venkat Ganesan. Multiscale simulations of lamellar ps–peo block copolymers doped with lipf6 ions. *Macromolecules*, 50(11):4542–4554, 2017.

[4] Michel Armand. Polymers with ionic conductivity. *Advanced Materials*, 2(6-7):278–286, 1990.

[5] Michel Armand. Polymer solid electrolytes - an overview. *Solid State Ionics*, 910, Part 2:745 – 754, 1983.

[6] Seong Jun Jeong, Guodong Xia, Bong Hoon Kim, Dong Ok Shin, Se Hun Kwon, Sang-Won Kang, and Sang Ouk Kim. Universal block copolymer lithography for metals, semiconductors, ceramics, and polymers. *Adv. Mater.*, 20(10):1898–1904, 2008.

[7] Yossef A. Elabd and Michael A. Hickner. Block copolymers for fuel cells. *Macromolecules*, 44(1):1–11, 2011.

[8] Elizabeth A. Jackson and Marc A. Hillmyer. Nanoporous membranes derived from block copolymers: From drug delivery to water filtration. *ACS Nano*, 4(7):3548–3553, 2010.

[9] Ho-Cheol Kim, Sang-Min Park, and William D. Hinsberg. Block copolymer based nanostructures: Materials, processes, and applications to electronics. *Chemical Reviews*, 110(1):146–177, 2010.

[10] C. Berthier, W. Gorecki, M. Minier, M.B. Armand, J.M. Chabagno, and P. Rigaud. Microscopic investigation of ionic conductivity in alkali metal salts-poly(ethylene oxide) adducts. *Solid State Ionics*, 11(1):91 – 95, 1983.

[11] C. T. Black, K. W. Guarini, K. R. Milkove, S. M. Baker, T. P. Russell, and M. T. Tuominen. Integration of self-assembled diblock copolymers for semiconductor capacitor fabrication. *Applied Physics Letters*, 79(3):409–411, 2001.

[12] Wen-Shiue Young, Wei-Fan Kuan, and Thomas H. Epps. Block copolymer electrolytes for rechargeable lithium batteries. *Journal of Polymer Science Part B: Polymer Physics*, 52(1):1–16, 2014.

[13] Peter V. Wright. Electrical conductivity in ionic complexes of poly(ethylene oxide). *British Polymer Journal*, 7(5):319–327, 1975.

[14] Santosh Mogurampelly, Oleg Borodin, and Venkat Ganesan. Computer simulations of ion transport in polymer electrolyte membranes. *Annual Review of Chemical and Biomolecular Engineering*, 7(1):349–371, 2016. PMID: 27070764.

[15] Byeongmoon Jeong, You Han Bae, Doo Sung Lee, and Sung Wan Kim. Biodegradable block copolymers as injectable drug-delivery systems. *Nature*, 388(6645):860–862, August 1997.

[16] Matthew D. Green, Dong Wang, Sean T. Hemp, Jae-Hong Choi, Karen I. Winey, James R. Heflin, and Timothy E. Long. Synthesis of imidazolium aba triblock copolymers for electromechanical transducers. *Polymer*, 53(17):3677 – 3686, 2012.

[17] Matthew D. Green, Jae-Hong Choi, Karen I. Winey, and Timothy E. Long. Synthesis of imidazolium-containing aba triblock copolymers: Role of charge placement, charge density, and ionic liquid incorporation. *Macromolecules*, 45(11):4749–4757, 2012.

[18] Sipei Zhang, Keun Hyung Lee, Jingru Sun, C. Daniel Frisbie, and Timothy P. Lodge. Viscoelastic properties, ionic conductivity, and materials design considerations for poly(styrene-b-ethylene oxide-b-styrene)-based ion gel electrolytes. *Macromolecules*, 44(22):8981–8989, 2011.

[19] Matthew T. Irwin, Robert J. Hickey, Shuyi Xie, Soonyong So, Frank S. Bates, and Timothy P. Lodge. Structure–conductivity relationships

in ordered and disordered salt-doped diblock copolymer/homopolymer blends. *Macromolecules*, 49(18):6928–6939, 2016.

[20] Glenn H Fredrickson and Frank S Bates. Dynamics of block copolymers: theory and experiment. *Annu. Rev. Mater. Sci.*, 26(1):501–550, 1996.

[21] Mahati Chintapalli, X. Chelsea Chen, Jacob L. Thelen, Alexander A. Teran, Xin Wang, Bruce A. Garetz, and Nitash P. Balsara. Effect of grain size on the ionic conductivity of a block copolymer electrolyte. *Macromolecules*, 47(15):5424–5431, 2014.

[22] Thomas H. Epps, Travis S. Bailey, Ryan Waletzko, and Frank S. Bates. Phase behavior and block sequence effects in lithium perchlorate-doped poly(isoprene-b-styrene-b-ethylene oxide) and poly(styrene-b-isoprene-b-ethylene oxide) triblock copolymers. *Macromolecules*, 36(8):2873–2881, 2003.

[23] Ho-Cheol Kim, Sang-Min Park, and William D Hinsberg. Block copolymer based nanostructures: materials, processes, and applications to electronics. *Chemical reviews*, 110(1):146–177, 2009.

[24] Ashoutosh Panday, Scott Mullin, Enrique D. Gomez, Nisita Wanakule, Vincent L. Chen, Alexander Hexemer, John Pople, and Nitash P. Balsara. Effect of molecular weight and salt concentration on conductivity of block copolymer electrolytes. *Macromolecules*, 42(13):4632–4637, 2009.

[25] Jie Shi and Colin A. Vincent. The effect of molecular weight on cation mobility in polymer electrolytes. *Solid State Ionics*, 60(1):11 – 17, 1993.

[26] Scott A. Mullin, Gregory M. Stone, Ashoutosh Panday, and Nitash P. Balsara. Salt diffusion coefficients in block copolymer electrolytes. *Journal Of The Electrochemical Society*, 158(6):A619–A627, 2011.

[27] Pepa Cotanda, Guillaume Sudre, Miguel A. Modestino, X. Chelsea Chen, and Nitash P. Balsara. High anion conductivity and low water uptake of phosphonium containing diblock copolymer membranes. *Macromolecules*, 47(21):7540–7547, 2014.

[28] Kyle M. Diederichsen, Ryan R. Brow, and Mark P. Stoykovich. Percolating transport and the conductive scaling relationship in lamellar block copolymers under confinement. *ACS Nano*, 9(3):2465–2476, 2015.

[29] Venkat Ganesan, Victor Pyramitsyn, Colleen Bertoni, and Manas Shah. Mechanisms underlying ion transport in lamellar block copolymer membranes. *ACS Macro Letters*, 1(4):513–518, 2012.

[30] Michael Murat, Gary S. Grest, and Kurt Kremer. Statics and dynamics of symmetric diblock copolymers: A molecular dynamics study. *Macromolecules*, 32(3):595–609, 1999.

[31] Robert D. Groot and Timothy J. Madden. Dynamic simulation of diblock copolymer microphase separation. *The Journal of Chemical Physics*, 108(20):8713–8724, 1998.

[32] Kostas Ch. Daoulas and Marcus Müller. Single chain in mean field simulations: Quasi-instantaneous field approximation and quantitative comparison with monte carlo simulations. *J. Chem. Phys.*, 125(18):–, 2006.

[33] Qiang Wang, Paul F. Nealey, and Juan J. de Pablo. Lamellar structures of symmetric diblock copolymers: Comparisons between lattice monte carlo simulations and self-consistent mean-field calculations. *Macromolecules*, 35(25):9563–9573, 2002.

[34] Mohammed Zakaria Slimani, Angel J. Moreno, and Juan Colmenero. Heterogeneity of the segmental dynamics in lamellar phases of diblock copolymers. *Macromolecules*, 44(17):6952–6961, 2011.

[35] Mohammed Zakaria Slimani, Angel J. Moreno, and Juan Colmenero. Heterogeneity of the segmental dynamics in cylindrical and spherical phases of diblock copolymers. *Macromolecules*, 45(21):8841–8852, 2012.

[36] Mohammed Zakaria Slimani, Angel J. Moreno, Giulia Rossi, and Juan Colmenero. Dynamic heterogeneity in random and gradient copolymers: A computational investigation. *Macromolecules*, 46(12):5066–5079, 2013.

[37] Y. Fink, A.M. Urbas, Moungi G. Bawendi, John D. Joannopoulos, and Edwin L. Thomas. Block copolymers as photonic bandgap materials. *J. Lightwave Technol*, 17(11):1963–1969, Nov 1999.

[38] Mariano Campoy-Quiles, Toby Ferenczi, Tiziano Agostinelli, Pablo G. Etchegoin, Youngkyoo Kim, Thomas D. Anthopoulos, Paul N. Stavrinou, Donal D. C. Bradley, and Jenny Nelson. Morphology evolution via self-organization and lateral and vertical diffusion in polymer:fullerene solar cell blends. *Nat. Mater.*, 7(2):158–164, February 2008.

[39] Reidar Lund, Lutz Willner, Dieter Richter, Peter Lindner, and Theyencheri Narayanan. Kinetic pathway of the cylinder-to-sphere transition in block copolymer micelles observed in situ by time-resolved neutron and synchrotron scattering. *ACS Macro Lett*, 2(12):1082–1087, 2013.

[40] Kurt Kremer and Gary S. Grest. Dynamics of entangled linear polymer melts: A molecular dynamics simulation. *The Journal of Chemical Physics*, 92(8):5057–5086, 1990.

[41] MW Matsen. The standard gaussian model for block copolymer melts. *J. Phys.: Condens. Matter*, 14(2):R21–R47, 2002.

[42] F Schmid. Self-consistent-field theories for complex fluids. *J. Phys: Condens. Matter*, 10(37):8105, 1998.

[43] I. Carmesin and Kurt Kremer. The bond fluctuation method: a new effective algorithm for the dynamics of polymers in all spatial dimensions. *Macromolecules*, 21(9):2819–2823, 1988.

[44] Kenneth S. Schweizer and Arun Yethiraj. Polymer reference interaction site model theory: New molecular closures for phase separating fluids and alloys. *J. Chem. Phys.*, 98(11):9053–9079, 1993.

[45] K Binder and M Müller. Monte carlo simulation of block copolymers. *Curr. Opin. Colloid Interface Sci.*, 5(56):314 – 322, 2000.

[46] François A. Detcheverry, Huiman Kang, Kostas Ch. Daoulas, Marcus Müller, Paul F. Nealey, and Juan J. de Pablo. Monte carlo simulations of a coarse grain model for block copolymers and nanocomposites. *Macromolecules*, 41(13):4989–5001, 2008.

[47] H. Fried and K. Binder. The microphase separation transition in symmetric diblock copolymer melts: A monte carlo study. *J. Chem. Phys.*, 94(12):8349–8366, 1991.

[48] Chunxia Chen, Praveen Depa, Victoria Garca Sakai, Janna K. Maranas, Jeffrey W. Lynn, Inmaculada Peral, and John R. D. Copley. A comparison of united atom, explicit atom, and coarse-grained simulation models for poly(ethylene oxide). *The Journal of Chemical Physics*, 124(23):–, 2006.

[49] Andrew J. Schultz, Carol K. Hall, and Jan Genzer. Computer simulation of block copolymer/nanoparticle composites. *Macromolecules*, 38(7):3007–3016, 2005.

[50] Hassei Takahashi, Nabil Laachi, Kris T. Delaney, Su-Mi Hur, Corey J. Weinheimer, David Shykind, and Glenn H. Fredrickson. Defectivity in laterally confined lamella-forming diblock copolymers: Thermodynamic and kinetic aspects. *Macromolecules*, 45(15):6253–6265, 2012.

[51] Shuyan Qi and Zhen-Gang Wang. Kinetics of phase transitions in weakly segregated block copolymers: Pseudostable and transient states. *Phys. Rev. E*, 55:1682–1697, Feb 1997.

[52] Florian Müller-Plathe. Coarse-graining in polymer simulation: From the atomistic to the mesoscopic scale and back. *ChemPhysChem*, 3(9):754–769, 2002.

[53] Gregory A Voth. *Coarse-graining of condensed phase and biomolecular systems*. CRC press, 2008.

[54] P. Español and P. Warren. Statistical mechanics of dissipative particle dynamics. *Europhys. Lett.*, 30(4):191, 1995.

[55] Guojie Zhang, Kostas C. Daoulas, and Kurt Kremer. A new coarse grained particle-to-mesh scheme for modeling soft matter. *Macromol Chem and Physic*, 214(2):214–224, 2013.

[56] K. Binder and H. Fried. Asymmetric block copolymer melts near the microphase separation transition: a monte carlo simulation. *Macromolecules*, 26(25):6878–6883, 1993.

[57] Rudolf M. Füchslin, Harold Fellermann, Anders Eriksson, and Hans-Joachim Ziock. Coarse graining and scaling in dissipative particle dynamics. *J. Chem. Phys.*, 130(21):–, 2009.

[58] Robert D. Groot and Patrick B. Warren. Dissipative particle dynamics: Bridging the gap between atomistic and mesoscopic simulation. *The Journal of Chemical Physics*, 107(11):4423–4435, 1997.

[59] Chunyu Li and Alejandro Strachan. Molecular dynamics predictions of thermal and mechanical properties of thermoset polymer epon862/detda. *Polymer*, 52(13):2920 – 2928, 2011.

[60] Nima Nouri and Saeed Ziaei-Rad. A molecular dynamics investigation on mechanical properties of cross-linked polymer networks. *Macromolecules*, 44(13):5481–5489, 2011.

[61] Glenn H. Fredrickson, Venkat Ganesan, and Franois Drolet. Field-theoretic computer simulation methods for polymers and complex fluids. *Macromolecules*, 35(1):16–39, 2002.

[62] Birger Steinmüller, Marcus Müller, Keith R. Hambrecht, Grant D. Smith, and Dmitry Bedrov. Properties of random block copolymer morphologies: Molecular dynamics and single-chain-in-mean-field simulations. *Macromolecules*, 45(2):1107–1117, 2012.

[63] Xiaoyu Chen, Paola Carbone, Giuseppe Santangelo, Andrea Di Matteo, Giuseppe Milano, and Florian Muller-Plathe. Backmapping coarse-

grained polymer models under sheared nonequilibrium conditions. *Phys. Chem. Chem. Phys.*, 11:1977–1988, 2009.

[64] Berk Hess, Salvador Leon, Nico van der Vegt, and Kurt Kremer. Long time atomistic polymer trajectories from coarse grained simulations: bisphenol-a polycarbonate. *Soft Matter*, 2:409–414, 2006.

[65] Alexander P. Lyubartsev and Aatto Laaksonen. Calculation of effective interaction potentials from radial distribution functions: A reverse monte carlo approach. *Phys. Rev. E*, 52:3730–3737, Oct 1995.

[66] Sergei Izvekov and Gregory A. Voth. A multiscale coarse-graining method for biomolecular systems. *J. Phys. Chem. B*, 109(7):2469–2473, 2005.

[67] Aviel Chaimovich and M. Scott Shell. Coarse-graining errors and numerical optimization using a relative entropy framework. *J. Chem. Phys.*, 134(9):–, 2011.

[68] Dirk Reith, Mathias Pütz, and Florian Müller-Plathe. Deriving effective mesoscale potentials from atomistic simulations. *J. Comput. Chem.*, 24(13):1624–1636, 2003.

[69] Theodora Spyriouni, Christos Tzoumanekas, Doros Theodorou, Florian Mller-Plathe, and Giuseppe Milano. Coarse-grained and reverse-mapped united-atom simulations of long-chain atactic polystyrene melts:

Structure, thermodynamic properties, chain conformation, and entanglements. *Macromolecules*, 40(10):3876–3885, 2007.

[70] Giuseppe Santangelo, Andrea Di Matteo, Florian Müller-Plathe, and Giuseppe Milano. From mesoscale back to atomistic models: A fast reverse-mapping procedure for vinyl polymer chains. *The Journal of Physical Chemistry B*, 111(11):2765–2773, 2007.

[71] Martin Lìsal and John K. Brennan. Alignment of lamellar diblock copolymer phases under shear: Insight from dissipative particle dynamics simulations. *Langmuir*, 23(9):4809–4818, 2007.

[72] Shuo Chen, Nhan Phan-Thien, Xi-Jun Fan, and Boo Cheong Khoo. Dissipative particle dynamics simulation of polymer drops in a periodic shear flow. *J. Nonnewton. Fluid. Mech.*, 118(1):65 – 81, 2004.

[73] Zhonglin Luo and Jianwen Jiang. Molecular dynamics and dissipative particle dynamics simulations for the miscibility of poly(ethylene oxide)/poly(vinyl chloride) blends. *Polymer*, 51(1):291 – 299, 2010.

[74] Amitesh Maiti and Simon McGrother. Bead-bead interaction parameters in dissipative particle dynamics: Relation to bead-size, solubility parameter, and surface tension. *The Journal of Chemical Physics*, 120(3):1594–1601, 2004.

[75] SarahG. Schulz, Hubert Kuhn, Gnter Schmid, Christian Mund, and Joachim Venzmer. Phase behavior of amphiphilic polymers: A dissipa-

tive particles dynamics study. *Colloid and Polymer Science*, 283(3):284–290, 2004.

[76] C. M. Wijmans, B. Smit, and R. D. Groot. Phase behavior of monomeric mixtures and polymer solutions with soft interaction potentials. *J. Chem. Phys.*, 114(17):7644–7654, 2001.

[77] Wolfgang Paul, Do Y Yoon, and Grant D Smith. An optimized united atom model for simulations of polymethylene melts. *J. Chem. Phys.*, 103(4):1702–1709, 1995.

[78] M. Mueller and K. Binder. Computer simulation of asymmetric polymer mixtures. *Macromolecules*, 28(6):1825–1834, 1995.

[79] Gary S. Grest, Martin-D. Lacasse, Kurt Kremer, and Anshu M. Gupta. Efficient continuum model for simulating polymer blends and copolymers. *J. Chem. Phys.*, 105(23):10583–10594, 1996.

[80] Piotr Grzywacz, Jian Qin, and David C. Morse. Renormalization of the one-loop theory of fluctuations in polymer blends and diblock copolymer melts. *Phys. Rev. E*, 76:061802, Dec 2007.

[81] Jian Qin and David C. Morse. Fluctuations in symmetric diblock copolymers: Testing theories old and new. *Phys. Rev. Lett.*, 108:238301, Jun 2012.

[82] David C. Morse and Jun Kyung Chung. On the chain length dependence of local correlations in polymer melts and a perturbation theory of symmetric polymer blends. *J. Chem. Phys.*, 130(22):–, 2009.

[83] Jens Glaser, Jian Qin, Pavani Medapuram, Marcus Muller, and David C. Morse. Test of a scaling hypothesis for the structure factor of disordered diblock copolymer melts. *Soft Matter*, 8:11310–11317, 2012.

[84] Jens Glaser, Jian Qin, Pavani Medapuram, and David C. Morse. Collective and single-chain correlations in disordered melts of symmetric diblock copolymers: Quantitative comparison of simulations and theory. *Macromolecules*, 47(2):851–869, 2014.

[85] Julian C. Shillcock and Reinhard Lipowsky. Equilibrium structure and lateral stress distribution of amphiphilic bilayers from dissipative particle dynamics simulations. *J. Chem. Phys.*, 117(10):5048–5061, 2002.

[86] Vanessa Ortiz, Steven O. Nielsen, Dennis E. Discher, Michael L. Klein, Reinhard Lipowsky, and Julian Shillcock. Dissipative particle dynamics simulations of polymersomes. *J. Phys. Chem. B*, 109(37):17708–17714, 2005.

[87] Y. Maruyama S. Yamamoto and S. Hyodo. Dissipative particle dynamics study of spontaneous vesicle formation of amphiphilic molecules. *J. Chem. Phys.*, 116(13):5842–5849, 2002.

[88] E. S. Boek, P. V. Coveney, H. N. W. Lekkerkerker, and P. van der Schoot. Simulating the rheology of dense colloidal suspensions using dissipative particle dynamics. *Phys. Rev. E*, 55:3124–3133, Mar 1997.

[89] P. Malfreyt and D. J. Tildesley. Dissipative particle dynamics simulations of grafted polymer chains between two walls. *Langmuir*, 16(10):4732–4740, 2000.

[90] Florent Goujon, Patrice Malfreyt, and Dominic J. Tildesley. Mesoscopic simulation of entanglements using dissipative particle dynamics: Application to polymer brushes. *J. Chem. Phys.*, 129(3):–, 2008.

[91] Rolf Auhl, Ralf Everaers, Gary S. Grest, Kurt Kremer, and Steven J. Plimpton. Equilibration of long chain polymer melts in computer simulations. *J. Chem. Phys.*, 119(24):12718–12728, 2003.

[92] Glenn H. Fredrickson and Eugene Helfand. Fluctuation effects in the theory of microphase separation in block copolymers. *J. Chem. Phys.*, 87(1):697–705, 1987.

[93] Jian Qin, Piotr Grzywacz, and David C Morse. Renormalized one-loop theory of correlations in disordered diblock copolymers. *J. Chem. Phys.*, 135(8):084902, 2011.

[94] Shuichi Nosé S. A unified formulation of the constant temperature molecular dynamics methods. *The Journal of Chemical Physics*, 81(1):511–519, 1984.

[95] M. P. Allen and D. J. Tildesley. *Computer Simulation of Liquids*. Oxford Science Publications, 1989.

[96] Steve Plimpton. Fast parallel algorithms for short-range molecular dynamics. *Journal of Computational Physics*, 117(1):1 – 19, 1995.

[97] J. P. Wittmer, P. Beckrich, H. Meyer, A. Cavallo, A. Johner, and J. Baschnagel. Intramolecular long-range correlations in polymer melts: The segmental size distribution and its moments. *Phys. Rev. E*, 76:011803, Jul 2007.

[98] H. Meyer, J. P. Wittmer, T. Kreer, A. Johner, and J. Baschnagel. Static properties of polymer melts in two dimensions. *J. Chem. Phys.*, 132(18):– , 2010.

[99] James A. Elliott, Dongsheng Wu, Stephen J. Paddison, and Robert B. Moore. A unified morphological description of nafion membranes from saxs and mesoscale simulations. *Soft Matter*, 7:6820–6827, 2011.

[100] Aleksey Vishnyakov, Ming-Tsung Lee, and Alexander V. Neimark. Prediction of the critical micelle concentration of nonionic surfactants by dissipative particle dynamics simulations. *The Journal of Physical Chemistry Letters*, 4(5), 2013.

[101] Zbyek Posel, Zuzana Limpouchov, Karel indelka, Martin Lsal, and Karel Prochzka. Dissipative particle dynamics study of the ph-dependent behavior of poly(2-vinylpyridine)-block-poly(ethylene oxide)

diblock copolymer in aqueous buffers. *Macromolecules*, 47(7):2503–2514, 2014.

[102] O. A. Guskova and C. Seidel. Mesoscopic simulations of morphological transitions of stimuli-responsive diblock copolymer brushes. *Macromolecules*, 44(3):671–682, 2011.

[103] Karel Šindelka, Zuzana Limpouchová, Martin Lísal, and Karel Procházka. Dissipative particle dynamics study of electrostatic self-assembly in aqueous mixtures of copolymers containing one neutral water-soluble block and one either positively or negatively charged polyelectrolyte block. *Macromolecules*, 47(17):6121–6134, 2014.

[104] Chen Wang and Stephen J. Paddison. Mesoscale modeling of hydrated morphologies of sulfonated polysulfone ionomers. *Soft Matter*, 10:819–830, 2014.

[105] Arup K. Chakraborty. Behavior of a random heteropolymer in mixed solvents. *J. Chem. Phys.*, 111(11):5232–5240, 1999.

[106] C. Loison, M. Mareschal, K. Kremer, and F. Schmid. Thermal fluctuations in a lamellar phase of a binary amphiphilic solvent mixture: A molecular-dynamics study. *J. Chem. Phys.*, 119(24):13138–13148, 2003.

[107] N. A. Spenley. Scaling laws for polymers in dissipative particle dynamics. *Europhys. Lett.*, 49(4):534, 2000.

[108] Dietmar Auhl, Jorge Ramirez, Alexei E. Likhtman, Pierre Chambon, and Christine Fernyhough. Linear and nonlinear shear flow behavior of monodisperse polyisoprene melts with a large range of molecular weights. *Journal of Rheology*, 52(3):801–835, May 2008.

[109] Michael Langeloth, Yuichi Masubuchi, Michael C. Boehm, and Florian Mueller-Plathe. Reptation and constraint release dynamics in bidisperse polymer melts. *Journal of Chemical Physics*, 141(19):194904, November 2014.

[110] Umi Yamamoto and Kenneth S. Schweizer. Theory of entanglements and tube confinement in rod-sphere nanocomposites. *ACS Macro Letters*, 2(11):955–959, November 2013.

[111] Zuowei Wang, Alexei E. Likhtman, and Ronald G. Larson. Segmental dynamics in entangled linear polymer melts. *Macromolecules*, 45(8):3557–3570, April 2012.

[112] Takashi Uneyama and Yuichi Masubuchi. Multi-chain slip-spring model for entangled polymer dynamics. *Journal of Chemical Physics*, 137(15):154902, October 2012.

[113] Maria Katzarova, Ling Yang, Marat Andreev, Andres Cordoba, and Jay D. Schieber. Analytic slip-link expressions for universal dynamic modulus predictions of linear monodisperse polymer melts. *Rheologica Acta*, 54(3):169–183, March 2015.

[114] Ronald G. Larson. Looking inside the entanglement "tube" using molecular dynamics simulations. *Journal of Polymer Science Part B-polymer Physics*, 45(24):3240–3248, December 2007.

[115] Alexei E. Likhtman. The tube axis and entanglements in polymer melts. *Soft Matter*, 10(12):1895–1904, 2014.

[116] Alexei E. Likhtman and M. Ponmurugan. Microscopic definition of polymer entanglements. *Macromolecules*, 47(4):1470–1481, February 2014.

[117] Alexei E. Likhtman, Mohamad S. Talib, Bart Vorselaars, and Jorge Ramirez. Determination of tube theory parameters using a simple grid model as an example. *Macromolecules*, 46(3):1187–1200, February 2013.

[118] Jian Qin and Scott T. Milner. Tubes, topology, and polymer entanglement. *Macromolecules*, 47(17):6077–6085, September 2014.

[119] Abelardo Ramirez-Hernandez, Francois A. Detcheverry, Brandon L. Peters, Veronica C. Chappa, Kenneth S. Schweizer, Marcus Mueller, and Juan J. de Pablo. Dynamical simulations of coarse grain polymeric systems: Rouse and entangled dynamics. *Macromolecules*, 46(15):6287–6299, August 2013.

[120] Yuichi Masubuchi. Simulating the flow of entangled polymers. *Annual Review of Chemical and Biomolecular Engineering, Vol 5*, 5:11–33, 2014.

[121] Rudi J. A. Steenbakkers, Christos Tzoumanekas, Ying Li, Wing Kam Liu, Martin Kroeger, and Jay D. Schieber. Primitive-path statistics of

entangled polymers: mapping multi-chain simulations onto single-chain mean-field models. *New Journal of Physics*, 16:015027, January 2014.

[122] D. J. Read, K. Jagannathan, and A. E. Likhtman. Entangled polymers: Constraint release, mean paths, and tube bending energy. *Macromolecules*, 41(18):6843–6853, September 2008.

[123] Jay D. Schieber. Fluctuations in entanglements of polymer liquids. *The Journal of Chemical Physics*, 118(11):5162–5166, 2003.

[124] L. Dai, C. B. Renner, and P. S. Doyle. Origin of metastable knots in single flexible chains. *Physical Review Letters*, 114(3):037801, January 2015.

[125] J. Cao, J. Qin, and S. T. Milner. Finding entanglement points in simulated polymer melts. *Macromolecules*, 48(1):99–110, January 2015.

[126] F. Zulli, M. Giordano, and L. Andreozzi. Onset of entanglement and reptation in melts of linear homopolymers: consistent rheological simulations of experiments from oligomers to high polymers. *Rheologica Acta*, 54(3):185–205, March 2015.

[127] Stefanos D. Anogiannakis, Christos Tzoumanekas, and Doros N. Theodorou. Microscopic description of entanglements in polyethylene networks and melts strong, weak, pairwise, and collective attributes. *Macromolecules*, 45(23):9475–9492, December 2012.

[128] Daniel M. Sussman and Kenneth S. Schweizer. Entangled polymer chain melts: Orientation and deformation dependent tube confinement and interchain entanglement elasticity. *Journal of Chemical Physics*, 139(23):234904, December 2013.

[129] M. H. N. Sefiddashti, B. J. Edwards, and B. Khomami. Individual chain dynamics of a polyethylene melt undergoing steady shear flow. *Journal of Rheology*, 59(1), January 2015.

[130] Z. Y. Gong and J. R. C. van der Maarel. Translational and reorientational dynamics of entangled dna. *Macromolecules*, 47(20):7230–7237, October 2014.

[131] Marat Andreev and Jay D. Schieber. Accessible and quantitative entangled polymer rheology predictions, suitable for complex flow calculations. *Macromolecules*, 48(5):1606–1613, March 2015.

[132] Daniel M. Sussman, Wei-Shao Tung, Karen I. Winey, Kenneth S. Schweizer, and Robert A. Riggleman. Entanglement reduction and anisotropic chain and primitive path conformations in polymer melts under thin film and cylindrical confinement. *Macromolecules*, 47(18):6462–6472, 2014.

[133] Marat Andreev, Renat N. Khaliullin, Rudi J. A. Steenbakkers, and Jay D. Schieber. Approximations of the discrete slip-link model and their effect on nonlinear rheology predictions. *Journal of Rheology*, 57(2):535–557, March 2013.

[134] Marat Andreev, Hualong Feng, Ling Yang, and Jay D. Schieber. Universality and speedup in equilibrium and nonlinear rheology predictions of the fixed slip-link model. *Journal of Rheology*, 58(3):723–736, May 2014.

[135] P. G. de Gennes. Reptation of a polymer chain in the presence of fixed obstacles. *The Journal of Chemical Physics*, 55(2):572–579, 1971.

[136] P. G. de Gennes and L Leger. Dynamics of entangle polymer chains. *Annual Review of Physical Chemistry*, 33:49–61, 1982.

[137] J. Klein. Evidence for reptation in an entangled polymer melt. *Nature*, 271(5641):143–145, January 1978.

[138] M. Doi and S. F. Edwards. *The Theory of Polymer Dynamics (International Series of Monographs on Physics)*. Oxford University Press, Nov 1988.

[139] Nikos Ch. Karayiannis and Martin Kröger. Combined molecular algorithms for the generation, equilibration and topological analysis of entangled polymers: Methodology and performance. *International Journal of Molecular Sciences*, 10(11):5054–5089, 2009.

[140] Robert S. Hoy, Katerina Foteinopoulou, and Martin Kröger. Topological analysis of polymeric melts: Chain-length effects and fast-converging estimators for entanglement length. *Phys. Rev. E*, 80:031803, Sep 2009.

[141] Martin Kröger. Shortest multiple disconnected path for the analysis of entanglements in two- and three-dimensional polymeric systems. *Computer Physics Communications*, 168(3):209 – 232, 2005.

[142] Sachin Shanbhag and Martin Kröger. Primitive path networks generated by annealing and geometrical methods: Insights into differences. *Macromolecules*, 40(8):2897–2903, 2007.

[143] Katerina Foteinopoulou, Nikos Ch. Karayiannis, Vlasis G. Mavrantzas, and Martin Kröger. Primitive path identification and entanglement statistics in polymer melts: Results from direct topological analysis on atomistic polyethylene models. *Macromolecules*, 39(12):4207–4216, 2006.

[144] Christos Tzoumanekas and Doros N. Theodorou. Topological analysis of linear polymer melts: A statistical approach. *Macromolecules*, 39(13):4592–4604, 2006.

[145] Ralf Everaers, Sathish K. Sukumaran, Gary S. Grest, Carsten Svaneborg, Arvind Sivasubramanian, and Kurt Kremer. Rheology and microscopic topology of entangled polymeric liquids. *Science*, 303(5659):823–826, 2004.

[146] SK Sukumaran, GS Grest, K Kremer, and R Everaers. Identifying the primitive path mesh in entangled polymer liquids. *Journal of Polymer Science Part B-Polymer Physics*, 43(8):917–933, APR 15 2005.

[147] Luca Tubiana, Enzo Orlandini, and Cristian Micheletti. Multiscale entanglement in ring polymers under spherical confinement. *Phys. Rev. Lett.*, 107:188302, Oct 2011.

[148] Ting Ge, Gary S. Grest, and Mark O. Robbins. Tensile fracture of welded polymer interfaces: Miscibility, entanglements, and crazing. *Macromolecules*, 47(19):6982–6989, October 2014.

[149] Ting Ge, Mark O. Robbins, Dvora Perahia, and Gary S. Grest. Healing of polymer interfaces: Interfacial dynamics, entanglements, and strength. *Physical Review E*, 90(1):012602, July 2014.

[150] Chuanfu Luo and Jens-Uwe Sommer. Frozen topology: Entanglements control nucleation and crystallization in polymers. *Phys. Rev. Lett.*, 112:195702, 2014.

[151] Robert A. Riggleman, Gregory Toepperwein, George J. Papakonstantopoulos, Jean-Louis Barrat, and Juan J. de Pablo. Entanglement network in nanoparticle reinforced polymers. *The Journal of Chemical Physics*, 130(24):–, 2009.

[152] Chi C. Hua and Jay D. Schieber. Segment connectivity, chain-length breathing, segmental stretch, and constraint release in reptation models. i. theory and single-step strain predictions. *The Journal of Chemical Physics*, 109(22):10018–10027, 1998.

[153] Yuichi Masubuchi, Jun-Ichi Takimoto, Kiyohito Koyama, Giovanni Ianniruberto, Giuseppe Marrucci, and Francesco Greco. Brownian simulations of a network of reptating primitive chains. *The Journal of Chemical Physics*, 115(9):4387–4394, 2001.

[154] S. Shanbhag and R. G. Larson. A slip-link model of branch-point motion in entangled polymers. *Macromolecules*, 37(21):8160–8166, 2004.

[155] Jay D. Schieber and Marat Andreev. Entangled polymer dynamics in equilibrium and flow modeled through slip links. *Annual Review of Chemical and Biomolecular Engineering*, 5(1):367–381, 2014.

[156] A. E. Likhtman. Single-Chain Slip-Link Model of Entangled Polymers: Simultaneous Description of Neutron Spin-Echo, Rheology, and Diffusion. *Macromolecules*, 38(14):6128–6139, 2005.

[157] Veronica C. Chappa, David C. Morse, Annette Zippelius, and Marcus Müller. Translationally invariant slip-spring model for entangled polymer dynamics. *Phys. Rev. Lett.*, 109:148302, Oct 2012.

[158] Takashi Uneyama and Yuichi Masubuchi. Multi-chain slip-spring model for entangled polymer dynamics. *The Journal of Chemical Physics*, 137(15), 2012.

[159] Abelardo Ramirez-Hernandez, Marcus Muller, and Juan J. de Pablo. Theoretically informed entangled polymer simulations: linear and nonlinear rheology of melts. *Soft Matter*, 9:2030–2036, 2013.

[160] Jay D. Schieber, Deepa M. Nair, and Thidaporn Kitkrailard. Comprehensive comparisons with nonlinear flow data of a consistently unconstrained brownian slip-link model. *Journal of Rheology (1978-present)*, 51(6):1111–1141, 2007.

[161] Julian Oberdisse, Giovanni Ianniruberto, Francesco Greco, and Giuseppe Marrucci. Mechanical properties of end-crosslinked entangled polymer networks using sliplink brownian dynamics simulations. *Rheologica Acta*, 46(1):95–109, 2006.

[162] D. M. Nair and J. D. Schieber. Linear viscoelastic predictions of a consistently unconstrained brownian slip-link model. *Macromolecules*, 39(9):3386–3397, May 2006.

[163] F. Tanaka and S. F.. Edwards. Viscoelastic properties of physically crosslinked networks - transient network theory. *Macromolecules*, 25(5):1516–1523, March 1992.

[164] Benjamin J. Anderson and Charles F. Zukoski. Rheology and microstructure of entangled polymer nanocomposite melts. *Macromolecules*, 42(21):8370–8384, 2009.

[165] K Gurunathan, A.Vadivel Murugan, R Marimuthu, U.P Mulik, and D.P Amalnerkar. Electrochemically synthesised conducting polymeric materials for applications towards technology in electronics, optoelectronics and energy storage devices. *Materials Chemistry and Physics*, 61(3):173 – 191, 1999.

[166] Andy Rudge, John Davey, Ian Raistrick, Shimshon Gottesfeld, and John P. Ferraris. Conducting polymers as active materials in electrochemical capacitors. *Journal of Power Sources*, 47(12):89 – 107, 1994.

[167] I. Villaluenga, X. C. Chen, D. Devaux, D. T. Hallinan, and N. P. Balsara. Nanoparticle-driven assembly of highly conducting hybrid block copolymer electrolytes. *Macromolecules*, 48(2):358–364, January 2015.

[168] Dean M. Tigelaar, Allyson E. Palker, Mary Ann B. Meador, and William R. Bennett. Synthesis and compatibility of ionic liquid containing rod-coil polyimide gel electrolytes with lithium metal electrodes. *Journal Of The Electrochemical Society*, 155(10):A768–A774, 2008.

[169] M. A. B. Meador, V. A. Cubon, D. A. Scheiman, and W. R. Bennett. Effect of branching on rod-coil block polyimides as membrane materials for lithium polymer batteries. *Chemistry of Materials*, 15(15):3018–3025, July 2003.

[170] C. C. Xue, M. A. B. Meador, L. Zhu, J. J. Ge, S. Z. D. Cheng, S. Putthanarat, R. K. Eby, A. Khalfan, G. D. Bennett, and S. G. Greenbaum. Morphology of pi-peo block copolymers for lithium batteries. *Polymer*, 47(17):6149–6155, August 2006.

[171] Vladimir Neburchilov, Jonathan Martin, Haijiang Wang, and Jiujun Zhang. A review of polymer electrolyte membranes for direct methanol fuel cells. *Journal of Power Sources*, 169(2):221 – 238, 2007.

[172] Brian C. H. Steele and Angelika Heinzel. Materials for fuel-cell technologies. *Nature*, 414(6861):345–352, November 2001.

[173] G Alberti, M Casciola, L Massinelli, and B Bauer. Polymeric proton conducting membranes for medium temperature fuel cells (110160c). *Journal of Membrane Science*, 185(1):73 – 81, 2001. Membrances in Fuel Cells.

[174] Qingfeng Li, Ronghuan He, Jens Oluf Jensen, and Niels J. Bjerrum. Approaches and recent development of polymer electrolyte membranes for fuel cells operating above 100 c. *Chemistry of Materials*, 15(26):4896–4915, 2003.

[175] K.D. Kreuer. On the development of proton conducting polymer membranes for hydrogen and methanol fuel cells. *Journal of Membrane Science*, 185(1):29 – 39, 2001. Membrances in Fuel Cells.

[176] Ulrich Wiesner. Lamellar diblock copolymers under large amplitude oscillatory shear flow: Order and dynamics. *Macromolecular Chemistry and Physics*, 198(11):3319–3352, 1997.

[177] Yuanming Zhang and Ulrich Wiesner. Symmetric diblock copolymers under large amplitude oscillatory shear flow: Entanglement effect. *The Journal of Chemical Physics*, 103(11):4784–4793, 1995.

[178] Yuanming Zhang, Ulrich Wiesner, and Hans W. Spiess. Frequency

dependence of orientation in dynamically sheared diblock copolymers. *Macromolecules*, 28(3):778–781, 1995.

[179] R. G. Larson and P. S. Desai. Modeling the rheology of polymer melts and solutions. *Annual Review of Fluid Mechanics, Vol 47*, 47:47–65, 2015.

[180] Arash Nikoubashman, Raleigh L. Davis, Brian T. Michal, Paul M. Chaikin, Richard A. Register, and Athanassios Z. Panagiotopoulos. Thin films of homopolymers and cylinder-forming diblock copolymers under shear. *ACS Nano*, 8(8):8015–8026, August 2014.

[181] Glenn Fredrickson. *The Equilibrium Theory of Inhomogeneous Polymers*. Oxford University Press, 2005.

[182] V. Pryamitsyn and V. Ganesan. Self-assembly of rod-coil block copolymers. *Journal of Chemical Physics*, 120(12):5824–5838, March 2004.

[183] M. Shah, V. Pryarnitsyn, and V. Ganesan. A model for self-assembly in side chain liquid crystalline block copolymers rid g-1845-2010. *Macromolecules*, 41(1):218–229, January 2008.

[184] Tom A. Kavassalis and Jaan Noolandi. A new theory of entanglements and dynamics in dense polymer systems. *Macromolecules*, 21(9):2869–2879, 1988.

[185] Tom A. Kavassalis and Jaan Noolandi. Entanglement scaling in polymer melts and solutions. *Macromolecules*, 22(6):2709–2720, 1989.

[186] Y. H. Lin. Number of entanglement strands per cubed tube diameter, a fundamental aspect of topological universality in polymer viscoelasticity. *Macromolecules*, 20(12):3080–3083, December 1987.

[187] S. T. Milner. Predicting the tube diameter in melts and solutions. *Macromolecules*, 38(11):4929–4939, May 2005.

[188] L. J. Fetters, D. J. Lohse, D. Richter, T. A. Witten, and A. Zirkel. Connection between polymer molecular weight, density, chain dimensions, and melt viscoelastic properties. *Macromolecules*, 27(17):4639–4647, 1994.

[189] Lewis J. Fetters, David J. Lohse, and William W. Graessley. Chain dimensions and entanglement spacings in dense macromolecular systems. *Journal of Polymer Science Part B: Polymer Physics*, 37(10):1023–1033, 1999.

[190] Lewis J. Fetters, David J. Lohse, Scott T. Milner, and William W. Graessley. Packing length influence in linear polymer melts on the entanglement, critical, and reptation molecular weights. *Macromolecules*, 32(20):6847–6851, 1999.

[191] Venkat Ganesan and Victor Pryamitsyn. Entanglements in inhomogeneous polymeric phases. *Macromolecules*, 35(24):9219–9231, 2002.

[192] Birger Steinmüller, Marcus Müller, Keith R. Hambrecht, Grant D. Smith, and Dmitry Bedrov. Properties of random block copolymer

morphologies: Molecular dynamics and single-chain-in-mean-field simulations. *Macromolecules*, 45(2):1107–1117, 2012.

[193] Vaidyanathan Sethuraman, Bryan H. Nguyen, and Venkat Ganesan. Coarse-graining in simulations of multicomponent polymer systems. *Journal of Chemical Physics*, 141(24):244904, December 2014.

[194] Antonino Salvatore Arico, Peter Bruce, Bruno Scrosati, Jean-Marie Tarascon, and Walter van Schalkwijk. Nanostructured materials for advanced energy conversion and storage devices. *Nat Mater*, 4(5):366–377, May 2005.

[195] Moon Jeong Park and Nitash P. Balsara. Anisotropic proton conduction in aligned block copolymer electrolyte membranes at equilibrium with humid air. *Macromolecules*, 43(1):292–298, 2010.

[196] Kenji Kishimoto, Tomoyuki Suzawa, Tomoki Yokota, Tomohiro Mukai, Hiroyuki Ohno, and Takashi Kato. Nano-segregated polymeric film exhibiting high ionic conductivities. *Journal of the American Chemical Society*, 127(44):15618–15623, 2005.

[197] Takeshi Niitani, Mikiya Shimada, Kiyoshi Kawamura, Kaoru Dokko, Young-Ho Rho, and Kiyoshi Kanamura. Synthesis of li+ ion conductive peo-pst block copolymer electrolyte with microphase separation structure. *Electrochemical and Solid-State Letters*, 8(8):A385–A388, 2005.

[198] Ashish K. Jha, Liang Chen, Richard D. Offeman, and Nitash P. Balsara. Effect of nanoscale morphology on selective ethanol transport through block copolymer membranes. *Journal of Membrane Science*, 373:112 – 120, 2011.

[199] Ashish K. Jha, So Ling Tsang, Ali Evren Ozcam, Richard D. Offeman, and Nitash P. Balsara. Master curve captures the effect of domain morphology on ethanol pervaporation through block copolymer membranes. *Journal of Membrane Science*, 401 - 402:125 – 131, 2012.

[200] Alexander A. Teran, Scott A. Mullin, Jr. Daniel T. Hallinan, and Nitash P. Balsara. Discontinuous changes in ionic conductivity of a block copolymer electrolyte through an orderdisorder transition. *ACS Macro Letters*, 1(2):305–309, 2012.

[201] Enrique D. Gomez, Ashoutosh Panday, Edward H. Feng, Vincent Chen, Gregory M. Stone, Andrew M. Minor, Christian Kisielowski, Kenneth H. Downing, Oleg Borodin, Grant D. Smith, and Nitash P. Balsara. Effect of ion distribution on conductivity of block copolymer electrolytes. *Nano Letters*, 9(3):1212–1216, 2009.

[202] Yu Seung Kim, Michael A. Hickner, Limin Dong, Bryan S. Pivovar, and James E. McGrath. Sulfonated poly(arylene ether sulfone) copolymer proton exchange membranes: composition and morphology effects on the methanol permeability. *Journal of Membrane Science*, 243(1-2):317 – 326, 2004.

[203] Stephen D. Druger, Mark A. Ratner, and A. Nitzan. Generalized hopping model for frequency-dependent transport in a dynamically disordered medium, with applications to polymer solid electrolytes. *Phys. Rev. B*, 31:3939–3947, Mar 1985.

[204] Zlatka Gadjourova, Yuri G. Andreev, David P. Tunstall, and Peter G. Bruce. Ionic conductivity in crystalline polymer electrolytes. *Nature*, 412(6846):520–523, August 2001.

[205] Connie B Roth and John R Dutcher. *Mobility on different length scales in thin polymer films*. University of Guelph, 2004.

[206] Connie B. Roth and John R. Dutcher. Glass transition and chain mobility in thin polymer films. *Journal of Electroanalytical Chemistry*, 584(1):13 – 22, 2005.

[207] Evangelos Voyiatzis, Mohammad Rahimi, Florian Müller-Plathe, and Michael C. Böhm. How thick is the polymer interphase in nanocomposites? probing it by local stress anisotropy and gas solubility. *Macromolecules*, 47(22):7878–7889, 2014.

[208] François A. Detcheverry, Guoliang Liu, Paul F. Nealey, and Juan J. de Pablo. Interpolation in the directed assembly of block copolymers on nanopatterned substrates: Simulation and experiments. *Macromolecules*, 43(7):3446–3454, 2010.

[209] Jane E. G. Lipson and Scott T. Milner. Local and average glass transitions in polymer thin films. *Macromolecules*, 43(23):9874–9880, 2010.

[210] W. Cheng, R. Sainidou, P. Burgardt, N. Stefanou, M. Kiyanova, A. Efremov, and P. F. Fytas, G.and Nealey. Elastic properties and glass transition of supported polymer thin films. *Macromolecules*, 40(20):7283–7290, 2007.

[211] David S. Fryer, Richard D. Peters, Eui Jun Kim, Jeanne E. Tomaszewski, Juan J. de Pablo, , Paul F. Nealey, Chris C. White, , and Wen-li Wu. Dependence of the glass transition temperature of polymer films on interfacial energy and thickness. *Macromolecules*, 34(16):5627–5634, 2001.

[212] J. A Torres, P. F. Nealey, and J. J. de Pablo. Molecular simulation of ultrathin polymeric films near the glass transition. *Phys. Rev. Lett.*, 85:3221–3224, Oct 2000.

[213] Roman R. Baglay and Connie B. Roth. Experimentally determined profile of local glass transition temperature across a glassy-rubbery polymer interface with a tg difference of 80 k. *Submitted*, -:–, 2015.

[214] Connie B. Roth and John M. Torkelson. Selectively probing the glass transition temperature in multilayer polymer films: Equivalence of block copolymers and multilayer films of different homopolymers. *Macromolecules*, 40(9):3328–3336, 2007.

[215] Christopher J. Ellison and John M. Torkelson. The distribution of glass-transition temperatures in nanoscopically confined glass formers. *Nat Mater*, 2(10):695–700, October 2003.

[216] P. Rittigstein, R. D. Priestley, L. J. Broadbelt, and J. M. Torkelson. Model polymer nanocomposites provide an understanding of confinement effects in real nanocomposites. *Nature Materials*, 6(4):278–282, April 2007.

[217] Roman R. Baglay and Connie B. Roth. Local glass transition temperature tg(z) of polystyrene next to different polymers: Hard vs. soft confinement. *The Journal of Chemical Physics*, 146(20):203307, 2017.

[218] R. D. Priestley and R Register. Private communication. *Private Communication, APS March Meeting 2016*, 2017.

[219] F. Alvarez, A. Alegra, and J. Colmenero. Relationship between the time-domain kohlrausch-williams-watts and frequency-domain havriliak-negami relaxation functions. *Phys. Rev. B*, 44:7306–7312, Oct 1991.

[220] Patrick Charbonneau, Atsushi Ikeda, Giorgio Parisi, and Francesco Zamponi. Dimensional study of the caging order parameter at the glass transition. *Proceedings of the National Academy of Sciences*, 109(35):13939–13943, 2012.

[221] Paul Hopkins, Andrea Fortini, Andrew J. Archer, and Matthias Schmidt. The van hove distribution function for brownian hard spheres: Dynam-

ical test particle theory and computer simulations for bulk dynamics. *The Journal of Chemical Physics*, 133(22):–, 2010.

[222] Andrew J. Archer, Paul Hopkins, and Matthias Schmidt. Dynamics in inhomogeneous liquids and glasses via the test particle limit. *Phys. Rev. E*, 75:040501, Apr 2007.

[223] M. Aichele and J. Baschnagel. Glassy dynamics of simulated polymer melts: Coherent scattering and van hove correlation functions. *The European Physical Journal E*, 5(2):229–243, 2001.

[224] Oleg Borodin, Grant D. Smith, Rajdip Bandyopadhyaya, and Oleksiy Byutner. Molecular dynamics study of the influence of solid interfaces on poly(ethylene oxide) structure and dynamics. *Macromolecules*, 36(20):7873–7883, 2003.

[225] J. Baschnagel and F. Varnik. Computer simulations of supercooled polymer melts in the bulk and in-confined geometry. *Journal of Physics-condensed Matter*, 17(32):R851–R953, August 2005.

[226] J. L. Barrat, J. Baschnagel, and A. Lyulin. Molecular dynamics simulations of glassy polymers. *Soft Matter*, 6(15):3430–3446, 2010.

[227] P. Z. Hanakata, J. F. Douglas, and F. W. Starr. Local variation of fragility and glass transition temperature of ultra-thin supported polymer films. *Journal of Chemical Physics*, 137(24):244901, December 2012.

[228] J. H. Mangalara, M. D. Marvin, N. R. Wiener, M. E. Mackura, and D. S. Simmons. Does fragility of glass formation determine the strength of t-g-nanoconfinement effects? *Journal of Chemical Physics*, 146(10):104902, March 2017.

[229] J. H. Mangalara, M. E. Mackura, M. D. Marvin, and D. S. Simmons. The relationship between dynamic and pseudo-thermodynamic measures of the glass transition temperature in nanostructured materials. *Journal of Chemical Physics*, 146(20):203316, May 2017.

[230] Wei-Fan Kuan, Roddel Remy, Michael E. Mackay, and Thomas H. Epps, III. Controlled ionic conductivity via tapered block polymer electrolytes. *RSC Adv.*, 5:12597–12604, 2015.

[231] M. W. Matsen, , and F. S. Bates. Unifying weak- and strong-segregation block copolymer theories. *Macromolecules*, 29(4):1091–1098, 1996.

[232] Youngmi Seo, Jonathan R. Brown, and Lisa M. Hall. Effect of tapering on morphology and interfacial behavior of diblock copolymers from molecular dynamics simulations. *Macromolecules*, 48(14):4974–4982, 2015.

[233] Raghunath Roy, Jong Keun Park, Wen-Shiue Young, Sarah E. Mastroianni, Maëva S. Tureau, and III Thomas H. Epps. Double-gyroid network morphology in tapered diblock copolymers. *Macromolecules*, 44(10):3910–3915, 2011.

[234] Vaidyanathan Sethuraman and Venkat Ganesan. Segmental dynamics in lamellar phases of tapered copolymers. *Soft Matter*, 12:7818–7823, 2016.

[235] Takeji Hashimoto, Yasuhisa Tsukahara, and Hiromichi Kawai. Structure and properties of tapered block polymers of styrene and isoprene ii. dynamic mechanical responses and their structural interpretations. *Polym J*, 15(10):699–711, 1983.

[236] P. Hodrokoukes, G. Floudas, S. Pispas, , and N. Hadjichristidis. Microphase separation in normal and inverse tapered block copolymers of polystyrene and polyisoprene. 1. phase state. *Macromolecules*, 34(3):650–657, 2001.

[237] Michelle M. Mok, Jungki Kim, Christopher L. H. Wong, Stephen R. Marrou, Dong Jin Woo, Christine M. Dettmer, SonBinh T. Nguyen, Christopher J. Ellison, Kenneth R. Shull, and John M. Torkelson. Glass transition breadths and composition profiles of weakly, moderately, and strongly segregating gradient copolymers: Experimental results and calculations from self-consistent mean-field theory. *Macromolecules*, 42(20):7863–7876, 2009.

[238] Jonathan R. Brown, Scott W. Sides, and Lisa M. Hall. Phase behavior of tapered diblock copolymers from self-consistent field theory. *ACS Macro Letters*, 2(12):1105–1109, 2013.

[239] Zuowei Wang and Ronald G. Larson. Constraint release in entangled

binary blends of linear polymers: A molecular dynamics study. *Macromolecules*, 41(13):4945–4960, July 2008.

[240] Oleg Borodin and Grant D. Smith. Litfsi structure and transport in ethylene carbonate from molecular dynamics simulations. *The Journal of Physical Chemistry B*, 110(10):4971–4977, 2006.

[241] William Hoover. Canonical dynamics: Equilibrium phase-space distributions. *Phys. Rev. A*, 31:1695–1697, Mar 1985.

[242] Glenn J. Martyna, Douglas J. Tobias, and Michael L. Klein. Constant pressure molecular dynamics algorithms. *The Journal of Chemical Physics*, 101(5):4177–4189, 1994.

[243] Mark P. Stoykovich and Paul F. Nealey. Block copolymers and conventional lithography. *Materials Today*, 9(9):20 – 29, 2006.

[244] Dan Peer, Jeffrey M. Karp, Seungpyo Hong, Omid C. Farokhzad, Rimona Margalit, and Robert Langer. Nanocarriers as an emerging platform for cancer therapy. *Nat Nano*, 2(12):751–760, December 2007.

[245] Andreas Taubert, Alessandro Napoli, and Wolfgang Meier. Self-assembly of reactive amphiphilic block copolymers as mimetics for biological membranes. *Current Opinion in Chemical Biology*, 8(6):598 – 603, 2004.

[246] T. Kreer, J. Baschnagel, M. Múller, and K. Binder. Monte carlo simulation of long chain polymer melts: Crossover from rouse to reptation dynamics. *Macromolecules*, 34(4):1105–1117, 2001.

[247] YN Kaznessis, DA Hill, and EJ Maginn. Molecular dynamics simulations of polar polymer brushes. *MACROMOLECULES*, 31(9):3116–3129, 1998.

[248] C. M. Roland and C. A. Bero. Normal mode relaxation in linear and branched polyisoprene. *Macromolecules*, 29(23):7521–7526, 1996.

[249] B. Stuehn and F. Stickel. Dielectric normal mode spectroscopy in the ordered and disordered states of diblock copolymers. *Macromolecules*, 25(20):5306–5312, 1992.

[250] Angel Alegria, Reidar Lund, Fabienne Barroso-Bujans, Arantxa Arbe, and Juan Colmenero. Component dynamics in nanostructured pi-pdms diblock copolymers with pi segregated in lamellas, cylinders, and spheres. *Colloid and Polymer Science*, 292(8):1863–1876, 2014.

[251] Jacek Jenczyk, Maria Dobies, Monika Makrocka-Rydzyk, Aleksandra Wypych, and Stefan Jurga. The segmental and global dynamics in lamellar microphase-separated poly(styrene-b-isoprene) diblock copolymer studied by h-1 nmr and dielectric spectroscopy. *EUROPEAN POLYMER JOURNAL*, 49(12):3986–3997, 2013.

[252] Michelle M. Mok, Kevin A. Masser, James Runt, and John M. Torkelson. Dielectric relaxation spectroscopy of gradient copolymers and block copolymers: Comparison of breadths in relaxation time for systems with increasing interphase. *Macromolecules*, 43(13):5740–5748, 2010.

[253] Tadao Kotaka and Keiichiro Adachi. Polymer liquid dynamics studied via dielectric normal mode spectroscopy. *Macromolecular Symposia*, 124(1):3–14, 1997.

[254] Alejandro Sanz, Aurora Nogales, and Tiberio A. Ezquerra. From hard to soft confinement in a symmetric block copolymer: local and segmental dynamics. *Soft Matter*, 7:6477–6483, 2011.

[255] Lourdes del Valle-Carrandi, Angel Alegría, Arantxa Arbe, and Juan Colmenero. Unexpected pdms behavior in segregated cylindrical and spherical nanophases of ps-pdms asymmetric diblock copolymers. *Macromolecules*, 45(1):491–502, 2012.

[256] Ming Long Yao, Hiroshi Watanabe, Keiichiro Adachi, and Tadao Kotaka. Dielectric relaxation behavior of styrene-isoprene diblock copolymers: bulk systems. *Macromolecules*, 24(10):2955–2962, 1991.

[257] Jörg Baschnagel, Kurt Binder, Pemra Doruker, AndreiA. Gusev, Oliver Hahn, Kurt Kremer, WayneL. Mattice, Florian Müller-Plathe, Michael Murat, Wolfgang Paul, Serge Santos, UlrichW. Suter, and Volker Tries. Bridging the gap between atomistic and coarse-grained models of polymers: Status and perspectives. In *Viscoelasticity, Atomistic Models, Statistical Chemistry*, volume 152 of *Advances in Polymer Science*, pages 41–156. Springer Berlin Heidelberg, 2000.

[258] Alexander Hoffmann, Jens-Uwe Sommer, and Alexander Blumen. Com-

puter simulations of asymmetric block copolymers. *J. Chem. Phys.*, 107(18):7559–7570, 1997.

[259] Marcus Müller and Kostas Ch. Daoulas. Single-chain dynamics in a homogeneous melt and a lamellar microphase: A comparison between smart monte carlo dynamics, slithering-snake dynamics, and slip-link dynamics. *The Journal of Chemical Physics*, 129(16), 2008.

[260] William W. Graessley. Entangled linear, branched and network polymer systems: Molecular theories. In *Synthesis and Degradation Rheology and Extrusion*, volume 47 of *Advances in Polymer Science*, pages 67–117. Springer Berlin Heidelberg, 1982.

[261] Martin Koch, Jens-Uwe Sommer, and Alexander Blumen. Polymer chains tethered to impenetrable interfaces: Broadening of relaxation spectra. *The Journal of Chemical Physics*, 106(3):1248–1256, 1997.

[262] Ming Long Yao, Hiroshi Watanabe, Keiichiro Adachi, and Tadao Kotaka. Dielectric relaxation of styrene-isoprene diblock copolymer solutions: a common solvent system. *Macromolecules*, 25(6):1699–1704, 1992.

[263] H. Meyer, J.P. Wittmer, T. Kreer, P. Beckrich, A. Johner, J. Farago, and J. Baschnagel. Static rouse modes and related quantities: Corrections to chain ideality in polymer melts. *The European Physical Journal E*, 26(1-2):25–33, 2008.

[264] Jens Glaser, Pavani Medapuram, Thomas M. Beardsley, Mark W. Matsen, and David C. Morse. Universality of block copolymer melts. *Phys. Rev. Lett.*, 113:068302, Aug 2014.

[265] Victor Pryamitsyn and Venkat Ganesan. Origins of linear viscoelastic behavior of polymernanoparticle composites. *Macromolecules*, 39(2):844–856, 2006.

[266] S. Peter, S. Napolitano, H. Meyer, M. Wbbenhorst, and J. Baschnagel. Modeling dielectric relaxation in polymer glass simulations: Dynamics in the bulk and in supported polymer films. *Macromolecules*, 41(20):7729–7743, 2008.

[267] A. Barbieri, E. Campani, S. Capaccioli, and D. Leporini. Molecular dynamics study of the thermal and the density effects on the local and the large-scale motion of polymer melts: Scaling properties and dielectric relaxation. *The Journal of Chemical Physics*, 120(1):437–453, 2004.

[268] Vaidyanathan Sethuraman, Dylan Kipp, and Venkat Ganesan. Entanglements in lamellar phases of diblock copolymers. *Macromolecules*, 48(17):6321–6328, 2015.

[269] C. Lorthioir, A. Alegría, J. Colmenero, and B. Deloche. Heterogeneity of the segmental dynamics of poly(dimethylsiloxane) in a diblock lamellar mesophase: dielectric relaxation investigations. *Macromolecules*, 37(20):7808–7817, 2004.

[270] Valle-Carrandi, L. del, Alegría, A., and Colmenero, J. Pdms behaviour under confinement in strongly segregated mesophases of ps-pdms diblock copolymers. *Eur. Phys. J. Special Topics*, 189:257–261, 2010.

[271] G.M. Geise, B.D. Freeman, and D.R. Paul. Characterization of a sulfonated pentablock copolymer for desalination applications. *Polymer*, 51(24):5815 – 5822, 2010.

[272] Wei Xie, Joe Cook, Ho Bum Park, Benny D. Freeman, Chang Hyun Lee, and James E. McGrath. Fundamental salt and water transport properties in directly copolymerized disulfonated poly(arylene ether sulfone) random copolymers. *Polymer*, 52(9):2032 – 2043, 2011.

[273] Didier Devaux, David Glé, Trang N. T. Phan, Didier Gigmes, Emmanuelle Giroud, Marc Deschamps, Renaud Denoyel, and Renaud Bouchet. Optimization of block copolymer electrolytes for lithium metal batteries. *Chemistry of Materials*, 27(13):4682–4692, 2015.

[274] Santosh Mogurampelly and Venkat Ganesan. Effect of nanoparticles on ion transport in polymer electrolytes. *Macromolecules*, 48(8):2773–2786, 2015.

[275] Rodger Yuan, Alexander A. Teran, Inna Gurevitch, Scott A. Mullin, Nisita S. Wanakule, and Nitash P. Balsara. Ionic conductivity of low molecular weight block copolymer electrolytes. *Macromolecules*, 46(3):914–921, 2013.

[276] Issei Nakamura, Nitash P. Balsara, and Zhen-Gang Wang. Thermodynamics of ion-containing polymer blends and block copolymers. *Phys. Rev. Lett.*, 107:198301, Nov 2011.

[277] Tim N. Heinz, Wilfred F. van Gunsteren, and Philippe H. Hnenberger. Comparison of four methods to compute the dielectric permittivity of liquids from molecular dynamics simulations. *The Journal of Chemical Physics*, 115(3):1125–1136, 2001.

[278] Nisita S. Wanakule, Justin M. Virgili, Alexander A. Teran, Zhen-Gang Wang, and Nitash P. Balsara. Thermodynamic properties of block copolymer electrolytes containing imidazolium and lithium salts. *Macromolecules*, 43(19):8282–8289, 2010.

[279] Zhiping Liu, Xiaoping Wu, and Wenchuan Wang. A novel united-atom force field for imidazolium-based ionic liquids. *Phys. Chem. Chem. Phys.*, 8:1096–1104, 2006.

[280] Hui Wu and Collin D. Wick. Computational investigation on the role of plasticizers on ion conductivity in poly(ethylene oxide) litfsi electrolytes. *Macromolecules*, 43(7):3502–3510, 2010.

[281] V. A. Harmandaris, N. P. Adhikari, N. F. A. van der Vegt, and K. Kremer. Hierarchical modeling of polystyrene: From atomistic to coarse-grained simulations. *Macromolecules*, 39(19):6708–6719, 2006.

[282] Marcus G. Martin and J. Ilja Siepmann. Transferable potentials for phase equilibria. 1. united-atom description of n-alkanes. *The Journal of Physical Chemistry B*, 102(14):2569–2577, 1998.

[283] Collin D. Wick, Marcus G. Martin, and J. Ilja Siepmann. Transferable potentials for phase equilibria. 4. united-atom description of linear and branched alkenes and alkylbenzenes. *The Journal of Physical Chemistry B*, 104(33):8008–8016, 2000.

[284] John M. Stubbs, Jeffrey J. Potoff, and J. Ilja Siepmann. Transferable potentials for phase equilibria. 6. united-atom description for ethers, glycols, ketones, and aldehydes. *The Journal of Physical Chemistry B*, 108(45):17596–17605, 2004.

[285] Giuseppe Milano, , and Florian Müller-Plathe. Mapping atomistic simulations to mesoscopic models:a systematic coarse-graining procedure for vinyl polymer chains. *The Journal of Physical Chemistry B*, 109(39):18609–18619, 2005.

[286] Dirk Reith, Hendrik Meyer, and Florian Mller-Plathe. Mapping atomistic to coarse-grained polymer models using automatic simplex optimization to fit structural properties. *Macromolecules*, 34(7):2335–2345, 2001.

[287] Dylan Kipp and Venkat Ganesan. Influence of block copolymer compatibilizers on the morphologies of semiflexible polymer/solvent blends. *The Journal of Physical Chemistry B*, 118(16):4425–4441, 2014.

[288] Kostas Ch. Daoulas, Marcus Muller, Juan J. de Pablo, Paul F. Nealey, and Grant D. Smith. Morphology of multi-component polymer systems: single chain in mean field simulation studies. *Soft Matter*, 2:573–583, 2006.

[289] Kostas Ch Daoulas, Victor Rúhle, and Kurt Kremer. Simulations of nematic homopolymer melts using particle-based models with interactions expressed through collective variables. *Journal of Physics: Condensed Matter*, 24(28):284121, 2012.

[290] Christine Peter and Kurt Kremer. Multiscale simulation of soft matter systems. *Faraday Discuss.*, 144:9–24, 2010.

[291] François A. Detcheverry, Darin Q. Pike, Paul F. Nealey, Marcus Müller, and Juan J. de Pablo. Monte carlo simulation of coarse grain polymeric systems. *Phys. Rev. Lett.*, 102:197801, May 2009.

[292] Marcus Múller and Juan J. de Pablo. Computational approaches for the dynamics of structure formation in self-assembling polymeric materials. *Annual Review of Materials Research*, 43(1):1–34, 2013.

[293] Christine Peter and Kurt Kremer. Multiscale simulation of soft matter systems - from the atomistic to the coarse-grained level and back. *Soft Matter*, 5:4357–4366, 2009.

[294] R. W. Hockney and J. W. Eastwood. *Computer simulation using particles*. CRC Press, 1988.

[295] Oleg Borodin and Grant D. Smith. Molecular dynamics simulations of poly(ethylene oxide)/lii melts. 1. structural and conformational properties. *Macromolecules*, 31(23):8396–8406, 1998.

[296] Jingze Li, Kaori Kamata, Motonori Komura, Takeshi Yamada, Hirohisa Yoshida, and Tomokazu Iyoda. Anisotropic ion conductivity in liquid crystalline diblock copolymer membranes with perpendicularly oriented peo cylindrical domains. *Macromolecules*, 40(23):8125–8128, 2007.

[297] Pawel W. Majewski, Manesh Gopinadhan, Woo-Sik Jang, Jodie L. Lutkenhaus, and Chinedum O. Osuji. Anisotropic ionic conductivity in block copolymer membranes by magnetic field alignment. *Journal of the American Chemical Society*, 132(49):17516–17522, 2010. PMID: 21090713.

[298] Pawel W. Majewski, Manesh Gopinadhan, and Chinedum O. Osuji. Understanding anisotropic transport in self-assembled membranes and maximizing ionic conductivity by microstructure alignment. *Soft Matter*, 9:7106–7116, 2013.

[299] Issei Nakamura. Ion solvation in polymer blends and block copolymer melts: Effects of chain length and connectivity on the reorganization of dipoles. *The Journal of Physical Chemistry B*, 118(21):5787–5796, 2014.

[300] Chun-Lai Ren, Issei Nakamura, and Zhen-Gang Wang. Effects of ion-induced cross-linking on the phase behavior in salt-doped polymer blends. *Macromolecules*, 49(1):425–431, 2016.

[301] Gyuha Jo, Hyungmin Ahn, and Moon Jeong Park. Simple route for tuning the morphology and conductivity of polymer electrolytes: One end functional group is enough. *ACS Macro Letters*, 2(11):990–995, 2013.

[302] Jie Huang, Zai-Zai Tong, Bing Zhou, Jun-Ting Xu, and Zhi-Qiang Fan. Salt-induced microphase separation in poly(-caprolactone)-b-poly(ethylene oxide) block copolymer. *Polymer*, 54(12):3098 – 3106, 2013.

[303] E. M. Sevick, P. A. Monson, and J. M. Ottino. Monte carlo calculations of cluster statistics in continuum models of composite morphology. *The Journal of Chemical Physics*, 88(2):1198–1206, 1988.

[304] K. M. Abraham, Z. Jiang, , and B. Carroll. Highly conductive peo-like polymer electrolytes. *Chemistry of Materials*, 9(9):1978–1988, 1997.

[305] Mark A. Ratner and Duward F. Shriver. Ion transport in solvent-free polymers. *Chemical Reviews*, 88(1):109–124, 1988.

[306] Wen-Shiue Young and Thomas H. Epps. Salt doping in peo-containing block copolymers: Counterion and concentration effects. *Macromolecules*, 42(7):2672–2678, 2009.

[307] Wen-Shiue Young, Julie N. L. Albert, A. Benjamin Schantz, and Thomas H. Epps. Mixed-salt effects on the ionic conductivity of lithium-

doped peo-containing block copolymers. *Macromolecules*, 44(20):8116–8123, 2011.

[308] Jae-Hong Choi, Yuesheng Ye, Yossef A. Elabd, and Karen I. Winey. Network structure and strong microphase separation for high ion conductivity in polymerized ionic liquid block copolymers. *Macromolecules*, 46(13):5290–5300, 2013.

[309] Mohit Singh, Omolola Odusanya, Gregg M. Wilmes, Hany B. Eitouni, Enrique D. Gomez, Amish J. Patel, Vincent L. Chen, Moon Jeong Park, Panagiota Fragouli, Hermis Iatrou, Nikos Hadjichristidis, David Cookson, and Nitash P. Balsara. Effect of molecular weight on the mechanical and electrical properties of block copolymer electrolytes. *Macromolecules*, 40(13):4578–4585, 2007.

[310] Dunyang Rita Wang, Kevin H. Wujcik, Alexander A. Teran, and Nitash P. Balsara. Conductivity of block copolymer electrolytes containing lithium polysulfides. *Macromolecules*, 48(14):4863–4873, 2015.

[311] Sharon Sharick, Jason Koski, Robert A. Riggleman, and Karen I. Winey. Isolating the effect of molecular weight on ion transport of non-ionic diblock copolymer/ionic liquid mixtures. *Macromolecules*, 49(6):2245–2256, 2016.

[312] Thomas H. Epps, Travis S. Bailey, Hoai D. Pham, and Frank S. Bates. Phase behavior of lithium perchlorate-doped poly(styrene-b-isoprene-b-

ethylene oxide) triblock copolymers. *Chemistry of Materials*, 14(4):1706–1714, 2002.

[313] Anne-Valrie G. Ruzette, Philip P. Soo, Donald R. Sadoway, and Anne M. Mayes. Melt-formable block copolymer electrolytes for lithium rechargeable batteries. *Journal of The Electrochemical Society*, 148(6):A537–A543, 2001.

[314] L. Xie and G.C. Farrington. Molecular mechanics and dynamics simulation of poly (ethylene oxide) electrolytes. *Solid State Ionics*, 53:1054 – 1058, 1992.

[315] C.R.A. Catlow and G.E. Mills. Computer simulation of ionically conducting polymers. *Electrochimica Acta*, 40(13):2057 – 2062, 1995. International symposium on polymer electrolytes.

[316] Sylvie Neyertz and David Brown. Local structure and mobility of ions in polymer electrolytes: A molecular dynamics simulation study of the amorphous peoxnai system. *The Journal of Chemical Physics*, 104(10):3797–3809, 1996.

[317] Oleg Borodin and Grant D. Smith. Molecular dynamics simulations of poly(ethylene oxide)/lii melts. 2. dynamic properties. *Macromolecules*, 33(6):2273–2283, 2000.

[318] Diddo Diddens, Andreas Heuer, and Oleg Borodin. Understanding the

lithium transport within a rouse-based model for a peo/litfsi polymer electrolyte. *Macromolecules*, 43(4):2028–2036, 2010.

[319] Florian Müller-Plathe and Wilfred F. van Gunsteren. Computer simulation of a polymer electrolyte: Lithium iodide in amorphous poly(ethylene oxide). *The Journal of Chemical Physics*, 103(11):4745–4756, 1995.

[320] A. Maitra and A. Heuer. Cation transport in polymer electrolytes: A microscopic approach. *Phys. Rev. Lett.*, 98:227802, May 2007.

[321] Vaidyanathan Sethuraman, Victor Pryamitsyn, and Venkat Ganesan. Influence of molecular weight and degree of segregation on local segmental dynamics of ordered block copolymers. *J. Polym. Sci. Part B: Polym. Phys.*, 54(9):859–864, 2016.

[322] N. Arun Kumar and Venkat Ganesan. Communication: Self-assembly of semiflexible-flexible block copolymers. *The Journal of Chemical Physics*, 136(10):101101, 2012.

[323] Dylan Kipp, Olga Wodo, Baskar Ganapathysubramanian, and Venkat Ganesan. Achieving bicontinuous microemulsion like morphologies in organic photovoltaics. *ACS Macro Letters*, 4(2):266–270, 2015.

[324] Dylan Kipp, Rafael Verduzco, and Venkat Ganesan. Design of bicontinuous donor/acceptor morphologies for use as organic solar cell active layers. *Journal of Polymer Science Part B: Polymer Physics*, 54(9):884–895, 2016.

[325] W. Tschöp, K. Kremer, O. Hahn, J. Batoulis, and T. Bürger. Simulation of polymer melts. ii. from coarse-grained models back to atomistic description. *Acta Polymerica*, 49(2-3):75–79, 1998.

[326] Cameron F. Abrams and Kurt Kremer. Combined coarse-grained and atomistic simulation of liquid bisphenol–polycarbonate: Liquid packing and intramolecular structure. *Macromolecules*, 36(1):260–267, 2003.

[327] J. Rieger. The glass transition temperature of polystyrene. *Journal of thermal analysis*, 46(3):965–972, 1996.

[328] Nicolaas A. Stolwijk, Christian Heddier, Manuel Reschke, Manfred Wiencierz, Joachim Bokeloh, and Gerhard Wilde. Salt-concentration dependence of the glass transition temperature in peo–nai and peo–litfsi polymer electrolytes. *Macromolecules*, 46(21):8580–8588, 2013.

[329] B. L. Bhargava, A. C. Krishna, and S. Balasubramanian. Molecular dynamics simulation studies of co2 – [bmim][pf6] solutions: Effect of co2 concentration. *AIChE Journal*, 54(11):2971–2978, 2008.

[330] Jae-Hong Choi, Carl L. Willis, and Karen I. Winey. Structure property relationship in sulfonated pentablock copolymers. *Journal of Membrane Science*, 394395:169 – 174, 2012.

[331] Peter H. Verdier and W. H. Stockmayer. Monte carlo calculations on the dynamics of polymers in dilute solution. *The Journal of Chemical Physics*, 36(1):227–235, 1962.

[332] Peter H. Verdier. Monte carlo studies of lattice model polymer chains. i. correlation functions in the statistical bead model. *The Journal of Chemical Physics*, 45(6):2118–2121, 1966.

[333] A.E. Likhtman. 1.06 - viscoelasticity and molecular rheology. In *Polymer Science: A Comprehensive Reference*, pages 133 – 179. Elsevier, Amsterdam, 2012.

Vita

Vaidyanathan Mathamangalath Sethuraman was born in Kerala, India. He received the Bachelor of Technology degree in Chemical Engineering from National Institute of Technology, Calicut, India in May 2010. Subsequently, he received his Masters' of Science in Chemical Engineering degree from Indian Institute of Science, Bangalore, India in June 2013. He joined The University of Texas at Austin for his PhD. under the guidance of Prof. Venkat Ganesan in January 2013.

Permanent address: msvaidyanathan1729@gmail.com

This dissertation was typeset with LaTeX[†] by the author.

[†]LaTeX is a document preparation system developed by Leslie Lamport as a special version of Donald Knuth's TeX Program.